Prediction of size effects and regularization of adiabatic shear band formation in single and poly-crystals : Gradient crystal plasticity approach

Vikram Phalke

PSL UNIVERSITÉ PARIS

THÈSE DE DOCTORAT

DE L'UNIVERSITÉ PSL

Préparée à MINES ParisTech

Prediction of size effects and regularization of adiabatic shear band formation in single and poly-crystals: Gradient crystal plasticity approach

–

Prédiction des effets de taille et régularisation de la formation de bandes de cisaillement adiabatiques dans les monocristaux et les polycristaux: Approche de plasticité cristalline à gradient

Soutenue par

Vikram PHALKE

Le 12/01/2022

École doctorale n°621

Ingénierie des Systèmes, Matériaux, Mécanique, Energétique

Spécialité

Mécanique

Composition du jury :

M. Olivier CAHUC Professeur, Université de Bordeaux, France	*Président du Jury*
M. Daniel RITTEL Professeur, Technion, Israël	*Rapporteur*
M. Patrice LONGERE Professeur, ISAE-SUPAERO Toulouse, France	*Rapporteur*
M. Alankar ALANKAR Associate Professeur, IIT Bombay, Inde	*Examinateur*
Mme. Tonya ROSE Ingénieur, Safran Tech, France	*Examinateur*
M. Samuel FOREST Professeur, Mines ParisTech, France	*Directeur de thèse*
M. Arjen ROOS Ingénieur, Safran Tech, France	*Co-directeur de thèse*

MINES ParisTech | PSL

This thesis is dedicated to my family!

Acknowledgement

I would like to express my deep gratitude and heartily thanks to my PhD supervisors, Samuel Forest, Hyung-Jun Chang, and Arjen Roos, for their immense support and valuable guidance. Samuel played a vital role in the success of this thesis. Samuel, thank you for your continuous encouragement and support throughout the thesis. The guidance and scientific discussions with Hyung-Jun gave me the understanding and clarity of the subject. Arjen enabled me to go through the PhD with ease.

I sincerely thank the PhD defense jury members, Professors Daniel Rittel, Patrice Longère, Olivier Cahuc, Alankar Alankar, and engineer Tonya Rose for taking time out of their busy schedules to attend my thesis defense. Their constructive comments helped me to rectify my thesis in a better way.

At the Centre des Matèriaux, I would like to thank Véronique Matos, Claudine Devemy, Sandrine Fontaine, Catherine Rouil, and Ziradjoudine Akber (Zak) for handling administrative issues. I especially thank Djamel Missoum-Benziane, Kais Ammar, and Basile Marchand for helping me in solving the software-related problems. I would extend my gratitude to Vladislav Yastrebov, Jacques Besson, and Jean-Michel Scherer for the scientific discussions. I would like to thank Franck N'guyen for providing meshed geometries for the indentation simulations. Many thanks to Grégory Sainte-Luce and Patrice Viotti for handling my IT related issues. I humbly thank Faisal Islam, Harris Farooq, Rami Bouaziz, and Jan Rojek for making my initial days in France compelling. Thanks to Mohamed Abatour, Xiang Kong, and Houssem Eddine Chaieb for always being there for me. My thanks are extended to my officemates Daniel Irmer and Chiraz Belhadj, for many exciting and funny conversations.

At Safran Tech, I especially thank to Audrey Gesret and Sandrine Duprey for taking care of administrative issues. I would like to thank Nicolas Feld and Tonya Rose for giving time from their busy schedule to read and correct my manuscript. I humbly thank Mouad Fergoug, Vicenzo Zarra, and Maurine Jacot for making my stay at Safran compelling all time. I would extend my thanks to all the Modeling & Simulation department people for their kindness and friendliness.

Apart from CdM and Safran Tech, I got an opportunity to work with people from different labs worldwide. I especially thank Tobias Kaiser (Technische Universität Dortmund) and Jean-Briac le Graverend (Texas A&M University).

My thesis was a part of the European project called ENABLE under the Horizon 2020 program, which allowed me to work in several universities and companies across Europe. The people at ENABLE project have honestly been one of the best parts of thesis work. I would like to thank ENABLE project coordinators Olivier Cahuc and Sara Marin for the coordination of this project. The support and guidance they have provided during

the past three years were outstanding. I extend my thanks to Franck Girot for providing scientific and non-scientific training during this project. During my secondments, I got an opportunity to work with Luleå University of Technology (LTU) - Sweden, ESI Group - France, and University of the Basque Country - UPV/EHU (UPV) - Spain. I would like to thank Paul Åkerström, Lars-Erik Lindgren, and all people from the Solid Mechanics division at LTU for allowing me to do my secondment at LTU. I humbly thank Didier Croizet and Mustapha Ziane for helping us to implement the micromorphic model in PAM-Crash during our secondment with ESI Group. Thanks to Franck Girot for providing a secondment opportunity at UPV. Finally, thanks to the heart of the ENABLE project, i.e., all ESRs, Marie-Anna Moretti, Biswajit Dalai, Trunal Dhawale, Raffaele Russo, Tamara Dancheva, Haythem Zouabi, Danilo Ambrosio, and Pinku Yadav, without who my thesis could have been incomplete. It's been great working together. This might be the end of the ENABLE project. But, it's definitely not the end of our friendship and collaborations. I am so thankful to Marie-Anna Moretti for reading and giving her feedback on one of the chapters of my thesis. Thanks to Raffaele Russo for the collaboration during secondment at ESI Group.

A special acknowledgment goes to my family and friends back in India. The constant encouragement from my late grandmother (Aai) and primary school teacher (Guruji) helped me to shape in a better way. Special thanks go to my parents (Aba and Mai), brother (Bhaiya), and sister (Tai) for their immense support in different phases of life. Things would have been very different without their support.

Notations

• Tensors

Description	*Notation*
Vector	$\underline{A}$
Second-order tensor	$\underset{\sim}{A}$
Transpose	$\underset{\sim}{A}^T$
Inverse	$\underset{\sim}{A}^{-1}$
Time derivative	$\dot{\underset{\sim}{A}}$

• Contractions

Description	*Index notation*
Simple contraction $(\underline{a} \cdot \underline{b})$	$a_i b_j$
Double contraction $(\underset{\sim}{A} : \underset{\sim}{B})$	$A_{ij} B_{ij}$

• Tensor product

Description	*Index notation*
$\underline{a} \otimes \underline{b}$	$a_i b_j \underline{e}_i \otimes \underline{e}_j$
$\underset{\sim}{A} \otimes \underset{\sim}{B}$	$A_{ij} B_{kl} \underline{e}_i \otimes \underline{e}_j \otimes \underline{e}_k \otimes \underline{e}_l$
$\underset{\sim}{A} \underline{\otimes} \underset{\sim}{B}$	$A_{ik} B_{jl} \underline{e}_i \otimes \underline{e}_j \otimes \underline{e}_k \otimes \underline{e}_l$
$\underset{\sim}{A} \overline{\otimes} \underset{\sim}{B}$	$A_{il} B_{jk} \underline{e}_i \otimes \underline{e}_j \otimes \underline{e}_k \otimes \underline{e}_l$

• Curl and spin operator

Description	*Index notation*
$(\mathrm{curl} \underset{\sim}{A})_{ij}$	$\epsilon_{ipq} A_{jq,p} \underline{e}_i \otimes \underline{e}_j$
$(\mathrm{spin} \underline{N})_{ij}$	$-\epsilon_{ijq} N_q \underline{e}_i \otimes \underline{e}_j$

• Other notations

Description	*Notation*
Nabla operator (*with respect to the Lagrange coordinates*)	∇_X
Nabla operator (*with respect to the Euler coordinates*)	∇

Abbreviations

ENABLE	European network for alloy behavior law enhancement
ESR	Early stage researcher
WP	Work package
CPFEM	Crystal plasticity finite element method
FCC	Face-centered cubic
SSD	Statistically stored dislocation
GND	Geometrically necessary dislocation
CRSS	Critical resolved shear stress
ASB	Adiabatic shear band
DRX	Dynamic recrystallization
TQC	Taylor-Quinney coefficient
FE	Finite element
DOF	Degree of freedom
PDE	Partial differential equation
RVE	Representative volume element

Table of contents

Chapter 1

Introduction

Ce chapitre présente le projet *European Network for Alloy Law Behavior Enhancement (ENABLE)*, ses objectifs ainsi que la méthode utilisée. Le projet ENABLE est financé par le réseau *Marie Skłodowska-Curie Actions Innovative Training Networks* dans le cadre du programme *Horizon 2020*. Ce projet implique activement des partenaires industriels et universitaires dans la formation d'une nouvelle génération de jeunes chercheurs pour l'avenir de l'industrie manufacturière. Le projet ENABLE a été conçu pour exploiter l'expertise complémentaire des membres du réseau et, par conséquent, aborder des questions ambitieuses et interdisciplinaires. Le thème de recherche comprend plusieurs disciplines telles que la science des matériaux, la mécanique, la thermodynamique, les mathématiques et l'informatique.

De plus, les objectifs de la thèse et la méthodologie utilisée pour atteindre ces objectifs sont détaillé. En outre, l'état de la technique concernant le présent travail est brièvement présenté. Ce chapitre présente la déformation plastique dans les matériaux métalliques, les observations expérimentales du comportement plastique non conventionnel comme le renforcement dépendant de la taille et la localisation des déformations, ansi que les mesures de l'énergie stockée dans les matériaux métalliques. Ensuite, l'état de l'art des différentes approches numériques utilisées pour prédire les effets de taille, régulariser les bandes de cisaillement formées dans les problèmes de localisation de déformation, et prédire l'énergie stockée est détaillé.

1.1 European Network for Alloy Law Behavior Enhancement (ENABLE)

The ENABLE[1] project is financed by the *Marie Skłodowska-Curie Actions Innovative Training Networks* under the Horizon 2020 program. It is coordinated by Prof. Olivier Cahuc from the University of Bordeaux, France. The ENABLE project actively involves industrial and academic partners in training a new generation of young researchers for the future of the manufacturing industry. The ENABLE project has been designed to exploit the

[1] https://enable-project.com/

complementary expertise of the network members and, therefore, to address ambitious and interdisciplinary problems. The research theme consists of several disciplines such as materials science, mechanics, thermodynamics, mathematics, and computer science.

The ever-increasing prominence of sustainable growth has affected manufacturing engineering. Manufacturing is often recognized as a process to convert raw materials or parts into finished goods. Innovative solutions to reduce weight and costs without compromising performance and service life require the expertise of the entire manufacturing chain. Developing a competitive manufacturing industry is mainly based on an interdisciplinary research program.

ENABLE aims to include all metallurgical aspects of materials such as hardening, grain size, precipitation, phase transformation, etc., to study the microstructural evolution under extreme environmental conditions. Moreover, ENABLE proposes a complete re-evaluation of usual process simulation methods in metallic alloys by developing new solutions. Furthermore, innovative multi-scale (from microscopic to macroscopic scales) and multi-physics (strong thermo-mechanical and microstructural couplings) approaches are addressed in advanced multi-level simulations.

A group of 9 Early Stage Researchers (ESRs) is trained within world-leading research teams, which consists of 17 institutes/companies located within 5 countries (Table 1.1).

Table 1.1 Different institutes/companies involved in the ENABLE project.

France	
Institutes	Mines ParisTech (MAT), Engineering school of Tarbes (ENIT), University of Bordeaux (UBx)
Companies	Safran Tech (SAF), ESI Group (ESI), Timet (TI), Metallicadeour (MET), Innovation Plasturgie Composites (IPC)
Spain	
Institutes	University of the Basque Country - UPV/EHU (UPV)
Companies	Tecnalia (TEC), Lortek (LOR), Basque Center for Applied Mathematics (BCA)
Sweden	
Institutes	Luleå University of Technology (LTU)
Companies	GKN Aerospace Sweden (GK), Sandvik Coromant (SVK)
Belgium	
Institutes	
Companies	SIRRIS (SIR)
Denmark	
Institutes	
Companies	Danish Advanced Manufacturing Research Center (DA)

ESRs have been introduced to novel approaches and applications while exploiting advances in fundamental research. Additional cross-disciplinary training such as communication, entrepreneurship, open science, intellectual property, patenting, gender balance awareness, etc., are provided to ESRs. In addition, ESRs are provided with transferable skills and complementary competencies, which improve their research abilities and enhance their future employability.

1.2 Objectives of the ENABLE project

Each manufactured structure results from the collective efforts of various processes encountered along the whole manufacturing chain. Manufacturers must improve their production processes to meet the high demand for new products of excellent value in productivity, profitability, and quality.

The production processes are difficult to control due to the presence of complex phenomena related to continuum mechanics, thermo-mechanics, metallurgy, and chemistry. These phenomena are even more complicated in the presence of high stains, high strain rates, and high temperatures. A component's final mechanical state subjected to dynamic loading goes through severe inhomogeneous deformations processes. Predicting such deformation behavior using numerical calculations requires a complete description of the material's dynamic behavior.

Many companies' research and development departments need appropriate models to predict material behavior under severe deformation. Unfortunately, companies are forced to use empirical laws that are poorly suited to an ever-greater need for precision. Moreover, the changes in materials occurring during severe deformation, such as residual stresses, phase transformation or particle precipitation, recrystallization, etc., are still insufficiently considered. The physics-based approach of ENABLE using advances in information technologies (High-performance computing, Crystal plasticity modeling, etc.) and advanced material characterization tools (Scanning electron microscope, Transmission electron microscopy, Electron backscatter diffraction, etc.) will be able to link the micro- and macro-scopic responses of the materials.

The modeling approach provided by ENABLE can be used to create specifically tailored materials that will improve the component's material properties required for improving performance. These advances will lead to new service life improved tools and ultimately reduce production time and hence production costs.

To extend the benefits of the ENABLE project to a wide range of industrial sectors, the numerical simulation will be performed on several widely-used processes such as friction stir welding, machining, and additive manufacturing. These processes are chosen because they are all thermo-mechanical and challenging to model and accomplish in practice. The most popular metallic materials in the industry, namely nickel-based super-alloys, titanium,

and aluminum alloys, are chosen for the scientific investigation. All the obtained results can be extended to other types of alloy.

The 9 ESRs involved in this project are divided into three work packages (WPs) (3 ESRs in each WP), namely, materials, modeling, and processes. Different WPs and collaborative partners involved in ENABLE project are shown in Fig. 1.1.

- WP1 (Materials): This package aims to identify the mechanisms governing the evolution of plastic behavior covering a wide range of strains, temperatures, and strain rates. Three ESRs working in this WP are Marie-Anna Moretti (ESR1), Biswajit Dalai (ESR2), and Trunal Dhawale (ESR3). Marie-Anna Moretti is studying phases transformations, recrystallization, and grain growth during hot deformation of Inconel 718 alloy. Biswajit Dalai is investigating, among other things: phases transformations, recrystallization, and grain growth during hot deformation of two grades of aluminum alloys commonly used in additive manufacturing and shaping processes. Besides, Trunal Dhawale provides a detailed experimental behavior law and performs microstructural investigations to establish interdependences between microstructure and strain.

- WP2 (Modeling): The global aim of this WP is to develop a new finite element theory based on the strain gradients approach to enable thermo-mechanical and microstructural coupling. This multi-scale modeling will then be optimized for high-performance computing and implemented in digital simulation software for new generation processes. Three ESRs working in this WP are Vikram Phalke (ESR4), Raffaele Russo (ESR5), and Tamara Dancheva (ESR6). The global objective of Vikram Phalke is to work on a finite deformation crystal plasticity model implemented in the implicit finite element code Zset (common code for Mines ParisTech and Safran Tech) to investigate the thermo-mechanical response of the single and poly-crystals. The global aim of Raffaele Russo (ESR5) is the formulation of a visco-plastic strain gradient continuum theory for macro-scale applications such as machining, friction stir welding, etc. Tamara Dancheva is developing and implementing computational methods for the future of metals manufacturing in the open-source automated massively parallel FEniCS framework in collaboration with leading researchers and companies in the ENABLE project.

- WP3 (Processes): The global aim of this WP is to identify and measure kinematic and temperature fields for standard test cases and thereby understand and improve the manufacturing processes. The three ESRs involved in this WP are Haythem Zouabi (ESR7), Danilo Ambrosio (ESR8), and Pinku Yadav (ESR9). Haythem Zouabi aims to measure kinematic and temperature fields in machining operations on a new experimental bench. The objective of Danilo Ambrosio is to determine kinematic and temperature fields during friction stir welding of the aluminum and nickel-based

super-alloys. Finally, Pinku Yadav investigates the metallurgical changes during additive manufacturing of AlSi7Mg0.6 aluminum alloy.

1.3 Objectives of this thesis as ESR4 in ENABLE project

This thesis is a part of WP2 presented above. The global aim of this thesis is to predict the thermo-mechanical response of the single and poly-crystalline metallic materials subject to severe inhomogeneous deformation taking the strain gradient crystal plasticity approach. The global aim of this thesis is divided into the following principle objectives.

When micron-scale components are subjected to inhomogeneous deformation, they show non-conventional plastic behavior such as size–dependent strengthening called size effect. It is well known that the classical crystal plasticity models fail to capture experimentally observed size effects due to the lack of characteristic length scales in the constitutive framework. This limitation of the classical crystal plasticity models can be overcome using strain gradient crystal plasticity models. Therefore, the first objective of the thesis is to predict the size–dependent response of the micron-scale components such as microwires under severe deformation using the strain gradient crystal plasticity model.

Strain softening, mainly due to the temperature rise, is a common phenomenon in severe deformation processes. This, in turn, reduces the stress carrying capacity of the material and results in the formation of an intense shear band called the adiabatic shear band (ASB). ASB formation is a common phenomenon observed in manufacturing processes such as machining, shearing, metal forming, and so forth. Applications of the classical crystal plasticity models to strain localization problems have limitations as the localization phenomenon shows spurious mesh dependency. Strain gradient crystal plasticity models can be used to overcome this limitation of classical crystal plasticity models. Therefore, another objective of the present work is to apply the strain gradient crystal plasticity model for numerical analysis of the ASB formation in single and poly-crystalline FCC metallic materials.

The recent experimental work from the literature has shown that the ASB formation process is governed by dynamic recrystallization along with thermal softening. Stored energy is the main driving force for the dynamic recrystallization and recovery process. The prediction of stored energy is vital to understanding the plastic deformation and subsequent recrystallization and recovery processes. Another important aspect related to stored energy is the fraction of plastic work converted into heat called the Taylor-Quinney coefficient (TQC). Numerical prediction of stored energy and TQC in line with the experimental measurements is a challenging task. The experimental observations showed that the TQC is not a constant but an evolving parameter during the deformation process. Therefore, another objective of this thesis is to predict the stored energy and TQC for single crystals and polycrystalline FCC metallic materials.

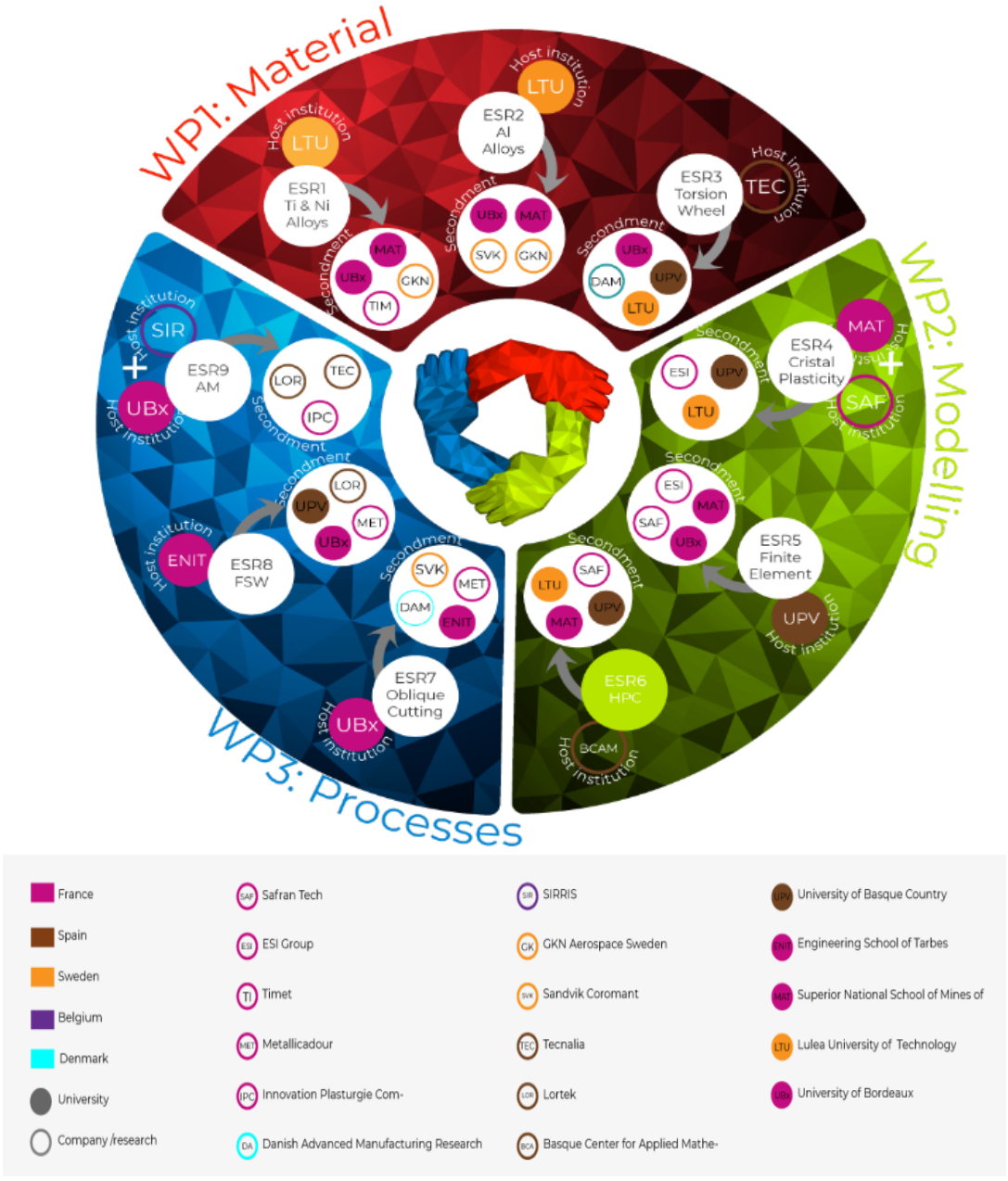

Fig. 1.1 Different work packages and collaborative partners in ENABLE project.

Implementing strain gradient plasticity theory in the FE code is challenging due to its complicated constitutive framework. Therefore, the final objective of this thesis is to propose a method to implement the strain gradient plasticity model in commercial FE software with little effort to regularize strain localization problems and predict size effects.

The principal objectives of this thesis and collaborative partners to achieve these objectives are summarized below.

- Prediction of size effect using strain gradient crystal plasticity model (**Mines ParisTech, Safran Tech**)
- Investigation of the ASB formation in single and poly-crystalline metallic materials (**Mines ParisTech, Safran Tech, Luleå University of Technology**)
- Prediction of stored energy and evolution of TQC in single and poly-crystalline metallic materials (**Mines ParisTech, Safran Tech, University of the Basque Country - UPV/EHU**)
- Implementation of the micromorphic plasticity model in commercial FE software (**ESI Group, Mines ParisTech, Safran Tech**). This objective is fulfilled by collaborating with **Raffaele Russo** (ESR5), a Ph.D. student at the University of the Basque Country - UPV/EHU and Mines ParisTech.

1.4 Methodology

Strain gradient crystal plasticity models have limited applications for practical engineering problems due to their high computational cost. As a simplified strain gradient crystal plasticity model, a reduced-order model has been introduced for complex applications with reduced computational cost in terms of CPU time. This model will be used to fulfill the first objective of predicting the size effect in single crystals microwire torsion tests.

Various types of strain gradient crystal plasticity theories can be found in the literature. Differences in the formulation of these strain gradient crystal plasticity theories result in distinct and sometimes non-physical responses, which raises the necessity of verifying the validity of the selected model for chosen applications. At first, a comparison of the reduced-order micromorphic and Lagrange multiplier-based models will be performed in predicting the size effect. These models were implemented in implicit FE code Zset[2], former model by Ling et al. (2018) and latter model by Scherer et al. (2020). Both models are a type of reduced-order models, but the Lagrange multiplier-based model has one more additional degree of freedom than the one used for the reduced-order micromorphic model. The second part compares the $CurlF^p$ model proposed by Kaiser and Menzel (2019a),

[2]http://www.zset-software.com/

which is a typical strain gradient plasticity model without simplification, and the Lagrange multiplier-based model in predicting the size effect under monotonic and cyclic loading of the microwire torsion tests.

To fulfill the second objective of studying the ASB formation process in single and polycrystalline FCC metallic materials, a thermodynamically consistent framework of the reduced-order micromorphic crystal plasticity model will be developed. Simulations will be performed on the single and polycrystalline hat-shaped specimens using this thermodynamically consistent framework.

A dislocation density-based hardening model will be used to fulfill the third objective of predicting the stored energy and TQC in single and poly-crystals. Firstly, the stored energy will be predicted by considering the contribution of Statistically Stored Dislocations (SSDs) only, i.e. using the classical crystal plasticity model. Next, the stored energy will be predicted considering the contribution of both SSDs and Geometrically Necessary Dislocations (GNDs), i.e. using the micromorphic crystal plasticity model and will be compared to that of the prediction made by considering SSDs only.

Finally, we propose an easy way to implement the micromorphic plasticity model in commercial explicit FE software VPS/Pam-Crash® from ESI Group[3]. We will use an analogy between the reduced-order micromorphic plasticity theory and classical thermo-mechanical analysis to easily implement this model for practical engineering problems.

[3]https://www.esi-group.com/pam-crash

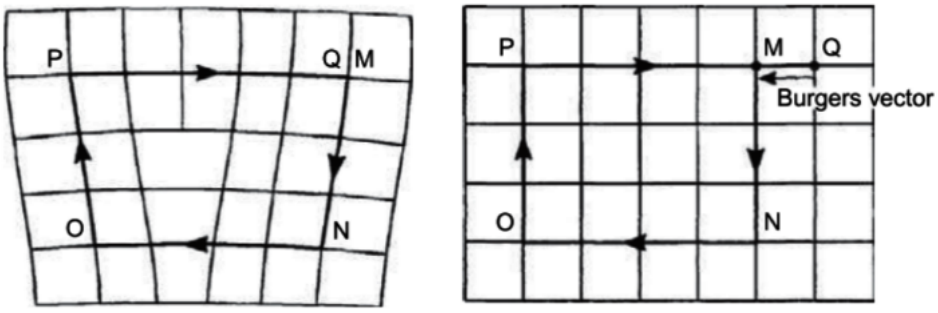

(a) (b)

Fig. 1.2 (a) Burgers circuit around the edge dislocation in a distorted lattice (b) same Burgers circuit in the perfect crystal; closure failure denotes the Burgers vector (Hull and Bacon, 2011).

1.5 State of the art in brief

This section introduces the plastic deformation in metallic materials, experimental observations of the non-conventional plastic behavior such as size–dependent strengthening and strain localization, and measurements of stored energy in metallic materials. Then, the state of the art of different numerical approaches used to predict size effects, regularize the shear bands formed in strain localization problems, and predict the stored energy is presented.

1.5.1 Plastic deformation in metallic materials

All crystalline materials contain imperfections in the crystal lattice which may be point, line, surface, or volume defects (Hull and Bacon, 2011). Plastic deformation in metallic materials occurs due to the presence, generation, multiplication, interaction, and movement of these defects present in the crystal lattice (Kubin et al., 1992; Arsenlis and Parks, 2002; Uchic et al., 2004). The line defects are called *dislocations* and are the main contributors to material strain hardening. The definition of dislocation can be given in terms of the Burgers circuit. The Burgers circuit is a close loop circuit formed by joining an atom-to-atom path in the crystal. Such a path is shown in Fig. 1.2a (i.e. MNOPQ). If the same atom-to-atom path is made in a perfect crystal (dislocation free), the circuit does not close (see Fig. 1.2b). This indicates that the circuit in Fig. 1.2a must contains one or more dislocations. The vector needed to complete the circuit is called the *Burgers vector* (Hull and Bacon, 2011) (QM in Fig. 1.2b). The specification of dislocation involves both the displacement vector and dislocation line, such that when the displacement vector is parallel to the dislocation line, then the dislocations are called *edge* dislocations. On the other hand, when the Burgers vector is perpendicular to the dislocation line, they are termed as *screw* dislocations (Hull and Bacon, 2011).

There are two main dislocation motions. The dislocation motion that happens due to the gliding along its direction is called *glide*. On the other hand, *climb* is the motion that occurs when the dislocation moves out of the glide surface. The glide of many dislocations

results in *slip*. Dislocation glide is the most common phenomenon in plastic deformation at room temperature. During plastic deformation, dislocations move along particular planes located between closest-packed atomic layers, called slip planes. The direction of dislocation motion is called the slip direction. The combination of slip plane and slip direction form the slip system. In FCC crystals, the crystallographic slip occurs on the twelve {111}<110> slip systems; four {111} planes and three <110> directions (see Fig. A.1). The definition of the octahedral slip systems can be found in appendix A (Table A.1). The dislocation glide depends on the number of independent slip systems. At least five independent slip systems are necessary for a homogeneous plastic flow by dislocation glide (Groves and Kelly, 1963).

Taylor and Elam (1923) established a relationship between the resolved shear stress and plastic yielding to facilitate the determination of active slip systems, commonly known as Schmid law. According to them, the active slip system is defined as the one with the highest component of shear stress (i.e., the resolved shear stress) in the direction of shear. In addition, they noted the influence of active slip systems on the hardening of inactive slip systems called *latent hardening*. Another important observation made by Koehler (1941) suggests that the amount of energy required for a certain amount of slip inside the solid is twice that needed for the same amount of slip at the surface.

These generated dislocations are hindered by other dislocations, precipitates, grains, and sub-grain boundaries in polycrystals. The presence of grain boundaries in polycrystalline materials results in a non-conventional plastic behavior, where the decrease in grain size leads to an increase in flow stress required for the plastic deformation (Hall, 1951).

The macroscopic behavior of materials stems from the underlying microstructure. The plastic deformation in materials at micron and sub-micron scales is due to the presence of characteristic length scales. In single crystals that are free from grain boundaries and defects other than dislocations, the characteristic length scale is described as the mean spacing between the dislocations. On the other hand, in polycrystalline materials, which consist of grain boundaries or defects beyond dislocations such as precipitates, the characteristic length scale is determined by the smallest distance between the dislocations and the next obstacle (Zhang et al., 2014; Bayerschen, 2017). In the next section, experimental evidence of different size–dependent behaviors due to the presence of characteristic length scales in the micron-scale structures are summarized.

1.5.2 Size effects in plasticity

When a material is deformed plastically, dislocations are generated, moved, and stored. There are two main types of dislocation families to be considered. The typical ensemble of dislocations generated during the plastic deformation through random trapping with each other is called SSDs. The other type, GNDs are required for the compatible deformation of the crystal under inhomogeneous plastic deformation processes (see Fig. 1.3) (Ashby, 1970). The GNDs are generated either due to the inhomogeneous local loading applied

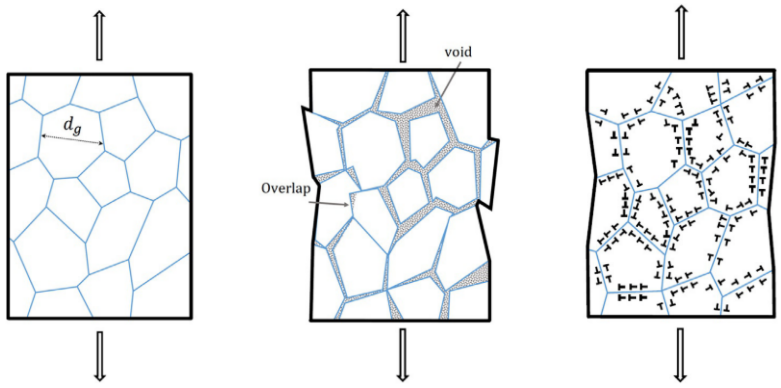

Fig. 1.3 Non-homogeneous deformation in polycrystals: (a) undeformed specimen, (b) homogeneous deformation of grains leads to the formation of overlaps and voids (c) non-homogeneous and local deformation provided by the GNDs removes overlaps and voids (Voyiadjis and Yaghoobi, 2019).

to the specimen, or if the material itself is non-homogeneous, e.g. due to the presence of precipitates. The GNDs can be quantified using Nye's dislocation density tensor $\underset{\sim}{D}_d$ (Nye, 1953) given by

$$\underset{\sim}{D}_d = N_d \underline{b}\,\underline{t}, \tag{1.1}$$

where N_d is the number of dislocation lines with Burgers vector $\underline{b}$, crossing a unit area normal to their unit tangent line vector $\underline{t}$. The gradient of shear strain is associated with the storage of GNDs described by Nye's tensor. As a result, GNDs along with SSDs control the material strain hardening and the size effects.

The size effects can be described as the change in material strength with a change in characteristic length scale. For instance, the indentation hardness of metals and ceramics increases as the size of the indenter decreases (Nix and Gao, 1998; Gao and Huang, 2001; Liu and Ngan, 2001). Micro-torsion tests show increasing shear strength with decreasing diameter of the microwire (Fleck and Hutchinson, 1997; Gao and Huang, 2001; Liu et al., 2012; Guo et al., 2017), and micro-bending tests show an increase of material strength with a decrease in beam thickness (Stölken and Evans, 1998; Gao and Huang, 2001; Haque and Saif, 2003).

One of the first size effects studied is the relation between precipitate size and flow strength. The flow strength of a material is affected by both the precipitate size and spacing. Fisher et al. (1953) showed that the presence of precipitates in the material causes the dislocations generated from Franck-Read sources to form a closed loop around the particles, and the back-stress thus generated increases the effective stress of the Franck-Read sources. Arzt (1998) reviewed the size effects due to the microstructural constraints such as precipitates and grain boundaries. He used a concept of Orowan mechanism (Orowan, 1947), i.e. obstacle (precipitates) spacing and dislocation curvature, to capture the size effects. Recently, Ralston et al. (2010) investigated the precipitate size effects for aluminum

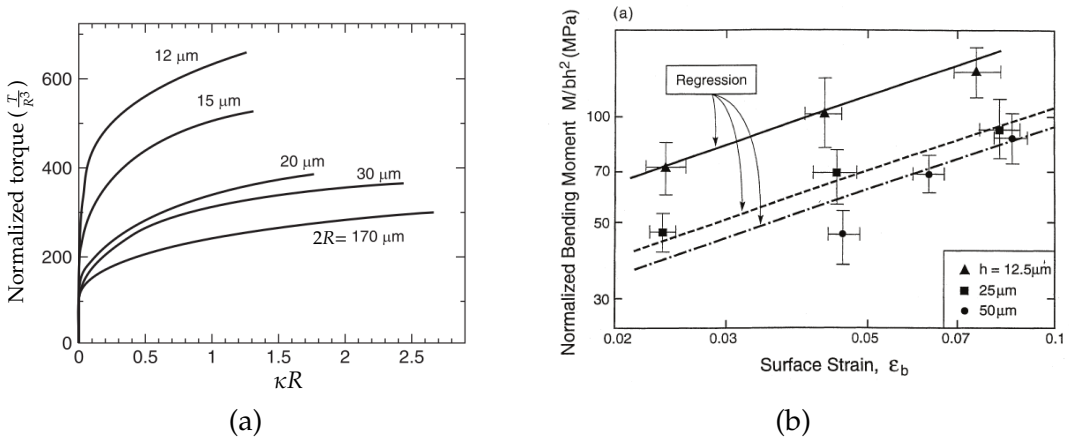

Fig. 1.4 (a) Plot of experimental results of polycrystalline copper microwire torsion tests for different diameters showing size effects (Fleck and Hutchinson, 1993). (b) Plot of experimental results of bending tests for different thicknesses of Nickel foil showing size effects (Stölken and Evans, 1998).

alloy Al-2.5 Cu-1.5 Mg (wt.%). It is shown that the fine nano-particles formed for the aging times less than 2 h at 200°C have a substantial effect on the yield stress.

Fleck et al. (1994) performed tension and torsion tests on polycrystalline copper microwires ranging in diameter from 12 μm to 170 μm to investigate the effect of loading type and specimen size on the torsional hardening response. It was observed that, in uniaxial tension tests, the plastic strain gradient is negligible, and no size effect is observed. On the other hand, it was observed that the torsion of microwires induces a strong strain gradient ($d\gamma_R/dR$) along the radial direction from the axis of twisting. In torsion of microwires, the surface strain γ_R varies along the radius R, such that $\gamma_R = \kappa R$, where κ is the twist per unit length. The hardening in the microwires is due to the presence of SSDs and GNDs. For a given surface strain, the thinner wire has the highest strain gradient ($d\gamma_R/dR$) and highest GND density, which causes faster work hardening. It can be seen from Fig. 1.4a that the torsion hardening increases systematically with a decrease in the diameter of the microwire.

More experimental evidence of size effects can be found in the micro-bending tests performed by Stölken and Evans (1998) on thin Nickel foils. They performed micro-bending tests for three thicknesses of 12.5 μm, 25 μm, and 50 μm. The normalized bending moment vs. surface strain curves are shown in Fig. 1.4b from the work of (Stölken and Evans, 1998). The normalized bending moment for a 12 μm foil is significantly higher compared to the other two foils (see Fig. 1.4b), confirming the presence of a size effect.

The intrinsic size effect can be attributed to the dependency of material yield strength on microstructural characteristics, such as average distance of precipitates, mean free path of the dislocations, and grain size (Arzt, 1998). In polycrystal aggregates, generally, two size effects are responsible for the increased strength and are called *specimen size effect* and *grain size effect* (Armstrong, 1961). The specimen size effect occurs when there are few grains in the specimen cross-section and due to the orientation dependency of the

crystal plastic flow. On the other hand, the grain size effect occurs when many grains are in the specimen cross-section. Moreover, the internal concentrations of stress are necessary at grain boundaries to cause yielding and subsequent plastic flow and the orientation dependence of plastic flow within grains. The well-known grain size effect in polycrystalline materials is often called the Hall-Petch size effect. Hall and Petch (Hall, 1951; Petch, 1953) gave an inverse relationship between flow stress and the square root of grain size, i.e., $\sigma - \sigma_0 \propto d_g^{-1/2}$, where σ is the yield strength of the material, σ_0 is the yield strength of single crystal, and d_g is the grain size. Generalizing the work of (Hall, 1951), the relation between the dependency of material strength on grain size is given by

$$\sigma = \sigma_0 + K_{HP} d_g^{-n_x}, \tag{1.2}$$

with K_{HP} being a material constant, and n_x is a constant in the range of 0 to 1.

According to the Hall-Petch relation (Eq. 1.2), the flow stress or yield stress increases as grain size decreases. However, material strength can not be unlimited. In general, two limit cases can be observed. In the first case, the flow stress shows a saturation with decreasing grain size after reaching a certain grain size. In the other case, the material strength starts decreasing with grain size, a phenomenon called *inverse grain size effect*. The first evidence of inverse grain size effect is reported in (Chokshi et al., 1989).

The grain size effect is associated with the spatial strain gradient in the grains because of the heterogeneous plastic deformation. The grain boundaries act as an obstacle to dislocation motion, and the strain gradient-induced GNDs pile up at the grain boundaries. In addition, with the decrease in grain size, the area at the grain boundaries with GND density increases and results in increased yield strength.

Another important size effect observed during the micro- and nano-indentation tests is called *indentation size effect*. Micro- and nano-indentation tests are popular tests to predict material behavior at the sub-micron scale. In micro- and nano-indentation tests, a hard indenter is pressed against the material to measure the applied load and penetration depth. In conventional indentation tests (at macro-scale), measured material hardness is independent of indentation depth. In contrast, in micro- and nano-indentation tests, the hardness decreases as the indentation depth increases, and the size effect is typically explained with an accumulation of GNDs beneath the indenter (Stelmashenko et al., 1993; Ma and Clarke, 1995).

Early attempts to measure the indentation size effect can be found in (Ma and Clarke, 1995; Poole et al., 1996; McElhaney et al., 1998). Ma and Clarke (1995) performed indentation tests on single crystal silver using a Berkovich indenter. They found that the hardness almost doubled with a decrease in indent size from 10 µm to 1 µm. Similar size effects were observed by Poole et al. (1996) in copper using a Vickers indenter. McElhaney et al. (1998) performed nano-indentation tests on carefully prepared (111) copper single crystal using a Berkovich indenter. Liu and Ngan (2001) showed that the indentation size effect is very sensitive to surface preparation. In polycrystalline indentation tests, GNDs are piled up at

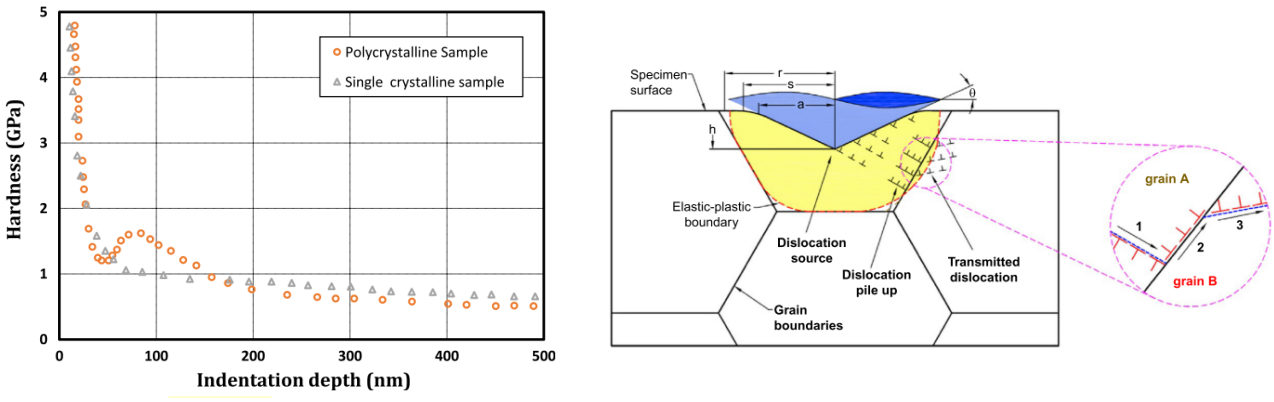

(a) (b)

Fig. 1.5 (a) Indentation size effect for single and polycrystalline metallic samples showing a decrease in hardness with an increase in indentation depth, from (Voyiadjis et al., 2011). (b) Schematic showing GND interaction with grain boundaries in nano-indentation tests (Voyiadjis and Zhang, 2015).

the grain boundaries to accommodate the imposed displacement (Fig. 1.4). The variation of hardness with indentation depth in nano-indentation of single and polycrystalline aluminum is shown in Fig. 1.5a. Voyiadjis et al. (2011) observed that the hardness of polycrystals decreases as indentation depth increases. After a certain indentation depth, it shows local hardening after which it decreases as indentation depth increases further (Fig. 1.5a).

Several attempts have been made to investigate experimental evidence of characteristic length scale and its correlation with material microstructure, for instance, in (Nix and Gao, 1998; Fleck et al., 1994; Stölken and Evans, 1998). Microwire torsion (Fleck et al., 1994) and micro-bending (Stölken and Evans, 1998) tests have been conducted to estimate the characteristic length scale, and the estimated value for nickel was 5 µm and 4 µm for copper. The micro- and nano-indentation tests carried out by (Abu Al-Rub and Voyiadjis, 2004; Voyiadjis and Al-Rub, 2005) found that the characteristic length scale is proportional to the mean free path of the dislocations. Qian et al. (2013) calibrated temperature-dependent characteristic length scale using indentation tests. This characteristic length scale is then used for the FE simulations based on strain gradient plasticity theory.

1.5.3 Strain localization: Theoretical and experimental aspects

Besides size effects, another non-conventional plastic behavior observed in the materials under severe deformation is called strain localization which may lead to initiation and propagation of fracture. This common phenomenon occurs in many metallic materials over a broad range of scales: from macro- to nano-scale. Strain localization phenomenon ultimately results in the loss of material strain hardening capacity and the formation of an intense strained band called *shear band* (Fig. 1.6). Early attempts of material modeling

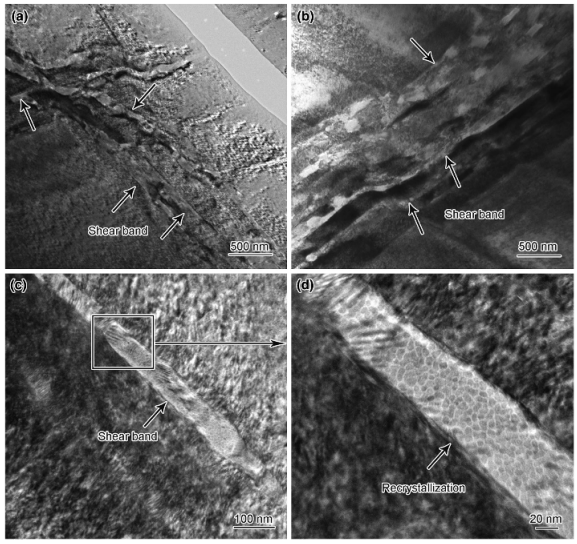

Fig. 1.6 Shear band in AA7055 aluminum alloy formed during the dynamic compression tests. (a)-(c) Transmission electronic micrograph of formed shear band, and (d) magnified micrograph of the formed shear band (Xiong et al., 2014).

for this phenomenon can be found in (Asaro, 1985). Strain localization can be associated with numerous mechanisms, for instance, non-uniform temperature rise caused by thermal softening and high strain rate deformation, microfractures due to void initiation and growth, and microstructural instabilities (Asaro and Rice, 1977; Bandstra and Koss, 2001; Gama et al., 2004; Dodd and Bai, 2012). There is experimental evidence of strain localization even in the strain hardening of materials caused by constitutive instabilities (Harren et al., 1988). Furthermore, the experimental and computational work performed by Harren et al. (1988) showed that the geometrical softening caused by non-uniform lattice rotation is responsible for the formation of shear bands in strain hardening materials.

There is numerous experimental and theoretical work available on shear banding. The two most common theories of shear banding are summarized here. The first theory, proposed by Hill (1962); Rudnicki and Rice (1975); Anand and Spitzig (1980), states that the shear band forms in the material undergoing plastic deformation due to the instabilities in the constitutive description of homogeneous deformation. The instability can be understood as the constitutive relations that may allow the homogeneous deformation to lead to a bifurcation point. The non-homogeneous deformation leads to a planar band while maintaining homogeneous deformation and equilibrium outside the localization region. According to this theory, shear banding is possible even in the strain hardening of materials.

The second theory proposed by Dillamore et al. (1979) has the following criterion: If σ is the stress measure and ε is the strain measure then localization of deformation occurs according to the condition $d\sigma/d\varepsilon \leq 0$. Similar to the first theory, this theory also leads to localization in strain hardening materials considering the geometrical softening.

In general, the formed shear bands are categorized into two: the shear bands formed parallel to the slip planes are called *slip bands*, while the formed bands normal to the slip

planes are termed as *kink bands* (Frank and Stroh, 1952; H. Neuhäuser, 1983). High lattice rotations are associated with the kink bands (Forest, 1998). In the experimental work of (Orowan, 1942), the cadmium single crystals having glide plane-parallel of the loading axis were compressed axially. In his work, as the load increased, the usual glide mechanism did not occur during the deformation; rather, crystals suddenly collapsed by forming kink bands.

The shear band formation under adiabatic conditions is a topic of practical importance in severe deformation processes associated with low energy or low ductility fracture. Such a deformation mode is encountered in materials that are subjected to dynamic deformation. The fundamental requirement to form an adiabatic shear band (ASB) is that no heat is exchanged with the surroundings. The materials with low heat capacity promote a local high-temperature rise and subsequently the ASB formation. The first evidence of ASB formation at a very high strain rate was found by Tresca (1878). Later on, the seminal work of (Basinski and Hume-Rothery, 1957) showed the interaction between applied strain rate and the physical material properties as a function of temperature. An extensive review of the ASB formation can be found in (Rogers, 1979; Timothy, 1987). Recently, it has been shown that dynamic recrystallization plays an important role in strain softening and subsequent adiabatic shear band formation (Mourad et al., 2016; Landau et al., 2016; Longère, 2018). Therefore, the stored energy is considered an important factor in the ASB formation process which will be reviewed in the next section.

1.5.4 Stored energy in metallic materials

When a material undergoes plastic deformation, part of the mechanical energy dissipates as heat, and part of it remains in the material as stored energy, which results in an increase of the internal energy (Bever et al., 1973; Aravas et al., 1990). There are three main types of stored energy, namely elastic energy, energy stored due to the dislocations, and energy due to the mean stresses in polycrystals (Biermann et al., 1993). Then the total stored energy E_s can be written as When a material undergoes plastic deformation, part of the mechanical energy dissipates as heat, and part of it remains in the material as stored energy, which results in an increase of the internal energy (Bever et al., 1973; Aravas et al., 1990). There are three main types of stored energy, namely elastic energy, energy stored due to the dislocations, and energy due to the mean stresses in polycrystals (Biermann et al., 1993). Then the total stored energy E_s can be written as

$$E_s = E_e + E_d + E_m, \tag{1.3}$$

where E_e is the elastic energy, E_d is the energy due to dislocations, and E_m is the energy due to mean stresses in the polycrystals. The elastic energy can be given by

$$E_e = \frac{\sigma^2}{2E}, \tag{1.4}$$

where σ is the stress, and E is the Young's modulus. The elastic energy is recoverable energy during unloading and hence does not contribute to total stored energy in crystals. Moreover, if the energy of the dislocation core is neglected and isotropic elasticity is considered, then the energy per unit length of dislocation line E_{unit} is given by

$$E_{unit} = \frac{\mu b^2 f(\nu)}{4\pi} \ln\left(\frac{R_0}{r_0}\right), \tag{1.5}$$

with R_0 and r_0 being the outer and inner cut-off radius of the dislocations, respectively. The radius r_0 is of the order of the Burgers vector. The core energy within the radius r_0 is only a fraction of the total stored energy (Bever et al., 1973). It is assumed that the volume fraction $f(\nu)$ of the dislocations is a function of Poisson's ratio ν and expressed as follows:

$$f(\nu) = 1 \quad \text{for screw dislocations,} \tag{1.6}$$

$$f(\nu) = \frac{1}{1-\nu} \quad \text{for edge dislocations.} \tag{1.7}$$

The stored energy due to SSDs is given by

$$E_d = \sum_{r=1}^{N} \rho^r E_{unit} = \sum_{r=1}^{N} \frac{\rho^r \mu b^2 f(\nu)}{4\pi} \ln\left(\frac{R_0}{r_0}\right), \tag{1.8}$$

with ρ^r being the SSD density on slip system r and N denote the total number of slip systems. An approximated form of the previous equation reads

$$E_d = c\mu b^2 \sum_{r=1}^{N} \rho^r, \quad \text{with} \quad c = \frac{f(\nu)}{4\pi} \ln\left(\frac{R_0}{r_0}\right), \tag{1.9}$$

where c is a constant approximately equal to 0.5.

The expression of the energy stored due to dislocations accounting for the energy of the dislocation core can be found in (Čebron and Kosel, 2014) assuming that the edge-type dislocations are predominately accumulated during the deformation process. It reads

$$E_d = \sum_{r=1}^{N} \frac{\rho^r \mu b^2}{4\pi(1-\nu)} \left(\ln\left[\frac{P_1}{\sqrt{\rho^r} b}\right] + P_2\right), \tag{1.10}$$

where P_1 and P_2 are the constants and $P_1/\sqrt{\rho^r}$ is used as the outer cut-off radius.

Finally, the term E_m in (1.3) is due to mean stresses in the polycrystals and can be approximated by taking into account GNDs as follows:

$$E_m = \sum_{r=1}^{N} \rho_G^r E_{unit} = \sum_{r=1}^{N} \rho_G^r \frac{\mu b^2 f(\nu)}{4\pi} \ln\left(\frac{R_0}{r_0}\right), \tag{1.11}$$

with ρ_G^r denoting GND density.

A review on stored energy measurements in materials deformed by cold working using experimental methods can be found in the pioneering work of (Bever et al., 1973). There are mainly two methods used for the measurement of stored energy: *single-step* methods and *two-step* methods. In single-step methods, all the measurements are made during the deformation process. Correspondingly, in two-step methods, the deformation is carried out first, and the stored energy is measured later. In single-step methods, the difference between the work applied to the specimen and the heat generated during the deformation process is used to measure the stored energy. The work applied to the specimen can be measured from the force-displacement curve. The heat generated during the deformation process can be measured by measuring the change in the temperature of the specimen and using the density and specific heat of the material. On the other hand, in two-step method difference in enthalpy between the cold worked specimen and standard state is determined to measure the stored energy.

Numerous experimental work has been performed to investigate the fraction of the plastic work converted into heat, for instance, in (Macdougall, 2000; Knysh and Korkolis, 2015; Fekete and Szekeres, 2015; Rittel et al., 2017). Early attempts made by Taylor and Quinney (1934) found this fraction to be constant between 0.8 and 0.95, which is the so-called Taylor-Quinney coefficient (TQC). When TQC reaches a value of one, most of the plastic work dissipates through heat, and it indicates that there is no energy stored in the material. Later experiments, for instance by Oliferuk et al. (1993) showed that this fraction varies between 0.6 and 1.0 for polycrystalline austenitic steel and depends upon the accumulated strain. Kapoor and Nemat-Nasser (1998) investigated the fraction of plastic work converted into heat by measuring the temperature using an infrared method during the plastic deformation of Tantalum-2.5% W alloy. They found a TQC (β) of the order of 0.68.

In high strain rate deformation processes, for instance, orthogonal cutting, shearing, or trimming operation, adiabatic shear band (ASB) formation occurs due to the rapid increase of temperature locally. The main source for the temperature rise in the absence of external sources is plastic dissipation (Mason et al., 1994; Rittel, 1999; Zaera et al., 2013). Following these pioneering contributions, β is defined as the fraction of plastic work converted into heat. The *differential* form of β, emphasizing the rate quantities, can be expressed as follows (Rittel, 1999):

$$\beta_{diff} = \frac{\dot{Q}}{\dot{W}_p} = \frac{\rho C_\varepsilon \dot{T}}{\dot{W}_p}, \tag{1.12}$$

where ρ is the mass density of the material, C_ε is the specific heat and $\dot{W}_p$ denotes the plastic power. The β ratio can also be expressed in *integral* form, which denotes the total

plastic work converted into heat (Rittel, 1999):

$$\beta_{int} = \frac{\rho C_\varepsilon \triangle T}{\int \dot{W}_p \, dt}, \tag{1.13}$$

where $\triangle T$ is the increment of temperature during the deformation. The advantage of selecting the β_{int} as a measure of the fraction of plastic work converted to heat is that its value cannot exceed one due to thermodynamic limitations unless the latent heat in the material is delivered (Rittel, 1999). There is no such limitation for the β_{diff}.

Experimental measurement of the rise of temperature during high strain rate plastic deformation of Tantalum-2.5 % W alloy was performed by Kapoor and Nemat-Nasser (1998). They predicted the stored energy based on the dislocation theory (Eq. (1.9)), and compared it with experimental measurements. The analytically calculated value of β was 0.995, in contrast to the experimentally observed value of 0.7. The analytical expression used by them is well known and widely used for the stored energy predictions. In a recent study, Nieto-Fuentes et al. (2018) showed that the universal expression for the stored energy is inadequate and needs modifications. They introduced an *ad-hoc* factor ξ to the analytical expression of the stored energy based on the dislocation theory as follows:

$$E_d = \xi c \mu b^2 \sum_{r=1}^{N} \rho^r, \quad \text{with} \quad \xi = \frac{(1-\beta_{int}) \int_0^t \dot{W}_p \, dt}{c \mu b^2 \sum_{r=1}^{N} \rho^r}, \tag{1.14}$$

as β_{int} is an evolving parameter with strain and strain rate; hence the ξ evolves with strain and strain rate.

With developments of numerical methods and increased capabilities of modern computers, numerical approaches are becoming popular. The next section summarizes numerical techniques used to predict the size effects and stored energy, and investigate the strain localization phenomenon.

1.5.5 Numerical approaches: size effects, strain localization and prediction of stored energy

• Numerical approaches to predict size effects

From the numerical point of view, classical continuum theories assume that the material properties are size–independent for the materials undergoing plastic deformation. However, the experimental results show that the material exhibits a size–dependent behavior at the sub-micron scale. Size–dependent crystal plasticity modeling is required when the specimen or grain size becomes comparable to the characteristic lengths of the underlying plastic deformation mechanisms (Fleck and Hutchinson, 1997; Kocks and Mecking, 2003).

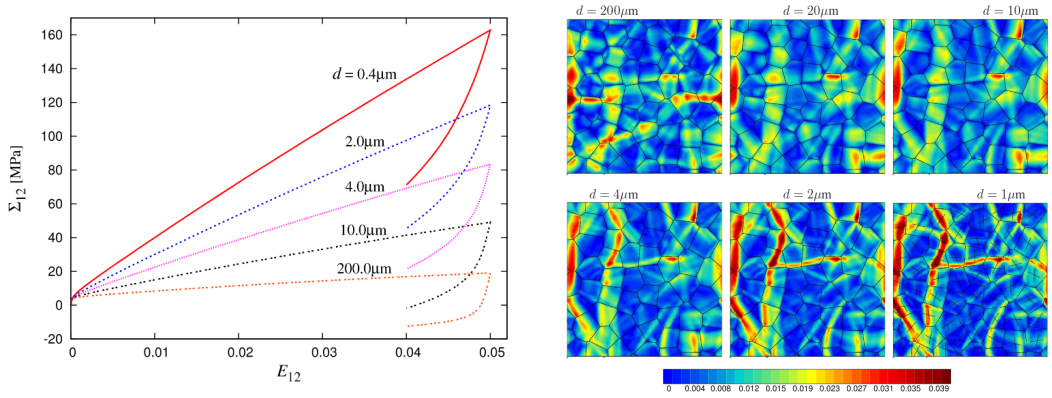

(a) (b)

Fig. 1.7 (a) Macroscopic stress-strain curve for the simple shear shear tests of different average grain size d. (b) Contours of cumulative plastic strain for different average grain size d (Cordero et al., 2013).

Strain gradient plasticity theories make use of the characteristic length scale(s) in the constitutive framework. These theories can be used to bridge the gap between plasticity at the macro-mechanical scale and plasticity at the micro-mechanical scale (Abu Al-Rub and Voyiadjis, 2004). A review of strain gradient plasticity models in the context of experimental, theoretical, and numerical investigations can be found in (Voyiadjis and Song, 2019). There are many names in this group of theories, but there is no dominant theory widely accepted. But all of these theories are proposed to account for the size effect phenomenon and introduce the characteristic length scales in the constitutive framework.

Strain gradient plasticity models can be used to predict grain size effects in polycrystalline materials, for instance, in (Acharya and Bassani, 2000; Evers et al., 2004; Aifantis and Willis, 2005; Borg, 2007; Cordero et al., 2013). Borg (2007) found the value of a constant n_x (refer Eq. (1.2)) to be in the range of $0.82-1.25$ at initial yield and in the range of $0.77-1.09$ after a true strain of 0.1. Cordero et al. (2013) used a micromorphic theory to introduce the dislocation density tensor in the classical crystal plasticity model to predict the grain size effect. An introduction of dislocation density tensor into the constitutive framework intrinsically gives rise to kinematic hardening, which is responsible for strong size effects. The predicted grain size effect for different average grain sizes and plastic strain fields taken from the work of (Cordero et al., 2013) are shown in Fig. 1.7a and 1.7b, respectively.

Size effects induced in microwire torsion tests or bending of thin foils are because of the inhomogeneous plastic deformation. The prediction of size effects in microwire torsion tests using strain gradient crystal plasticity, including full dislocation tensor into the constitutive framework, can be found in (Kaiser and Menzel, 2019b). Their paper analyzed the response of three microwires of different radii under monotonic loading. They observed that the decrease in the size of the microwire results in a significant increase in the overall strain hardening rate. Size effects predictions in monotonic and cyclic loading of polycrystalline microwires can be found in (Bardella and Panteghini, 2015) using a strain gradient plasticity

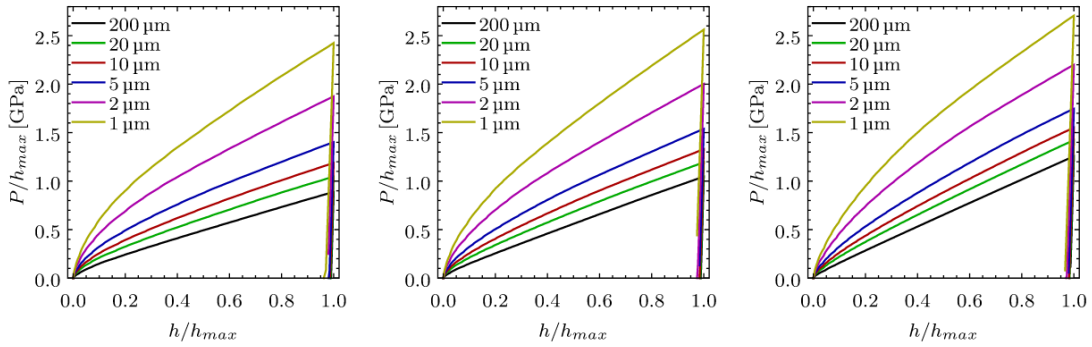

(a) 60° wedge (b) 90° wedge (c) 120° wedge

Fig. 1.8 Indentation size effect: Dependency of normalized load-penetration curve on the maximum indetation depth h_{max} varied from 200 µm to 1 µm. (Lewandowski and Stupkiewicz, 2018).

approach that includes plastic spin in the constitutive framework called distortion gradient plasticity. They found that this theory is satisfactory to capture the size effects in monotonic loading. Scherer et al. (2020) recently studied the size effect in microwire torsion tests using the reduced-order micromorphic crystal plasticity and Lagrange multiplier-based models.

Another important size effect observed due to inhomogeneous plastic deformation is in micro-bending tests. The non-local plasticity models often used to explore the size–dependent bending moment, for instance, in (Wang et al., 2003; Kuroda and Tvergaard, 2006; Keller et al., 2012). Gupta et al. (2015) studied the effect of crystal orientation on size–dependent response of single crystal beams using a higher-order nonlocal crystal plasticity model. They observed that the crystal orientation significantly affects the size effect. In addition, the slip system activity is important to analyze the orientation dependency.

The study of indentation size effect using the FE modeling is popular among the continuum mechanics community. Lewandowski and Stupkiewicz (2018) studied the indentation size effect in wedge indentation for nickel single crystal using gradient-enhanced crystal plasticity model. They compared the numerical results such as load-penetration depth curve, GND density distribution, lattice rotation, and net Burgers vector with the experimental results, and good agreement was found. In addition, they studied the indentation size effects for the indentation depth varied between 200 µm to 1 µm. It was observed that the maximum normalized load increases drastically with a decrease in indentation depth from 200 µm to 1 µm. The load is normalized by the maximum penetration depth h_{max}. Fig. 1.8 taken from (Lewandowski and Stupkiewicz, 2018) shows the dependence of the normalized load-penetration depth curve on the maximum penetration depth for three different wedge angles.

• **Numerical approaches to strain localization problems**

FE simulations of strain localization phenomenon show spurious mesh dependency, and classical plasticity models are inadequate to solve such strain localization problems (Asaro and Rice, 1977). The possible loss of ellipticity of the partial differential equations in strain-softening materials results in an ill-posed boundary-value problem and classically shows dependency on mesh size or density (Fig. 1.9a). Without regularization, meaning that mesh independent solution, the classical continuum models can not be used to solve strain localization problems (Needleman, 1988).

Shear band dependency on the mesh size or density can be overcome by introducing characteristic length scales in the classical plasticity models according to (Kuroda and Tvergaard, 2006; Voyiadjis and Al-Rub, 2005; Anand et al., 2012; Vignjevic et al., 2018; Wolf et al., 2019; Kaiser and Menzel, 2019b). Strain gradient plasticity models, which include a characteristic length scale in the constitutive framework, are often used to regularize the strain localization problems, e.g., Aifantis (1984); Abu Al-Rub and Voyiadjis (2006); Anand et al. (2012); Ahad et al. (2014). Aifantis (Aifantis, 1984, 1987) proposed a strain gradient theory by adding the gradient of plastic strain term in the yield function of classical plasticity theory to solve the issues related to the thickness of the localization regime. The characteristic length scales introduced in the gradient plasticity models can be associated with the width of the shear band as demonstrated in (Aifantis, 1984, 1987; Zbib and Aifantis, 1988; Chambon et al., 1998). The effect of higher-order gradients on ASB formation was investigated by Zhu et al. (1995) and two length scales, respectively, the deformation and thermal were considered in the analysis. They showed that the width of shear bands scales with the square root of strain gradient coefficient in the absence of heat conduction and the square root of the thermal conductivity in the absence of strain gradients. The micromorphic theory proposed by Eringen (1999) relies on the second-order microdeformation tensor as an additional degree of freedom. The application of micromorphic theory for the strain localization phenomenon can be found in (Dillard et al., 2006; Anand et al., 2012; Mazière and Forest, 2015). In contrast to Eringen's micromorphic theory, a reduced-order micromorphic crystal plasticity theory proposed by Ling et al. (2018) involving a scalar-valued variable as the additional degree of freedom is used for the strain localization phenomenon in (Scherer et al., 2019). The mesh dependency issues in the shear localization problem can also be eliminated by the sub-grid method proposed in (Mourad et al., 2017; Jin et al., 2018).

• **Numerical approaches to predict stored energy**

Stored energy is a function of total dislocation density. The prediction of stored energy related to an internal stress field surrounding dislocation structures using the discrete dislocation dynamic simulations can be found in (Zehnder, 1991; Mura, 1994; Benzerga et al., 2005; Déprés et al., 2006). The use of a CPFEM for prediction of stored energy

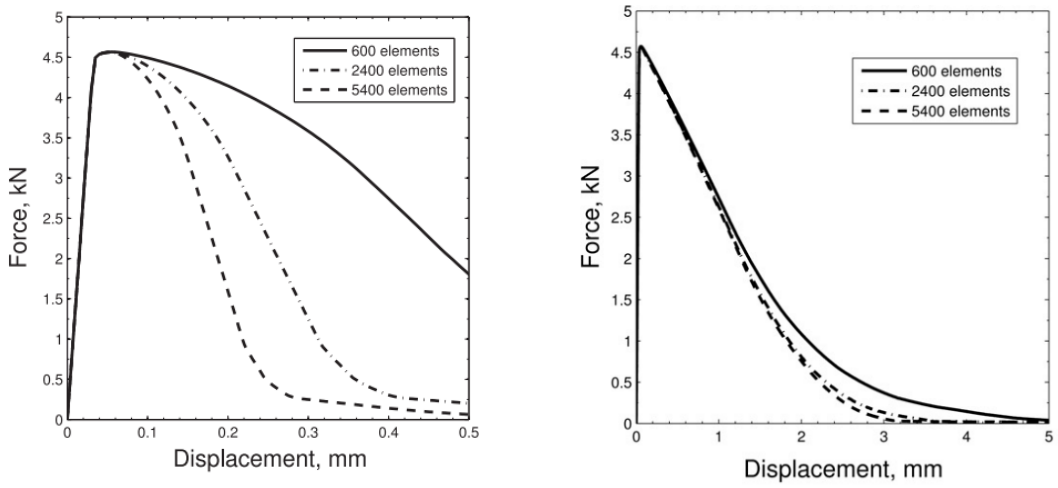

(a) (b)

Fig. 1.9 Simulation of plane strain tension tests with three different meshes using the (a) classical plasticity model, and (b) gradient-regularization (Anand et al., 2012).

can be found in (Čebron and Kosel, 2014; Jafari et al., 2017). Čebron and Kosel (2014) used a dislocation density-based crystal plasticity model to predict the stored energy in polycrystalline copper under tensile loading. Jafari et al. (2017) used a thermodynamically consistent framework for the prediction of stored energy in FCC single and bi-crystals. Furthermore, molecular dynamics simulations are proven to be advantageous in dislocation density evolution and, consequently, in predicting stored energy. Prediction of stored energy by employing molecular dynamics simulations can be found in (Kositski and Mordehai, 2021; Xiong et al., 2021). Kositski and Mordehai (2021) performed molecular dynamics simulations to study the TQC parameter evolution in single and polycrystalline aluminum, iron, copper, and tantalum at high strain rates. They found that some energy stored in polycrystalline simulations is due to the distribution of grain boundaries and the evolution of the morphology.

1.5.6 Gradient plasticity models: Applications to practical engineering problems

Nowadays, micro-machining and micro-forming processes have become increasingly important due to the extensive use of micron-scale components in the defense, automotive, medical, and aerospace industries. From a numerical point of view, strain gradient plasticity models can be used to simulate real-life manufacturing processes. In this section, applications of the gradient plasticity models to practical engineering problems are reviewed.

Most of the real-life manufacturing processes involve severe deformation. A review on the influence of size effects in micro-manufacturing processes can be found in (Pradeep Raja and Ramesh, 2021). Numerical modeling of the non-conventional plastic behavior

of micron-scale structures needs strain gradient crystal plasticity models. However, the complexity of the numerical implementation and increased computational cost leads to limited use of these models in practical engineering problems. An extensive review of the application of strain gradient plasticity models to manufacturing processes can be found in (Russo et al., 2020b).

The application of strain gradient plasticity model to micro-machining of FCC single crystal copper is discussed in (Demiral et al., 2014). They implemented this model in commercial software ABAQUS/Explicit using a user-defined subroutine VUMAT. They investigated the influence of strain gradients on the deformation mechanism in crystalline materials. Micro-forming such as micro-bending is a promising technology in manufacturing micron-scale components in mass production, for example, connectors and contact springs (Engel and Eckstein, 2002). Zhang et al. (2013) used a non-local crystal plasticity model to micro-bending of metallic foils to study the deformation mechanism and dislocation density evolution.

Despite several attempts in applying strain gradient plasticity models to practical engineering problems, for instance, in (Royer et al., 2011, 2012) for machining, they still have limited applications. Ease of implementation in commercial FE software and reduced computational cost in terms of CPU time may expand their applications to various engineering problems. One of the easy and efficient ways to implement these models in commercial FE software is by use of an analogy between the non-local model and classical continuum mechanics. For instance, an analogy between the chemical diffusion and mechanics is used to implement gradient plasticity and gradient damage models in an implicit version of the code ABAQUS in (Seupel et al., 2018).

1.6 Outline of the thesis

The outline of this work is as follows:

• Chapter 2 is dedicated to presenting an overview of the constitutive frameworks of crystal plasticity modeling. Firstly, the kinematic of the large deformation framework, definition of stresses, single crystal elasto-visco-plastic flow rule, and dislocation density-based hardening model used in this work are presented. Then, the constitutive framework of the reduced-order micromorphic crystal plasticity model, Lagrange multiplier-based model, and *CurlF*^{p} model is summarized. Finally, polycrystalline plasticity models from the literature are discussed.

• In Chapter 3, the size effects in monotonic loading of the single crystal microwire torsion tests are predicted using the micromorphic crystal plasticity and Lagrange multiplier-based models. Furthermore, a comparison is presented and discussed for the prediction of size effects using the reduced-order micromorphic crystal plasticity and *CurlF*^{p} models under monotonic and cyclic loading of the microwire torsion tests. In addition, SSD and GND density distribution using the Lagrange multiplier-based model for the monotonic and

cyclic loading of the microwire torsion tests is presented. To this end, scaling laws are developed using the reduced-order models for the monotonic loading of the microwire torsion tests.

• Chapter 4 is devoted to the investigation of the ASB formation process in single crystals and polycrystalline FCC metallic materials subjected to the *adiabatic* heating. A thermodynamically consistent framework of the classical and micromorphic crystal plasticity models is introduced. The capability of the micromorphic crystal plasticity model for the regularization of ASB formation in single and poly-crystals is demonstrated. In addition, the prediction of the grain size effect is performed in polycrystalline simulations under *isothermal* condition.

• In chapter 5, a thermodynamically consistent classical and micromorphic crystal plasticity models are used to predict the stored energy and TQC in single and poly-crystalline FCC metallic materials.

• Chapter 6 is dedicated to the implementation of the micromorphic plasticity theory in an explicit FE software VPS/Pam-Crash® from ESI Group. Then, this implemented model is employed for the regularization of shear band formation in *shearing operation* and prediction of size effect in *micro-bending* tests.

• Conclusions and outlook follow in chapter 7.

Note that the results shown in chapter 3, 4, and 5 are from the classical and micromorphic single crystal plasticity model implemented in implicit FE code Zset[4]. In addition, the results shown in chapter 6 are from the classical and micromorphic plasticity model implemented in explicit FE software VPS/Pam-Crash® from ESI Group[5].

[4]http://www.zset-software.com/
[5]https://www.esi-group.com/pam-crash

Chapter 2

Overview of constitutive frameworks: From classical to strain gradient crystal plasticity models

2.1 Introduction

The continuum crystal plasticity model considers the material strain hardening in plastically deforming material due to dislocation glide, dislocation multiplication, and interaction. Single crystals are of interest in structural materials, such as turbine blades and propellers, and are considered as a basis for polycrystalline materials. An early attempt to define the plastic deformation of single crystals can be found in (Taylor and Elam, 1923, 1925). This single crystal model was further utilized to analyze the deformation of polycrystalline aggregates in (Taylor, 1938). Furthermore, the single crystal model proposed by Taylor and Elam (1923, 1925) was put into a continuum framework by Mandel (1965) and Hill (1966) for small deformations. The extension based on a general thermodynamic formulation for finite deformation was proposed in (Rice, 1971; Hill and Rice, 1972; Mandel, 1973a; Asaro and Rice, 1977).

Metallic materials are generally polycrystalline in nature. When polycrystalline aggregates are subjected to severe deformation, significant changes in the microstructural and mechanical properties can be observed. One of the significant changes in microstructure is the re-orientation of crystal lattice towards a preferential orientation distribution, called crystallographic texture (Marin and Dawson, 1998). The prediction of plastic anisotropy and texture is the essence of polycrystal models. An anisotropic elasto-plastic deformation of crystalline aggregates, including shape change, crystallographic texture, and strain hardening, can be predicted by continuum crystal plasticity models (Cailletaud et al., 2003b; Roters et al., 2010). Moreover, it is possible to infer the behavior of polycrystalline aggregates from single crystals.

This chapter is dedicated to an overview of the constitutive framework of the CPFEM used in this work. The outline of the chapter is as follows: section 2.2 summarizes the kinematics of the large deformation framework and elasto-viscoplastic flow rule to evaluate the slip rate and internal variables. Section 2.3 is dedicated to the constitutive framework of the strain gradient crystal plasticity models, specifically the reduced-order micromorphic crystal plasticity model, Lagrange multiplier-based model, and *CurlF*^{p} model. Finally, in section 2.4 different homogenization methods used in polycrystalline simulations to study the mechanics of heterogeneous materials from the literature are summarized.

2.2 Finite deformation framework

2.2.1 Kinematics

A finite deformation framework is used throughout the work and is based on the multiplicative decomposition of the total deformation gradient $\underset{\sim}{F}$ into an elastic part $\underset{\sim}{F}^e$ and a plastic part $\underset{\sim}{F}^p$ (see Fig. 2.1), i.e. $\underset{\sim}{F} = \underset{\sim}{F}^e \cdot \underset{\sim}{F}^p$ (see, e.g., Lee and Liu (1967); Willis (1969); Rice (1971); Mandel (1973b); Teodosiu and Sidoroff (1976)). The volumetric mass densities with respect to the reference, the intermediate and the current configuration are ρ_0, $\rho_\#$, and ρ, respectively, and related via

$$J = \det(\underset{\sim}{F}) = \frac{\rho_0}{\rho}, \quad J^e = \det(\underset{\sim}{F}^e) = \frac{\rho_\#}{\rho}, \quad J^p = \det(\underset{\sim}{F}^p) = \frac{\rho_0}{\rho_\#}. \tag{2.1}$$

Moreover, it is assumed that the plastic flow is incompressible such that

$$J^p = \det \underset{\sim}{F}^p = 1, \quad J^e = J = \det \underset{\sim}{F}. \tag{2.2}$$

The spatial, a plastic, and an elastic velocity gradients are $\underset{\sim}{l}$, $\underset{\sim}{l}^p$, and $\underset{\sim}{l}^e$, respectively, and defined as follows:

$$\underset{\sim}{l} = \dot{\underset{\sim}{F}} \cdot \underset{\sim}{F}^{-1}, \quad \underset{\sim}{l}^p = \dot{\underset{\sim}{F}}^p \cdot \underset{\sim}{F}^{p-1}, \quad \underset{\sim}{l}^e = \dot{\underset{\sim}{F}}^e \cdot \underset{\sim}{F}^{e-1}. \tag{2.3}$$

The multiplicative decomposition of $\underset{\sim}{F}$ leads to the partition of the spatial velocity gradient $\underset{\sim}{l}$ into $\underset{\sim}{l}^e$ and $\underset{\sim}{l}^p$ as follows:

$$\underset{\sim}{l} = \underset{\sim}{l}^e + \underset{\sim}{l}^p, \quad \underset{\sim}{l} = \underset{\sim}{l}^e + \underset{\sim}{F}^e \cdot \underset{\sim}{l}^p \cdot \underset{\sim}{F}^{e-1}. \tag{2.4}$$

The Green-Lagrange strain tensor $\underset{\sim}{E}^e_{GL}$ is introduced as

$$\underset{\sim}{E}^e_{GL} = \frac{1}{2}(\underset{\sim}{F}^{eT} \cdot \underset{\sim}{F}^e - \underset{\sim}{1}), \tag{2.5}$$

with $\underset{\sim}{1}$ denoting the second-order identity tensor.

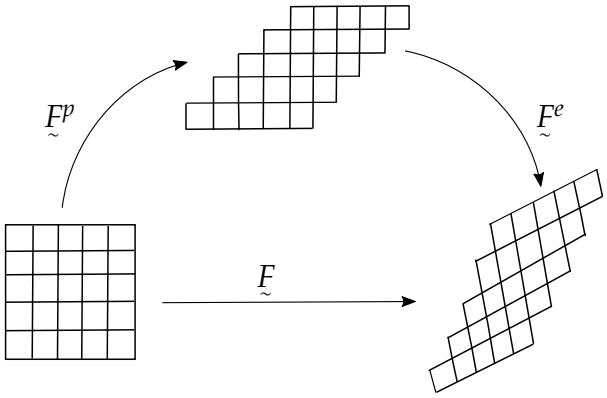

Fig. 2.1 A schematic representation of multiplicative decomposition of the total deformation gradient $\underset{\sim}{F}$ into an elastic $\underset{\sim}{F}^e$ and a plastic part $\underset{\sim}{F}^p$.

2.2.2 Definition of stresses

The second Piola-Kirchhoff stress tensor $\underset{\sim}{\Pi}^e$ is defined with respect to the intermediate configuration by

$$\underset{\sim}{\Pi}^e = J^e \underset{\sim}{F}^{e-1} \cdot \underset{\sim}{\sigma} \cdot \underset{\sim}{F}^{e-T}. \tag{2.6}$$

where $\underset{\sim}{\sigma}$ is the Cauchy stress tensor. The tensor $\underset{\sim}{\Pi}^e$ is related to the Green-Lagrange strain tensor $\underset{\sim}{E}^e_{GL}$ by elastic law

$$\underset{\sim}{\Pi}^e = \underset{\approx}{\Lambda} : \underset{\sim}{E}^e_{GL}. \tag{2.7}$$

where $\underset{\approx}{\Lambda}$ is the fourth-order tensor of elastic moduli. The first Piola-Kirchhoff stress tensor $\underset{\sim}{\Pi}^p$ related to the Cauchy stress tensor $\underset{\sim}{\sigma}$ is given by

$$\underset{\sim}{\Pi}^p = J \underset{\sim}{\sigma} \underset{\sim}{F}^{-T}. \tag{2.8}$$

Moreover, the Mandel stress tensor $\underset{\sim}{\Pi}^M$ which is work-conjugate to $\underset{\sim}{l}^p$ can be defined with respect to the intermediate configuration as follows:

$$\underset{\sim}{\Pi}^M = J^e \underset{\sim}{F}^{eT} \cdot \underset{\sim}{\sigma} \cdot \underset{\sim}{F}^{e-T}. \tag{2.9}$$

2.2.3 Flow rule

Most rate-independent crystal plasticity theories lead to an ill-conditioned problem regarding the selection of active slip systems and the increments of shear on the active slip systems as emphasized in (Anand and Kothari, 1996; Miehe et al., 1999; Busso and Cailletaud, 2005). This difficulty can be overcome by using rate-dependent framework. Here, a rate-dependent overstress-type flow rule is adopted to facilitate the determination of the set of active slip systems. It is based on a Schmid-type yield function defined as

$$f^r = |\tau^r| - \tau^r_c, \tag{2.10}$$

involving the resolved shear stress τ^r on the slip system r, which is the driving force to trigger plastic slip, and the corresponding critical resolved shear stress τ_c^r. The resolved shear stress τ^r on slip system r is defined as

$$\tau^r = \underset{\sim}{\Pi}^M : (\underline{m}^r \otimes \underline{n}^r), \tag{2.11}$$

where $\underline{m}^r$ is the slip direction and $\underline{n}^r$ is the slip normal.

The slip rate $\dot{\gamma}^r$ on each slip system r is then given by the following rate-dependent flow rule

$$\dot{\gamma}^r = \left\langle \frac{f^r}{K} \right\rangle^m \text{sign}(\tau^r), \tag{2.12}$$

with Macauley brackets $< \bullet >$ denoting the positive part of $\bullet$, and K and m are the viscosity parameters. The higher value of power m and lower value of K lead to an almost ideal elasto-plastic behavior in a given strain rate range.

It is assumed that the plastic deformation rate is the result of slip processes on N distinct slip systems, i.e.

$$\underset{\sim}{l}^p = \sum_{r=1}^{N} \dot{\gamma}^r (\underline{m}^r \otimes \underline{n}^r). \tag{2.13}$$

The validity of the finite deformation framework presented above is checked with the single crystal volume element undergoing simple shear. The details can be found in appendix B.

2.2.4 Dislocation density-based hardening model

Phenomenological flow rules are frequently used in crystal plasticity modeling. They have a drawback that the material state is only described in terms of critical resolved shear stress and not in terms of lattice defect population such as dislocation densities. This limitation can be overcome by the physics-based crystal plasticity models. The physics-based plasticity models provide a strong physical relationship with the microscopic mechanisms of plastic deformation by introducing microscopic internal variables such as dislocation density in the constitutive framework. The dislocation density-based models have better predictability compared to the phenomenological models over a wide range of strain, strain rates, and temperatures (Čebron and Kosel, 2014).

In the present work strain hardening behaviour is based on the dislocation density-based hardening model, which takes into account dislocation interactions. Following Kubin et al. (2008), the rate of the critical resolved shear stress τ_c^r is based on the scalar dislocation density as follows:

$$\tau_c^r = \tau_0 + \mu \sqrt{\sum_{u=1}^{N} h^{ru} \varrho^u}, \tag{2.14}$$

where τ_0 is the initial critical resolved shear stress, h^{ru} is the interaction matrix describing long-range interaction between the dislocations, ϱ^u ($= \rho^u b^2$) is the adimentional dislocation

density, and ρ^u is the usual dislocation density, i.e. the length of dislocation lines per unit volume with b being the norm of the dislocation Burgers vector $\underline{b}$. The following equation gives the evolution of the dislocation density

$$\dot{\varrho}^r = |\dot{\gamma}^r| \left(\frac{\sqrt{\sum_{u=1}^{N} b^{ru} \varrho^u}}{\kappa_c} - d_c \varrho^r \right). \tag{2.15}$$

The dislocation interaction is described by the matrix b^{ru}, κ_c is a constant material parameter proportional to the number of obstacles crossed by a dislocation before being immobilized, and d_c is the critical distance controlling the annihilation of dislocations with opposite signs. The structure of the matrices h^{ru} and b^{ru} can be found in appendix A. The total adimensional dislocation density can be expressed as follows:

$$\varrho_s = \sum_{r=1}^{N} \varrho_0^r + \int_0^t \sum_{r=1}^{N} \dot{\varrho}^r dt, \tag{2.16}$$

where ϱ_0^r is the initial adimensional dislocation density.

2.3 Strain gradient crystal plasticity theory

2.3.1 Reduced-order micromorphic crystal plasticity model

According to the micromorphic approach, the variables carrying the targeted gradient effects are selected from the available state variables and can be tensors of any rank (Forest, 2016b). The model is called reduced-order micromorphic when the micromorphic variable is a scalar quantity, as in the model proposed by Ling et al. (2018) summarized in this section.

The material points are defined by the position vector $\underline{X}$ in the reference configuration Ω^0 and the position vector $\underline{x}$ in the current configuration Ω^t. They possess two types of degrees of freedom: the displacement vector $\underline{u}(\underline{X}, t) = \underline{x} - \underline{X}$ and the micromorphic scalar microslip variable $\gamma_\chi(\underline{X}, t)$. The associated scalar internal variable is the cumulative plastic strain γ_{cum} introduced as

$$\gamma_{cum} = \int_0^t \sum_{r=1}^{N} |\dot{\gamma}^r| dt. \tag{2.17}$$

In the present formulation, the set of degrees of freedom (DOFs) is, therefore

$$\text{DOFs} = \{\underline{u}, \gamma_\chi\}. \tag{2.18}$$

The gradients of the degrees of freedom with respect to the reference configuration are

$$\underset{\sim}{H} = \frac{\partial \underline{u}}{\partial \underline{X}} = \operatorname{Grad} \underline{u}, \quad \underline{K} = \frac{\partial \gamma_\chi}{\partial \underline{X}} = \operatorname{Grad} \gamma_\chi. \tag{2.19}$$

The static balance equations and Neumann boundary conditions expressed with respect to the reference configuration are as follows:

$$\operatorname{Div} \underset{\sim}{\Pi}^p = \underline{0} \quad \text{and} \quad \operatorname{Div} \underline{M} - S = 0, \quad \forall \underline{X} \subset \Omega^0, \tag{2.20}$$

$$\underline{T} = \underset{\sim}{\Pi}^p \cdot \underline{N} \quad \text{and} \quad M = \underline{M} \cdot \underline{N}, \quad \forall \underline{X} \subset \partial\Omega^0, \tag{2.21}$$

with S and $\underline{M}$ being the generalized stresses, M is the generalized surface traction and $\underline{N}$ the outward unit normal vector at a boundary of the reference body.

The cumulative plastic strain γ_{cum} is related to the microslip variable γ_χ via the relative plastic strain $e_p(\underline{X}, t)$ as

$$e_p(\underline{X}, t) := \gamma_{cum} - \gamma_\chi. \tag{2.22}$$

The material under consideration is assumed to be characterized by the Helmholtz free energy density function

$$\Psi = \tilde{\Psi}(\underset{\sim}{E}^e_{GL}, e_p, \underline{K}, \zeta), \tag{2.23}$$

in terms of the Green-Lagrange strain tensor $\underset{\sim}{E}^e_{GL}$ (Eq. (2.5)), the relative plastic strain e_p, the gradient of the microslip variables $\underline{K}$ and the internal hardening variable ζ. The Helmholtz free energy density function is taken as a quadratic potential in the form:

$$\rho_0 \tilde{\Psi}(\underset{\sim}{E}^e_{GL}, e_p, \underline{K}, \zeta) = \frac{1}{2} \underset{\sim}{E}^e_{GL} : \underset{\approx}{\Lambda} : \underset{\sim}{E}^e_{GL} + \frac{1}{2} H_\chi e_p^2 + \frac{1}{2} \underline{K} \cdot \underset{\sim}{A} \cdot \underline{K} + \rho_0 \tilde{\Psi}(\zeta), \tag{2.24}$$

In the micromorphic approach, two additional material parameters are introduced, namely the coupling modulus H_χ and the higher-order micromorphic stiffness $\underset{\sim}{A}$.

The Clausius-Duhem inequality takes the form

$$\left(\underset{\sim}{\Pi}^e - \rho_0 \frac{\partial \tilde{\Psi}}{\partial \underset{\sim}{E}^e_{GL}} \right) : \dot{\underset{\sim}{E}}^e_{GL} - \left(S + \rho_0 \frac{\partial \tilde{\Psi}}{\partial e_p} \right) \dot{e}_p + \left(\underline{M} - \rho_0 \frac{\partial \tilde{\Psi}}{\partial \underline{K}} \right) \cdot \dot{\underline{K}} + \underset{\sim}{\Pi}^M : \underset{\sim}{l}^p + S \dot{\gamma}_{cum} - \rho_0 \frac{\partial \tilde{\Psi}}{\partial \zeta} \dot{\zeta} \geq 0, \tag{2.25}$$

from which the following state laws and residual dissipation inequality are adopted:

$$\underset{\sim}{\Pi}^e = \rho_0 \frac{\partial \tilde{\Psi}}{\partial \underset{\sim}{E}^e_{GL}}, \quad S = -\rho_0 \frac{\partial \tilde{\Psi}}{\partial e_p}, \quad \underline{M} = \rho_0 \frac{\partial \tilde{\Psi}}{\partial \underline{K}}, \quad X = \rho_0 \frac{\partial \tilde{\Psi}}{\partial \zeta}. \tag{2.26}$$

where X is the thermodynamic force associated with internal hardening variable ζ. The definition of the second Piola-Kirchhoff stress tensor $\underset{\sim}{\Pi}^e$ can be found in Eq. (2.6).

Moreover, the specific quadratic form of the potential (2.24) then leads to the following relations:

$$\underset{\sim}{\Pi}^e = \underset{\approx}{\Lambda} : \underset{\sim}{E}^e_{GL}, \quad S = -H_\chi e_p = -H_\chi(\gamma_{cum} - \gamma_\chi), \quad \underline{M} = \underset{\sim}{A} \cdot \underline{K}. \tag{2.27}$$

For isotropic and cubic materials, the second-order tensor $\underset{\sim}{A} = A\underset{\sim}{1}$ involves a single generalized modulus A which is assumed to be constant in space. Additionally, PDE connecting γ_χ and γ_{cum} follows from the previous state laws and the balance equation in (2.20) as

$$\gamma_\chi - \frac{A}{H_\chi} \triangle_X \gamma_\chi = \gamma_{cum}, \tag{2.28}$$

where $\triangle_X$ stands for the Laplace operator with respect to the reference configuration.

The residual dissipation inequality takes the form

$$D_{res} = \underset{\sim}{\Pi}^M : \underset{\sim}{l}^p + S\dot{\gamma}_{cum} - \sum_{r=1}^{N} X^r \dot{\zeta}^r = \sum_{r=1}^{N} \tau^r \dot{\gamma}^r + S\dot{\gamma}_{cum} - \sum_{r=1}^{N} X^r \dot{\zeta}^r \geq 0, \tag{2.29}$$

after consideration of (2.13) and of plastic incompressibility. The part of the free energy $\rho_0 \tilde{\Psi}(\zeta^r)$ due to the internal hardening variable ζ^r is assumed to be of the form (Abrivard et al., 2012):

$$\rho_0 \tilde{\Psi}^r(\zeta^r) = \frac{1}{2}\mu(\zeta^r)^2, \tag{2.30}$$

where $\rho_0 \tilde{\Psi}^r(\zeta^r)$ is the free energy function related to the internal hardening variable ζ^r on slip system r (= 1, 2....., N) with N being the total number of slip systems. The dissipation due to the internal hardening variable ζ^r in (2.25) on each slip system r is given by

$$X^r = \rho_0 \frac{\partial \tilde{\Psi}^r}{\partial \zeta^r} = \mu \zeta^r, \quad \text{with} \quad \zeta^r = \sqrt{\sum_{u=1}^{N} h^{ru} \varrho^u}. \tag{2.31}$$

The dissipation rate form from Eq. (2.29) suggests introducing the following generalized Schmid yield function:

$$f^r = |\tau^r| + S - \tau^r_c = |\tau^r| - (\tau^r_c - S), \tag{2.32}$$

which leads to a yield function of the form

$$f^r = |\tau^r| - (\tau^r_c - S) = |\tau^r| - (\tau^r_c - \mathrm{Div}\,\underline{M}), \tag{2.33}$$

once the generalized static balance law (2.20) is taken into account. In that way, the generalized stress S in the previous equation results in an enhancement of the hardening law and can be regarded as a source of isotropic hardening (or softening). After inserting (2.19) and (2.27) in (2.33), the yield function can be expressed as

$$f^r = |\tau^r| - (\tau^r_c - A\,\mathrm{Div}(\mathrm{Grad}\,\gamma_\chi)) = |\tau^r| - (\tau^r_c - A\,\triangle_X \gamma_\chi). \tag{2.34}$$

This generalized yield function is then inserted into the flow rule (2.12) to compute the plastic slip rate of each slip system.

The application of this model in numerical simulations can be found in chapter 3, 4 and 5. A thermodynamically consistent framework of this model is derived in chapter 4.

2.3.2 Lagrange multiplier-based model

The Lagrange multiplier-based model was proposed by Fortin and Glowinski (1983) and successfully implemented in (Zhang et al., 2018; Scherer et al., 2020). In this section, the Lagrange multiplier-based model presented in (Scherer et al., 2020) is summarized. The Lagrange multiplier λ is introduced to enforce the strict equality between γ_{cum} and γ_χ in order to transform the previous micromorphic model into a strain gradient crystal plasticity model. It replaces the penalty coefficient represented by the coupling modulus H_χ of the micromorphic model summarized in section 2.3.1. Therefore, the set of DOFs is given by

$$\text{DOFs} = \{\underline{u}, \gamma_\chi, \lambda\}. \tag{2.35}$$

It turns out that the free energy density function in (2.23) becomes a Lagrangian function L_0. More specifically speaking, the material under consideration is assumed to be characterized by the Lagrangian function $L_0(\underset{\sim}{E}^e_{GL}, e_p, \underline{K}, \lambda, \zeta)$, in terms of the Green-Lagrange strain tensor $\underset{\sim}{E}^e_{GL}$, the relative plastic strain e_p, the gradient of the microslip variable $\underline{K}$, the Lagrange multiplier λ, which is treated as an additional degree of freedom and the internal hardening variable ζ. The considered form of the Lagrangian function is

$$\rho_0 L_0(\underset{\sim}{E}^e_{GL}, e_p, \underline{K}, \lambda, \zeta) = \frac{1}{2}\underset{\sim}{E}^e_{GL} : \underset{\approx}{\Lambda} : \underset{\sim}{E}^e_{GL} + \frac{1}{2}\mu_\chi e_p^2 + \frac{1}{2}\underline{K} \cdot \underset{\sim}{A} \cdot \underline{K} + \lambda e_p + \rho_0 L_0(\zeta), \tag{2.36}$$

where μ_χ is a Lagrangian penalty modulus. The Clausius-Duhem inequality then takes the form

$$\left(\underset{\sim}{\Pi}^e - \rho_0 \frac{\partial L_0}{\partial \underset{\sim}{E}^e_{GL}}\right) : \dot{\underset{\sim}{E}}^e_{GL} - \left(S + \rho_0 \frac{\partial L_0}{\partial e_p}\right)\dot{e}_p + \left(\underline{M} - \rho_0 \frac{\partial L_0}{\partial \underline{K}}\right) \cdot \dot{\underline{K}} + \underset{\sim}{\Pi}^M : \underset{\sim}{l}^p + S\dot{\gamma}_{cum} - \rho_0 \frac{\partial L_0}{\partial \zeta}\dot{\zeta} \geq 0. \tag{2.37}$$

This gives rise to the following state laws:

$$\underset{\sim}{\Pi}^e = \rho_0 \frac{\partial L_0}{\partial \underset{\sim}{E}^e_{GL}}, \quad S = -\rho_0 \frac{\partial L_0}{\partial e_p}, \quad \underline{M} = \rho_0 \frac{\partial L_0}{\partial \underline{K}}, \quad X = \rho_0 \frac{\partial L_0}{\partial \zeta}. \tag{2.38}$$

Furthermore, evaluating (2.38) for the specific quadratic form of the Lagrangian (2.36) leads to the following relations

$$\underset{\sim}{\Pi}^e = \underset{\approx}{\Lambda} : \underset{\sim}{E}^e_{GL}, \quad S = \lambda - \mu_\chi(\gamma_{cum} - \gamma_\chi), \quad \underline{M} = \underset{\sim}{A} \cdot \underline{K}. \tag{2.39}$$

The part of the free energy $\rho_0 L_0(\zeta^r)$ due to the internal hardening variable ζ^r has the form as given in Eq. (2.30). Moreover, the expression for the thermodynamic force X^r is as given in Eq. (2.31).

The residual dissipation has the same form as (2.29) and leads to the introduction of the following generalized Schmid yield function:

$$f^r = |\tau^r| + S - \tau_c^r = |\tau^r| - (\tau_c^r - S) = |\tau^r| - (\tau_c^r - \lambda + \mu_\chi(\gamma_{cum} - \gamma_\chi)). \tag{2.40}$$

Again, this generalized yield function can be inserted into the flow rule (2.12) to evaluate the plastic slip rate of each slip system. The penalty parameter μ_χ is similar to the micromorphic penalization term H_χ but bears a different meaning. In simulations, the parameter μ_χ can take a much lower value than H_χ and provides additional coercivity.

The application of this model in numerical simulations can be found in chapter 3.

2.3.3 *CurlF^p* model

In this section, the gradient plasticity theory based on the complete dislocation density tensor elaborated in (Kaiser and Menzel, 2019b) is briefly summarized. The *CurlF^p* framework proposed by Kaiser and Menzel (2019b) relies on the interpretation of incompatible plastic deformation processes in terms of the dislocation density tensor. The model formulation is based on introducing the dislocation density tensor as an argument of the free energy density function and assumes an extended non-local form of the dissipation inequality as proposed by Polizzotto and Borino (1998).

The material under consideration is assumed to be characterized by the free energy density function

$$\Psi = \tilde{\Psi}(\underset{\sim}{F}, \underset{\sim}{F}^p, \underset{\sim}{D}_d, \zeta), \tag{2.41}$$

with ζ denoting a scalar-valued internal variable, which may be interpreted as of measure of the cumulative plastic strain. Moreover, it is assumed that the gradient-enhanced energy density function can additively be decomposed as

$$\rho_0 \tilde{\Psi} = \rho_0 \tilde{\Psi}^e(\underset{\sim}{F}, \underset{\sim}{F}^p) + \rho_0 \tilde{\Psi}^g(\underset{\sim}{D}_d) + \rho_0 \tilde{\Psi}^p(\zeta), \tag{2.42}$$

where $\tilde{\Psi}^e$, $\tilde{\Psi}^g$, and $\tilde{\Psi}^p$ are the elastic contribution, the energy contribution due to the gradient effect and the energy contribution due to the internal hardening variable, respectively. The energy contribution $\tilde{\Psi}^g$ is expressed as a quadratic function

$$\rho_0 \tilde{\Psi}^g(\underset{\sim}{D}_d) = H_D \underset{\sim}{D}_d : \underset{\sim}{D}_d, \tag{2.43}$$

where H_D is a material parameter proposed in (Kaiser and Menzel, 2019b), which can be interpreted as a characteristic length scale parameter. The part of the free energy due to the

hardening variable ζ is chosen as

$$\rho_0 \tilde{\Psi}^p(\zeta) = \tau_0 \zeta + \frac{(\tau_\infty - \tau_0)^2}{H_0} \ln\left(\cosh\left(\frac{H_0 \zeta}{\tau_\infty - \tau_0}\right)\right), \tag{2.44}$$

where the material parameters τ_∞ and H_0 are the saturation strength and the initial hardening rate, respectively. The extended form of the dissipation inequality is

$$D_{res} = \underset{\sim}{\Pi}^p : \dot{\underset{\sim}{F}} - \left(\rho_0 \frac{\partial \tilde{\Psi}}{\partial \underset{\sim}{F}} : \dot{\underset{\sim}{F}} + \rho_0 \frac{\partial \tilde{\Psi}}{\partial \underset{\sim}{F}^p} : \dot{\underset{\sim}{F}}^p + \rho_0 \frac{\partial \tilde{\Psi}}{\partial \underset{\sim}{D}_d} : \dot{\underset{\sim}{D}}_d + \rho_0 \frac{\partial \tilde{\Psi}}{\partial \zeta} : \dot{\zeta}\right) + \mathcal{P}_0 \geq 0, \tag{2.45}$$

with $\mathcal{P}_0$ denoting the non-locality residual. The first Piola-Kirchhoff stress tensor is given by

$$\underset{\sim}{\Pi}^p = \rho_0 \frac{\partial \tilde{\Psi}}{\partial \underset{\sim}{F}}. \tag{2.46}$$

The reduced form of the dissipation inequality reads

$$D_{res} = \overline{\underset{\sim}{\Pi}}^M : \underset{\sim}{l}^p + \underset{\sim}{\Xi} : \dot{\underset{\sim}{D}}_d - X\dot{\zeta} + \mathcal{P}_0 \geq 0. \tag{2.47}$$

where $\overline{\underset{\sim}{\Pi}}^M$ is a Mandel-type stress tensor defined in the intermediate configuration by

$$\overline{\underset{\sim}{\Pi}}^M = \underset{\sim}{F}^{eT} \cdot \underset{\sim}{\Pi}^p \cdot \underset{\sim}{F}^{pT}, \tag{2.48}$$

and related to the Mandel stress tensor $\underset{\sim}{\Pi}^M$ defined in (2.9) by $\overline{\underset{\sim}{\Pi}}^M = J^p \underset{\sim}{\Pi}^M$, as the incompressibility condition ($J^p = 1$) is not explicitly assumed in this particular model.

The thermodynamic force associated with the internal hardening variable is defined as

$$X = \rho_0 \frac{\partial \tilde{\Psi}}{\partial \zeta} = \left(\tau_0 + (\tau_\infty - \tau_0)\tanh\left(\frac{H_0 \zeta}{\tau_\infty - \tau_0}\right)\right), \tag{2.49}$$

and the energetic dual to the dislocation density tensor reads

$$\underset{\sim}{\Xi} = -\rho_0 \frac{\partial \tilde{\Psi}}{\partial \underset{\sim}{D}_d}. \tag{2.50}$$

Moreover, the evaluation of (2.50) for the specific form of the energy contribution (2.43) yields

$$\underset{\sim}{\Xi} = -2H_D \mathrm{Curl}^T(\underset{\sim}{F}^p). \tag{2.51}$$

The balance equation of linear momentum expressed with respect to the reference configuration

$$\mathrm{Div}\, \underset{\sim}{\Pi}^p = \underline{0}, \quad \text{in} \quad B^0 \tag{2.52}$$

which is complemented by boundary condition

$$\underline{T} = \underset{\sim}{\Pi}^{p} \cdot \underline{N}, \quad \text{on} \quad \partial B_t^0, \tag{2.53}$$

By considering an insulation condition $\mathcal{P}_0 = 0$ as in (Kaiser and Menzel, 2019a), the reduced form of the dissipation inequality may be written in terms of

$$D_{res} = \overline{\underset{\sim}{M}} : \underset{\sim}{l}^{p} - X\dot{\zeta} \geq 0, \tag{2.54}$$

giving rise to a balance equation for the generalized stress tensor as

$$\overline{\underset{\sim}{M}} = \overline{\underset{\sim}{\Pi}}^{M} + \mathrm{Curl}^{T}(\underset{\sim}{\Xi}) \cdot \underset{\sim}{F}^{pT}, \quad \text{in} \quad B_{dis}^0. \tag{2.55}$$

The generalized stress tensor $\overline{\underset{\sim}{M}}$ consist of the Mandel-type stress tensor $\overline{\underset{\sim}{\Pi}}^{M}$ defined in the intermediate configuration and a back-stress term $\mathrm{Curl}^{T}(\underset{\sim}{\Xi}) \cdot \underset{\sim}{F}^{pT}$, which is closely related to incompatibilities in the plastic deformation field such that when gradient effects are neglected, $\overline{\underset{\sim}{M}}$ reduces to $\overline{\underset{\sim}{\Pi}}^{M}$. The generalized stress tensor is identified as the driving force for plastic deformation processes based on (2.54). The yield function and the evolution equations are accordingly formulated in terms of the generalized stress tensor. Moreover, the non-ambiguous constitutive boundary condition associated with (2.55) reads

$$\underset{\sim}{\Xi} \cdot \mathrm{Spin}(\underline{N}) \cdot \underset{\sim}{F}^{pT} = \mathbf{0}, \quad \text{on} \quad \partial B_{dis,ext}^0, \tag{2.56}$$

where Spin is a spin operator which relate the axial vector to the corresponding skew-symmetric second-order tensor in the reference configuration is defined as $(\mathrm{Spin}\,\underline{N})_{ij} = -\epsilon_{ijq} N_q \underline{e}_i \otimes \underline{e}_j$. The detailed derivation of (2.55) and (2.56) can be found in (Kaiser and Menzel, 2019b). The generalized stress tensor in (2.55) and the constitutive boundary condition in (2.56) are originally derived on the domain B_{dis}^0, where dissipative processes occur, and on the corresponding external boundary $\partial B_{dis,ext}^0$.

In addition, the relative Mandel stress tensor is introduced as a primary field variable

$$\overline{\underset{\sim}{M}}^{(\mathrm{rel})} = \overline{\underset{\sim}{M}} - \overline{\underset{\sim}{\Pi}}^{M}, \tag{2.57}$$

so that (2.55) can be written as

$$\overline{\underset{\sim}{M}}^{(\mathrm{rel})} - \mathrm{Curl}^{T}(\underset{\sim}{\Xi}) \cdot \underset{\sim}{F}^{pT} = \underset{\sim}{0}, \quad \text{in} \quad B_{dis}^0. \tag{2.58}$$

Substituting (2.51) in (2.58) yields the specific form of the relative Mandel stress tensor

$$\overline{\underset{\sim}{M}}^{(\mathrm{rel})} = -2H_D \mathrm{Curl}^{T}(\mathrm{Curl}^{T}(\underset{\sim}{F}^{p})) \cdot \underset{\sim}{F}^{pT}, \tag{2.59}$$

which is responsible for the back-stress associated with the kinematic hardening. Additionally, field variable $\underset{\sim}{\theta}^{p}$ is introduced which is coupled to $\underset{\sim}{F}^{p}$ in terms of an L_2-projection as

follows:

$$0 = \int_{B^0} \underset{\sim}{\eta}^{\theta^p} : (\underset{\sim}{F}^p - \underset{\sim}{\theta}^p) dV, \tag{2.60}$$

where $\underset{\sim}{\eta}^{\theta^p}$ is the corresponding test function.

Different definitions of the curl of a second-order tensor often used by researchers and analytical expressions of the dislocation density tensor in small and large deformation frameworks are given in appendix C.

In order to identify the differences between the Lagrange multiplier-based model and the *CurlF*^{p} model, the constitutive equations of both models are summarized in Table 2.1.

Table 2.1 Summary of constitutive equations used in reduced-order and the *CurlF*^{p} models.

Constitutive equations	Reduced-order model (Lagrange multiplier-based) (Scherer et al., 2020)	*CurlF*^{p} model (Kaiser and Menzel, 2019b)
DOFs (three-dimensional setting)	$\{\underline{u}, \gamma_\chi, \lambda\}$ Total DOFs per node = 5	$\{\underline{u}, \overline{\underset{\sim}{M}}^{(\mathrm{rel})}, \underset{\sim}{\theta}^p\}$ Total DOFs per node = 21
Free energy density function	$L_0(\underset{\sim}{E}^e_{GL}, e, \underline{K}, \lambda, \zeta)$	$\Psi = \hat{\Psi}(\underset{\sim}{F}, \underset{\sim}{F}^p, \underset{\sim}{D}_d, \zeta)$
State laws	$\underset{\sim}{\Pi}^e = \rho_0 \frac{\partial L_0}{\partial \underset{\sim}{E}^e_{GL}}$ $S = -\rho_0 \frac{\partial L_0}{\partial e}$ $\underline{M} = \rho_0 \frac{\partial L_0}{\partial \underline{K}}$ $X = \rho_0 \frac{\partial L_0}{\partial \zeta}$	$\underset{\sim}{\Pi}^p = \rho_0 \frac{\partial \Psi}{\partial \underset{\sim}{F}}$ $\underset{\sim}{\Xi} = -\rho_0 \frac{\partial \Psi}{\partial \underset{\sim}{D}_d}$ $X = \rho_0 \frac{\partial \Psi}{\partial \zeta}$
Balance laws	$\mathrm{Div}\, \underset{\sim}{\Pi}^p = \underline{0}$ and $\mathrm{Div}\, \underline{M} - S = 0$, $\forall\, \underline{X} \subset \Omega^0$	$\mathrm{Div}\, \underset{\sim}{\Pi}^p = \underline{0}$ in B^0 and $\overline{\underset{\sim}{M}} = \overline{\underset{\sim}{\Pi}}^M + \mathrm{Curl}(\underset{\sim}{\Xi}) \cdot \underset{\sim}{F}^{pT}$ in B^0_{dis}
Boundary conditions	$\underline{T} = \underset{\sim}{\Pi}^p \cdot \underline{N}$ and $M = \underline{M} \cdot \underline{N}$, $\forall\, \underline{X} \subset \partial\Omega^0$	$\underline{T} = \underset{\sim}{\Pi}^p \cdot \underline{N}$ on ∂B^0_t and $\underset{\sim}{\Xi} \cdot \mathrm{Spin}(\underline{N}) \cdot \underset{\sim}{F}^{pT} = \underset{\sim}{0}$, on $\partial B^0_{dis,ext}$
Residual dissipation inequality	$\underset{\sim}{\Pi}^M : \underset{\sim}{l}^p + S\dot{\gamma}_{cum}$ $-X\dot{\zeta} \geq 0$	$\underset{\sim}{\Pi}^M : \underset{\sim}{l}^p + \underset{\sim}{\Xi} : \underset{\sim}{\dot{D}}_d$ $-X\dot{\zeta} + \mathcal{P}_0 \geq 0$
Thermodynamic force associate with the internal hardening variable	$X = \mu \sqrt{\sum_{u=1}^{N} h^{ru} \varrho^u}$	$X = \left(\tau_0 + (\tau_\infty - \tau_0) \tanh\left(\frac{H_0 \zeta}{\tau_\infty - \tau_0} \right) \right)$
Material parameters related to characteristic length scale	A, H	H_D

In the comparison of gradient crystal plasticity models, the Lagrange multiplier-based model is used to compare the size effects predicted by the *CurlF*^{p} model because the *CurlF*^{p} model is a strain gradient plasticity model and thus should be compared more directly to the Lagrange multiplier-based model. This comparison can be found in chapter 3.

2.4 Polycrystalline plasticity models

The single crystal behavior can be used to predict the behavior of polycrystalline aggregates. Grains in a polycrystal are defined according to crystal orientations such that grains having the same Euler angles with a given tolerance are all within the same class. The homogenization models proposed for polycrystals differ in the scale transition rule used to predict the local stresses and strains. Several authors made various hypotheses for strain redistribution within the phases. For instance, Taylor (1938) made an assumption of a uniform plastic strain, $\underset{\sim}{\varepsilon}^{pg} = \underset{\sim}{E}^{p}$. The assumption of uniform plastic strain is somewhat crude, and it fails because the experimental results show evidence of plastic strain heterogeneity, for instance, in uniaxial compression of FCC metallic materials. Furthermore, Lin-Taylor (Lin, 1957) assumed a uniform total strain such that $\underset{\sim}{\varepsilon}^{g} = \underset{\sim}{E}$. All uniform strain theories satisfy the compatibility condition; however, they do not satisfy the equilibrium at grain boundaries.

The scale transition rule links the mean local stress $\underset{\sim}{\sigma}^{g}$ to macroscopic stress $\underset{\sim}{\Sigma}$ and mean visco-plastic strain $\underset{\sim}{E}^{p}$ to local visco-plastic strain $\underset{\sim}{\varepsilon}^{pg}$ (Cailletaud and Pilvin, 1994; Barbe et al., 2001b) such that

$$\underset{\sim}{\Sigma} = \sum_{g=1}^{N_g} f_g \underset{\sim}{\sigma}^{g}, \quad \underset{\sim}{\dot{E}}^{p} = \sum_{g=1}^{N_g} f_g \underset{\sim}{\dot{\varepsilon}}^{pg}, \tag{2.61}$$

where g denotes the grain or phase, N_g is the number of grains and f_g is the volume fraction of grain or phase g.

The homogenization models such as mean-field and full-field models are quite extensively used to determine macroscopic properties from geometrical features of the microstructure. In the following sections, these homogenization models are reviewed.

• Mean-field models

Generalizing the work of (Eshelby and Peierls, 1957) different mean-field homogenization models were developed for instance in (Kröner, 1958; Hill, 1965; Berveiller and Zaoui, 1978; Tandon and Weng, 1988). Kröner's (Kröner, 1958) model gives an elastic accommodation such that in case of isotropic materials, the local stress $\underset{\sim}{\sigma}^{g}$ is given by

$$\underset{\sim}{\sigma}^{g} = \underset{\sim}{\Sigma} + 2\mu(1-\Lambda)(\underset{\sim}{E}^{p} - \underset{\sim}{\varepsilon}^{pg}), \quad \text{with} \quad \Lambda = \frac{2(4-5\nu)}{15(1-\nu)}, \tag{2.62}$$

where the constant Λ only depends on the Poisson ratio and is approximately equal to 0.5. Kröner's model results in very high value of internal stresses due to assumption of elastic accommodation, $2\mu(1-\Lambda)(\underset{\sim}{E}^{p} - \underset{\sim}{\varepsilon}^{pg})$, via large value of shear modulus μ. The approximation can be made to consider the plastic accommodation by replacing the elastic shear modulus with an adequate elastoplastic modulus.

A more precise formulation can be derived from Hill's approximation (Hill, 1965) by assuming an isotropic elasto-plastic interaction between one grain and the matrix of other grains. The self-consistent approximation considers each phase as an ellipsoid embedded in a homogeneous equivalent medium.

There are two main limitations of mean-field models. First, these models consider the description of microstructure based on average grain size, shape, and orientation and cannot take into account the local heterogeneity within grains. The second limitation concerns micro-mechanical fields, which are considered constant within grains. Therefore, these models cannot be applied to the phenomenon in which micromechanical fields are localized in narrow bands (Segurado et al., 2018). Full-field models can overcome these limitations.

• Full-field models

Full-field homogenization models predict the macroscopic response and microscopic field distribution in heterogeneous materials based on the simulation of representative volume element (RVE) (Böhm, 2004). The method is computationally expensive because it involves the solution of the boundary-value problem, which may contain a large number of degrees of freedom. Full-field models are more accurate than the mean-field models and are generally used as reference models (Segurado et al., 2018). They can predict the local stress-strain fields and state variables throughout the microstructure, which is important information, for instance, in damage prediction and localization problems.

Several numerical methods are available to predict the response of RVE. One of the most common methods is based on FE modeling as demonstrated in (Cailletaud et al., 2003b,a; Coudon et al., 2019; Flipon et al., 2020). Early attempts to simulate polycrystals using the FE method can be found in (Kalidindi et al., 1992; Bronkhorst et al., 1992). They considered a 2D model where each element represents a grain. This model is similar to a mean-field model in that the local fields are missing. Moreover, the field in each grain is considered to be constant, hence not able to model the strong deformation gradient usually seen in polycrystals. Later on, 3D microstructure modeled with each grain represented by several elements with the regular mesh was presented by (Mika and Dawson, 1999). Finally, a more realistic microstructure with several elements per grain was modeled in (Barbe et al., 2001b).

The homogenization using FE methods requires solving boundary-value problems that require a mesh discretized geometry of the microstructure. The first approach, sometimes called the multiphase element technique, consists of superposing a regular 3D mesh on the image of the microstructure (Fig. 2.2a). The drawback of this method is an inadequate description of interfaces. The proper meshing of the interfaces is possible with the second approach of Voronoï polyhedra using standard 2D and 3D free meshing techniques (Fig. 2.2b). Fig. 2.3 taken from (Marchenko et al., 2016) shows 2D and 3D polycrystalline aggregates with several grains generated using Voronoï tessellation.

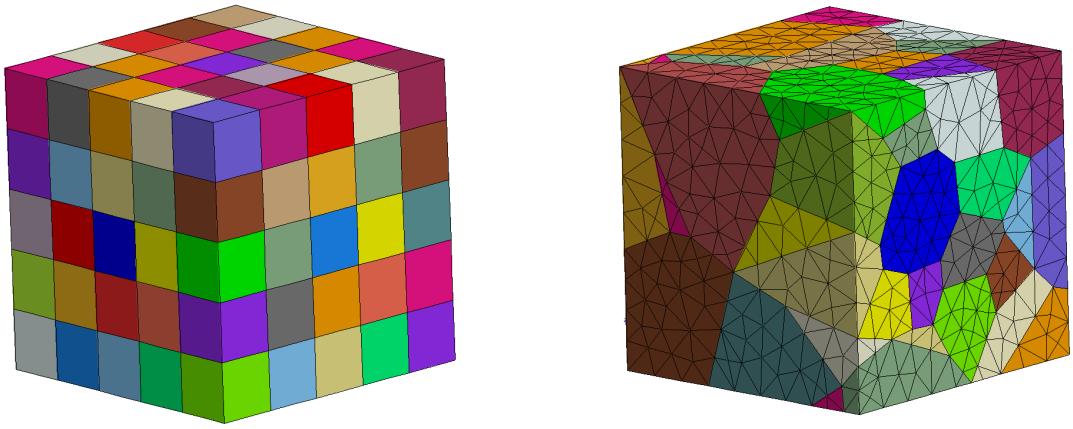

(a) (b)

Fig. 2.2 Two meshing techniques used for RVE: (a) regular mesh, and (b) mesh representing grain boundaries created using Voronoï tessellation. Color represents the each individual grain.

The application of boundary conditions to RVEs is one of the main issues in full-field modeling. Four different types of boundary conditions can be applied to RVEs (Barbe et al., 2001b; Cailletaud et al., 2003b; Segurado et al., 2018): (a) periodic boundary conditions, (b) statically uniform boundary conditions, where applied surface tractions are homogeneous over RVE faces, (c) kinematically uniform boundary conditions in which uniform displacements are applied to the RVE boundary, and (d) mixed boundary conditions combining uniform tractions and displacements on RVE surfaces.

Furthermore, it is essential to define the size of the RVE properly. An early attempt to determine the size of the RVE can be found in (Kanit et al., 2003). The size of the RVE depends upon the studied properties (mechanical, thermal), phase morphology, and boundary conditions. The effective properties can be determined using large size RVE with a small number of realizations. A smaller size of the RVE is possible when a sufficient number of realizations of the microstructure are considered.

In the present work, we use a full-field model to simulate the behavior of polycrystalline aggregates. A single crystal plasticity model is used to represent the behavior of each grain of the polycrystalline aggregate. Besides, mixed boundary conditions presented above are applied to the RVE surface.

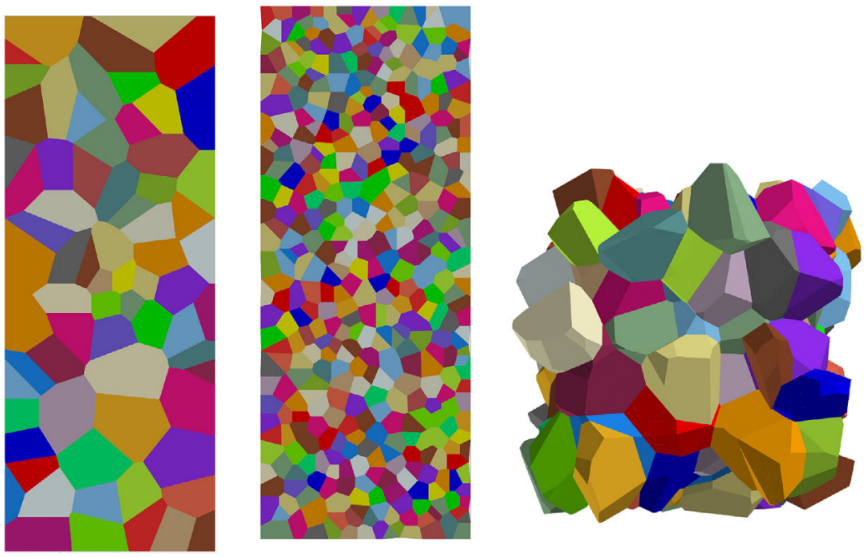

(a) (b) (c)

Fig. 2.3 Polycrystal morphologies generated using Voronoï tessellation: (a) 71 2D grains (b) 432 2D grains, and (c) 150 3D grains (Marchenko et al., 2016).

Chapter 3

Prediction of size effect in microwire torsion tests

Abstract

The size-dependent response of metallic microwires under monotonic and cyclic torsion is modeled taking a reduced-order strain gradient crystal plasticity approach involving a single scalar-valued micromorphic variable. At first, size effects predicted by the reduced-order micromorphic and Lagrange multiplier-based formulations are assessed under monotonic microwire torsion tests. Then it is compared with the response predicted by the CurlF^p model proposed in (Kaiser and Menzel, 2019a), which is based on the complete dislocation density tensor. It is shown that, in cyclic non-uniform plastic deformation processes, the gradient of the scalar-valued internal variable in the reduced-order model predicts isotropic hardening in contrast to kinematic-type hardening produced by the CurlF^p model due to a dislocation-induced back-stress component. The arising size effect in the monotonic torsion tests is described by the normalized torque T/R^3 as a function of the ratio of the microwire radius R and the characteristic length scale ℓ. In the size-dependent domain, characterized by an inflection point on the corresponding curve, the scaling law $T/R^3 \sim (R/\ell)^n$ can be identified, and explicit relations are found for the power n. The relative evolution of Statistically Stored Dislocation (SSD) and Geometrically Necessary Dislocation (GND) densities during torsion is described in detail.

3.1 Introduction

The torsion of single and polycrystal wires has been the subject of intensive experimental and computational research. Nouailhas and Cailletaud (1995) discovered that the torsion of a single crystal bar or tube is characterized by two types of strain gradients: a radial gradient from the center to the outer surface due to the loading, but also a gradient along

Part of this chaper has been published in *Lagrange multiplier based vs micromorphic gradient-enhanced rate-(in)dependent crystal plasticity modelling and simulation. Computer Methods in Applied Mechanics and Engineering 372, 113426.* Also, part of this chapter has been submitted to a journal.

the outer circumference due to the anisotropic activation of slip systems. This was observed experimentally using strain gauges placed along the circumference (Forest et al., 1996). The transition from single to poly-crystals for microwires of increasing diameters was computed using CPFEM in (Quilici et al., 1998) and more recently in (Bayerschen et al., 2016).

Implementation of strain gradient crystal plasticity theory in a finite element code is a challenging task that has been performed for example by Shu (1998); Borg et al. (2008); Yalcinkaya et al. (2012); Bardella et al. (2013); Nellemann et al. (2017, 2018); Panteghini and Bardella (2016) at small strains and by Niordson and Kysar (2014); Lewandowski and Stupkiewicz (2018); Ling et al. (2018); Kaiser and Menzel (2019b) at finite deformations. An efficient method to implement strain gradient plasticity models is to resort to the micromorphic approach proposed by Forest (2009) at small strains and Forest (2016a) at finite deformation, as demonstrated by Anand et al. (2012) and Brepols et al. (2017) for conventional plasticity, and by Cordero et al. (2010); Aslan et al. (2011); Ryś et al. (2020) for crystal plasticity based on the dislocation density tensor. According to this approach, additional plastic microdeformation degrees of freedom, in the sense of (Eringen and Suhubi, 1964), are introduced at each node, and the curl part of the microdeformation tensor is assumed to expend work with a conjugate couple stress tensor. A penalty parameter, which can be interpreted as a higher-order elasticity modulus, is used to constrain the plastic microdeformation to be as close as possible to the usual plastic deformation. As a consequence, the curl of the microdeformation tensor almost coincides with the dislocation density tensor.

Gradient plasticity and micromorphic models involving the gradient or rotational part of the plastic deformation tensor generally requires a large number of additional internal variables and nodal degrees of freedom leading to a significant increase in the computational cost. For instance, the full-order microcurl model proposed by Cordero et al. (2010) and the gradient plasticity model by Panteghini and Bardella (2018) require at least 16 and 12 additional nodal degrees of freedom, respectively, in a two-dimensional setting. The complexity in the numerical implementation further increases the computational modeling efforts. The differences in the formulation of various gradient plasticity theories result in distinct and sometimes non-physical responses, which raises the necessity of comparing different gradient plasticity models (Peerlings et al., 2001). A comparison between five gradient-enhanced phenomenological approaches in a continuum damage setting can be found in (Geers et al., 2000), and between implicit and explicit gradient formulations in (Peerlings et al., 2001). The computational advantages of an implicit formulation, which includes the equivalent plastic strain as an additional degree of freedom over an explicit formulation, are investigated in (Wulfinghoff and Böhlke, 2012). Moreover, the non-local crystal plasticity theory proposed by Gurtin (2002) is used in (Bittencourt et al., 2003) to explore to which extent the results from the discrete dislocation simulations can be reproduced. It is found that the non-local plasticity reproduces the behavior seen in the discrete dislocation simulations in remarkable detail. However, only a few studies are

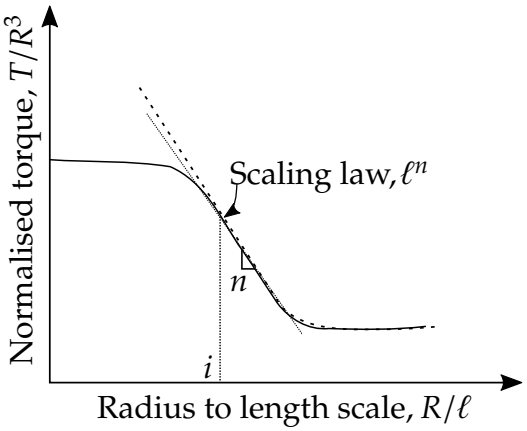

Fig. 3.1 Schematic log-log plot characterizing the effect of the ratio of the microwire radius R to the characteristic length scale ℓ on the normalized torque T/R^3: size effect with bounded (solid line) and unbounded (dashed line) asymptotic regimes, power law in the transition domain (dotted line), n is the slope of the size dependent domain and i is the inflection point of the curve.

dedicated to comparing various gradient crystal plasticity approaches and determining the advantages and drawbacks of the many existing theories. For instance, the detailed comparison of the micropolar crystal plasticity model (Mayeur et al., 2011) and the non-local crystal plasticity model proposed by Gurtin (2002) can be found in (Mayeur and McDowell, 2014).

Therefore, the first objective of the present chapter is to compare the micromorphic crystal plasticity and Lagrange multiplier-based implementation of strain gradient crystal plasticity for the prediction of size effect in microwire torsion tests. The size and orientation dependent torsion of FCC single crystal wires is investigated showing that both models coincide at intermediate wire diameters but differ in their asymptotic behavior.

Another original objective of this work is to compare a computationally efficient Lagrange multiplier-based model that involves a single scalar-valued variable with the $CurlF^p$ model proposed in (Kaiser and Menzel, 2019a) for monotonic and cyclic microwire torsion tests. The scaling law $T/R^3 \propto (R/\ell)^n$ for the microwire torsion tests, which characterizes the effect of the ratio of the microwire radius R and characteristic length scale ℓ on the normalized torque T/R^3, is obtained using both reduced-order micromorphic crystal plasticity and Lagrange multiplier-based models. Such scaling laws were derived for the periodic shearing of a laminate at small strains and small rotations in (Cordero et al., 2010; Ryś et al., 2020). Fig. 3.1 schematically shows the effect of R/ℓ ratios on the normalized torque T/R^3, which is found in the present work. The main features of the diagram are the inflection point i and the slope n of the size-dependent domain. For small values of R/ℓ ratio, a bounded (for the micromorphic crystal plasticity model), or an unbounded (for the Lagrange multiplier-based model), asymptotic behavior can be obtained. At large values of R/ℓ ratio, the observed asymptotic behavior corresponds to the size-independent response of classical crystal plasticity models.

The outline of the chapter is as follows: In section 3.2, geometry and boundary conditions of the single crystal microwire torsion tests for the comparison of the micromorphic crystal plasticity and Lagrange multiplier-based models are presented. Moreover, comparison of the predicted size effect using the micromorphic crystal plasticity and Lagrange multiplier-based models is demonstrated. In section 3.3, the equivalence between the higher-order modulus A from the Lagrange multiplier-based model and the material parameter H_D from the *CurlF*^{p} model are demonstrated in the single-slip problem. In addition, this section dedicated to the simulation of representative boundary-value problems, and size effects predicted by the Lagrange multiplier-based model are compared to the *CurlF*^{p} model predictions for monotonic and cyclic microwire torsion tests. Concluding remarks follow in section 3.4.

3.2 Size effect: Comparison of micromorphic crystal plasticity and Lagrange multiplier-based models

3.2.1 Geometry, boundary conditions and material parameters

Simulations are performed with a single crystal cylindrical microwire of diameter D (= $2R$) meshed with quadratic elements for displacements DOF and linear for γ_χ and λ. Quadratic shape functions are used for displacements DOF because they are known to provide better interpolation accuracy than linear shape functions. Furthermore, quadratic elements are also known to be less subject to locking issues. However, linear shape functions are used for γ_χ to limit the number of degrees of freedom. In fact, it is assumed that plastic deformations differ less rapidly than displacements in such a way that linear shape functions provide sufficient precision to interpolate accumulated plastic slip.

The bottom face of the microwire is clamped, while the top surface undergoes a rigid body rotation around the wire axis. The lateral faces are kept traction free, which means that $\underline{T} = 0$ and $M = 0$ from Eq. (2.21). Two orientations of the single crystal considered are <001> and <111> with crystallographic direction [001] and [111], respectively aligned with the microwire axis. The geometry and the boundary conditions are as shown in Fig. 3.2. The basis vectors of the Cartesian coordinate system are parallel to the cubic lattice unit cell vectors:

$$\underline{e}_1 = [110] \quad \underline{e}_2 = [1\bar{1}0] \quad \underline{e}_3 = [001], \tag{3.1}$$

and

$$\underline{e}_1 = [\bar{1}\bar{1}2] \quad \underline{e}_2 = [1\bar{1}0] \quad \underline{e}_3 = [111], \tag{3.2}$$

respectively.

The various characteristic length scale to diameter ratios ($\ell/2R$) considered in the simulations are given in Table 3.2.

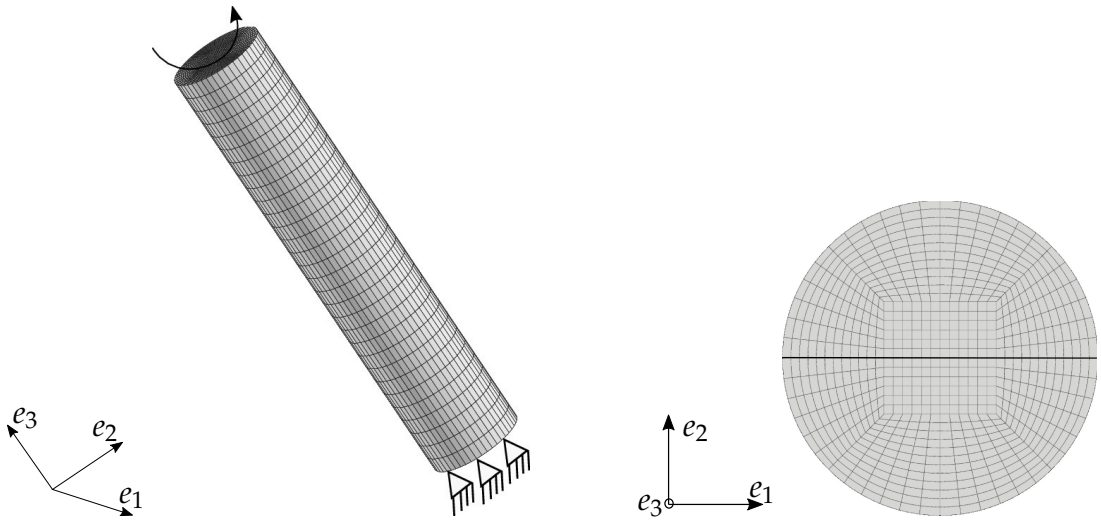

(a) (b)

Fig. 3.2 Microwire torsion tests: (a) boundary conditions (b) example mesh from the top side in which the black line represents an initial material line. For the <001> crystal orientation, the black line is oriented along a <110> direction. For the <111> crystal orientation, it is oriented along a <11$\bar{2}$> direction.

Table 3.1 Numerical values of material parameters for the simulation of microwires in torsion.

C_{11}	C_{12}	C_{44}	τ_0 Eq. (2.14)	m Eq. (2.12)	K Eq. (2.12)	μ Eq. (2.14)
259.6 GPa	179 GPa	109.6 GPa	320 MPa	20	15 MPa.s$^{1/m}$	77.2 GPa
d_c Eq. (2.15)	κ_c Eq. (2.15)	ϱ_0^r Eq. (2.16)	h^{ru} Eq. (2.14)	$b^{ru}(r \neq u)$ Eq. (2.15)	b^{uu} Eq. (2.15)	H_χ Eq. (2.27)
10.4	42.8	5.38×10^{-11}	0.124	1	0	10^4 MPa
μ_χ Eq. (2.39)						
10^3 MPa						

Table 3.2 Numerical values of $\ell/2R$ ratios for the simulation of microwires in torsion.

$\ell/2R$ <001>	0.03	0.07	0.10	0.31	0.44	0.54
$\ell/2R$ <111>	0.03	0.08	0.11	0.35	0.50	0.61

3.2.2 Application to microwire torsion tests

Fig. 3.3 and 3.4 show the accumulated plastic strain fields in the deformed configuration for FCC single crystals with wire axis parallel to <001> and <111> respectively. A cross-section of each sample is illustrated in Fig. 3.3 and 3.4. The radial and circumferential plastic strain gradients are clearly visible. A four-fold pattern is observed for the <001> specimen with maximum plastic strain values along <100> directions. A six-fold pattern is observed for the <111> specimen with maximum plastic strain values along <11$\bar{2}$> directions. The overall curves are presented using normalized torque T/R^3 as a function of surface strain γ_R defined as

$$\gamma_R = \kappa R, \tag{3.3}$$

where κ is the applied twist per unit length (θ/L). They are given in Fig. 3.5 for the two single crystal orientations <001> and <111> using classical crystal plasticity. This definition of γ_R is only an approximation of the actual slip value along the circumference since the plastic activity is not constant along the circumference for a cubic single crystal. The <001> crystal orientation is found to be significantly stronger than the <111> wire. The orientation of the crystal to the loading direction causes different slip activities and results in different mechanical responses. The twist angle at the cross-section of the microwire is calculated as $\theta_h = \theta h_t/L$, where h_t is the height from the bottom end. The initial material line for <001> and <111> crystal orientation is shown in Fig. 3.2b. The rotation of material line with increasing surface strain is as shown in Fig. 3.3 and 3.4. The response of the micromorphic wire is also provided in Fig. 3.5 for comparison for a given characteristic length scale value. In the micromorphic crystal plasticity approach, the penalty parameter H_χ is chosen sufficiently large for γ_{cum} and γ_χ to almost coincide. The chosen value of H_χ in the simulation is 10^4 MPa. The characteristic length scale ℓ considered in the simulation is defined by $\ell = \sqrt{A/|H|}$, as proposed in (Ling et al., 2018), where H is the initial equivalent linear hardening modulus. Moreover, H is estimated by performing a uniaxial tensile test on one element as proposed in (Ling, 2017). Its value is given by the ratio of τ^r and γ^r for one activated slip system at the beginning of its activation. Thus the estimated H values for <001> and <111> crystal orientation are 2500 MPa and 2000 MPa, respectively. The characteristic length scale can be varied by varying the gradient parameter A (MPa mm^2 or N). The various values of A and of the characteristic length scale to diameter ratio ($\ell/2R$) of microwires are given in Table 3.2. The micromorphic response in Fig. 3.5 exhibits a linear hardening of the wire in contrast to the saturated classical crystal plasticity response.

The effect of different $\ell/2R$ ratios on the size effects in torsion microwires have been studied for the two models considered in this work, namely the micromorphic crystal plasticity and Lagrange multiplier-based formulations. The torque vs. surface strain curves of the micromorphic crystal plasticity model (section 2.3.1) is compared with the Lagrange multiplier-based model (section 2.3.2). The cumulative plastic strain γ_{cum} fields for different $\ell/2R$ ratio of microwire ($\ell/2R = 0.03, 0.07, 0.10$ and 0.44 for <001> and

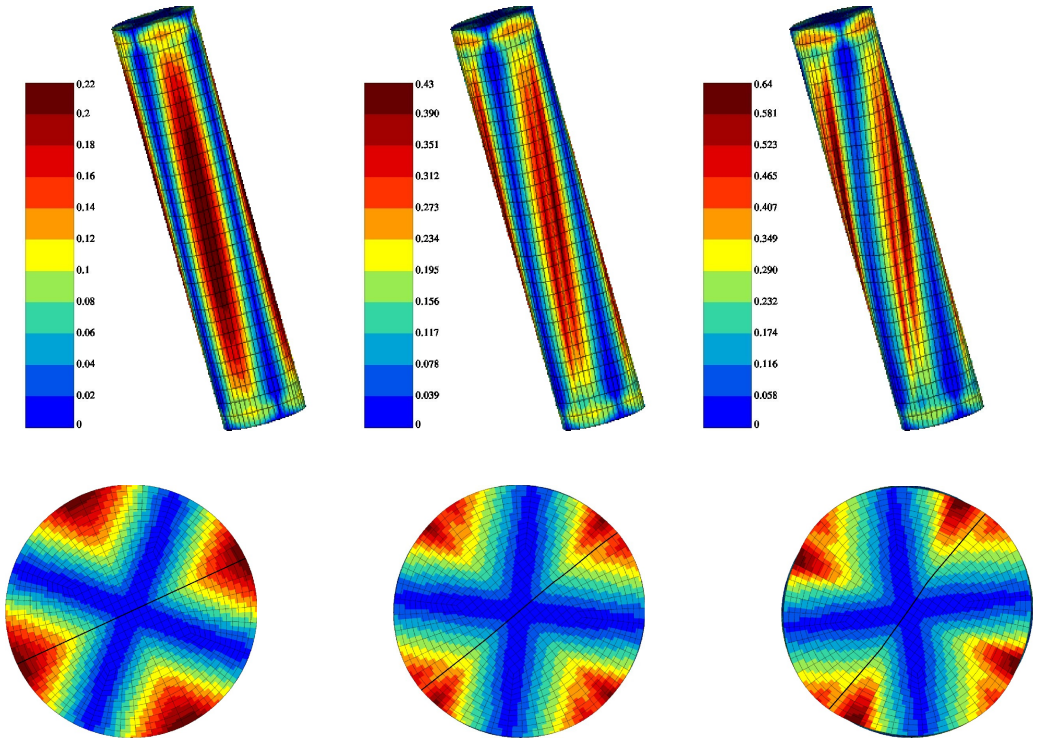

$\gamma_R = 6\%, \theta_h = 23°$ $\gamma_R = 10\%, \theta_h = 37°$ $\gamma_R = 14\%, \theta_h = 52°$

Fig. 3.3 Cumulative plastic strain γ_{cum} field in FCC single crystal (<001> crystal orientation) using the classical crystal plasticity model according to section 2.2.3 with respect to deformed configuration. The rotation of material line shown in Fig. 3.2b with increasing surface strain is shown by a black line on the cross-section.

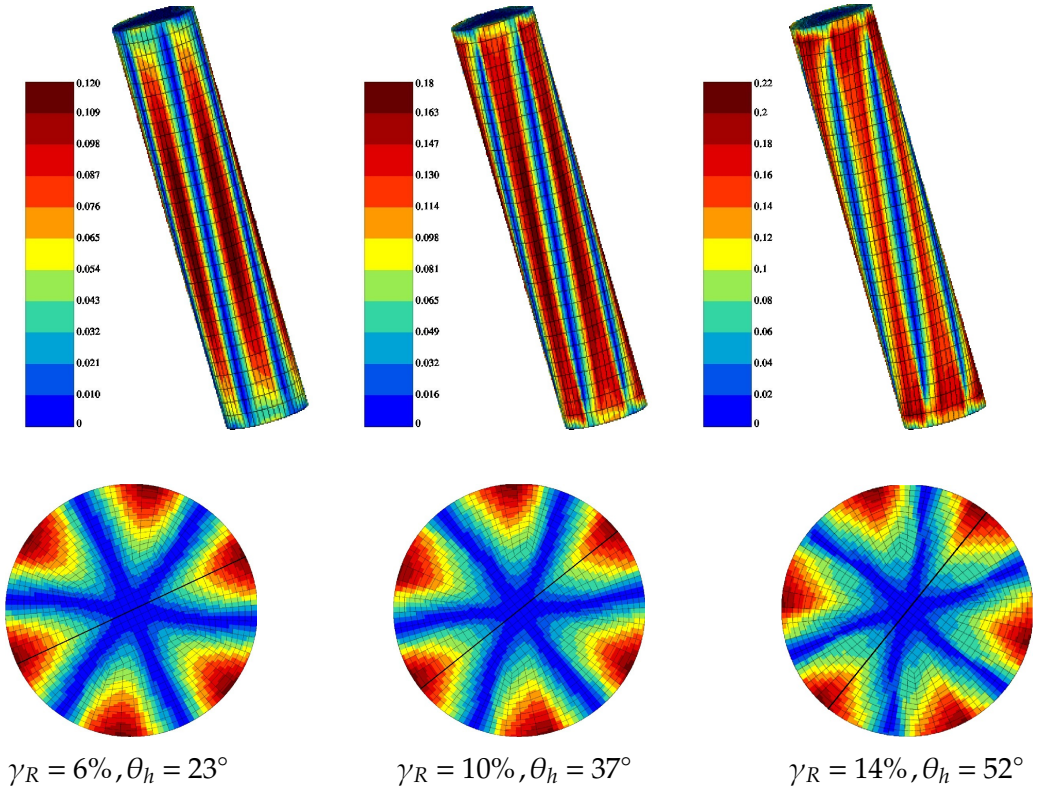

Fig. 3.4 Cumulative plastic strain γ_{cum} field in FCC single crystal (<111> crystal orientation) using the classical crystal plasticity model with respect to deformed configuration. The material line shown in Fig. 3.2b and its rotation with increasing surface strain are shown by a black line on the cross-section.

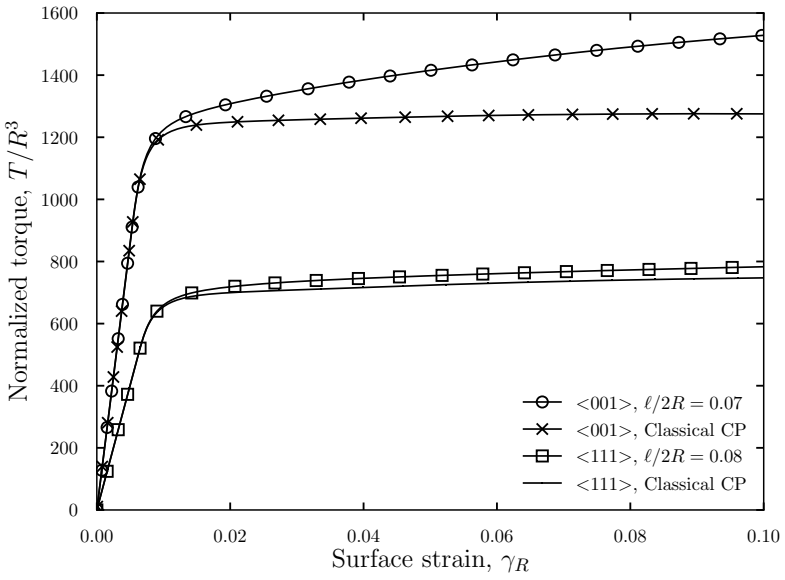

Fig. 3.5 Shear stress vs. surface strain in FCC single crystal wires for <001> and <111> crystal orientations using the classical crystal plasticity and micromorphic crystal plasticity models.

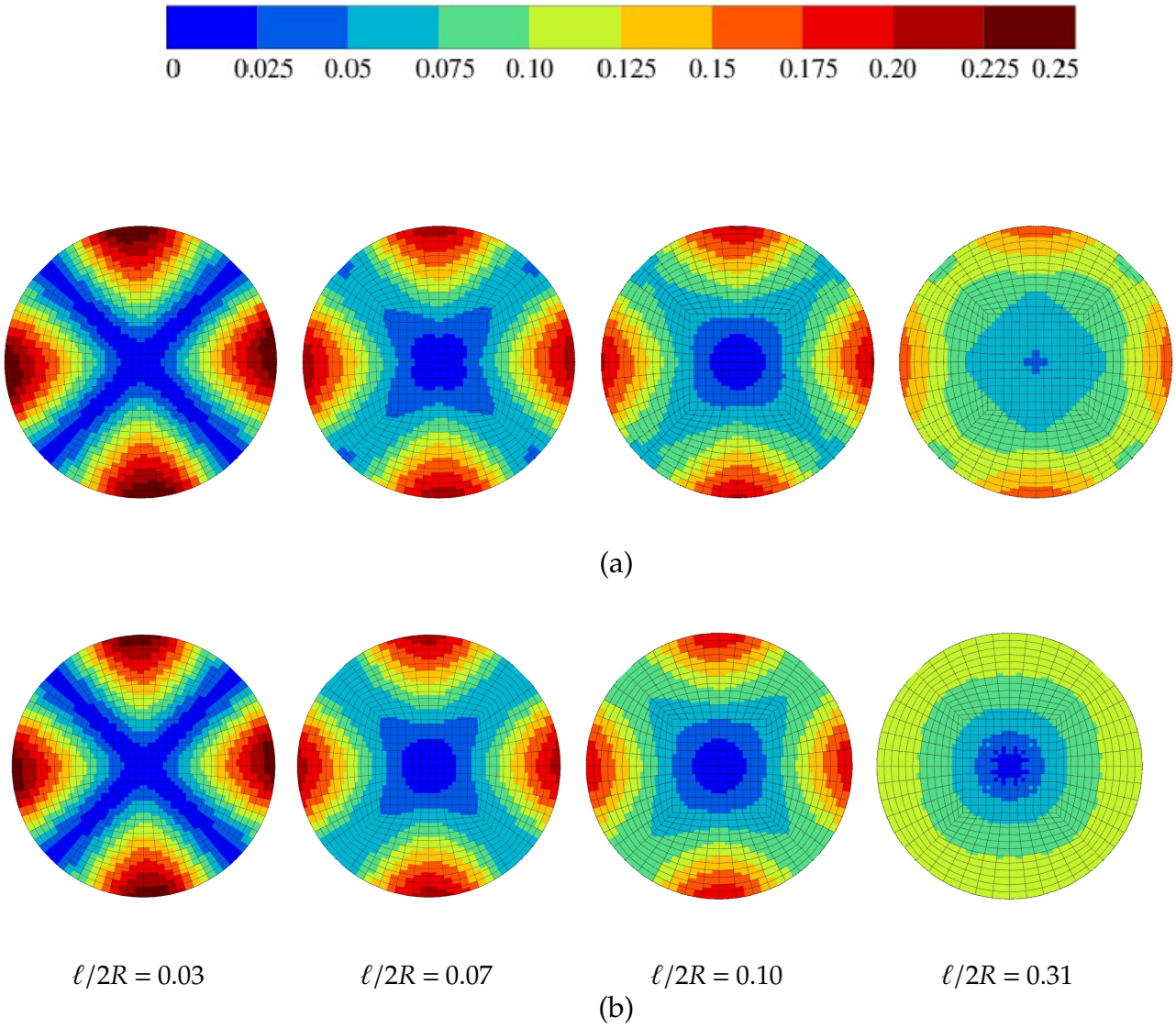

Fig. 3.6 Cumulative plastic strain distribution in FCC single crystal (<001> crystal orientation) for different values $\ell/2R$ ratio using the (a) micromorphic crystal plasticity, and (b) Lagrange multiplier-based models at surface strain of 0.08 (fields reported on the reference configuration).

$\ell/2R = 0.03, 0.08, 0.11$ and 0.50 for <111> crystal orientation) obtained using both models are shown in Fig. 3.6 and 3.7. It can be seen that, for low and intermediate values of the ratio $\ell/2R$, the two models predict the same accumulated plastic slip fields. In contrast, for the larger value $\ell/2R = 0.31$, the circumferential gradient has almost disappeared according to the Lagrange multiplier-based model. In contrast, it is still present in the micromorphic crystal plasticity simulation. Increasing the characteristic length scale for a fixed wire diameter leads to a substantial decrease in the plastic strain gradient. This can be attributed to the fact that the energetic cost of plastic strain gradient increases with ℓ and the free energy of the sample is minimum for a limited value of the gradient. These observations are valid for both orientations <001> and <111>. It is remarkable that the four-fold and six-fold patterns disappear for large enough characteristic length scale values.

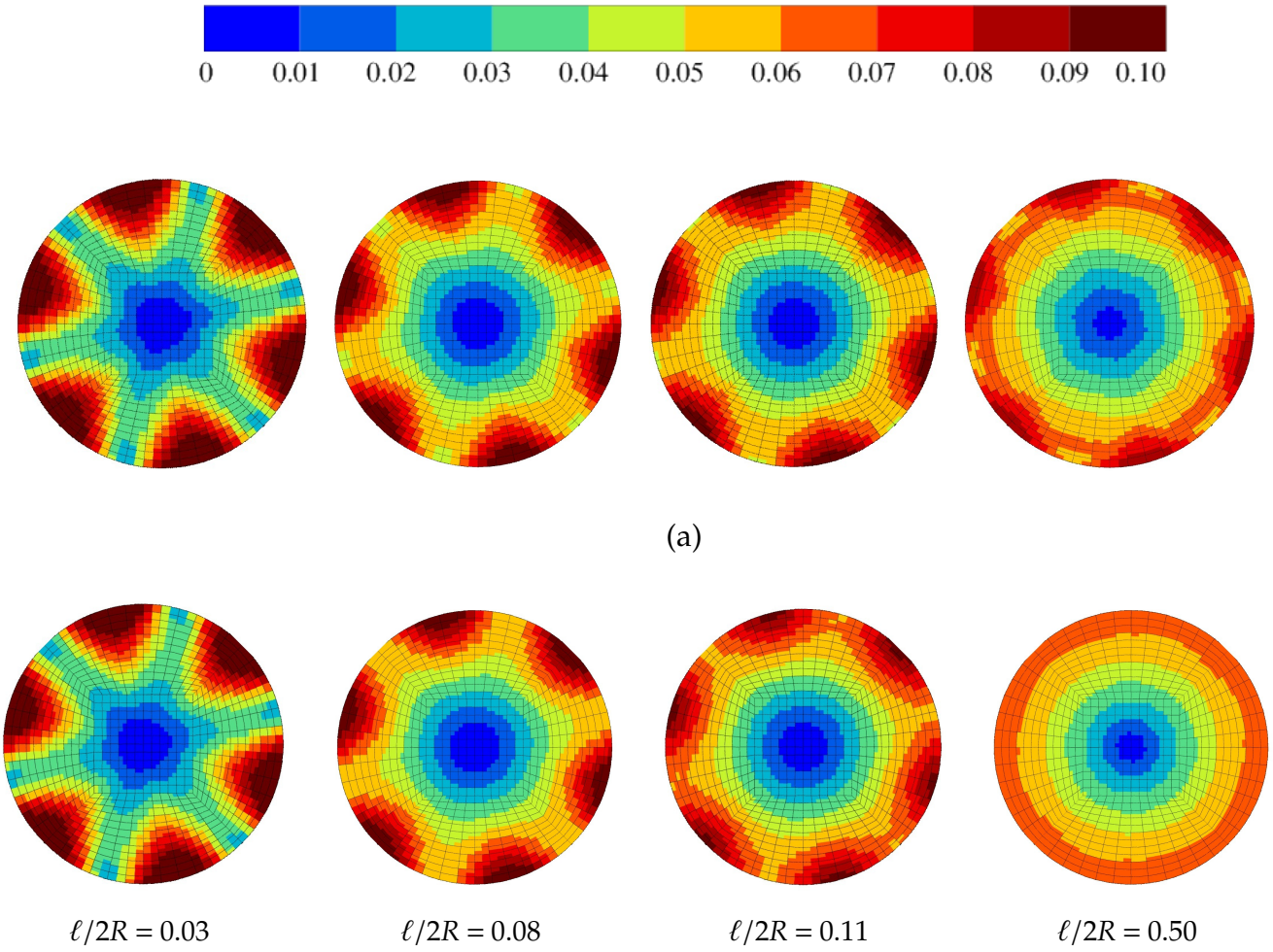

Fig. 3.7 Cumulative plastic strain distribution in FCC single crystal (<111> crystal orientation) for different values $\ell/2R$ ratio using the (a) micromorphic crystal plasticity, and (b) Lagrange multiplier-based models at surface strain of 0.08 (fields reported on the reference configuration).

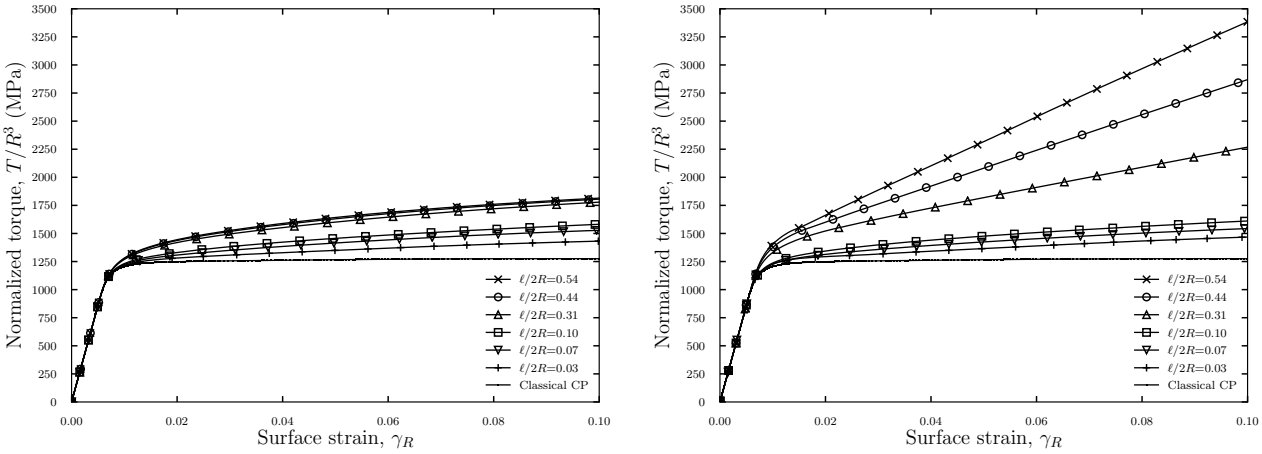

Fig. 3.8 Normalized torque vs. surface strain curves (<001> crystal orientation) for different values $\ell/2R$ ratio using the (a) micromorphic crystal plasticity, and (b) Lagrange multiplier-based models.

The corresponding torque vs. surface strain curves are provided in Fig. 3.8 and 3.9. They clearly show the size–dependent hardening effect for both models. For small and intermediate values of the characteristic length scale, the micromorphic crystal plasticity and Lagrange multiplier-based models are found to deliver the same overall responses. This result is expected since the value of the penalty parameter in the micromorphic crystal plasticity model has been chosen so as to ensure such a correspondence. However, keeping the same value of the penalty parameter H_χ and increasing the characteristic length scale, or equivalently the value of the parameter A, leads to a saturation of the torque vs. surface strain curves for the micromorphic crystal plasticity model. In contrast, the Lagrange multiplier-based model predicts ever-increasing hardening. Fig. 3.8a and 3.9a show almost the same response obtained by the micromorphic crystal plasticity model for the two largest $\ell/2R$ ratios, whereas distinct curves are obtained with the Lagrange multiplier-based approach, see Fig. 3.8b and 3.9b. This saturation of size effects predicted by a micromorphic crystal plasticity formulation has already been demonstrated analytically for the microcurl theory by Cordero et al. (2010) in the case of periodic shearing of a laminate at small strains and small rotations. The present new results show that this feature also exists at large strains for torsion. These observations apply to both orientations <001> and <111>. As expected, the strongest additional hardening effect is obtained when the characteristic length scale takes values comparable to the wire diameter.

The predictions of the Lagrange multiplier-based formulation can be considered, in fact, as the limit case when the penalty modulus H_χ goes to infinity in the micromorphic crystal plasticity formulation. The predictions obtained with the micromorphic crystal plasticity formulation for several values of H_χ are plotted in Fig. 3.10. As H_χ rises, the prediction of the micromorphic crystal plasticity formulation goes closer to the prediction obtained with the Lagrange multiplier-based formulation. However, increasing H_χ builds

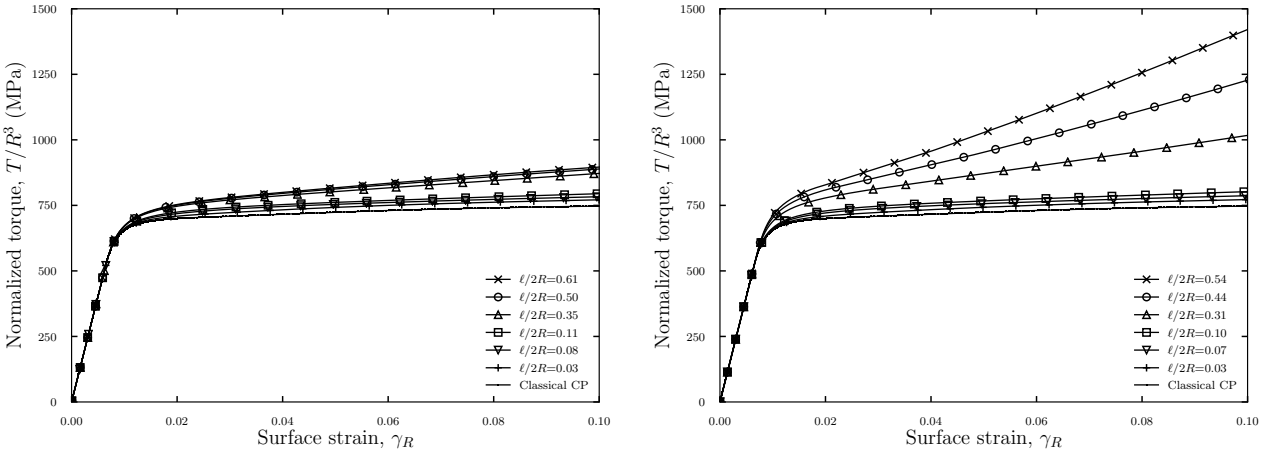

(a) (b)

Fig. 3.9 Normalized torque vs. surface strain curves (<111> crystal orientation) for different values $\ell/2R$ ratio using the (a) micromorphic crystal plasticity (b) Lagrange multiplier-based models.

up drastically the computation time since the penalization becomes very stiff. In practice, one could use the penalty term H_χ in the micromorphic crystal plasticity formulation as a parameter to fit the scaling law measured in experiments. This possibility was discussed for the micromorphic crystal plasticity and Cosserat models in (Cordero et al., 2010).

3.3 Size effect: Comparison of reduced-order model with *CurlF*^{p} model

In this section, the predicted size effects using the reduced-order model (Lagrange multiplier-based model) are compared against the predictions by *CurlF*^{p} model for the monotonic and cyclic loading of microwire torsion tests. The constitutive framework of the Lagrange multiplier-based model and *CurlF*^{p} model is presented in section 2.3.2 and 2.3.3, respectively.

3.3.1 Equivalence of higher-order modulus A and material parameter H_D in single-slip

The higher-order modulus A from the reduced-order model, refer (2.34), and material parameter H_D from the *CurlF*^{p} theory, refer (2.51), bear similar physical interpretations. This is demonstrated in this section for a simplified two-dimensional single-slip problem.

A single crystal with a single-slip system is considered. The slip direction $\underline{m}$ and the slip plane normal $\underline{n}$ are

$$\underline{m} = (1,0,0), \quad \underline{n} = (0,1,0). \tag{3.4}$$

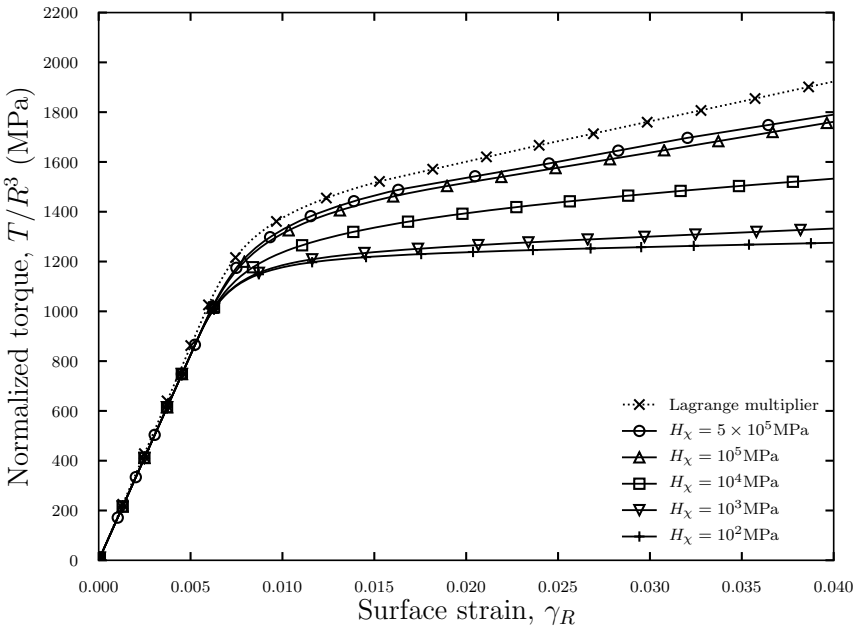

Fig. 3.10 Normalized torque vs. surface strain curves (FCC <001> crystal orientation) for different values of H_χ and for $\ell/2R = 0.44$.

Consider a situation where only one slip system is active. In the absence of lattice distortion and rotation, the plastic part of the deformation gradient $\underset{\sim}{F}^p$ takes the form

$$\underset{\sim}{F}^p = \underset{\sim}{1} + \gamma\,(\underline{m} \otimes \underline{n}), \tag{3.5}$$

$$[\underset{\sim}{F}^p]_{ij} = \begin{bmatrix} 1 & \gamma & 0 \\ 0 & 1 & 0 \\ 0 & 0 & 1 \end{bmatrix}. \tag{3.6}$$

The dislocation density tensor $[\underset{\sim}{D}_d]_{ij} = [\mathrm{Curl}^T(\underset{\sim}{F}^p)]_{ij}$ is given by

$$[\underset{\sim}{D}_d]_{ij} = \begin{bmatrix} F^p_{13,2} - F^p_{12,3} & F^p_{11,3} - F^p_{13,1} & F^p_{12,1} - F^p_{11,2} \\ F^p_{23,2} - F^p_{22,3} & F^p_{21,3} - F^p_{23,1} & F^p_{22,1} - F^p_{21,2} \\ F^p_{33,2} - F^p_{32,3} & F^p_{31,3} - F^p_{33,1} & F^p_{32,1} - F^p_{31,2} \end{bmatrix}. \tag{3.7}$$

Therefore, for the 2-dimensional case and the specific simple shear problem studied,

$$[\underset{\sim}{D}_d]_{ij} = \begin{bmatrix} 0 & 0 & \gamma_{,1} \\ 0 & 0 & 0 \\ 0 & 0 & 0 \end{bmatrix}. \tag{3.8}$$

The only active component of the dislocation density tensor is

$$(D_d)_{13} = \gamma_{,1}\,. \tag{3.9}$$

The equivalence of higher-order modulus A and the material parameter H_D from the *CurlF^p* model can be derived as follows. For a crystal deforming under single-slip conditions, the plastic deformation rate is given by

$$\dot{\underset{\sim}{F}}^p = \dot{\gamma}(\underline{m} \otimes \underline{n}). \tag{3.10}$$

Inserting (2.57) in (2.54) for $\overline{\underset{\sim}{M}}$ gives

$$(\tau + J^p \overline{\underset{\sim}{M}}^{(\mathrm{rel})} : \underline{m} \otimes \underline{n})\dot{\gamma} + X\dot{\zeta} \geq 0. \tag{3.11}$$

In absence of hardening variable, ζ, for simplicity, the generalized Schmid law for the *CurlF^p* model, in the rate-independent case, can be defined as

$$|\tau - x| = \tau_c, \quad \text{with} \quad x = -J^p \overline{\underset{\sim}{M}}^{(\mathrm{rel})} : \underline{m} \otimes \underline{n}. \tag{3.12}$$

From the specific form of the generalized stress tensor $\overline{\underset{\sim}{M}}^{(\mathrm{rel})}$ given by (2.59), the back-stress x can be written as

$$x = 2H_D[\mathrm{Curl}^T(\mathrm{Curl}^T(\underset{\sim}{F}^p)) \cdot \underset{\sim}{F}^{pT}] : \underline{m} \otimes \underline{n}, \tag{3.13}$$

and

$$\begin{aligned}[\mathrm{Curl}^T(\mathrm{Curl}^T(\underset{\sim}{F}^p))]_{ij} = &\begin{bmatrix} F^p_{12,12} + F^p_{13,13} & F^p_{11,21} + F^p_{13,23} & F^p_{11,31} + F^p_{12,32} \\ F^p_{22,12} + F^p_{23,13} & F^p_{21,21} + F^p_{23,23} & F^p_{21,31} + F^p_{22,32} \\ F^p_{32,12} + F^p_{33,13} & F^p_{31,21} + F^p_{33,23} & F^p_{31,31} + F^p_{32,32} \end{bmatrix} \\ &- \begin{bmatrix} F^p_{11,22} + F^p_{11,33} & F^p_{12,11} + F^p_{12,33} & F^p_{13,11} + F^p_{13,22} \\ F^p_{21,22} + F^p_{21,33} & F^p_{22,11} + F^p_{22,33} & F^p_{23,11} + F^p_{23,22} \\ F^p_{31,22} + F^p_{31,33} & F^p_{32,11} + F^p_{32,33} & F^p_{33,11} + F^p_{33,22} \end{bmatrix}. \end{aligned} \tag{3.14}$$

For the particular single-slip problem considered, the back-stress takes the form

$$2H_D[\mathrm{Curl}^T(\mathrm{Curl}^T(\underset{\sim}{F}^p)) \cdot \underset{\sim}{F}^{pT}] : \underline{m} \otimes \underline{n} = -2H_D\gamma_{,11}\,. \tag{3.15}$$

Substituting (3.15) in (3.12) leads to another form of the generalized Schmid law

$$|\tau + 2H_D\gamma_{,11}| = \tau_c. \tag{3.16}$$

This equation clearly shows the emerging kinematic hardening component proportional to the second gradient of slip in the slip direction.

On the other hand, the generalized Schmid law for a single-slip problem with the Lagrange multiplier-based model can be written from (2.40) in the rate-independent case as

$$|\tau| + S = \tau_c. \tag{3.17}$$

Recalling the balance law in (2.20), the generalized Schmid law in (3.17) can be written as

$$|\tau| + \mathrm{Div}\,\underline{M} = \tau_c. \tag{3.18}$$

Making use of (2.27) in the previous equation leads to another form of the generalized Schmid law

$$|\tau| + A(\mathrm{Div}\underline{K}) = \tau_c, \tag{3.19}$$

$$A(\mathrm{Div}\underline{K}) = A\,\mathrm{Div}\left(\frac{\partial \gamma_\chi}{\partial X_1}\underline{m} + \frac{\partial \gamma_\chi}{\partial X_2}\underline{n}\right) = A\frac{\partial^2 \gamma_\chi}{\partial X_2^2} = A\gamma_{,11} \quad \text{with} \quad \gamma_\chi \simeq \gamma. \tag{3.20}$$

Finally, the form of the generalized Schmid law in (3.19) can be written as

$$|\tau| + A\gamma_{,11} = \tau_c. \tag{3.21}$$

This equation clearly shows the emerging isotropic hardening component proportional to the second gradient of slip in the slip direction. From (3.16) and (3.21), it is concluded that the higher-order moduli A and H_D can be related to each other for monotonic loading such that $\tau > 0$ and $\tau + 2H_D\gamma_{,11} > 0$. In this instance, we can identify $A = 2H_D$. The Lagrange multiplier-based and $CurlF^p$ models are equivalent in this specific situation. It will not be the case anymore, in general, under multi-slip conditions and considering the different hardening laws. Proving the importance of these differences is the subject of the following sections for monotonic and cyclic loading conditions.

In the presence of linear hardening with modulus H, it is possible to derive from (3.19) the definition of a characteristic length scale

$$\ell = \sqrt{A/|H|}, \tag{3.22}$$

as demonstrated in (Ling et al., 2018; Scherer et al., 2019). For more general hardening laws, a similar characteristic length scale can be defined as discussed in section 3.3.2.3.

3.3.2 Application to microwire torsion tests

Recently, experimental investigations of microwire torsion tests on single crystal copper under monotonic loading were performed by Horstemeyer et al. (2002) with the [110] crystallographic direction being aligned with the axis of rotation. An observation of the kinematics of the deformation fields at the outer surface of the specimen was made. A wavy deformation pattern of sinusoidal waves comprising of four periods was observed and believed to be the result of four-fold symmetry of the slip plane around the circumference. Moreover, experimental assessments of polycrystalline microwire torsion tests with different specimen diameters and same grain size to study the size effects under monotonic loading were performed in (Liu et al., 2012; Guo et al., 2017). Furthermore, the experimental studies

of size effects, hysteresis loops, Bauschinger effects, and anomalous plastic recovery in polycrystalline cyclic torsion tests can be found in (Liu et al., 2013; Guo et al., 2020).

From a numerical point of view, Weinberger and Cai (2010) investigated the orientation dependent plasticity in metallic nanowires by using molecular dynamics and dislocation dynamics simulations. Molecular dynamics simulations showed that the mechanism of plastic deformation is controlled by the orientation of the single crystal wires. The wires oriented along <110> direction shows the coaxial dislocation nucleation, making the deformation homogeneous. Furthermore, these wires maintain most of their strength after yielding. On the other hand, <001> and <111> crystal orientations deform through formation of twist boundaries which localizes the deformation and lose most of their strength after yielding. Besides, dislocation dynamics simulations are used to investigate the stability of the dislocation structures observed in molecular dynamics simulations. The prediction of size effects in monotonic and cyclic loading of polycrystalline microwires were performed in (Bardella and Panteghini, 2015). To this end, they used a phenomenological strain gradient plasticity approach called distortion gradient theory which relies on the dislocation density tensor with taking *less-than-quadratic* defect energies into consideration. These less-than-quadratic defect energies allow the prediction of size effects consisting of an increase of the yield point with diminishing size. It was observed that this distortion gradient theory is satisfactory to capture the size effects in monotonic loading. However, it leads to anomalous cyclic behavior in the case of cyclic loading due to the less-than-quadratic defect energies. They related the anomalous cyclic behavior to the changes of concavity of the stress-strain curves, which is absent in the experiments. Panteghini and Bardella (2020) recently proposed a strain gradient plasticity theory characterized by a higher-order plastic potential to overcome this issue in the cyclic loading of polycrystalline microwires. The predictions made by taking the above-mentioned approach are in good agreement with the experimental data of (Liu et al., 2013) and predictions on the size-dependent response of microwires under cyclic loading.

In this section, the size effect predicted by the Lagrange multiplier-based model for monotonic or cyclic microwire torsion tests is compared to the predictions by the $CurlF^p$ model taken from Kaiser and Menzel (2019a). The relation $A = 2H_D$ is used in the simulations, following the identification presented in section 3.3.1.

Moreover, in the present work, the GND density distribution in monotonic and cyclic loading of microwires using the Lagrange multiplier-based model is calculated from the Euclidean norm of $\mathrm{Curl}^T(\underset{\sim}{F}^p)$. A post-processing technique is used to evaluate $\mathrm{Curl}^T(\underset{\sim}{F}^p)$ (see also, Busso et al. (2000); Abrivard (2009)). The first step in determining $\mathrm{Curl}^T(\underset{\sim}{F}^p)$ is to calculate the gradient of $\underset{\sim}{F}^p$ at the integration points. To this end, the known values of $\underset{\sim}{F}^p$ at the integration points are extrapolated to nodes using the shape functions of the elements. The gradients of $\underset{\sim}{F}^p$ at the nodes can next be obtained from the spatial derivatives of the shape functions. Finally, known nodal values of the gradient of $\underset{\sim}{F}^p$ are interpolated back to the integration points. The Euclidean norm of the dislocation density tensor $\underset{\sim}{D}_d$ provides

an effective measure of GND density as follows:

$$\|\mathrm{Curl}^T(\underset{\sim}{F}^p)\| = b\sum_{r=1}^{N}\rho_G^r, \tag{3.23}$$

where $\|\bullet\|$ denotes the Euclidean norm of $\bullet$. FE validation of the above mentioned post-processing technique is performed using pure bending tests. This validation can be found in appendix C.

3.3.2.1 Problem setup

The simulations are performed using single crystal cylindrical microwires with a height of 80 mm and three different radii R = 20 mm, 10 mm and 5 mm, that are meshed with reduced integration 20 node brick elements. The simulation results are not affected by the absolute values of the wire dimensions but rather by the ratio of their radii to the characteristic length scale ℓ.

The applied boundary conditions are shown in Fig. 3.2. The geometry is discretized with 3600 elements for monotonic loading and with 450 elements for cyclic loading. The same finite element meshes as in (Kaiser and Menzel, 2019a) are used for the simulations performed with the Lagrange multiplier-based model in order to allow for direct comparison. The latter model was recently used to simulate torsion tests of single crystals with various orientations and finer meshes in (Scherer et al., 2020). Isotropic elasticity is considered. The bottom face of the microwire is clamped, while the top surface undergoes a rigid body rotation around the wire axis. The lateral faces are kept traction-free and free of generalized forces. The relative rotation between the upper and lower face is linearly increased to an angle of 45° for monotonic loading. For the cyclic loading test, the following conditions are enforced: The relative rotation between the upper and lower faces is first linearly increased to an angle value of 45°. Next, the relative rotation is linearly decreased to −45°. Finally, the loading is again reversed, and simulation is stopped when a relative rotation of 45° is reached.

The orientation of the single crystal considered is such that the [001] crystal direction is aligned with the wire axis. The basis vectors of the Cartesian coordinate system are parallel to the cubic lattice unit cell vectors:

$$\underline{e}_1 = [100] \quad \underline{e}_2 = [010] \quad \underline{e}_3 = [001],$$

and are indicated in Fig. 3.2.

3.3.2.2 Identification of material parameters

The material parameters of the FCC single crystal for the dislocation-density based model presented in section 2.2.4 are now calibrated based on simple tension and simple shear

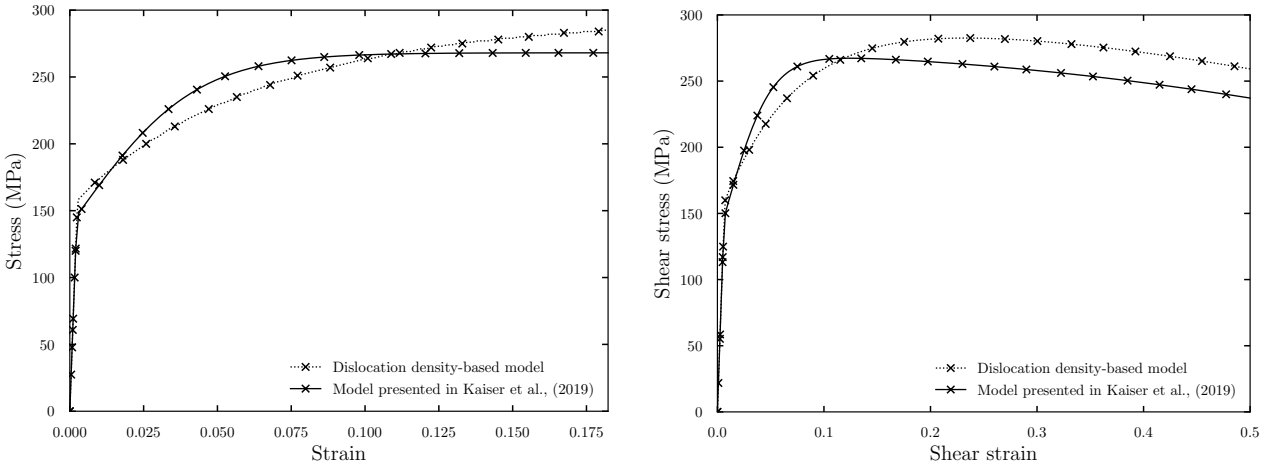

(a) (b)

Fig. 3.11 Constitutive response of the classical crystal plasticity formulation (section 2.2.3) and the material model considered in (Kaiser and Menzel, 2019b) for a <001> FCC single crystal and material parameters according to Table 3.3: (a) tensile test, (b) shear test.

predictions obtained on a single volume element with the constitutive law considered in (Kaiser and Menzel, 2019b) and recalled in section 3.3. Such a calibration is necessary because the two models compared in the present work rely on different hardening rules. The *CurlF^p* model includes a phenomenological hardening law with internal variables ζ whereas the reduced-order model incorporates evolution equations for dislocation densities according to the section 2.2.4. The calibrated material parameters used in the numerical simulations and the material parameters used in the *CurlF^p* model are summarized in Table 3.3. Moreover, the corresponding tensile and shear stress-strain responses of a <001> FCC single crystal are provided for both models in Fig. 3.11.

The FCC crystal possesses the usual 12 slip systems with 6 slip directions <110> and 4 slip planes {111}.

3.3.2.3 Results and discussion

• Comparison of predicted size effects

Fig. 3.13 and 3.18 respectively show the cumulative plastic strain γ_{cum} fields plotted in the reference configuration for the considered single crystal microwire under monotonic and cyclic loading with wire axis parallel to [001] crystal direction. The characteristic length scale ℓ considered in the simulations is defined as $\ell = \sqrt{A/|H|}$, cf. section 3.3.1, (Eq. (3.22)). The hardening modulus H varies during straining, and an approximate expression of the characteristic length scale is chosen to normalize the presented results. For that purpose, the initial equivalent linear hardening modulus for the tensile test is selected. Its value is given by the ratio of resolved shear stress τ^r and shear strain γ^r for one activated slip system at the beginning of its activation as proposed in (Ling, 2017). In the present case, the estimated H value for <001> crystal orientation is 3100 MPa. It is not possible to derive

Table 3.3 Numerical values of material parameters used for the simulation of microwire torsion tests in the reduced-order model and by Kaiser and Menzel (2019a) in the *CurlF*^{p} model.

E	τ_0 Eq. (2.14)	m Eq. (2.12)	K Eq. (2.12)	μ Eq. (2.14)	b	d_c Eq. (2.15)
60.8 MPa	60 MPa	10	10 MPa.s$^{1/m}$	23400 MPa	0.286 nm	100.5
κ_c Eq. (2.15)	ϱ_0^r Eq. (2.16)	h_0 Eq. (2.14)	h_1 Eq. (2.14)	h_2 Eq. (2.14)	h_3 Eq. (2.14)	h_4 Eq. (2.14)
10.92	5.38×10^{-11}	1.0	0	0	0	0
h_5 Eq. (2.14)	$b^{ru}(r\neq u)$ Eq. (2.15)	b^{uu} Eq. (2.15)	μ_χ Eq. (2.39)	A Eq. (2.34)	τ_∞ Eq. (2.49)	H_0 Eq. (2.49)
0	1	0	10^3 MPa	$10^4, 2\times10^4$ N	110 MPa	540
H_D Eq. (2.51)						
$5\times10^3, 10^4$ N						

an analytical expression of the relevant characteristic length scale emerging in the torsion problem. That is why the proposed estimate is chosen.

The comparison of the size effects predicted by the Lagrange multiplier-based model and the *CurlF*^{p} model for three different values of the radius of the microwire under monotonic loading using higher-order modulus $A = 20000$ N is shown in Fig. 3.12a. This feature can be observed in Fig. 3.13. The slip activity is maximal at four locations corresponding to the direction [110]. Fig. 3.12a shows that for the radii $R = 20$ mm and $R = 10$ mm, the torque vs. surface strain responses predicted by both models are almost the same, while for the radius $R = 5$ mm, the Lagrange multiplier-based model leads to a slightly harder response.

The cumulative plastic strain and dislocation density fields shown next are based on a finite element discretization with 10000 elements for resolution reasons. Moreover, the computational efficiency of the Lagrange multiplier-based model in terms of CPU time allows the faster computation of size effect even with finer mesh discretization. Fig. 3.14 and 3.16 respectively shows the spatial distributions of SSD and GND density for the three considered radii. It is observed that the dislocation density nucleation starts at the surface of the microwire and driven towards the center. During the deformation process, the evolution of the SSD density is due to the dislocation generation and annihilation mechanisms. The initial dislocation density $\rho^r (= \varrho^u/b^2)$ is assumed to be $6.5\times10^8\,\mathrm{m}^{-2}$ and chosen to be the same for all slip systems. Distinct four-fold patterns of the SSD density distribution are observed for all three radii of the microwire. On the other hand, the GND density distribution shows distinct four-fold patterns for the radii $R = 5$ mm and $R = 10$ mm, while it shows more localized distribution for $R = 20$ mm making the four-fold symmetry of FCC single-crystal almost disappear. Furthermore, the SSD and GND density distribution at different stages of the relative rotation are shown in Fig. 3.15 and 3.17, respectively. At

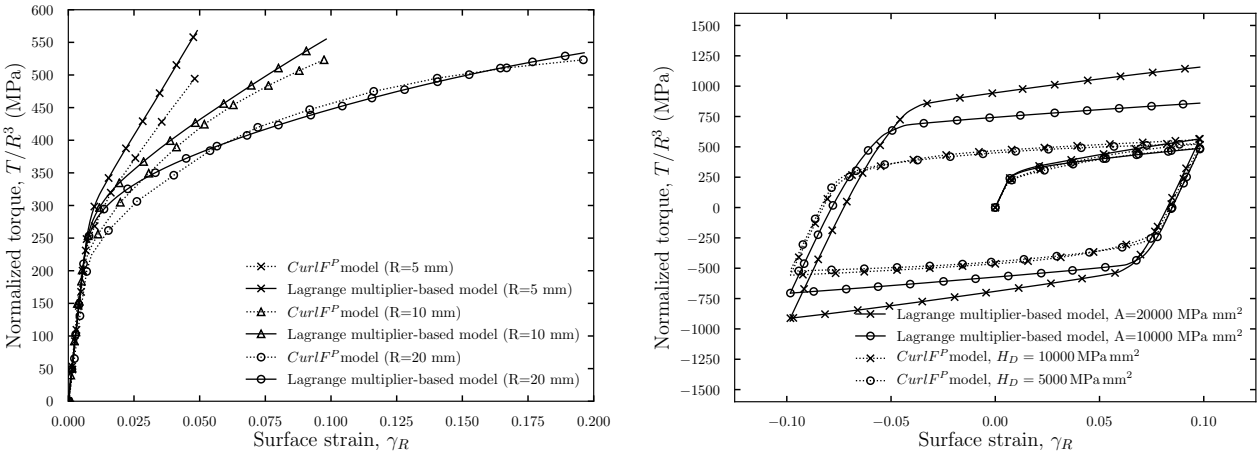

(a) (b)

Fig. 3.12 Comparison of normalized torque vs. surface strain curves (<001> crystal orientation) using the Lagrange multiplier-based model and the $CurlF^p$ model for: (a) monotonic loading (R = 20 mm, 10 mm, and 5 mm), and (b) cyclic loading (R = 10 mm).

the initial stage of the deformation, the maximum SSD density is observed at four locations corresponding to the [110] crystal direction (see Fig. 3.15a). However, as the deformation progresses, the maximal dislocation density locations are observed at the corresponding [100] crystal direction as shown in Fig. 3.15c for the relative rotation of 22.5°. With the deformation, the difference between the magnitude of the maximal and minimal increment of the cumulative plastic strain, $\sum_{r=1}^{N} |\triangle\gamma^r|$, along the circumference decreases and the field becomes almost homogeneous. This may explain the shift in the maximal SSD density locations with the deformation. On the other hand, at the initial stage of the relative rotation, the GND density is maximal at four locations corresponding to the direction [100] (see Fig. 3.17a) and remains at the corresponding [100] crystal direction with further increase in the relative rotation (see Fig. 3.17c). Moreover, it is observed that there is a slight evolution of the GND density field with more localized distribution compared to the SSD density field.

Fig. 3.21a and 3.21b show the profiles of the cumulative plastic strain γ_{cum} for three different radii along the circumferential and radial direction, respectively. For the given relative rotation angle, distinct four-fold patterns of the plastic strain field can be observed for R = 20 mm and R = 10 mm. The plastic strain field is smoother along the circumference for R = 5 mm because the smaller radius gives a stiffer response and limits the strain localization in these zones. The radial distributions in Fig. 3.21b are almost linear.

The comparison of the size effect predicted by the Lagrange multiplier-based model and the $CurlF^p$ model in the case of cyclic loading conditions is shown in Fig. 3.12b. These simulations were performed for two values of the gradient parameter, namely A = 10000 N and 20000 N. The ratio $A = 2H_D$ is kept constant in both cases to allow for the comparison of both models. The Lagrange multiplier-based model predicts isotropic hardening as shown in Fig. 3.12b. In contrast, the higher-order stresses act as a back-stress in the $CurlF^p$ model, resulting in kinematic hardening. Fig. 3.22a shows the saturation of cyclic curves after 5

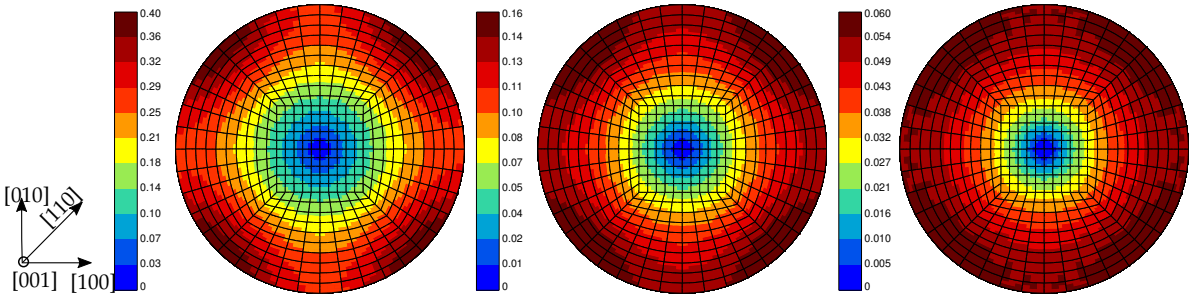

$R = 20$ mm $R = 10$ mm $R = 5$ mm

Fig. 3.13 Cumulative plastic strain field in <001> FCC single crystals predicted by a Lagrange multiplier-based model with $A = 20000$ N and a finite element discretization featuring 10000 elements. The results for an applied relative rotation of 45° between the upper and lower face are shown on the undeformed configuration.

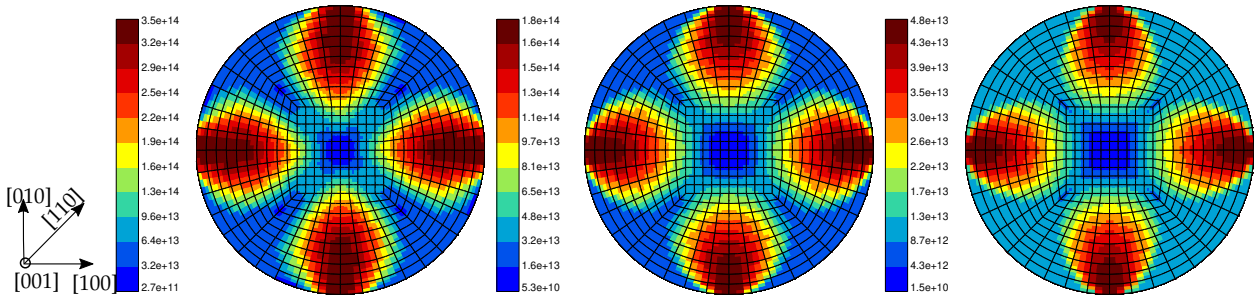

$R = 20$ mm $R = 10$ mm $R = 5$ mm

Fig. 3.14 SSD density distribution in FCC single crystals (<100> crystal orientation) predicted by using a Lagrange multiplier-based model with $A = 20000$ N and a finite element discretization featuring 10000 elements. The results for an applied relative rotation of 45° between the upper and lower face are shown on the undeformed configuration.

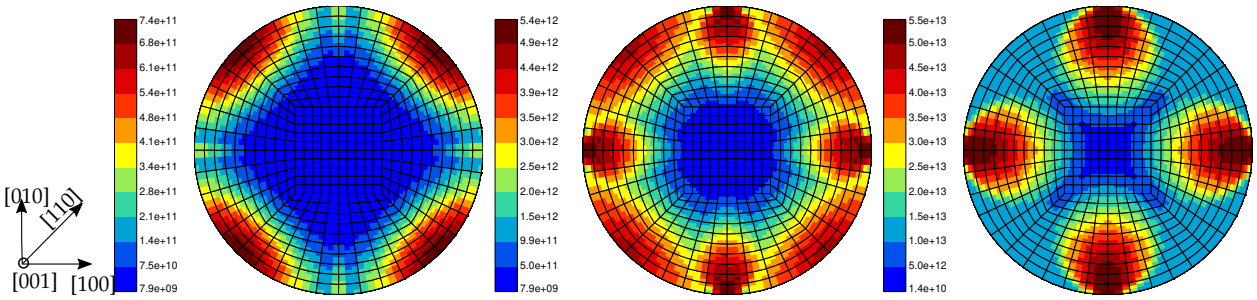

(a) (b) (c)

Fig. 3.15 SSD density distribution in FCC single crystal (<100> crystal orientation, $R = 10$ mm) predicted by using a Lagrange multiplier-based model with $A = 20000$ N and a finite element discretization featuring 10000 elements at an applied relative rotation of (a) 4.5° (b) 9° and (c) 22.5° shown on the undeformed configuration.

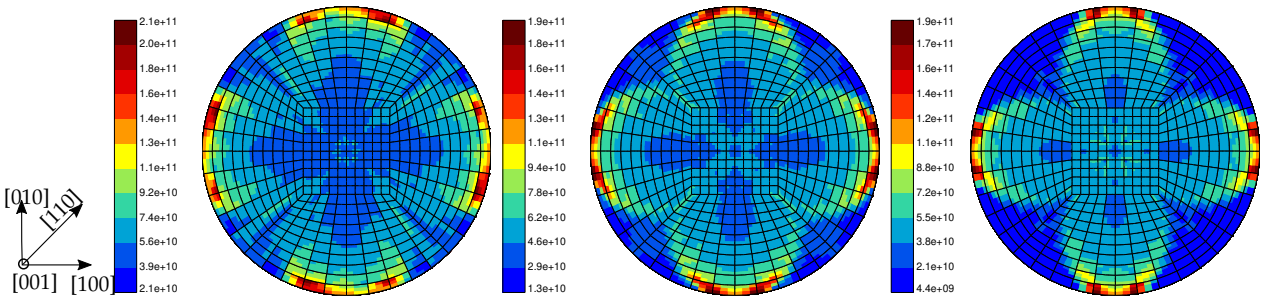

R = 20 mm R = 10 mm R = 5 mm

Fig. 3.16 GND density distribution in FCC single crystals (<100> crystal orientation) predicted by using a Lagrange multiplier-based model with A = 20000 N and a finite element discretization featuring 10000 elements. The results are shown on the undeformed configuration for an applied relative rotation of 45° between the upper and lower face.

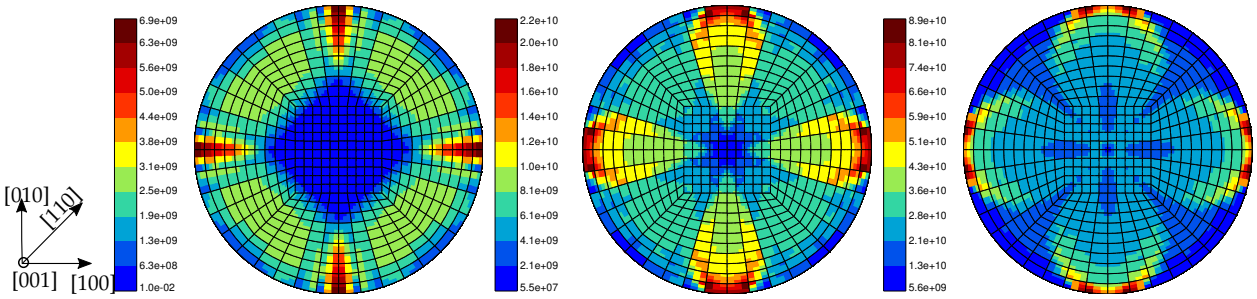

(a) (b) (c)

Fig. 3.17 GND density distribution in FCC single crystal (<100> crystal orientation, R = 10 mm) predicted by using the Lagrange multiplier-based model with A = 20000 N at an applied relative rotation of (a) 4.5°, (b) 9°, and (c) 22.5° shown on the undeformed configuration.

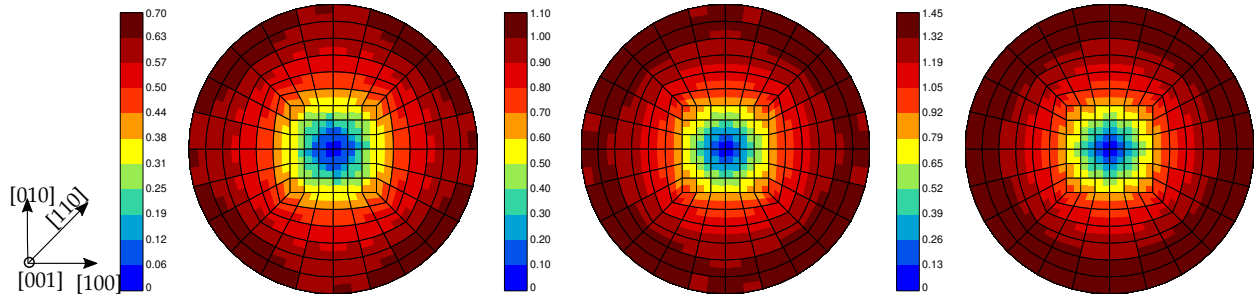

Cycle 1 Cycle 2 Cycle 3

Fig. 3.18 Cumulative plastic strain γ_{cum} distribution in FCC single crystal (<100> crystal orientation, R = 10 mm) predicted by using the Lagrange multiplier-based model with A = 20000 N and a finite element discretization featuring 3600 elements.

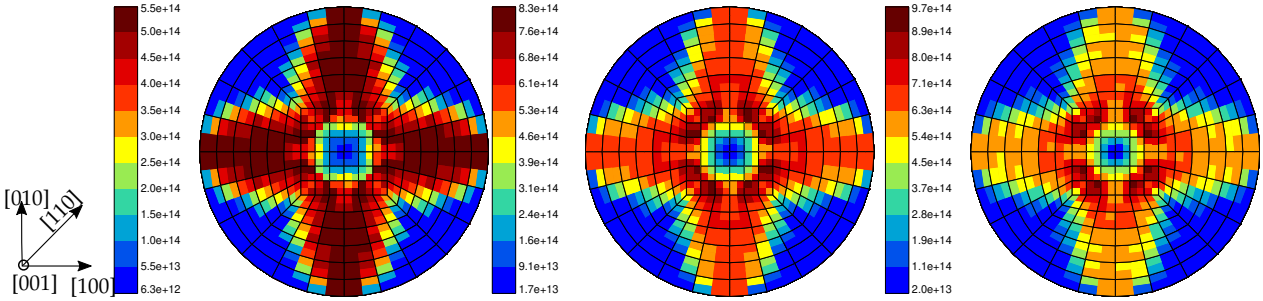

Cycle 1 Cycle 2 Cycle 3

Fig. 3.19 SSD density distribution in FCC single crystal (<100> crystal orientation, $R = 10$ mm, $A = 20000$ N) predicted by using the Lagrange multiplier-based model and a finite element discretization featuring 3600 elements.

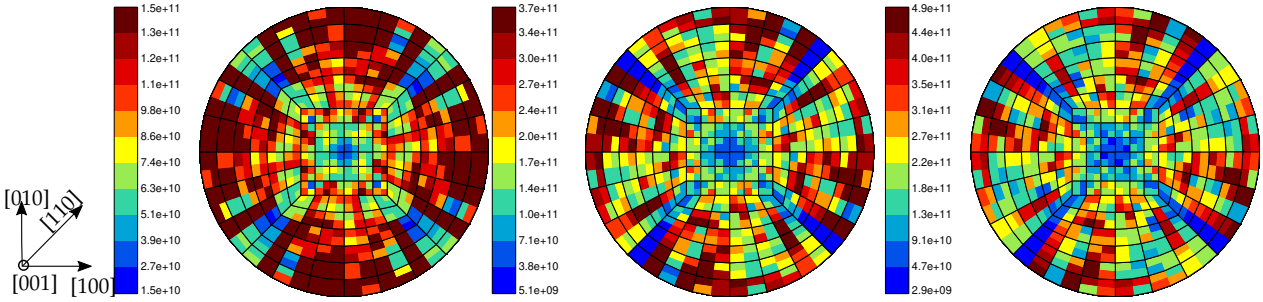

Cycle 1 Cycle 2 Cycle 3

Fig. 3.20 GND density distribution in FCC single crystal (<100> crystal orientation, $R = 10$ mm, $A = 20000$ N) predicted by using the Lagrange multiplier-based model and a finite element discretization featuring 3600 elements.

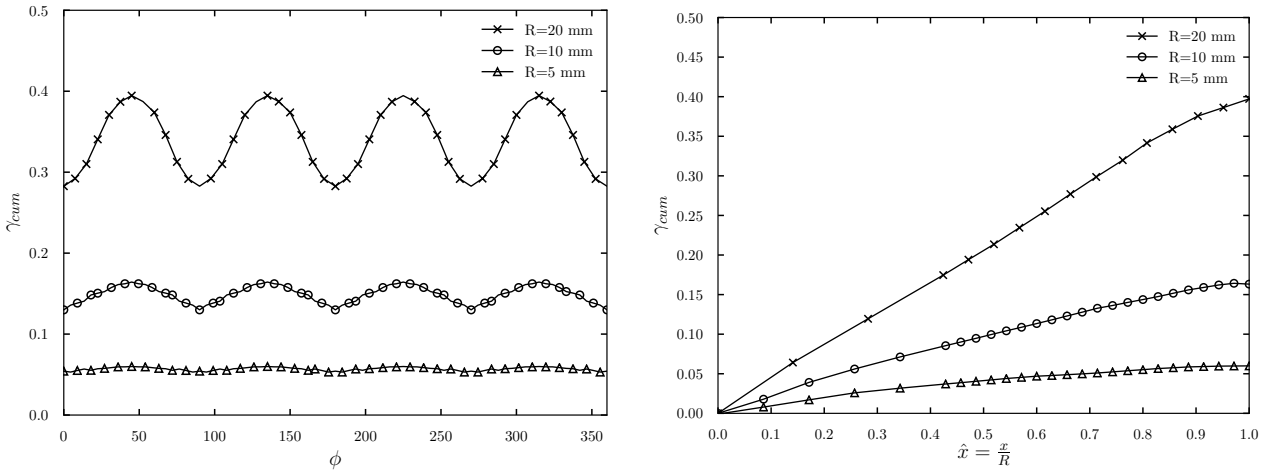

(a) (b)

Fig. 3.21 Cumulative plastic strain γ_{cum} variation predicted by the Lagrange multiplier-based model along the (a) circumferential and (b) radial direction of the microwire for monotonic loading and for three radii of microwire using A = 20000 N. The radial distance from the center of the specimen is denoted by x and the radius of the microwire by R.

cycles using classical crystal plasticity model with dislocation density-based hardening. In contrast, the gradient effect associated with parameter A leads to strong additional isotropic hardening as depicted in Fig. 3.22b with no apparent saturation.

The cumulative plastic strain and dislocation density fields shown next are plotted for the microwire of radius $R = 10\,\text{mm}$ and based on a finite element discretization with 3600 elements for resolution reasons.. Fig. 3.19 and 3.20 show the SSD and GND density distribution over the cross section at the end of each cycle. As the deformation progresses, the dislocation density significantly increases with the plastic strain, and SSD density gets much larger than GND density. In particular, the SSD and GND densities increase from an initial value of $6.5\times10^{8}\,\text{m}^{-2}$ to $9.7\times10^{14}\,\text{m}^{-2}$ and $4.9\times10^{11}\,\text{m}^{-2}$, respectively at the end of cycle 3. In addition, the dislocation density distribution maintains the distinct four-fold symmetry pattern even at the end of cycle 3.

The plastic strain distribution and profiles along the circumferential and radial directions for cyclic loading are shown in Fig. 3.18 and 3.23. Accumulation of plastic deformation during cycling in the four zones of favored plastic slip leads to an increased gradient values and subsequent additional hardening, thus explaining the cyclic hardening of Fig. 3.22b. With further increase in number of cycles, the cumulative plastic strain increases and becomes homogeneous along the circumference, making the four-fold symmetry of FCC single crystal almost disappear as shown in Fig. 3.18 and 3.23a. This may explain the trend to some saturation of cyclic hardening in Fig. 3.22b. It is observed that the magnitude of the plastic strain field increases in the radial direction with an increasing number of cycles as shown in Fig. 3.23b.

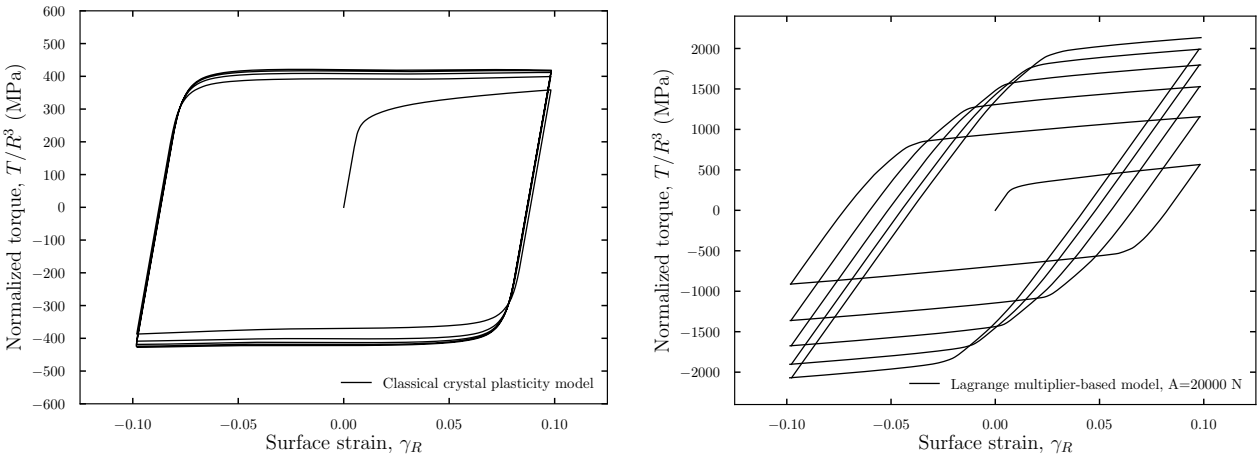

(a) (b)

Fig. 3.22 Comparison of normalized torque vs. surface strain curves (<001> crystal orientation) and for cyclic loading using the (a) classical crystal plasticity formulation according to section 2.2.3, and (b) Lagrange multiplier-based model using A = 20000 N. The microwire of radius R = 10 mm discretized using 3600 finite elements.

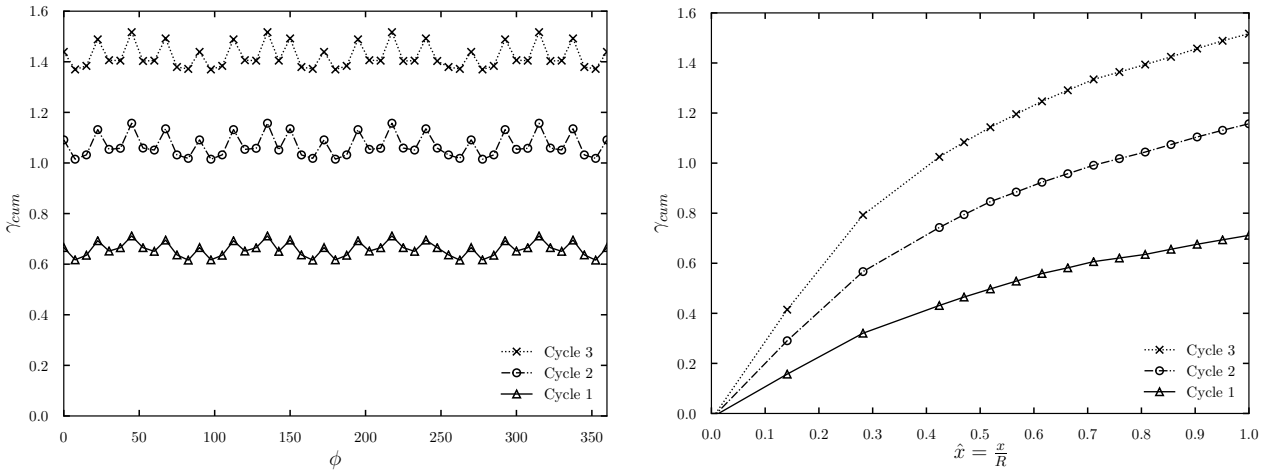

(a) (b)

Fig. 3.23 Cumulative plastic strain γ_{cum} variation along the (a) circumferential and (b) radial direction of the microwire for cyclic loading using the Lagrange multiplier-based model (A = 20000 N, R = 10 mm, and a finite element discretization with 3600 elements). The radial distance from the center of the specimen is denoted by x and the radius of the microwire by R.

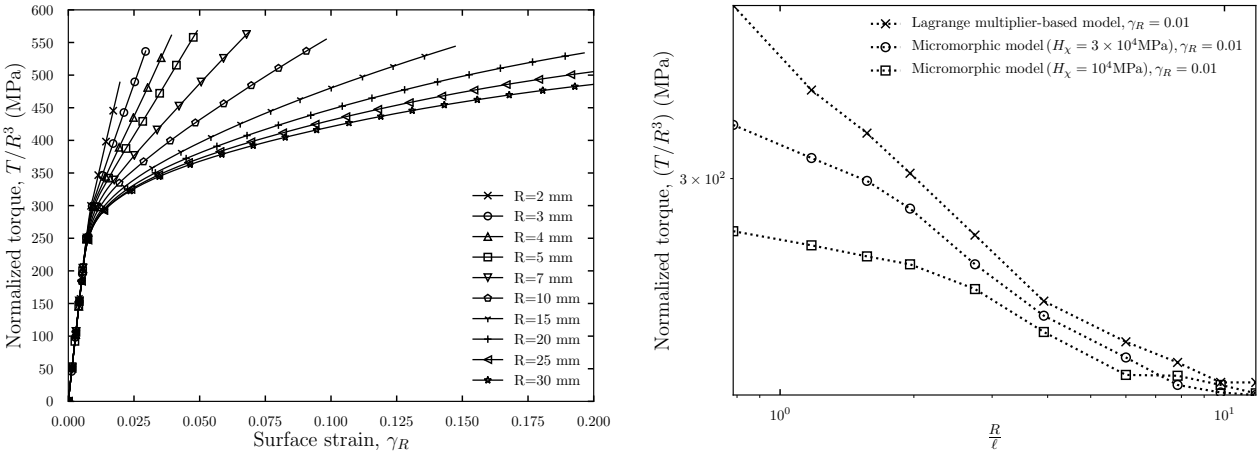

(a) (b)

Fig. 3.24 Normalized torque vs. surface strain curves for <001> crystal orientation: (a) influence of the microwire radius when using a Lagrange multiplier-based model, (b) normalized torque as a function of R/ℓ ratio at a surface strain γ_R of 0.01 for the micromorphic crystal plasticity and Lagrange multiplier-based models.

• Scaling law

In this section, the scaling behavior is studied for the micromorphic crystal plasticity model presented in section 2.3.1 and the Lagrange multiplier-based model presented in section 2.3.2. The dependence of the normalized torque on the R/ℓ ratios is analyzed for the monotonic microwire torsion tests. The simulations are performed for several radii of the microwire ranging from $R = 2$ mm to $R = 30$ mm and by using the value of the higher-order modulus $A = 20000$ N. The scaling laws in the form of the power law $T/R^3 \propto (R/\ell)^n$ for microwire torsion tests characterizing the effect of the R/ℓ ratio on the normalized torque T/R^3 are shown in Fig 3.24a. The characteristic length scale ℓ defined as $\sqrt{A/|H|}$ is 2.55 mm. The log-log plot of the normalized torque values as a function of R/ℓ ratio at a surface strain of 0.01 are plotted in Fig. 3.24b for the micromorphic crystal plasticity model using $H_\chi = 10^4$ MPa and $H_\chi = 3\times10^4$ MPa, and for the Lagrange multiplier-based model using $\mu_\chi = 10^3$ MPa, respectively. For lower values of the coupling modulus H_χ the micromorphic crystal plasticity model predicts a typical *tanh* shape (Cordero et al., 2010) with saturation for small ($R/\ell < 0.8$) and large ($R/\ell > 6$) values of the R/ℓ ratio. The slope of the bounded intermediate regime for the micromorphic crystal plasticity model using $H_\chi = 10^4$ MPa and $H_\chi = 3\times10^4$ MPa is found to be $n = -0.6$ and $n = -0.85$, respectively. The Lagrange multiplier-based model can be considered as a limiting case of the micromorphic crystal plasticity model for large values of H_χ, which leads to a power-law exponent $n = -1.0$ of asymptotic regime towards zero. In the latter case, no saturation is expected.

The power-law exponent n of the micromorphic crystal plasticity model depends on the material parameters H_χ and A, whereas it is independent of material parameters in the Lagrange multiplier-based model. The critical value of the R/ℓ ratio is defined by the

inflection point i of the plot in Fig. 3.24b. The value of i depends on the coupling modulus H_χ and is found to be 4 and 3 for $H_\chi = 10^4\,\text{MPa}$ and $H_\chi = 3\times10^4\,\text{MPa}$, respectively, which represents the size-dependent domain of the material response.

3.4 Concluding remarks

The main findings obtained in this contribution can be summarized as follows:

1. The prediction of size effects with the micromorphic crystal plasticity and Lagrange multiplier-based approaches are compared for single crystals torsion tests. It is shown that both models provide similar results for small and intermediate characteristic length scales. However, for larger characteristic length scales, the hardening due to strain gradients saturates according to the micromorphic crystal plasticity approach. A similar saturation effect is observed on the grain size effect on the yield stress in polycrystals using the microcurl model at small strains in (Cordero et al., 2012b). The scaling law is different for the Lagrange multiplier-based formulation since such a saturation is not observed.

2. The size effects predicted by the Lagrange multiplier-based model are found to be in good agreement with the predictions made by the *CurlF*^{p} model. They are analyzed for monotonic and cyclic microwire torsion tests.

3. The Lagrange multiplier-based model induces an isotropic hardening because it is based on the gradient of a scalar-valued cumulative plastic strain variable. This is in contrast to the kinematic hardening induced by the *CurlF*^{p} model due to the back-stress resulting from the action of higher-order stresses. This leads to significantly different responses under cyclic loading conditions.

4. The analysis of the cyclic torsion tests shows the evolution of plastic slip gradients along the circumference with a trend towards more homogeneous distributions for larger cycle numbers according to the Lagrange multiplier-based model. A significant increase in SSD and GND density is observed at the end of each cycle compared to previous cycles.

5. The size effects are characterized by power law relationships between the normalized torque and R/ℓ, with ℓ being a characteristic length of the model. The reduced micromorphic crystal plasticity model saturates for small and large values of this ratio. It possesses an intermediate domain with powers $n = -0.6$ and $= -0.85$, which were found for $H_\chi = 10^4$ MPa and $H_\chi = 3\times10^4$ MPa, respectively. In contrast, the augmented Lagrangian version of the model, which corresponds to a strict strain gradient plasticity model, predicts no saturation at small R/ℓ ratios and a power law with $n = -1$.

An equivalence between the Lagrange multiplier-based model and the *CurlF*^{p} model exists in the case of a single-slip under monotonic loading. The *CurlF*^{p} model has a clear physical interpretation in terms of the dislocation density tensor in contrast to the reduced-order models, which incorporate the gradient of cumulative slip in a purely phenomenological way. Reduced-order models are advantageous from a computational point of view and lead to significantly lower computation times in the presented examples. The computational efficiency in terms of CPU time of the Lagrange multiplier-based model and of the micromorphic crystal plasticity model that was studied in this contribution is investigated in (Scherer et al., 2020). The *CurlF*^{p} model, which includes 21 DOF at each node in three-dimensional settings, is computationally expensive compared to the Lagrange multiplier-based model, which includes 5 DOF per node. It has been demonstrated that the *CurlF*^{p} and reduced-order models can deliver similar predictions related to size effect, at least for monotonic tests. The reduced-order models can therefore be applied for faster evaluation of size effects in structural computations. More physical understanding can be gained using the full gradient model.

The full gradient and reduced-order models could further be compared in the case of localization phenomena in crystalline materials as recently explored by Marano et al. (2021). Regularization of strain localization phenomena in single crystals such as slip, kink, and shear bands was demonstrated in (Ling et al., 2018).

A limitation of the reduced-order micromorphic crystal plasticity and Lagrange multiplier-based formulations presented in this work is that the gradient terms essentially affect the isotropic hardening and do not incorporate a size-dependent back-stress, in contrast to full-order micromorphic crystal plasticity and the gradient plasticity models. The simulation of kinematic-type hardening is, in fact, possible with a reduced-order model using an alternative formulation in which the free energy potential depends on the gradient of the microslip variable as pointed out in (Forest, 2016b; Ling et al., 2018). Another possibility is to consider the gradient of the equivalent plastic strain instead of the cumulative one. This will cause size-dependent kinematic hardening effects, as recently demonstrated by Jebahi and Forest (2021).

Chapter 4

Adiabatic shear banding in single and poly-crystals: Numerical approach

Abstract

Finite element (FE) simulations are performed for hat-shaped specimens made of face-centered cubic (FCC) metallic single and poly–crystals in order to investigate the adiabatic shear band (ASB) formation process. A micromorphic crystal plasticity model is used to overcome the main limitation of classical plasticity models, namely the mesh size dependency in strain localization problems. A thermodynamically consistent formulation of the constitutive equations is proposed for micromorphic thermo-elasto-viscoplasticity of single crystals. The temperature evolution under adiabatic conditions is derived from the competition between plastic power and energy storage. The micromorphic crystal plasticity model is used first to simulate strain localization induced by thermal softening in a metallic single crystal strip loaded in simple shear undergoing single-slip. The FE solution of this boundary-value problem is validated using an analytical solution. Regarding single crystal hat-shaped specimen simulations, five different crystal orientations are considered to study the formation, intensity and orientation of shear bands. In particular, one special crystal orientation is found resistant to shear banding. In addition, the formation of shear bands in hat-shaped polycrystalline aggregates is investigated. The specimens are polycrystalline aggregates with different grain sizes, namely the coarse-grained and fine-grained specimens with random crystal orientation distribution. Furthermore, several realizations of the microstructures are taken into account for statistical considerations. The micromorphic crystal plasticity model incorporates a characteristic length scale, which induces a grain size effect in the simulation of polycrystalline specimens. The grain boundaries act as obstacles against shear band formation. A significant grain size effect, namely the finer the grain size the higher the resulting load, is predicted by the simulations under isothermal conditions. However, the fine-grained specimens are found to fail earlier by shear banding than some coarse–grained samples, the latter being associated with significant dispersion of the results depending on grain orientations. The effect of grain size on the width of the shear band is

This chapter has been submitted to a journal.

also analyzed. The temperature-dependent material parameters and shear band widths considered in the paper correspond to Nickel-based superalloy Inconel 718 in a large temperature range. The considered material behavior is elastic-perfectly plastic.

4.1 Introduction

The ASB formation process originates from the rapid increase of local temperature due to plastic work dissipation under high strain rate loading conditions. This, in turn, reduces the stress carrying capacity of the material and results in highly localized and unstable plastic deformation (Gilman, 1994; Zhu et al., 1995; Dodd and Bai, 2012). The flow stress dependency on temperature is associated with thermal softening, causing the stress to drop from its maximum point, thus leading to intense shear band formation. In addition, microscopic deformation mechanisms in the material play a crucial role in triggering the shear band when the wavelength of the deformation field is larger than the characteristic length scale of the material microstructure (Zhao et al., 2005). The formation of shear bands may not be considered as failure of ductile material, but as a precursor to the catastrophic fracture (Anand et al., 1987; Zhu et al., 1995). It influences the texture development and the material constitutive behavior (Dève and Asaro, 1989). The phenomenon of ASB formation can be observed in many industrial processes, for instance, machining and high-speed shaping, shearing, metal forming (Burns and Davies, 2002; Molinari et al., 2002; Longère et al., 2008; Dodd and Bai, 2012), and so forth.

In recent years, considerable experimental research has been conducted to investigate the ASB formation in FCC metallic materials. The experimental shear tests on hat-shaped specimens using Split-Hopkinson pressure bars in compression mode are often used to study the material resistance to shear localization, for instance, in (Nemat-Nasser et al., 1998; Meyers et al., 2003; Xue et al., 2005; Xu et al., 2008). Meyers et al. (2003) studied the microstructural evolution of adiabatic shear localization in stainless steel. Experimental investigations of the effect of strain rates, heat treatments, and grain size on the ASB formation in hat-shaped polycrystalline Inconel 718 specimens using Split-Hopkinson pressure bar test can be found in (Johansson et al., 2016, 2017; dong Song et al., 2018). Furthermore, dong Song et al. (2018) observed that the aged top-hat sample with small grain size and fillet radius has the largest tendency to form a shear band compared to the solution treated Inconel 718 specimens. They observed shear bands of 10 µm width in aged Inconel 718 samples of average grain size 28 μm and $10-13$ µm in solution treated samples of average grain size 18 µm. DeMange et al. (2009) found that the precipitation hardened material more readily exhibits shear localization than the solution treated material in the shear deformation of top-hat samples. Moreover, in metallic materials and alloys, it was believed that only the dislocation mobility due to a rise in temperature causes the strain-softening. However, the recent studies, e.g. (Landau et al., 2016; Mourad et al., 2017;

Longère, 2018) showed that the dynamic recrystallization (DRX) is also playing an essential part in strain softening.

From the computational perspective, it is well–known that finite element simulations of strain localization phenomena exhibit spurious mesh dependency, and the classical plasticity models are inadequate to solve the strain localization problems (Asaro and Rice, 1977; de Borst et al., 1993; Besson, 2009). The possible loss of ellipticity of the partial differential equations in strain-softening materials results in an ill-posed boundary-value problem and classically displays dependency on mesh size or density and element orientation. The loss of ellipticity of the PDE is a local condition that concerns rate-independent constitutive equations in the static case. It implies the non-positive value of the determinant of the material's acoustic tensor (Forest and Lorentz, 2004; Wcisło et al., 2018). Rate-dependence of the material behavior can improve the situation but it is not sufficient to regularize the general localization problem (Needleman, 1988). Numerical analyses of strain localization problems within the conventional continuum mechanics framework can be found in (Batra and Kim, 1991, 1992; Duszek-Perzyna and Perzyna, 1993, 1996; Perzyna and Korbel, 1996, 1998). Moreover, a large scale postulate to simulate the ASB formation can be found in (Longère et al., 2003; Longère et al., 2005). In large scale postulate, shear band is considered as a structure contained within the representative volume element (RVE), and not the opposite as usually assumed (Dorothy, 2018).

The shear band width dependency on mesh size can be overcome by introducing a characteristic length scale in the classical plasticity models according to (Kuroda and Tvergaard, 2006; Voyiadjis and Al-Rub, 2005; Anand et al., 2012; Pamin et al., 2017; Vignjevic et al., 2018; Kaiser and Menzel, 2019b). Strain gradient plasticity models, which include an characteristic length scale in the constitutive framework, are often used to regularize strain localization problems, e.g., (Aifantis, 1984; Abu Al-Rub and Voyiadjis, 2006; Anand et al., 2012; Ahad et al., 2014). Aifantis (1984, 1987) proposed a strain gradient theory by adding the Laplacian of a scalar measure of plastic strain in the yield function of the classical plasticity theory to solve the issues related to the width of the shear bands. The characteristic length scale introduced in the gradient plasticity models can be associated with the width of the shear band as demonstrated in (Zbib and Aifantis, 1988; Chambon et al., 1998). The effect of higher-order gradients on ASB formation was investigated by Zhu et al. (1995) and more recently by Tsagrakis and Aifantis (2015). Two length scales, respectively associated with strain gradients and thermal conduction, were considered in the analysis. They showed that the width of the shear band scales with the square root of strain gradient coefficient in the absence of conduction and square root of the thermal conductivity in absence of strain gradient effects. The micromorphic theory proposed by Eringen (1999) relies on the second-order microdeformation tensor as an additional degree of freedom. The application of micromorphic theory for the strain localization phenomenon can be found in (Dillard et al., 2006; Anand et al., 2012; Mazière and Forest, 2015). In contrast to Eringen's full micromorphic theory, a reduced-order micromorphic crystal

plasticity theory was proposed by Ling et al. (2018) involving a scalar-valued variable as the additional degree of freedom. It was used to analyze strain localization phenomena at finite deformation by Scherer et al. (2019). The mesh dependency issues in the shear localization problem can also be eliminated by the sub-grid method proposed in (Mourad et al., 2017; Jin et al., 2018) in the case dynamic loading conditions applied to hat-shaped specimens.

As the yielding starts in a metallic material, the work done by the stresses is partly transferred to heat and partly to the reversible or irreversible microstructural changes in the material and leads to a rise in temperature locally affecting the elastic-plastic behavior of the material. Therefore, it is necessary to introduce thermodynamics into the plasticity framework (Bertram and Krawietz, 2012). Thermodynamically consistent formulations of the constitutive equations in classical plasticity models for the small strain strain can be found in (Bertram and Krawietz, 2012) and for finite strain gradient plasticity in (Forest and Sievert, 2003; Bertram, 2015). The second law of thermodynamics in the form of Clausius-Duhem inequality is used to find the necessary conditions required for the thermodynamically consistent formulation. A fully coupled thermo-plasticity model can also be found in (Simo and Miehe, 1992; Duszek-Perzyna and Perzyna, 1993; Yang et al., 2006; Ristinmaa et al., 2007). In many works in the literature (see, e.g., Osovski et al. (2013); Zhang et al. (2016); Lieou et al. (2019)), use is made of the TQC (Taylor and Quinney, 1934), a constant parameter related to the amount of plastic work converted into heat. A more precise thermodynamic description requires the definition of the stored energy function with appropriate internal variables and of the dissipative mechanisms. Thermo-mechanical couplings can in that way be derived in the heat equation.

Many numerical studies on adiabatic shear localization in metallic single crystals have been completed in recent years, for instance, in (Baucom and Zikry, 1999; Perzyna, 2002; Zhang et al., 2016). However, less attention has been given to the effect of crystal orientation on the shear band formation in single crystals. It is, therefore, one of the objectives of the present work to investigate the effect of various initial crystal orientations on the ASB formation in single crystals. In the present study, the ASB formation is only related to thermal softening, letting aside the effect of DRX. The applicability of the reduced-order micromorphic crystal plasticity model involving a single scalar-valued variable as a degree of freedom (Ling et al., 2018) is demonstrated for regularizing the ASB. A thermodynamically consistent formulation of the constitutive equations for the micromorphic crystal plasticity model is presented. At first, an analytical reference solution is developed in the case of a periodic strip loaded in simple shear undergoing single-slip with linear strain and thermal softening. The FE solution of the same boundary-value problem is validated using an analytical solution initially developed for the rate-independent *isothermal* case. The temperature-dependent material parameters and shear band widths considered in the paper correspond to Nickel-based super-alloy Inconel 718 in a large temperature range. Furthermore, simulations are performed with the single crystals hat-shaped specimens with

different initial crystal orientations. The considered material behavior is elastic-perfectly plastic.

The second original objective of the present work is to study the transition of ASB formation from single to polycrystals. To this end, the micromorphic approach is applied to polycrystalline hat-shaped specimens simulations to predict the role of grain boundaries as obstacles to ASB, the orientation dependency, and the influence of grain size on the width of the ASB.

The outline of the chapter is as follows: Section 4.3 is dedicated to the validation of the numerical solution for a periodic strip loaded in simple shear undergoing single-slip with linear thermal softening based on the analytical solution developed for the rate-independent case. Section 4.4 reports on the simulations of single crystals hat-shaped specimens under static loading conditions. In section 4.5, the micromorphic crystal plasticity model is used to investigate ASB formation in polycrystalline hat-shaped specimens. Concluding remarks follow in section 4.6.

4.2 Thermo-elasto-viscoplasticity of single crystals at finite deformation

4.2.1 Kinematics

In the present work, a large deformation framework of thermo-plasticity is adopted, based on the multiplicative decomposition of total deformation gradient $\underset{\sim}{F}$ into a recoverable thermo-elastic part $\underset{\sim}{F}^{the}$ and a plastic part $\underset{\sim}{F}^{p}$ combining concepts put forward by (Bertram, 2003; Ristinmaa et al., 2007):

$$\underset{\sim}{F} = \underset{\sim}{F}^{the} \cdot \underset{\sim}{F}^{p}. \tag{4.1}$$

The volume mass densities with respect to the reference configuration, the intermediate configuration, and the current configuration are ρ_0, $\rho_\#$ and ρ, respectively, given by

$$J = \det(\underset{\sim}{F}) = \frac{\rho_0}{\rho}, \quad J^{the} = \det(\underset{\sim}{F}^{the}) = \frac{\rho_\#}{\rho}, \quad J^{p} = \det(\underset{\sim}{F}^{p}) = \frac{\rho_0}{\rho_\#}. \tag{4.2}$$

It is assumed that plastic flow is isochoric such that

$$J^{p} = \det \underset{\sim}{F}^{p} = 1, \quad J^{the} = \det \underset{\sim}{F}^{the} = J = \det \underset{\sim}{F}. \tag{4.3}$$

Crystal plasticity in dense metals is incompressible so that $J^p = 1$. However, J^p can be different from one in the case of compressible plasticity. This situation was studied for ductile fracture of porous the single crystals in (Ling et al., 2016). Moreover, the thermo-elastic strain tensor $\underset{\sim}{E}^{the}$ is introduced as follows:

$$\underset{\sim}{E}^{the} = \frac{1}{2}[(\underset{\sim}{F}^{the})^T \cdot (\underset{\sim}{F}^{the}) - \underset{\sim}{1}], \tag{4.4}$$

with $\underset{\sim}{1}$ denoting the second order identity tensor. The Mandel stress tensor $\underset{\sim}{\Pi}^M$ with respect to the intermediate configuration is related to the Cauchy stress tensor $\underset{\sim}{\sigma}$ by $\underset{\sim}{\Pi}^M = J^{the}(\underset{\sim}{F}^{the})^T \cdot \underset{\sim}{\sigma} \cdot (\underset{\sim}{F}^{the})^{-T}$.

4.2.2 Thermodynamic formulation

The energy balance (first law of thermodynamics) with respect to the current configuration is written in the local form:

$$\rho \dot{e} = \underset{\sim}{\sigma} : \underset{\sim}{D} + Q, \tag{4.5}$$

with $\underset{\sim}{D} = (\underset{\sim}{l} + \underset{\sim}{l}^T)/2$ as the strain rate tensor, e the internal energy per unit mass and Q the heat supply per unit volume and unit time, which results from an external heat source r and heat conduction $\underline{q}$ such that

$$Q = r - \operatorname{div} \underline{q}. \tag{4.6}$$

The second law of thermodynamics in the form of the local dissipation rate inequality with respect to the current configuration can be written as

$$\rho \dot{\eta} + \operatorname{div} \frac{\underline{q}}{T} - \frac{r}{T} \geq 0, \tag{4.7}$$

where η is the entropy per unit mass and T is the absolute temperature. The Helmholtz free energy density function is introduced as

$$\Psi := e - T\eta. \tag{4.8}$$

The Clausius-Duhem inequality is now expressed with respect to the reference configuration as

$$J \underset{\sim}{\sigma} : \underset{\sim}{D} - \rho_0(\dot{\Psi} + \eta \dot{T}) - \underline{Q} \cdot \frac{\nabla_X T}{T} \geq 0, \tag{4.9}$$

where $\underline{Q}$ is the heat conduction with respect to the reference configuration and given by $\underline{Q} = J^{the} \underset{\sim}{F}^{-1} \cdot \underline{q}$ and $\nabla_X T$ is the Lagrangian gradient of temperature. The stress power term $J \underset{\sim}{\sigma} : \underset{\sim}{D}$ is given by

$$J \underset{\sim}{\sigma} : \underset{\sim}{D} = J^p \underset{\sim}{\Pi}^e : \dot{\underset{\sim}{E}}^{the} + J^p \underset{\sim}{\Pi}^M : \underset{\sim}{l}^p, \tag{4.10}$$

with $\underset{\sim}{\Pi}^e$ the second Piola-Kirchhoff stress tensor defined with respect to the intermediate configuration by $\underset{\sim}{\Pi}^e = J^{the}(\underset{\sim}{F}^{the})^{-1} \cdot \underset{\sim}{\sigma} \cdot (\underset{\sim}{F}^{the})^{-T}$.

The dissipation rate in the Clausius-Duhem inequality consists of mechanical and thermal dissipation rates. The mechanical dissipation rate is given by

$$\Delta_m = J \underset{\sim}{\sigma} : \underset{\sim}{D} - \rho_0(\dot{\Psi} + \eta \dot{T}), \tag{4.11}$$

and the thermal dissipation by

$$\Delta_{th} = -\underline{Q} \cdot \frac{\nabla_X T}{T}. \tag{4.12}$$

The material under consideration is assumed to be characterized by the Helmholtz free energy density function

$$\Psi = \tilde{\Psi}(\underset{\sim}{E}^{the}, T, \zeta), \tag{4.13}$$

The quadratic form of the free energy familiar from the thermo-elasticity is assumed to be a function of the thermo-elastic strain tensor $\underset{\sim}{E}^{the}$, the temperature T and the internal hardening variables ζ as follows:

$$\rho_0\tilde{\Psi}(\underset{\sim}{E}^{the}, T, \zeta) = \frac{1}{2}\underset{\sim}{E}^{the} : \underset{\approx}{\Lambda} : \underset{\sim}{E}^{the} + \rho_0 C_\varepsilon\Big[(T-T_0) - T\log\Big(\frac{T}{T_0}\Big)\Big] + (T-T_0)\underset{\sim}{P} : \underset{\sim}{E}^{the} + \rho_0\tilde{\Psi}(\zeta), \tag{4.14}$$

where $\underset{\approx}{\Lambda}$ is the fourth-order tensor of elastic moduli, T_0 is a reference temperature, C_ε is the specific heat of the material and $\underset{\sim}{P}$ is a constant symmetric thermal stress tensor.

Expanding the time derivative of the free energy density function gives

$$\left(\underset{\sim}{\Pi}^e - \rho_0\frac{\partial\tilde{\Psi}(\underset{\sim}{E}^{the}, T)}{\partial\underset{\sim}{E}^{the}}\right) : \dot{\underset{\sim}{E}}^{the} + \underset{\sim}{\Pi}^M : \underset{\sim}{l}^p - \rho_0\left(\eta + \frac{\partial\tilde{\Psi}}{\partial T}\right)\dot{T} - \rho_0\frac{\partial\tilde{\Psi}}{\partial\zeta}\dot{\zeta} - \underline{Q}\cdot\frac{\nabla_X T}{T} \geq 0, \tag{4.15}$$

The following state laws are adopted:

$$\underset{\sim}{\Pi}^e = \rho_0\frac{\partial\tilde{\Psi}(\underset{\sim}{E}^{the}, T)}{\partial\underset{\sim}{E}^{the}}, \quad \eta = -\frac{\partial\tilde{\Psi}}{\partial T}, \quad X = \rho_0\frac{\partial\tilde{\Psi}}{\partial\zeta}, \tag{4.16}$$

where X is the thermodynamic force associated with the internal variable ζ. The reduced dissipation rate, which restricts the material flow and hardening rules in connection with the yield condition, is given by

$$\underset{\sim}{\Pi}^M : \underset{\sim}{l}^p - X\dot{\zeta} - \underline{Q}\cdot\frac{\nabla_X T}{T} \geq 0. \tag{4.17}$$

Based on the potential (4.14) the thermoelastic relation for the second Piola-Kirchhoff stress tensor is obtained as

$$\underset{\sim}{\Pi}^e = \underset{\approx}{\Lambda} : \underset{\sim}{E}^{the} - \underset{\sim}{P}(T-T_0) = \underset{\approx}{\Lambda} : (\underset{\sim}{E}^{the} - \underset{\approx}{\Lambda}^{-1} : \underset{\sim}{P}(T-T_0)) = \underset{\approx}{\Lambda} : (\underset{\sim}{E}^{the} - \underset{\sim}{E}^{th}), \tag{4.18}$$

and the thermal strain tensor $\underset{\sim}{E}^{th}$ is defined as

$$\underset{\sim}{E}^{th} = (T-T_0)\underset{\approx}{\Lambda}^{-1} : \underset{\sim}{P} = (T-T_0)\alpha\underset{\sim}{1}, \tag{4.19}$$

which involves the thermal expansion coefficient α in the case of isotropic or cubic thermo-elasticity.

4.2.3 Reduced-order micromorphic crystal plasticity model

The material under consideration is assumed to be characterized by the coupled thermo-mechanical Helmholtz free energy density function defined in terms of the thermo-elastic strain tensor $\underset{\sim}{E}^{the}$, the relative plastic strain e_p, the gradient of the microslip variable $\underline{K}$, temperature T and the internal hardening variable ζ as follows:

$$\Psi = \tilde{\Psi}(\underset{\sim}{E}^{the}, e_p, \underline{K}, T, \zeta). \tag{4.20}$$

It is assumed that the Helmholtz free energy density function takes the form:

$$\begin{aligned}\rho_0\tilde{\Psi}(\underset{\sim}{E}^{the}, e_p, \underline{K}, T, \zeta) = \frac{1}{2}\underset{\sim}{E}^{the} : \underset{\approx}{\Lambda} : \underset{\sim}{E}^{the} + \frac{1}{2}H_\chi e_p^2 + \frac{1}{2}\underline{K}\cdot\underset{\sim}{A}\cdot\underline{K} + \rho_0 C_\varepsilon\Big[(T-T_0) - T\log\Big(\frac{T}{T_0}\Big)\Big] \\ + (T-T_0)\underset{\sim}{P} : \underset{\sim}{E}^{the} + \rho_0\tilde{\Psi}(T,\zeta).\end{aligned} \tag{4.21}$$

Expanding the time derivative of the free energy density function leads to the following form of the Clausius-Duhem inequality

$$\begin{aligned}\left(\underset{\sim}{\Pi}^e - \rho_0\frac{\partial\tilde{\Psi}}{\partial\underset{\sim}{E}^{the}}\right) : \dot{\underset{\sim}{E}}^{the} - \left(S + \rho_0\frac{\partial\tilde{\Psi}}{\partial e_p}\right)\dot{e}_p + \left(\underline{M} - \rho_0\frac{\partial\tilde{\Psi}}{\partial\underline{K}}\right)\cdot\dot{\underline{K}} + S\dot{\gamma}_{cum} + \underset{\sim}{\Pi}^M : \underset{\sim}{l}^p \\ - \rho_0\left(\eta + \frac{\partial\tilde{\Psi}}{\partial T}\right)\dot{T} - \rho_0\frac{\partial\tilde{\Psi}}{\partial\zeta}\dot{\zeta} - \underline{Q}\cdot\frac{\nabla_X T}{T} \geq 0.\end{aligned} \tag{4.22}$$

The following state laws are adopted:

$$\underset{\sim}{\Pi}^e = \rho_0\frac{\partial\tilde{\Psi}}{\partial\underset{\sim}{E}^{the}}, \quad S = -\rho_0\frac{\partial\tilde{\Psi}}{\partial e_p}, \quad \underline{M} = \rho_0\frac{\partial\tilde{\Psi}}{\partial\underline{K}}, \quad \eta = -\frac{\partial\tilde{\Psi}}{\partial T}, \quad X = \rho_0\frac{\partial\tilde{\Psi}}{\partial\zeta}. \tag{4.23}$$

The residual dissipation rate, which restricts the material flow and hardening rules in connection with the yield condition, is given by

$$\underset{\sim}{\Pi}^M : \underset{\sim}{l}^p + S\dot{\gamma}_{cum} - X\dot{\zeta} - \underline{Q}\cdot\frac{\nabla_X T}{T} \geq 0. \tag{4.24}$$

The thermodynamic forces associated with arguments of the Helmholtz free energy function are derived from the potential (4.21):

$$\underset{\sim}{\Pi}^e = \underset{\approx}{\Lambda} : (\underset{\sim}{E}^{the} - \underset{\sim}{E}^{th}), \quad S = -H_\chi e_p = -H_\chi(\gamma_{cum} - \gamma_\chi), \quad \underline{M} = \underset{\sim}{A}\cdot\underline{K}. \tag{4.25}$$

4.2.4 Temperature evolution under adiabatic conditions

The energy balance for the micromorphic crystal plasticity model with respect to the reference configuration is written in the form

$$\rho_0 \dot{e} = J\underset{\sim}{\sigma} : \underset{\sim}{D} + S\dot{\gamma}_\chi + \underline{M} \cdot \underline{\dot{K}} + Q. \tag{4.26}$$

The Clausius-Duhem inequality then reads

$$J\underset{\sim}{\sigma} : \underset{\sim}{D} + S\dot{\gamma}_\chi + \underline{M} \cdot \underline{\dot{K}} - \rho_0(\dot{\tilde{\Psi}} + \eta\dot{T}) - \underline{Q} \cdot \frac{\nabla_X T}{T} \geq 0. \tag{4.27}$$

The previous equation consists of mechanical and thermal dissipation. The mechanical dissipation is given by

$$\Delta_m = J\underset{\sim}{\sigma} : \underset{\sim}{D} + S\dot{\gamma}_\chi + \underline{M} \cdot \underline{\dot{K}} - \rho_0(\dot{\tilde{\Psi}} + \eta\dot{T}), \tag{4.28}$$

and the thermal dissipation is still given by Eq. (4.12). Substituting free energy production rate obtained from Eq. (4.8) and (4.26) in previous equation lead to

$$J\underset{\sim}{\sigma} : \underset{\sim}{D} + S\dot{\gamma}_\chi + \underline{M} \cdot \underline{\dot{K}} - \mathrm{div}\underline{q} + r = \rho_0 \dot{e} = \rho_0 \left[\frac{\partial \tilde{\Psi}}{\partial \underset{\sim}{E}^{the}} : \underset{\sim}{\dot{E}}^{the} + \frac{\partial \tilde{\Psi}}{\partial e_p}\dot{e}_p + \frac{\partial \tilde{\Psi}}{\partial \underline{K}} \cdot \underline{\dot{K}} + \frac{\partial \tilde{\Psi}}{\partial T}\dot{T} + \frac{\partial \tilde{\Psi}}{\partial \zeta}\dot{\zeta} + \dot{T}\eta + T\dot{\eta} \right]. \tag{4.29}$$

Simplification of the previous equation after taking the state laws from (4.23) into account provides

$$\underset{\sim}{\Pi}^M : \underset{\sim}{\dot{F}}^p \underset{\sim}{F}^{p-1} + S\dot{\gamma}_{cum} - \mathrm{div}\underline{q} + r = \rho_0 \left[\frac{\partial \tilde{\Psi}}{\partial \zeta}\dot{\zeta} + T\dot{\eta} \right]. \tag{4.30}$$

The expression for the entropy from (4.21) is given by

$$\begin{aligned} \rho_0 \eta = -\rho_0 \frac{\partial \tilde{\Psi}}{\partial T} = -\frac{1}{2}\underset{\sim}{E}^{the} : \underset{\approx}{\frac{\partial \Lambda}{\partial T}} : \underset{\sim}{E}^{the} + \rho_0 C_\varepsilon \log\left(\frac{T}{T_0}\right) - \rho_0 \frac{\partial C_\varepsilon}{\partial T}\left[(T - T_0) - T\log\left(\frac{T}{T_0}\right)\right] \\ + (T - T_0)\underset{\sim}{\frac{\partial P}{\partial T}} : \underset{\sim}{E}^{the} + \underset{\sim}{P} : \underset{\sim}{E}^{the} - \rho_0 \frac{\partial \tilde{\Psi}}{\partial T}. \end{aligned} \tag{4.31}$$

Furthermore, the variation of entropy with respect to time is computed as

$$\begin{aligned} \rho_0 \dot{\eta} = -\underset{\sim}{E}^{the} : \underset{\approx}{\frac{\partial \Lambda}{\partial T}} : \underset{\sim}{\dot{E}}^{the} - \dot{T}\frac{1}{2}\underset{\sim}{E}^{the} : \underset{\approx}{\frac{\partial^2 \Lambda}{\partial T^2}} : \underset{\sim}{E}^{the} + \rho_0 C_\varepsilon \dot{T} + \rho_0 \frac{\partial C_\varepsilon}{\partial T}\left[\log\left(\frac{T}{T_0}\right)\right]\dot{T} \\ - \rho_0 \frac{\partial^2 C_\varepsilon}{\partial T^2}\left[(T - T_0) - T\log\left(\frac{T}{T_0}\right)\right]\dot{T} + \dot{T}\underset{\sim}{\frac{\partial P}{\partial T}} : \underset{\sim}{E}^{the} + \dot{T}(T - T_0)\underset{\sim}{\frac{\partial^2 P}{\partial T^2}} : \underset{\sim}{E}^{the} \\ + (T - T_0)\underset{\sim}{\frac{\partial P}{\partial T}} : \underset{\sim}{\dot{E}}^{the} + \dot{T}\underset{\sim}{\frac{\partial P}{\partial T}} : \underset{\sim}{E}^{the} + \underset{\sim}{P} : \underset{\sim}{\dot{E}}^{the} - \rho_0 \left(\frac{\partial^2 \tilde{\Psi}}{\partial T^2}\dot{T} + \frac{\partial^2 \tilde{\Psi}}{\partial T \partial \zeta}\dot{\zeta} \right). \end{aligned} \tag{4.32}$$

Substituting the previous equation into the right hand side of (4.30)

$$\rho_0\left[\frac{\partial\tilde{\Psi}}{\partial\zeta}\dot{\zeta}+T\dot{\eta}\right]=\rho_0\frac{\partial\tilde{\Psi}}{\partial\zeta}\dot{\zeta}+T\Bigg[-\underset{\sim}{E}^{the}:\frac{\partial\underset{\approx}{\Lambda}}{\partial T}:\dot{\underset{\sim}{E}}^{the}-\dot{T}\frac{1}{2}\underset{\sim}{E}^{the}:\frac{\partial^2\underset{\approx}{\Lambda}}{\partial T^2}:\underset{\sim}{E}^{the}+\rho_0 C_\varepsilon\dot{T} \tag{4.33}$$

$$+\rho_0\frac{\partial C_\varepsilon}{\partial T}\left[\log\left(\frac{T}{T_0}\right)\right]\dot{T}-\rho_0\frac{\partial^2 C_\varepsilon}{\partial T^2}\left[(T-T_0)-T\log\left(\frac{T}{T_0}\right)\right]\dot{T}+\dot{T}\frac{\partial\underset{\sim}{P}}{\partial T}:\underset{\sim}{E}^{the}$$

$$+\dot{T}(T-T_0)\frac{\partial^2\underset{\sim}{P}}{\partial T^2}:\underset{\sim}{E}^{the}+(T-T_0)\frac{\partial\underset{\sim}{P}}{\partial T}:\dot{\underset{\sim}{E}}^{the}+\dot{T}\frac{\partial\underset{\sim}{P}}{\partial T}:\dot{\underset{\sim}{E}}^{the}+\underset{\sim}{P}:\dot{\underset{\sim}{E}}^{the}$$

$$-\rho_0\left(\frac{\partial^2\tilde{\Psi}}{\partial T^2}\dot{T}+\frac{\partial^2\tilde{\Psi}}{\partial T\partial\zeta}\dot{\zeta}\right)\Bigg]. \tag{4.34}$$

Finally, the rate of temperature change is obtained as

$$\dot{T}=\Bigg[\underset{\sim}{\Pi}^M:\underset{\sim}{l}^p+S\dot{\gamma}_{cum}-\mathrm{div}\underline{q}+r-\rho_0\frac{\partial\tilde{\Psi}}{\partial\zeta}\dot{\zeta}-T\Bigg(-\underset{\sim}{E}^{the}:\frac{\partial\underset{\approx}{\Lambda}}{\partial T}:\dot{\underset{\sim}{E}}^{the}+(T-T_0)\frac{\partial\underset{\sim}{P}}{\partial T}:\dot{\underset{\sim}{E}}^{th}$$

$$+\underset{\sim}{P}:\dot{\underset{\sim}{E}}^{the}-\rho_0\frac{\partial^2\tilde{\Psi}}{\partial T\partial\zeta}\dot{\zeta}\Bigg)\Bigg]\Bigg[-T\frac{1}{2}\underset{\sim}{E}^{the}:\frac{\partial^2\underset{\approx}{\Lambda}}{\partial T^2}:\underset{\sim}{E}^{the}+\rho_0 C_\varepsilon+\rho_0\frac{\partial C_\varepsilon}{\partial T}\left[\log\left(\frac{T}{T_0}\right)\right]T$$

$$-\rho_0\frac{\partial^2 C_\varepsilon}{\partial T^2}\left[(T-T_0)-T\log\left(\frac{T}{T_0}\right)\right]T+T\frac{\partial\underset{\sim}{P}}{\partial T}:\underset{\sim}{E}^{the}+T(T-T_0)\frac{\partial^2\underset{\sim}{P}}{\partial T^2}:\underset{\sim}{E}^{the}$$

$$+T\frac{\partial\underset{\sim}{P}}{\partial T}:\underset{\sim}{E}^{the}-\rho_0\frac{\partial^2\tilde{\Psi}}{\partial T^2}T\Bigg]^{-1}, \tag{4.35}$$

up to $T=T_{melt}$, where T_{melt} is the melting temperature of the material.

• Adiabatic processes

In this work, the thermodynamic processes are assumed to be *adiabatic* in nature, wherein there is no heat transfer to the surrounding and no external heat source present such that

$$\underline{q}=0,\quad r=0. \tag{4.36}$$

Therefore, terms $\mathrm{div}\,\underline{q}$ and r in (4.35) vanish. The following two simplified cases can be considered for the temperature evolution:

case 1: It is assumed that the contribution of the temperature dependence of the elastic constants and specific heat of the material can be neglected compared to plastic power. Also, the contributions of second order derivatives (variation of thermal stress with respect to the temperature) are considered very small compared to internal dissipation terms. Then (4.35) can be written as follows:

$$\rho C_\varepsilon\dot{T}=\underset{\sim}{\Pi}^M:\underset{\sim}{l}^p+S\dot{\gamma}_{cum}-X\dot{\zeta}\quad\text{with}\quad X=\rho_0\frac{\partial\tilde{\Psi}}{\partial\zeta}. \tag{4.37}$$

In addition, in the present work, hat-shaped specimen simulations are performed in the absence of classical hardening, which means that $\tau_c^r = \tau_0$ is a constant in (2.32). Therefore, the contribution of internal hardening variable to the stored energy is not considered. The resulting form of temperature evolution is given in case 2.

case 2: The two first terms in (4.37) denote the heat generated by the plastic power and represent the main contribution to thermo-mechanical phenomenon. It is assumed that all the plastic work done is converted into heat so that

$$\rho C_\varepsilon \dot{T} = \underset{\sim}{\Pi}^M : \underset{\sim}{l}^p + S\dot{\gamma}_{cum}. \tag{4.38}$$

4.3 Simple shear test with strain or thermal softening

An analytical reference solution initially developed for the rate-independent case with linear strain softening for a periodic strip loaded in simple shear undergoing single-slip in (Scherer et al., 2019) is first recalled. The introduction of softening induces strain localization in a band of finite width characterized by the parameters of the micromorphic model. This solution will be adapted to account for thermal softening and provide a validation test for the FE implementation of the thermomechanical micromorphic model in the code.

4.3.1 Analytical solution

Consider a periodic strip made of a thick rectangular plate of width W along the $\underline{X}_1$ direction, length L along the $\underline{X}_2$ direction, and thickness T along the $\underline{X}_3$ direction (Fig. 4.1). It is made of a single crystal material possessing a single slip system under simple shear conditions. The slip direction $\underline{m}$ and the normal to the slip plane $\underline{n}$ are respectively parallel to $\underline{X}_1$ and $\underline{X}_2$. The strain rate sensitivity parameters m, K in Eq. (2.12) are chosen in such a way that the material response is almost rate-independent. A macroscopic deformation gradient $\underset{\sim}{\bar{F}}$ is applied such that

$$\underline{u} = (\underset{\sim}{\bar{F}} - \underset{\sim}{1}) \cdot \underline{X} + \underline{v}(\underline{X}), \quad \text{with} \quad \underset{\sim}{\bar{F}} = \underset{\sim}{1} + \bar{F}_{12}(\underline{m} \otimes \underline{n}), \tag{4.39}$$

where $\underline{v}$ is a periodic fluctuation of the displacement. The origin O of the strip is constrained such that

$$\underline{u}(X_1 = 0, X_2 = 0, X_3 = 0) = 0. \tag{4.40}$$

It is assumed that elastic deformations remain small in the absence of lattice rotation in the considered slip configuration, i.e. $|F_{12}^e| \ll 1$ with

$$\underset{\sim}{F}^e = \underset{\sim}{F} \cdot \underset{\sim}{F}^{p-1} = \underset{\sim}{1} + F_{12}^e(\underline{m} \otimes \underline{n}), \tag{4.41}$$

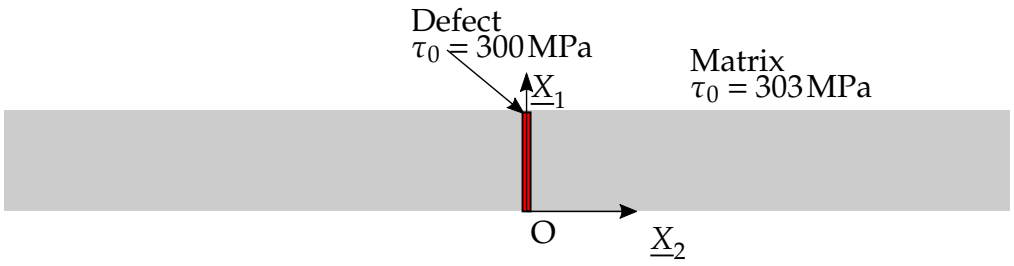

Fig. 4.1 Single crystal trip with a central defect (red line).

and therefore, the Green-Lagrange elastic strain tensor can be expressed as follows:

$$\underset{\sim}{E}^{the} \simeq \frac{F^e_{12}}{2}(\underline{m}\otimes\underline{n}+\underline{n}\otimes\underline{m}). \tag{4.42}$$

where thermal expansion is set to zero in the present isothermal example. Moreover, the second Piola-Kirchhoff stress tensor $\underset{\sim}{\Pi}^e$ in this instance is given by

$$\underset{\sim}{\Pi}^e = \underset{\approx}{\Lambda} : \underset{\sim}{E}^{the} \simeq \Pi^e_{12}(\underline{m}\otimes\underline{n}+\underline{n}\otimes\underline{m}). \tag{4.43}$$

For small elastic deformations, the second Piola-Kirchhoff and Mandel stresses coincide: $\underset{\sim}{\Pi}^M \simeq \underset{\sim}{\Pi}^e$. The resolved shear stress τ^r on the single slip system is given by

$$\tau = \underset{\sim}{\Pi}^M : (\underline{m}\otimes\underline{n}). \tag{4.44}$$

Furthermore, equilibrium requires the shear stress component to be uniform which implies that the resolved shear stress τ is also invariant along $\underline{X}_1$, $\underline{X}_2$ and $\underline{X}_3$.
The quasi-equality between the microslip variable γ_χ and the accumulated plastic strain γ is ensured by the coupling modulus H_χ. The yield condition including the linear strain softening can be written as follows:

$$f = |\tau| - (\tau_0 + H\gamma + H_\chi(\gamma - \gamma_\chi)) = 0 \quad \text{with} \quad H < 0. \tag{4.45}$$

A partial differential equation governing the microslip is given by

$$A\frac{\partial^2\gamma_\chi}{\partial X_2^2} = H_\chi(\gamma_\chi - \gamma). \tag{4.46}$$

Substituting (4.45) for γ into (4.46) leads to another form of the partial differential equation

$$A\frac{\partial^2\gamma_\chi}{\partial X_2^2} - \frac{HH_\chi}{H+H_\chi}\gamma_\chi + \frac{H_\chi}{H+H_\chi}(|\tau| - \tau_0) = 0. \tag{4.47}$$

In the case of linear strain softening, it can be shown that (4.47) takes the form

$$\frac{\partial^2 \gamma_\chi}{\partial X_2^2} - \left(\frac{2\pi}{\lambda}\right)^2 \gamma_\chi = -\left(\frac{2\pi}{\lambda}\right)^2 \kappa, \tag{4.48}$$

where λ is a characteristic length and κ a constant. They are defined as follows:

$$\lambda = 2\pi \sqrt{\frac{A(H+H_\chi)}{|H|H_\chi}}, \quad \kappa = \left(\frac{\lambda}{2\pi}\right)^2 \frac{H_\chi}{A(H+H_\chi)}(|\tau| - \tau_0). \tag{4.49}$$

The differential equation in (4.48) governing γ_χ is only valid in the region where plastic loading takes place which can be identified with the interval $X_2 \in [\frac{-\lambda}{2}, \frac{\lambda}{2}]$. This interval is the strain localization zone and outside elastic unloading takes place. The solution is of the form

$$\gamma_\chi(X_2) = a_1 \cos\left(2\pi \frac{X_2}{\lambda}\right) + a_2 \sin\left(2\pi \frac{X_2}{\lambda}\right) - \kappa. \tag{4.50}$$

where a_1,a_2 are integration constants. For symmetry reasons, $\gamma_\chi(X_2) = \gamma_\chi(-X_2)$ which requires that $a_2 = 0$. At the elastic/plastic interfaces, i.e at $X_2 = \pm\frac{\lambda}{2}$, continuity of microslip γ_χ and of the generalized stress normal to the interface $\underline{M} \cdot \underline{X}_2$ must hold, therefore

$$\gamma_\chi\left(\pm\frac{\lambda}{2}\right) \simeq \gamma\left(\pm\frac{\lambda}{2}\right) = 0, \tag{4.51}$$

$$\underline{M}\left(\pm\frac{\lambda}{2}\right) \cdot \underline{X}_2 = A \frac{d\gamma_\chi}{dX_2}\bigg|_{X_2 = \pm\frac{\lambda}{2}} = 0. \tag{4.52}$$

In (4.51), we have assumed that the penalty parameter H_χ is high enough for γ_χ and γ almost to coincide, i.e. $e_p \simeq 0$. Combining (4.51) and (4.52) with (4.50) gives

$$a_1 = \frac{|\tau| - \tau_0}{H}. \tag{4.53}$$

Moreover, the resolved shear stress is expressed as

$$\tau = \Pi_{12}^e = 2C_{44}E_{12}^{the} = \frac{2C_{44}}{L}\int_{\frac{-L}{2}}^{\frac{L}{2}} \left(\frac{F_{12} - \gamma}{2}\right) dX_2, \tag{4.54}$$

with C_{44} being the elastic shear modulus. From the yield condition given in (4.45), γ can be replaced by $\frac{|\tau| - \tau_0 + H_\chi \gamma_\chi}{H + H_\chi}$ in (4.54) and integration gives an expression for τ as a function of applied macroscopic shear $\bar{F}_{12}$:

$$\tau = \frac{\bar{F}_{12} + \frac{\tau_0}{Z_e}}{\frac{1}{C_{44}} + \frac{1}{Z_e}}, \quad \text{with} \quad \frac{1}{Z_e} = \frac{\lambda}{HL}. \tag{4.55}$$

Table 4.1 Numerical values of material parameters used for the numerical simulation of simple shear test at the initial temperature of 923 K.

C_{11}	C_{12}	C_{44}	τ_0 Eq. (4.45)	H Eq. (4.45)	H_χ Eq. (4.45)
208.1 GPa	144.7 GPa	97.6 GPa	303 MPa	−45 MPa	10^3MPa
A	λ Eq. (4.49)	L Eq. (4.55)			
0.04 N	0.073 mm	1.0 mm			

4.3.2 FE solution with linear strain softening

The implementation of the isothermal micromorphic single crystal plasticity model in the finite element code Zset is described in detail in (Ling et al., 2018). The interpolation of displacement and microslip degrees of freedom is respectively quadratic and linear. The geometry considered in the FE simulations is shown in Fig. 4.1. It is discretized into 400 C3D20R elements, which are 20 node reduced integration brick elements. A material defect is introduced at the center to trigger strain localization in the periodic strip, (see Fig. 4.1). The defect is of one element size and assigned with an initial critical resolved shear stress 1% smaller than the matrix. The material parameters used for the FE solution are summarized in Table 4.1. The elasticity moduli correspond to a nickel–base superalloy at 923 K, see Abdul-Aziz and Kalluri (1991). Periodicity conditions are applied and the tensor $\underset{\sim}{\bar{F}}$ is prescribed according to Eq. (4.39).

Fig. 4.2a displays the cumulative plastic strain field predicted by the micromorphic crystal plasticity model. The FE solution is validated with respect to the variation of γ_χ along X_2 direction at $\bar{F}_{12} = 0.01$ with the analytical solution given by Eq. (4.51). This comparison is shown in Fig. 4.2b. Perfect agreement is observed for $\bar{F}_{12} = 0.01$ and for all other values of $\bar{F}_{12}$. The analytically calculated, refer Eq. (4.49), and numerically observed width of the localization zone is measured to be 2.6λ.

4.3.3 FE solution with linear thermal softening

In the studied simplified problem of single-slip periodic strip undergoing simple shear, the rate of plastic work $\underset{\sim}{\Pi}^M : \underset{\sim}{l}^p + S\dot{\gamma}_{cum}$ becomes$(\tau + S)\dot{\gamma}$, which gives the temperature evolution according to (4.38) as

$$\dot{T} = \frac{(\tau + S)\dot{\gamma}}{\rho C_\varepsilon}. \tag{4.56}$$

In the rate independent limit, the yield function (2.32) is equal to zero under plastic loading so that $\tau + S = \tau_0$ in the absence of classical hardening. The critical resolved shear stress $\tau_0(T)$

http://www.zset-software.com/
with appropriate choice of the orientation of slip direction vector $\underline{m}$ so that $\tau > 0$.

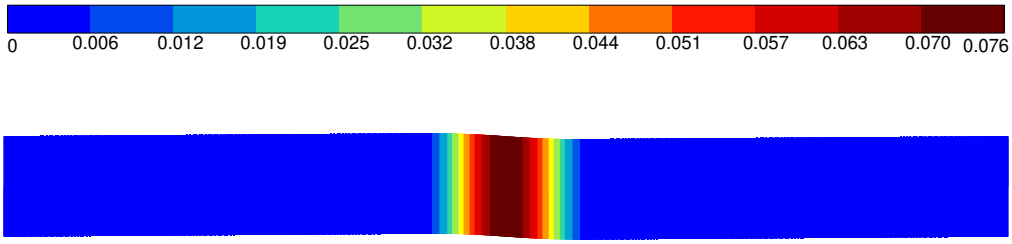

(a)

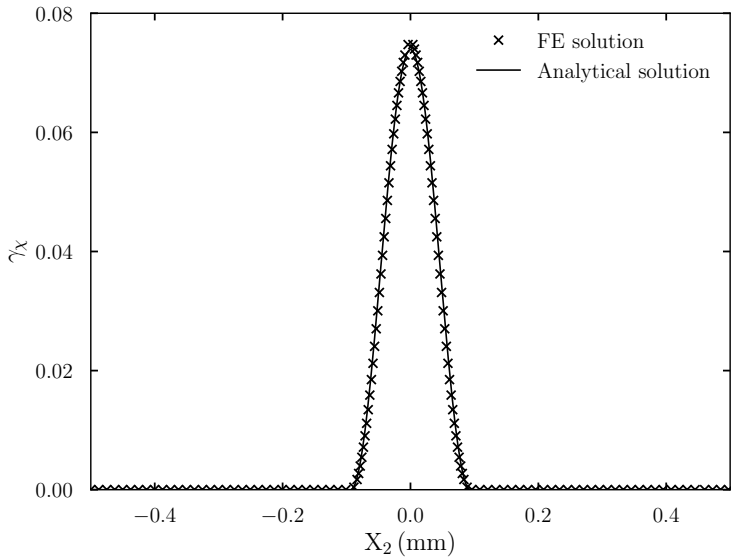

(b)

Fig. 4.2 (a) Contour plot of cumulative plastic strain γ_{cum} in a single-slip simple shear test with linear strain softening using the micromorphic crystal plasticity model ($H = -45$MPa, A=0.04N). (b) Comparison of FE solution with the analytical solution for the variation of γ_χ along X_2 at $\bar{F}_{12} = 0.01$.

is a function of temperature. An affine dependence is chosen for this analytical example

$$\tau_0 = \tau_{RT} + H_T(T - T_{RT}), \tag{4.57}$$

where $H_T < 0$ is the negative slope of the linear variation of τ_0 with temperature, T_{RT} is the room temperature and τ_{RT} is the critical resolved shear stress (CRSS) value at room temperature. Then, Eq. (4.56) becomes

$$\dot{T} = \frac{\tau_0 \dot{\gamma}}{\rho C_\varepsilon}. \tag{4.58}$$

In order to obtain a simple analytic solution for the temperature, τ_0 is approximated by the constant value: $\hat{\tau}_0 = \tau_{RT} + H_T(T_i - T_{RT})$ where T_i is some initial temperature value. In that conditions, the previous equation can be integrated, assuming monotonic loading, which leads to the following form of the temperature rise:

$$T = \frac{\tau_0 \gamma}{\rho C_\varepsilon} + T_i, \quad \text{when} \quad \gamma = 0, \quad T = T_i. \tag{4.59}$$

The yield condition (2.32), which includes the temperature dependent softening can now be written as follows:

$$f = |\tau| - (\hat{\tau}_0(1 + \frac{H_T \gamma}{\rho C_\varepsilon}) + H_\chi(\gamma - \gamma_\chi)) = 0. \tag{4.60}$$

Combining (4.46) and (4.60) leads to the same partial differential equation governing the microslip variable as (4.47) provided that τ_0 is replaced by $\hat{\tau}_0$ and the hardening modulus H has the following definition

$$H \equiv \frac{H_T \tau_0}{\rho C_\varepsilon}. \tag{4.61}$$

The solution of the PDE (4.47) still has the form (4.50) where the constants λ and κ are given by Eq. (4.49) with the new definition of H and $\tau_0 \equiv \hat{\tau}_0$.

This approximate solution is now compared to the FE prediction. For that purpose, the evolution of the temperature driven by the adiabatic condition (4.38) is numerically integrated in the code by means of a second order Runge-Kutta method with automatic time stepping Besson (2009). The material parameters used for the FE solution with the linear thermal softening are given in Table 4.2. The value of H_T has been chosen so that the associated modulus given by (4.61) takes the same value $H = -45$ MPa as in the example of linear strain softening, see Section 4.3.2.

In the FE analysis, no approximation is introduced and the CRSS has the temperature dependent expression (4.57). The cumulative plastic strain and temperature fields predicted by the micromorphic crystal plasticity model with linear thermal softening are shown in Fig. 4.3a and 4.3b, respectively. The temperature evolution due to *adiabatic* heating is considered as in the *case 2* presented in section 4.2.3, cf. Eq. (4.38). The comparison of the

Table 4.2 Numerical values of the material parameters used in the simulations of single-slip periodic strip undergoing simple shear with thermal softening using the micromorphic crystal plasticity model.

C_{11}	C_{12}	C_{44}	H_χ Eq. (4.60)	H_T Eq. (4.60)	T_{RT}
208.1 MPa	144.7 MPa	97.6 MPa	10^3 MPa	-0.48 MPaK^{-1}	293 K
τ_{RT}	τ_{1523K}	A	T_i	ρ Eq. (4.58)	C_ε Eq. (4.58)
606 MPa	10 MPa	0.04 N	923 K	7.8×10^{-6} kg mm^{-3}	412 Jkg^{-1}K^{-1}

FE solution for γ_χ variation with the approximate analytical solution obtained from Eq. (4.50) is displayed in Fig. 4.3c at $\bar{F}_{12} = 0.01$. The analytically calculated and numerically simulated width of the deformation zone is 2.6λ, which is equal to the value obtained with linear strain softening. This is due to the fact that the temperature softening modulus H_T has been chosen so that the equivalent modulus H is the same as the softening modulus used in Section 4.3.2. The approximation of τ_0 by $\hat{\tau}_0$ in the analytical solution does not lead to significant differences compared to the full FE solution, due to the fact that the temperature changes remain limited, see Fig. 4.3cb. The limited heating was however sufficient to trigger plastic strain localization.

This study shows that the analytical solution initially developed for the rate-independent case for the linear strain softening can be used in the linear thermal softening case after establishing a relation between the slope of the linear variation of the CRSS with respect to temperature, H_T, and an equivalent linear strain softening modulus H. Furthermore, the FE implementation with linear strain, and thermal softening has been validated by means of this analytical solution.

4.4 Application to single crystals hat-shaped specimens

This section presents the application of the proposed thermo-mechanical micromorphic constitutive framework to single crystal hat-shaped specimens. The aim is to investigate the effects of initial crystal orientation on the formation and orientation of adiabatic shear bands. The material behavior considered in the simulations is elastic-perfectly plastic, and the material parameters correspond to nickel-based super-alloy Inconel 718. Furthermore, the temperature evolution due to *adiabatic* heating is considered as in the *case 2* presented in section 4.2.3 (Eq. (4.38)).

The outline of this section is as follows. The temperature-dependent material parameters of Inconel 718 are summarized in section 4.4.1. The criteria for the selection of gradient parameters (A and H_χ) are given in section 4.4.2. Then, the geometry, boundary conditions and considered crystal orientations are presented in section 4.4.3. In section 4.4.4, mesh

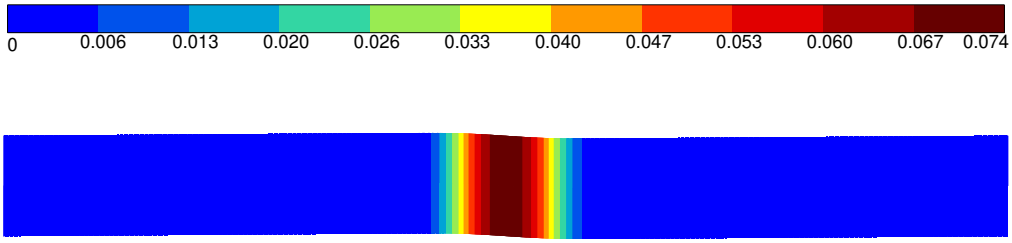

(a)

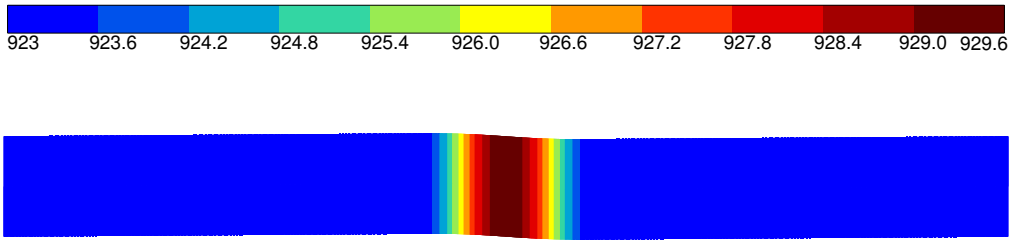

(b)

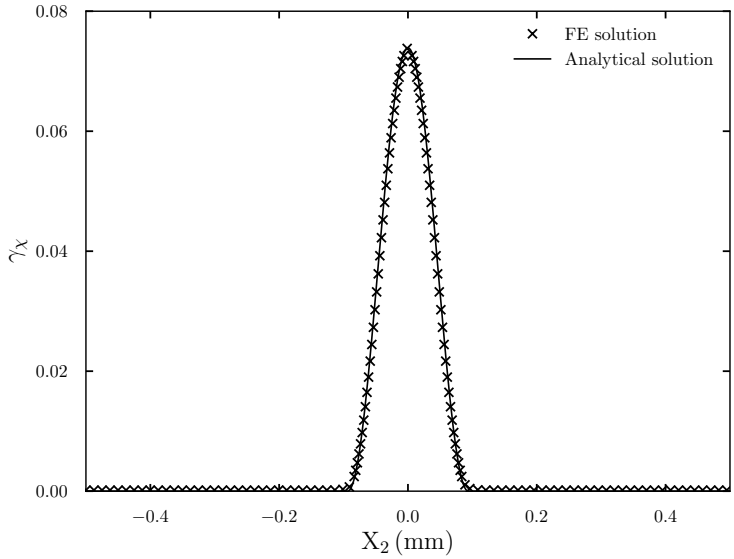

(c)

Fig. 4.3 Contour plots of (a) cumulative plastic strain γ_{cum}, and (b) temperature in the single-slip simple shear test with thermal softening using the micromorphic crystal plasticity model (T_i=923 K, A=0.04 N) subjected to *adiabatic* heating. (c) Comparison of the FE solution obtained using the micromorphic crystal plasticity model with the analytical solution for the variation of microslip variable γ_χ along X_2 at $\bar{F}_{12} = 0.01$.

sensitivity analysis is performed with the classical and micromorphic crystal plasticity models. Results and discussion follow in section 4.4.5.

4.4.1 Material properties of Inconel 718

The temperature-dependent material parameters considered in this paper correspond to Nickel-based superalloy Inconel 718 in a large temperature range. The characterization of high strain rate compressive loading behavior within a wide range of temperature for Inconel 718 was performed in (Iturbe et al., 2017). In this paper, the material properties investigated are in the temperature range of $294-1323$ K, close to those found in machining at high strain rates ($1-100$ s^{-1}). The stress-strain behavior of Inconel 718 in the temperature range of $294-1323$ K (strain rate = 1 s^{-1}) and variation of the yield strength (YS) and ultimate tensile strength (UTS) with respect to the temperature are shown in Fig. 4.4a and Fig. 4.4b, respectively. In general, the flow stress of Inconel 718 increases with increasing strain rate and decreasing temperature. It can be seen from Fig. 4.4b that the strength of the material decreases with increasing temperature at a specified strain rate. This thermal softening behavior is not very noticeable until the temperature of 923 K.

The material parameters τ_0, K, and m are identified against the experimental stress-strain curves obtained from the work of (Iturbe et al., 2017) with simple tension tests performed on a single Gauss point using the classical crystal plasticity model presented in section 4.2. The material constants used in the numerical simulations are presented in Table 4.3. Moreover, the material parameters τ_0, K, and m are introduced as functions of temperature in the present simulations as given in Table 4.4. Linear interpolation is used for temperature values other than those listed in the table. For simplicity, elasticity moduli are taken as temperature independent since their variation is not the main driving force for shear banding. A typical value of 1550 K is considered for the melting temperature.

The thermodynamically consistent framework of the constitutive equations for the micromorphic crystal plasticity model presented in this work can predict a more realistic temperature rise in line with the experimental measurements in the case of elasto-plastic material behavior. With consideration of elasto-plastic material behavior, including strain-hardening, the stored energy rate term in Eq. (4.37) will significantly contribute to temperature evolution under adiabatic conditions. It is common practice to assume a constant value 0.9 of the Taylor-Quinney parameter. However, in reality, its value can be much less than 0.9. This framework with work-hardening will allow for evolving Taylor-Quinney parameters predicted by suitable free energy density functions. The present work is limited to no-hardening crystals for the sake of simplicity. Evolution equations for dislocation densities were used in the micromorphic model by Ling et al. (2018) and could also be considered in the hat-shaped specimen tests.

Table 4.3 Values of the material parameters used in the single crystalline and polycrystalline hat-shaped specimen simulations.

C_{11}	C_{12}	C_{44}	H_χ	A
208.1 MPa	144.7 MPa	97.6 MPa	10^3 MPa	0.004 - 0.04 N
T_{RT}	T_i	ρ Eq. (4.38)	C_ε Eq. (4.38)	
293 K	923 K	$7.8\times10^{-6}\,\mathrm{kg\,mm^{-3}}$	$412\,\mathrm{Jkg^{-1}K^{-1}}$	

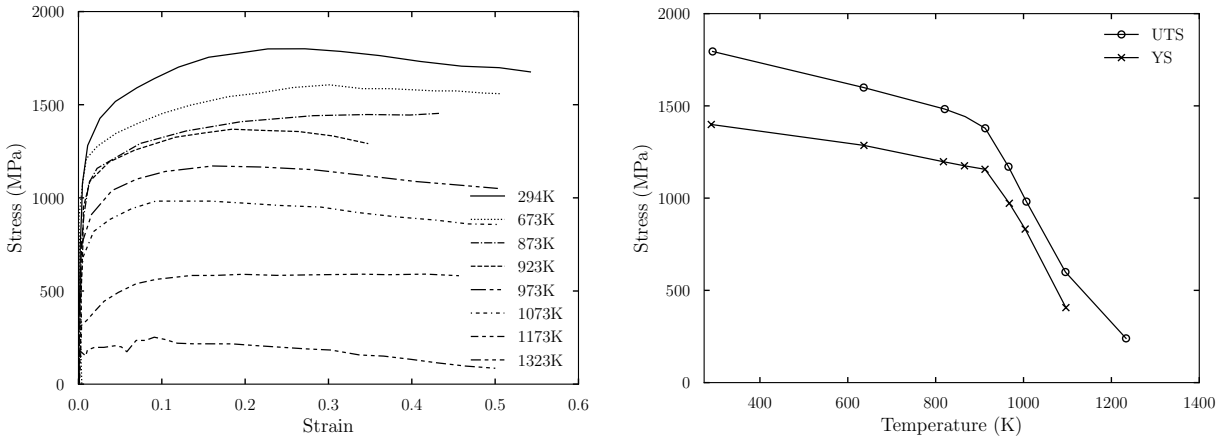

(a) (b)

Fig. 4.4 Influence of the temperature on (a) stress-strain behavior (b) yield strength and ultimate tensile strength of the Inconel 718 when compressed at a strain rate of 1 s^{-1} (Iturbe et al., 2017).

Table 4.4 Temperature dependent material parameters used in the single crystalline and polycrystalline hat-shaped specimen simulations. These parameters are related to the strain rate range of $0.1\,s^{-1}$ to $1\,s^{-1}$.

Temperature (K)	τ_0 (MPa) Eq. (4.57)	K (MPa.s$^{1/m}$) Eq. (2.12)	m Eq. (2.12)
298	570	5	15
923	520	5	15
1073	340	8	10
1173	170	20	5.5
1323	61	35	4
1523	10	50	2

4.4.2 Selection of the gradient parameters A and H_χ

The characteristic length scale emerges in the development of shear bands and is related to their width. The width of the shear band is finite and set by the material microstructure. In general, this characteristic length scale differs depending on the specific localization pattern observed for the particular boundary-value problem considered. The width of the shear band exhibited by the solution of the multislip boundary-value problems is generally linked to the characteristic length scale ℓ defined as

$$\ell = \sqrt{\frac{A(H + H_\chi)}{|H|H_\chi}}. \tag{4.62}$$

This definition is taken from the simple localization analysis of Section 4.3.1 and involves the coupling modulus H_χ, the higher order modulus A, and the strain softening modulus H. Moreover, the size effects in crystal plasticity occur at a scale ranging from hundreds of nanometers to a few tens of microns. This sets bounds for the values of the chosen characteristic length scale of the model. Usually, the coupling modulus H_χ is chosen large enough so that the cumulative plastic strain γ_{cum} and microslip variable γ_χ almost coincide. In that case, the micromorphic model can be regarded as an actual strain gradient plasticity model. On the other hand, the micromorphic model response saturates for smaller sizes if the chosen value of H_χ is not large enough as demonstrated for single crystal microwire torsion test simulations in (Scherer et al., 2020) and in polycrystal simulations when d_{avg} is of the order of or smaller than ℓ (Cordero et al., 2012a). When the average grain size $d_{avg} \gg \ell$, strain gradient effects vanish and the deformation field predicted by the micromorphic crystal plasticity model is almost identical to that of the classical crystal plasticity model. The gradient parameter A controls the width of the shear band in strain localization problem. Based on these requirements, the gradient parameters A and H_χ are chosen such that the width of formed shear band in the single crystal simulations remains always smaller than horizontal shift of the corners which is 0.1 mm. On the other hand, the gradient parameters are such that ℓ is of the order of the smallest grain size to be considered in the shear region in polycrystalline simulations. Two values of the gradient parameter A, 0.004 N, and 0.04 N are chosen for the analysis which satisfy the aforementioned conditions. Moreover, the selected value of H_χ is 10^3 MPa. It has been checked to be high enough to get values of e_p sufficiently close to zero, and in the mean time small enough to avoid numerical problems associated with ill-conditioned matrices in the presence of penalty terms.

4.4.3 Simulation setup, slip systems, and initial crystal orientations

In the first part of the study, shear tests of single crystal hat-shaped specimens are performed to investigate the development of ASB in the post-localization regime. The shape and geometry of the hat-shaped specimen promote shear failure even in materials which are not

Table 4.5 Initial crystal orientations used in the single crystal hat-shaped specimen simulations.

Crystal orientations	Short notation
[100]-[010]-[001]	[100]-[010]
[110]-[001]-[1$\bar{1}$0]	[110]-[001]
[001]-[110]-[1$\bar{1}$0]	[001]-[110]
[$\bar{1}\bar{1}$2]-[111]-[1$\bar{1}$0]	[$\bar{1}\bar{1}$2]-[111]
[111]-[$\bar{1}\bar{1}$2]-[1$\bar{1}$0]	[111]-[$\bar{1}\bar{1}$2]

sensitive to shear localization (Peirs et al., 2008). A symmetric hat-shaped specimen under plane strain condition with one element along the thickness of 0.025 mm is considered for the study. In practice, axi-symmetric geometries are often used but their analysis would require too large 3D simulations in the case of polycrystals considered in the present work. The geometry, dimensions, and the applied boundary conditions of the specimen are shown in Fig. 4.5. The height of the shear zone is $h = 1$ mm. The corners of the shear region are rounded with a radius of $R = 0.05$ mm. Rounded corners allow for the reduction of stress concentration and postpone strain localization (Peirs et al., 2008). Note that the geometry is such that there is an horizontal shift of 0.1 mm between the two corners, see Fig. 4.5. The FE mesh of this geometry is made of 20 node brick elements with reduced integration (C3D20R). The macroscopic strain rate which the specimens are subjected to in the numerical simulations is defined a $\Delta U/h\Delta t$, where ΔU is the relative displacement linearly applied during the test duration of Δt. It has the value of $0.1\,\mathrm{s}^{-1}$.

The five different initial crystal orientations investigated in the study are given in Table 4.5. The crystal orientations are defined with respect to the basis frame $\underline{e}_1\underline{e}_2\underline{e}_3$, with $\underline{e}_2$ being in the direction of applied load and $\underline{e}_3$ in the direction normal to the plane. For instance, the single crystal orientation [100] – [010] – [001] is such that the axes of the specimen are

$$\underline{e}_1 = [100] \quad \underline{e}_2 = [010] \quad \underline{e}_3 = [001],$$

as shown in Fig. 4.5. For the sake of simplicity, crystal orientations are represented only by the basis plane $\underline{e}_1 - \underline{e}_2$ (see Table 4.5) in the following sections. The definition of the octahedral slip systems in FCC lattice structure is specified in Table A.1.

4.4.4 Mesh sensitivity analysis

Three distinct mesh discretizations in the shear region with 66720, 88560, and 135540 nodes shown in Fig. 4.6 are used to investigate the effect of mesh density on the normalized load–displacement curves and the shear band structure. The load and displacements are normalized by the height of the shear region $h = 1$ mm. The simulations are performed

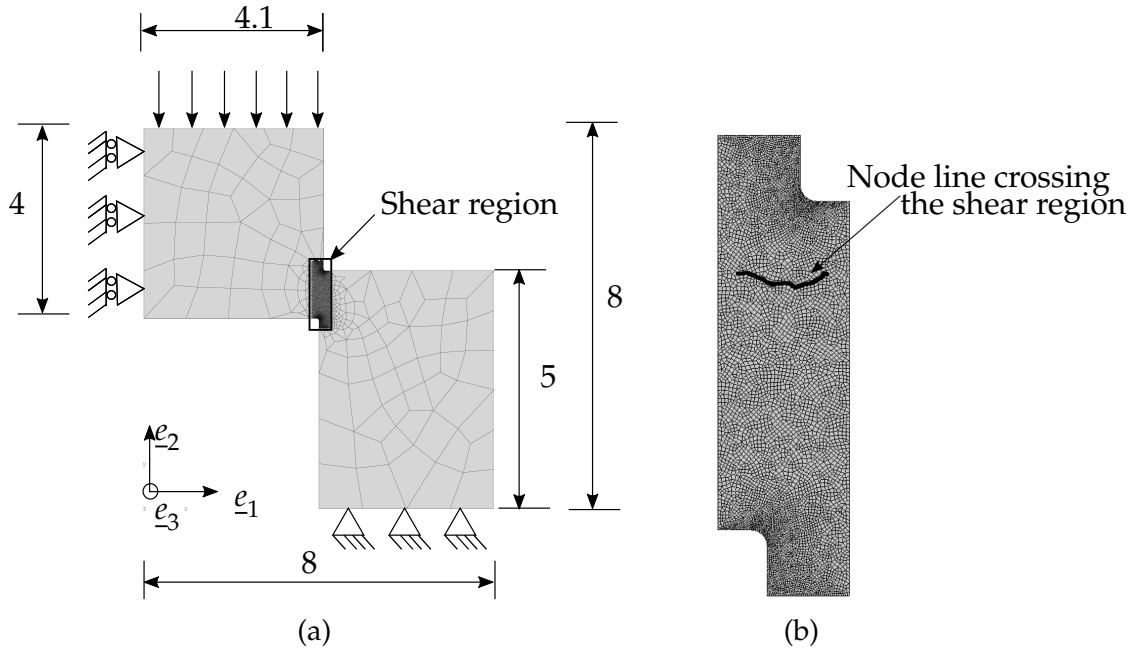

Fig. 4.5 Hat-shaped specimen: (a) geometry, boundary conditions and FE mesh (all dimensions are in mm). (b) Zoom at the shear region: mesh in the shear region; the black line on the figure denotes a line of nodes of the FE mesh crossing the shear region along which the cumulative plastic strain and temperature fields will be plotted.

with the classical and micromorphic crystal plasticity models with *adiabatic* heating for [001] – [110] initial crystal orientation. The initial temperature, T_i, of the specimens is assumed to be 923 K. The limitation of the classical crystal plasticity model, namely the mesh size dependency in strain localization problems, is demonstrated by Fig. 4.7a. The load-displacement curves with the classical crystal plasticity model are different for the three discretizations and do not converge upon mesh refinement as demonstrated in Fig. 4.7a. In contrast, the load-displacement curves with the micromorphic crystal plasticity model for three discretizations are almost the same and converge upon mesh refinement as shown in Fig. 4.7b. The cumulative plastic strain fields and corresponding deformed geometries for the three discretizations with the classical and the micromorphic crystal plasticity models are shown in Fig. 4.8a and 4.8b, respectively. The formed shear bands width with the classical crystal plasticity model exhibits well-known pathological mesh dependency, which always collapses to one element size irrespective of the mesh size. In contrast, with the micromorphic crystal plasticity model, the width of the formed shear band is finite and independent of used spatial discretization. This suggests that the 88560 nodes in the shear region are sufficient to produce mesh-independent results. However, discretization with 135540 nodes in the shear region is used for further investigations.

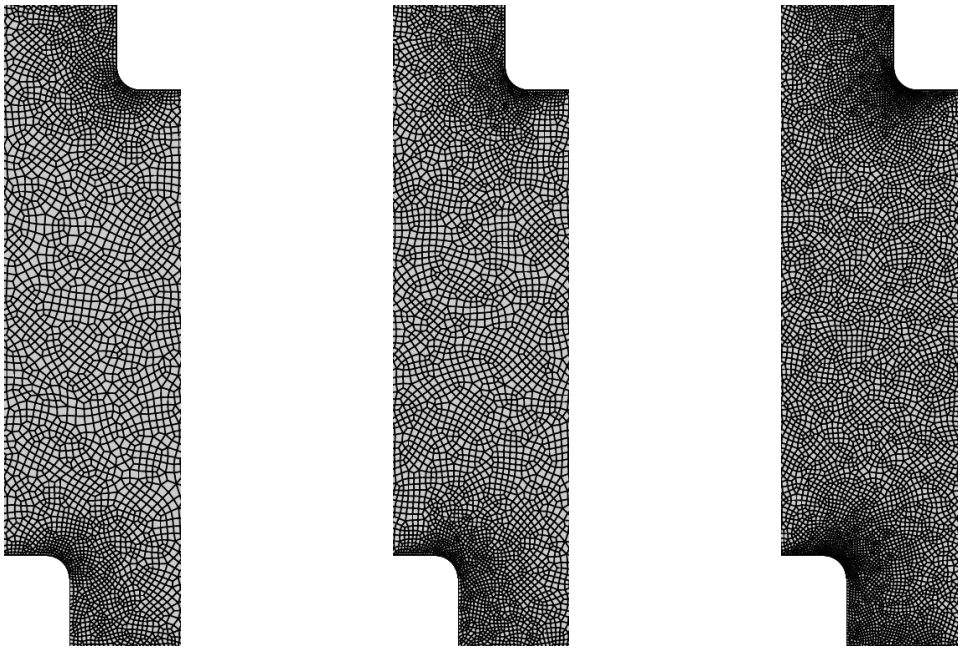

(a) (b) (c)

Fig. 4.6 Three discretizations in the shear region used for the mesh sensitivity analysis with (a) 66720, (b) 88560, and (c) 135540 nodes.

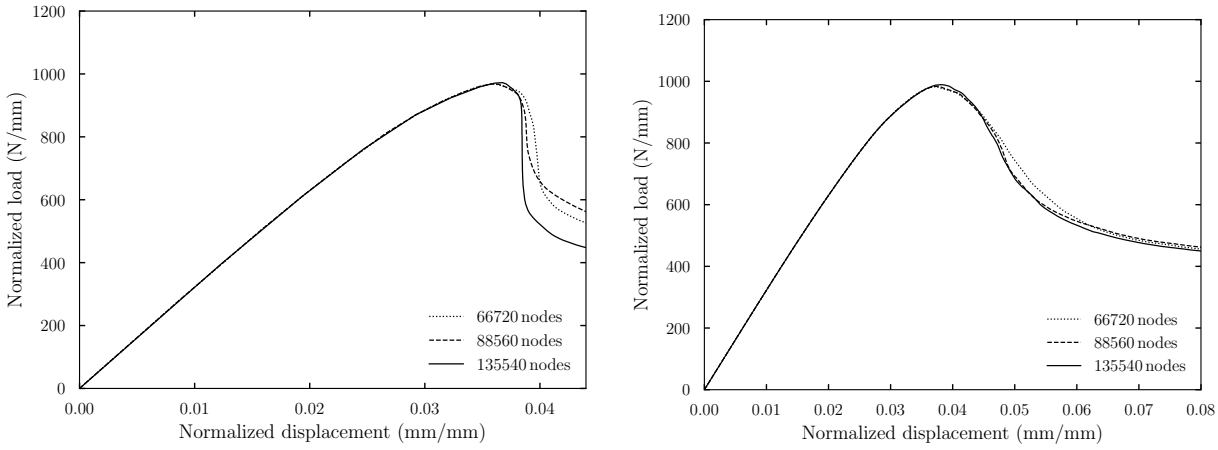

(a) (b)

Fig. 4.7 Load-displacement curves for [001] – [110] initially oriented crystal subjected to *adiabatic* heating (T_i =923 K) for three discretizations using the (a) classical crystal plasticity model (b) micromorphic crystal plasticity model (A = 0.004 N).

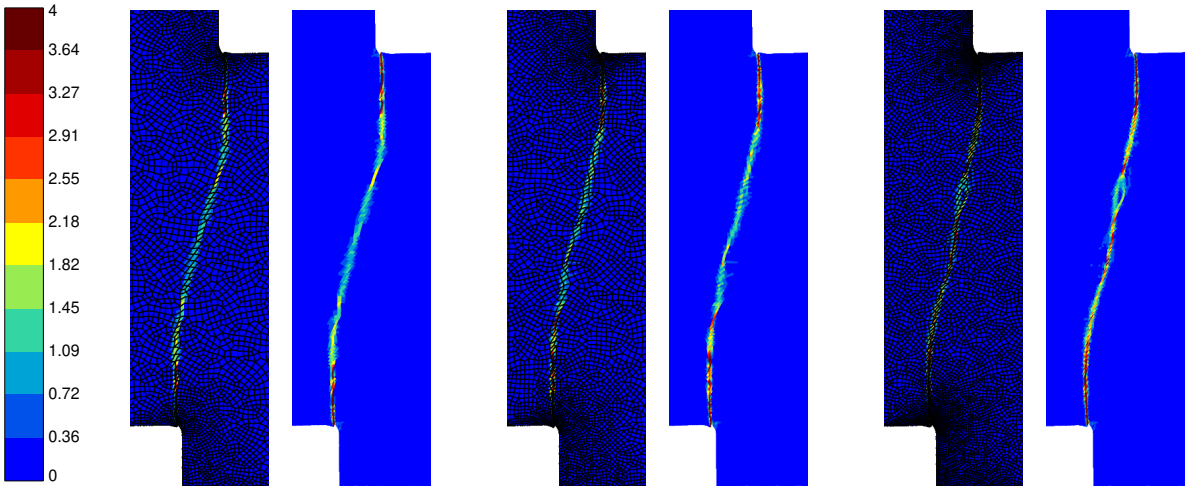

(a)

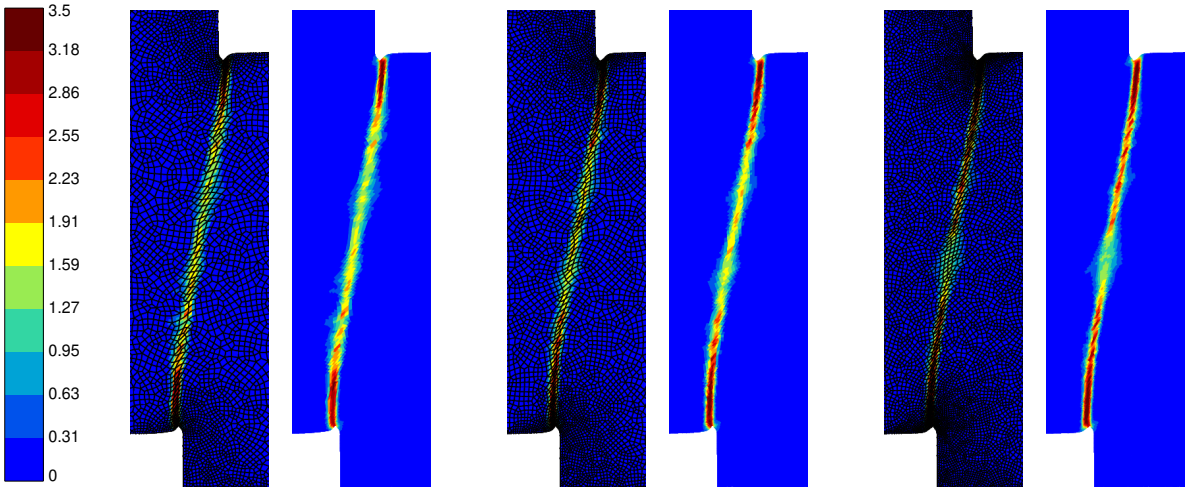

(b)

Fig. 4.8 Contour plots of cumulative plastic strain γ_{cum} for [001] – [110] initially oriented crystal with three discretizations (66720, 88560, and 135540 nodes in the shear region) subjected to *adiabatic* heating using the (a) classical crystal plasticity model, and (b) micromorphic crystal plasticity model (A = 0.004 N) at a normalized displacement of 0.041 mm/mm and T_i =923 K, with and without showing the mesh.

4.4.5 Results and discussion

4.4.5.1 Slip system activity

The activated slip systems for different initially oriented crystals are listed in Table 4.6 as significant plastic deformation occurs on these slip systems. Numerically, the activated slip systems are identified when the shear band is fully formed and before the temperature within the band reaches the melting temperature. The four activated slip systems ($B4, D1, A2$ and $C3$) for [100] – [010] initially oriented crystal are neither co-planar nor co-directional to each other and show identical absolute slip rates ($|\dot{\gamma}^{B4}|=|\dot{\gamma}^{D1}|=|\dot{\gamma}^{A2}|=|\dot{\gamma}^{C3}|$). For [110] – [001] initially oriented crystal, one pair of co-directional ($C3$ and $C1$, $|\dot{\gamma}^{C3}|=|\dot{\gamma}^{C1}|$) and one pair of co-planar ($D6$ and $A6$, $|\dot{\gamma}^{D6}|=|\dot{\gamma}^{A6}|$) slip systems are activated, while in [001] – [110] initially oriented crystal, one pair of co-directional ($D6, A6$, $|\dot{\gamma}^{D6}|=|\dot{\gamma}^{A6}|$) and two pairs of co-planar ($B4, B2$ $|\dot{\gamma}^{B4}|=|\dot{\gamma}^{B2}|$ and $C3, C1$, $|\dot{\gamma}^{C3}|=|\dot{\gamma}^{C1}|$) slip systems are activated. On the other hand, for both asymmetric initially oriented crystals, $[\bar{1}\bar{1}2]$-[111] and [111]-$[\bar{1}\bar{1}2]$ activated pairs of slip system are co-planar, ($B4, B2, C3, C1$, $|\dot{\gamma}^{B4}|=|\dot{\gamma}^{B2}| = |\dot{\gamma}^{C3}|=|\dot{\gamma}^{C1}|$) and ($B4, B2$, $|\dot{\gamma}^{B4}|=|\dot{\gamma}^{B2}|$), respectively.

4.4.5.2 Influence of initial crystal orientation on the shear band formation

Fig. 4.9 shows the load-displacement curves for five different crystal orientations. The resulting load on the hat-shaped specimen increases to its peak value, and then drops abruptly from its peak value as a consequence of thermal softening inside the bands. Furthermore, it is observed that the initiation of shear band is orientation-dependent. The normalized displacement needed for the initiation of shear band for the asymmetric crystal orientations $[\bar{1}\bar{1}2]$ – [111] and [111] – $[\bar{1}\bar{1}2]$ is lower than that for the symmetric crystal orientations [100] – [010], [001] – [110] and [110] – [001] (see Fig. 4.9). The evolution of the cumulative plastic strain within shear bands at various deformation stages is shown in Fig. 4.10 for [001] – [110] crystal orientation at the normalized displacement values of 0.04, 0.045, 0.050 and 0.055. The onset of ASB is observed at the specimen's corner at a normalized displacement of 0.04. It propagates from the corners with further increase in deformation, and the shear band is fully formed at a normalized displacement of 0.055.

The cumulative plastic strain and temperature fields in the single crystals hat-shaped specimens for five different initial crystal orientations are shown in Fig. 4.11 and 4.12, respectively. High values are observed at the corners of the specimens and lower ones at the center of the sheared region. The simulation results show that the formation and orientation of the ASB with respect to the loading axis significantly depends on the initial crystal orientation. The [100] – [010] initial crystal orientation shows a stiffer response to the shear banding than the other ones. A remarkable feature is that no shear band forms connecting the corners. Instead, two parallel shear bands tend to form, oriented at an angle of about 16° clockwise with respect to the loading axis. With further straining, only one shear band remains. This band does not seem to have a crystallographic nature

Table 4.6 Slip systems activity inside the ASB in single crystal hat-shaped specimens.

Crystal orientations	Activated slip systems
[100]-[010]	B4,D1,A2,C3
[110]-[001]	D6,A6,C3,C1
[001]-[110]	B4,B2,D6,A6,C3,C1
$[\bar{1}\bar{1}2]$-[111]	B4,B2,C3,C1
[111]-$[\bar{1}\bar{1}2]$	B4,B2

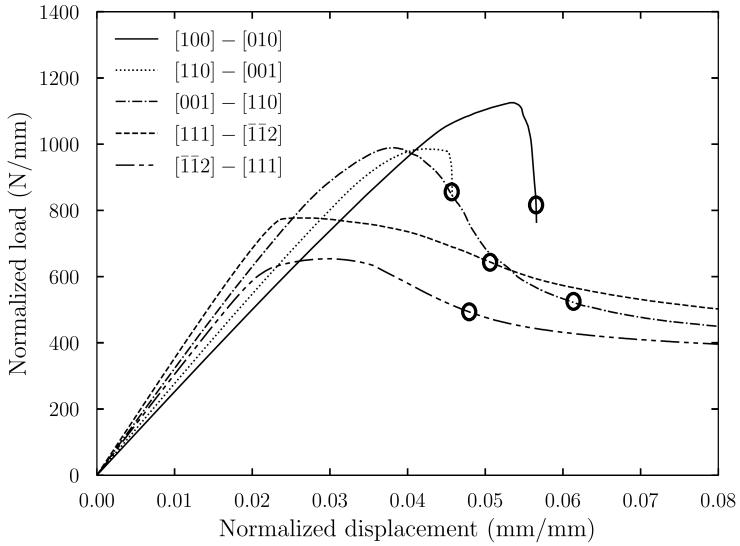

Fig. 4.9 Load-displacement curves for five different crystal orientations subjected to *adiabatic* heating using the micromorphic crystal plasticity model (T_i = 923 K, A = 0.004 N). Circles on the plot are corresponding to the normalized displacement at which cumulative plastic strain, temperature and lattice rotation fields shown next are plotted.

because the activated slip systems are neither co-planar nor co-directional. This particular situation does not favor the shear band formation. On the other hand, activated pairs of co-planar and co-directional slip systems in $[001]-[110]$, $[110]-[001]$ and $[\bar{1}\bar{1}2]-[111]$ favor the shear band formation. The initially oriented crystal $[111]-[\bar{1}\bar{1}2]$, exhibits the lowest tendency to shear band formation, and no evident shear banding is observed prior to melting temperature as it promotes less octahedral slip systems (only two slip systems are activated). On the other hand, distinct shear banding patterns are observed for the other four initially oriented crystals as it facilitates the activation of more numerous octahedral slip systems.

As the deformation becomes unstable and the shear band is fully formed, the plastic strain within the shear band increases with further deformation, but the gradient parameter A limits the width of the shear band. Fig. 4.13 show the γ_{cum} variation along the node line crossing the shear region of Fig. 4.5 when the shear band is fully formed for different initial crystal orientations. The band width w is defined as the width of the shear region surrounding the band center over which the cumulative plastic strain remains larger than 10% of the its peak value (Batra and Chen, 2001). Moreover, the observed width of the shear band is also orientation-dependent. The observed widths of the shear band from Fig. 4.13a in symmetric crystal orientations $[100]-[010]$, $[110]-[001]$ and $[001]-[110]$ using gradient parameter A of 0.004 N are 0.05 mm, 0.075 mm and 0.08 mm, respectively. On the other hand, for both asymmetric crystal orientations $[\bar{1}\bar{1}2]-[111]$ and $[111]-[\bar{1}\bar{1}2]$ the observed width is 0.075 mm (see Fig. 4.13b). In addition, the predicted temperature fields and variation of temperature across the node line crossing the shear region is shown in Fig. 4.12 and 4.14. The peak temperature is observed at the center of the shear band.

4.4.5.3 Lattice rotation fields

Non-homogeneous plastic strain fields are usually accompanied with significant lattice rotation. The non-uniform lattice rotation in strain localization problems results in a local geometrical softening of the slip plane with which the shear band is aligned according to (Chang and Asaro, 1980; Lisiecki et al., 1982). Shear band formation is therefore possible even in work-hardening materials due to such geometric softening (Dillamore et al., 1979). Strain softening and non-homogeneous lattice rotations induce instabilities in the plastic deformation. The formation of deformation bands in crystalline materials is very often associated with lattice rotations. The lattice rotation angle ϕ_L can be measured using the polar decomposition of the elastic part of the deformation gradient $\underset{\sim}{F}^e$ into elastic rotation tensor $\underset{\sim}{R}^e$ and the elastic right stretch tensor $\underset{\sim}{U}^e$ as $\underset{\sim}{F}^e = \underset{\sim}{R}^e \cdot \underset{\sim}{U}^e$. For small elastic distortions usual in metals, the elastic rotation tensor $\underset{\sim}{R}^e$ is interpreted as the lattice rotation. The corresponding lattice rotation angle ϕ_L is computed as

$$\phi_L = \arccos\Big[\frac{1}{2}\Big(\mathrm{tr}(\underset{\sim}{R}^e) - \underset{\sim}{1}\Big)\Big]. \tag{4.63}$$

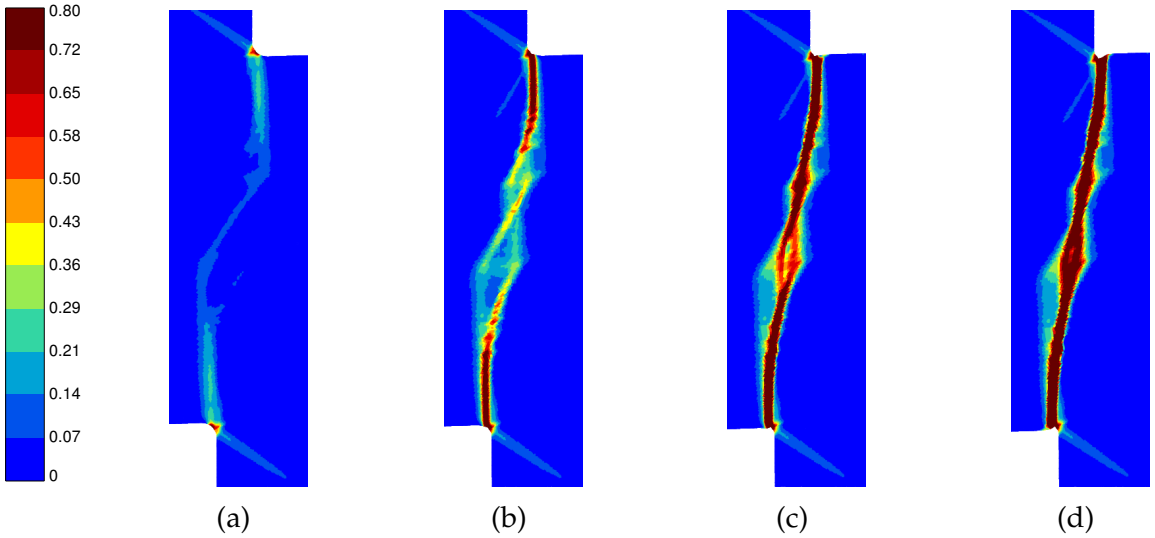

Fig. 4.10 Contour plots of cumulative plastic strain at different stages showing the shear band formation with adiabatic heating using the micromorphic crystal plasticity model ([001] – [110] crystal orientation, T_i = 923 K, A = 0.004 N) at normalized displacements of (a) 0.04 mm/mm, (b) 0.045 mm/mm, (c) 0.050 mm/mm, and (d) 0.055 mm/mm.

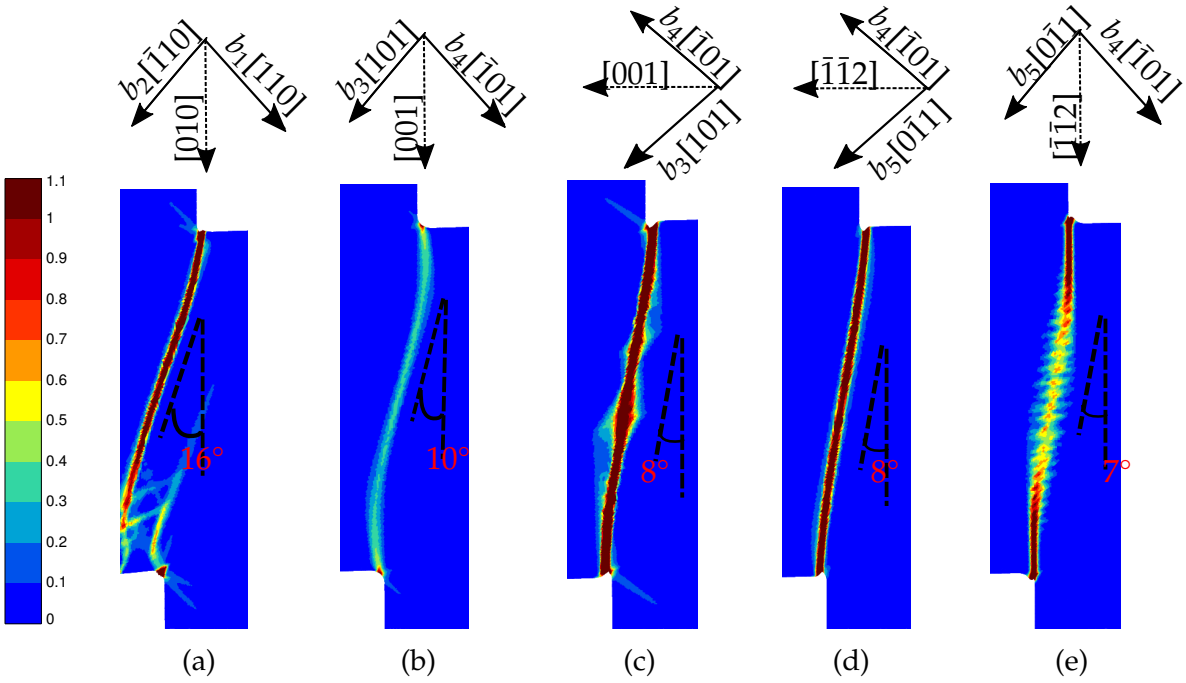

Fig. 4.11 Contour plots of cumulative plastic strain γ_{cum} in the shear region with *adiabatic* heating using the micromorphic crystal plasticity model (T_i = 923 K, A = 0.004 N) for (a) [100] – [010], (b) [110] – [001], (c) [001] – [110], (d) $[\bar{1}\bar{1}2]$ – [111], and (e) [111] – $[\bar{1}\bar{1}2]$ initially oriented crystals. The fields are shown at loading steps corresponding to the circles in Fig. 4.9. Compensation of the loading direction by Burgers vector of the activated slip systems is also shown.

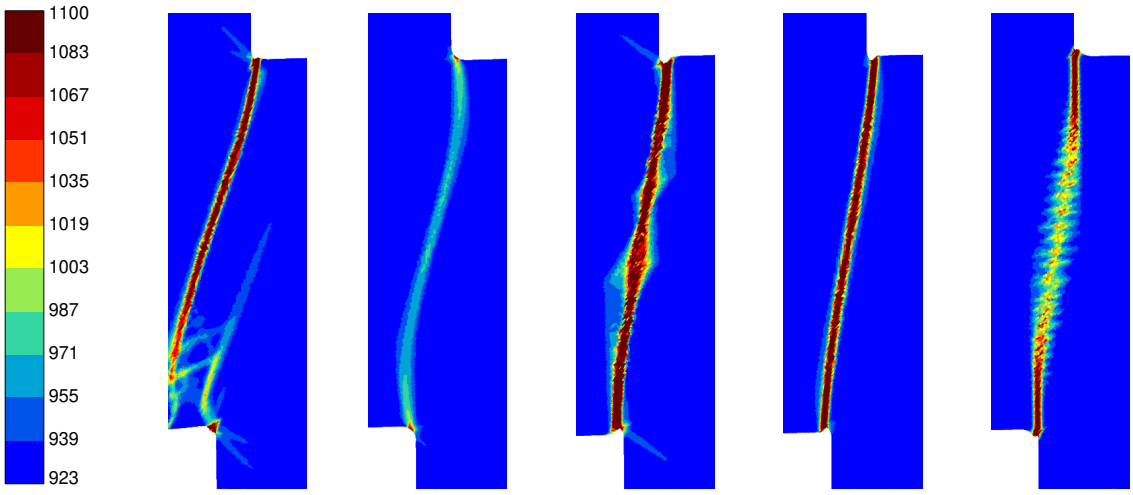

Fig. 4.12 Contour plots of temperature using the micromorphic crystal plasticity model (T_i = 923 K, A = 0.004 N) in the shear region for (a) [100] – [010], (b) [110] – [001], (c) [001] – [110], (d) $[\bar{1}\bar{1}2]$ – [111], and (e) [111] – $[\bar{1}\bar{1}2]$ initially oriented crystals. The fields are shown at the loading steps corresponding to the circles in Fig. 4.9.

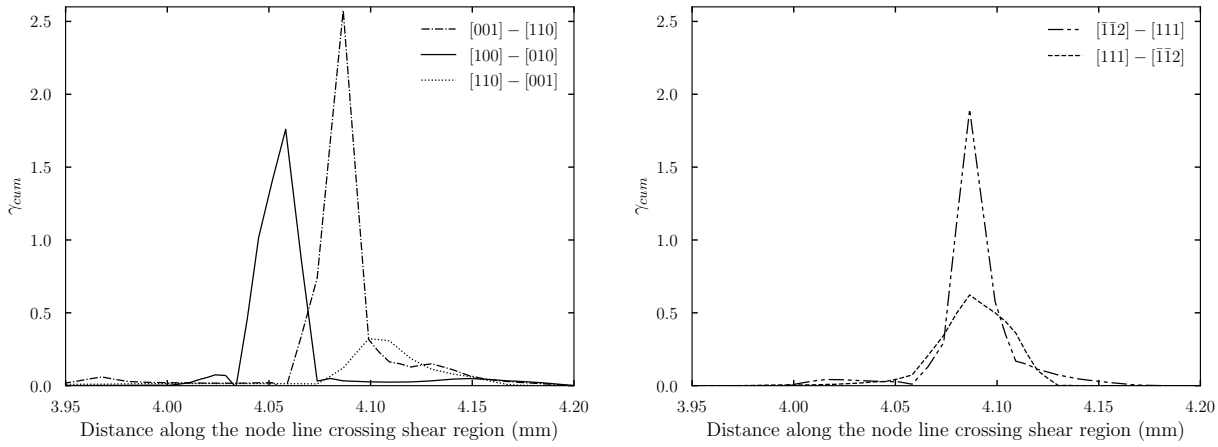

Fig. 4.13 Cumulative plastic strain variation along the node line crossing the shear region (see Fig. 4.5) with *adiabatic* heating using the micromorphic crystal plasticity model (T_i = 923 K, A = 0.004 N) for (a) symmetric, and (b) asymmetric crystal orientations. The variation of cumulative plastic strain is plotted at loading steps corresponding to the circles in Fig. 4.9.

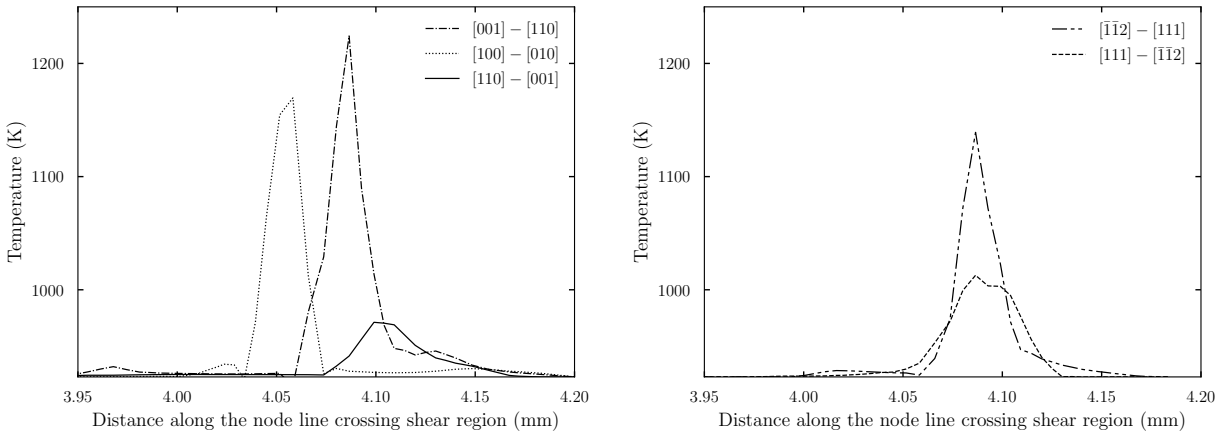

(a) (b)

Fig. 4.14 Temperature variation along the node line crossing the shear region for (a) symmetric, and (b) asymmetric crystal orientations. The variation of temperature across the shear band is plotted at loading steps corresponding to the circles in Fig. 4.9.

The lattice rotation fields for the various initially oriented crystals are shown in Fig. 4.15. The rotation of crystal lattice in the fully formed shear band is different for each considered initially oriented crystal and increases with increase in deformation. The discontinuous lattice rotation field is observed in [001] – [110] and [111] – [$\bar{1}\bar{1}$2] initially oriented crystals as a consequence of the complex plastic strain fields observed in Fig. 4.11. In comparison, single lattice rotation bands with smaller magnitude are observed for the [100] – [010], [110] – [001] and [$\bar{1}\bar{1}$2] – [111] crystal orientations. Some lattice rotation field patterns are reminiscent of kink banding structures studied in (Marano et al., 2021) but the situation is more complicated in the shear bands due to the simultaneous activation of several slip systems.

4.4.5.4 Effect of the gradient parameter A on shear band structure

The cumulative plastic strain γ_{cum} fields and formed ASB for the three different values of the gradient parameter A are shown in Fig. 4.16. With a decreasing value of A, the severity of plastic strain localization within the shear band increases, and a significant thermal softening is observed in the post-localization regime (see Fig. 4.17a). The effect of parameter A on the width of the shear bands can be seen from Fig. 4.17b. As expected from the analytical expression of the characteristic length scale, Eq. (4.62), the width of the shear band decreases with decrease in A value. The observed widths of the shear band with three different values of A, 0.04 N, 0.02 N, and 0.004 N are found to be 0.085 mm, 0.07 mm, and 0.05 mm, respectively.

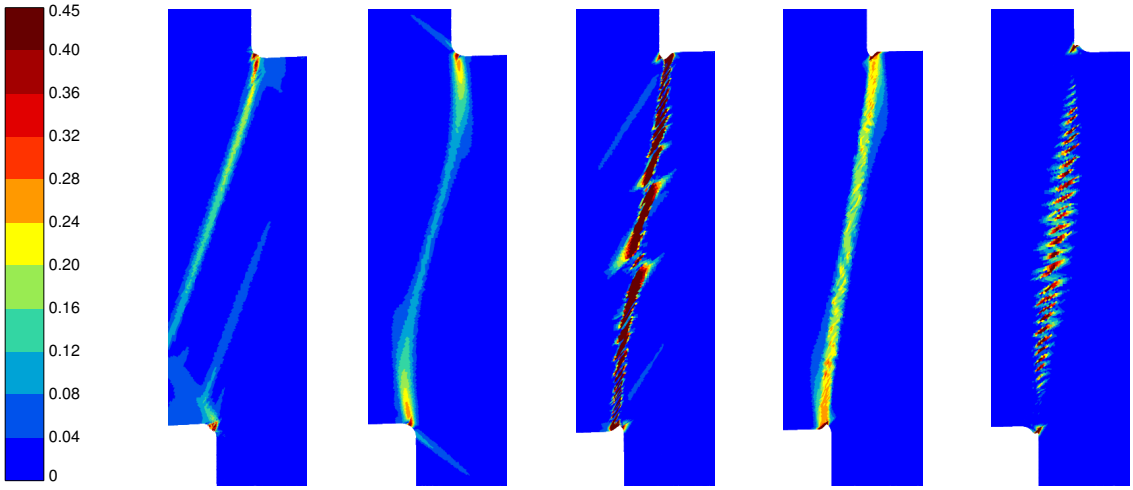

Fig. 4.15 Contour plots of lattice rotation fields in the shear region (T_i = 923 K, A = 0.004 N) for (a) [100] – [010], (b) [110] – [001], (c) [001] – [110], (d) $[\bar{1}\bar{1}2]$ – [111], and (e) [111] – $[\bar{1}\bar{1}2]$ initially oriented crystals subjected to *adiabatic* heating. Fields are shown at loading steps corresponding to the circles in Fig. 4.9.

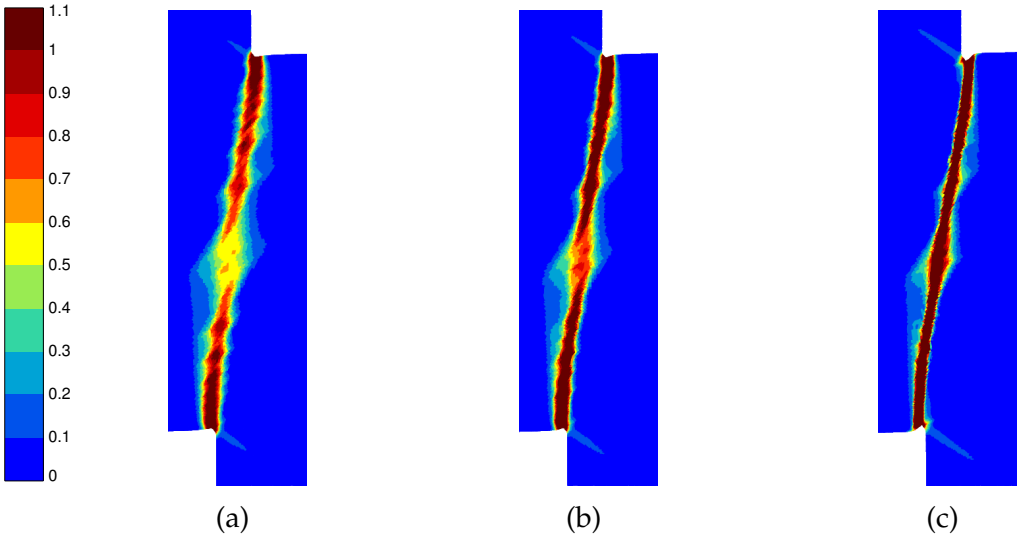

Fig. 4.16 Contour plots of cumulative plastic strain γ_{cum} using the micromorphic crystal plasticity model (T_i = 923 K) with three different values of (a) A = 0.04 N, (b) A = 0.02 N, and (c) A = 0.004 N. Fields are shown for the [001] – [110] initially oriented crystal subjected to *adiabatic* heating. Fields are shown at a normalized displacement of 0.06 mm/mm

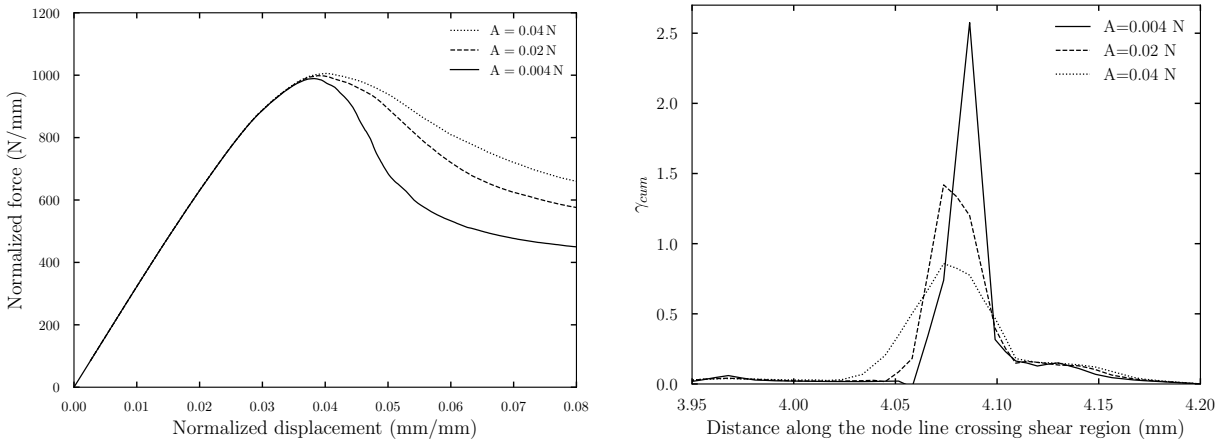

(a) (b)

Fig. 4.17 Effect of different values of the gradient parameter A on the (a) load-displacement curves, and (b) cumulative plastic strain γ_{cum} variation along the node line crossing the shear region for [001] – [110] initially oriented crystal plotted at a normalized displacement of 0.06 mm/mm.

4.5 Application to polycrystalline hat-shaped specimens

In this section, the micromorphic crystal plasticity model is applied to study the ASB formation in polycrystalline hat-shaped specimens. The single crystal constitutive behavior used in the numerical simulations is elastic-perfectly plastic and involves the same parameter values as in the previous sections. The material parameters used in the simulations are given in Table 4.3 and 4.4. First, orientation dependency of the shear band formation is investigated. Next, the grain size effect is predicted in the *isothermal* case. Then, the effect of *adiabatic* heating on the resulting load is evaluated for the considered polycrystalline aggregates. The temperature evolution due to *adiabatic* heating is computed using the expression in *case 2* presented in section 4.2.3 (Eq. (4.38)). Finally, the grain size effect on shear band width is predicted by the micromorphic model.

4.5.1 Polycrystal generation and finite element meshing

Polycrystalline aggregates generated by the Voronoï tessellation using the polycrystal generation package Neper (Quey and Renversade, 2018) are shown in Fig. 4.18 and 4.19. The application of Voronoï tessellation to create an actual geometry with the grains is a powerful tool to predict grain size effects, for example on the overall mechanical response of the material under deformation. Two polycrystalline aggregates, namely the *coarse-grained* and *fine-grained* with an average grain size of 0.80 mm and 0.15 mm, respectively, are generated. The smallest grain size in the shear region of the generated polycrystalline aggregates is 0.38 mm and 0.10 mm, respectively. Moreover, the pole figure showing the

crystallographic texture for each realization is plotted by means of the open-source software toolbox MTEX (Bachmann et al., 2010).

Mesh independent numerical results are ensured using fine enough mesh size within the grains of the shear region combined with the use of the micromorphic crystal plasticity model. Meshing is performed using an open-source package Gmsh (Geuzaine and Remacle, 2009). A bottom-up approach is used for the meshing, i.e. in the order of 0D, 1D, and 2D entities (i.e. vertices, edges, and polygons) for the 2D simulations under plane strain conditions (Quey et al., 2011).

The applied boundary conditions in the present polycrystalline simulations were described in section 4.4.3. In addition, each realization of polycrystalline aggregate is assigned with different random crystal orientations. No special interface condition is applied to grain boundaries. The interface conditions arise from balance equations in the continuum model: Continuity of the displacement vector components, and continuity of the traction vector components at least in the weak form according to the finite element method.

In the present work, γ_χ is assumed to be continuous at the interface. This type of interface condition is intermediate between microfree and microhard. In microfree interface condition, dislocations are free to escape interfaces; thus, no dislocation pile-up occurs at the interface. This interface condition corresponds to vanishing tractions for the micro-stresses. The surface traction ($\underline{T}$) and generalized surface traction (M) in Eq. (2.21) are also continuous. On the other hand, microhard interface condition. corresponds to a large plastic strain on one side of the interface and a small on the other side. In this interface condition, plastic slip vanishes at the interfaces ($\gamma_\chi = 0$); hence dislocation pile-up occurs. Furthermore, the traction vectors in Eq. (2.21) are discontinuous. These two choices are discussed in (Gurtin and Needleman, 2005). However, these two interface conditions are not applicable to all sorts of interface behavior. One approach to obtain interface behavior inbetween these two extreme conditions is by introducing interface energy as in (Aifantis and Willis, 2005).

In the present work we believed that the continuity of γ_χ carries the main physical constituent to predict the grain size effects in polycrystals.

4.5.2 Results and discussion

4.5.2.1 Grain orientation dependency of the shear band

The effect of grain orientations on the shear band predicted by the numerical simulations is investigated first for polycrystalline aggregates subjected to *isothermal* deformation using the micromorphic crystal plasticity model. Two distinct crystal orientation distributions are assigned to the grains in the shear region, namely the *orientation 1* and *orientation 2*. The realizations of the *coarse-grained* and *fine-grained* polycrystalline aggregates with corresponding pole figures are shown in Fig. 4.20a and 4.20b, respectively. The predicted load-displacement curves for the *coarse-grained* and *fine-grained* polycrystalline aggregates

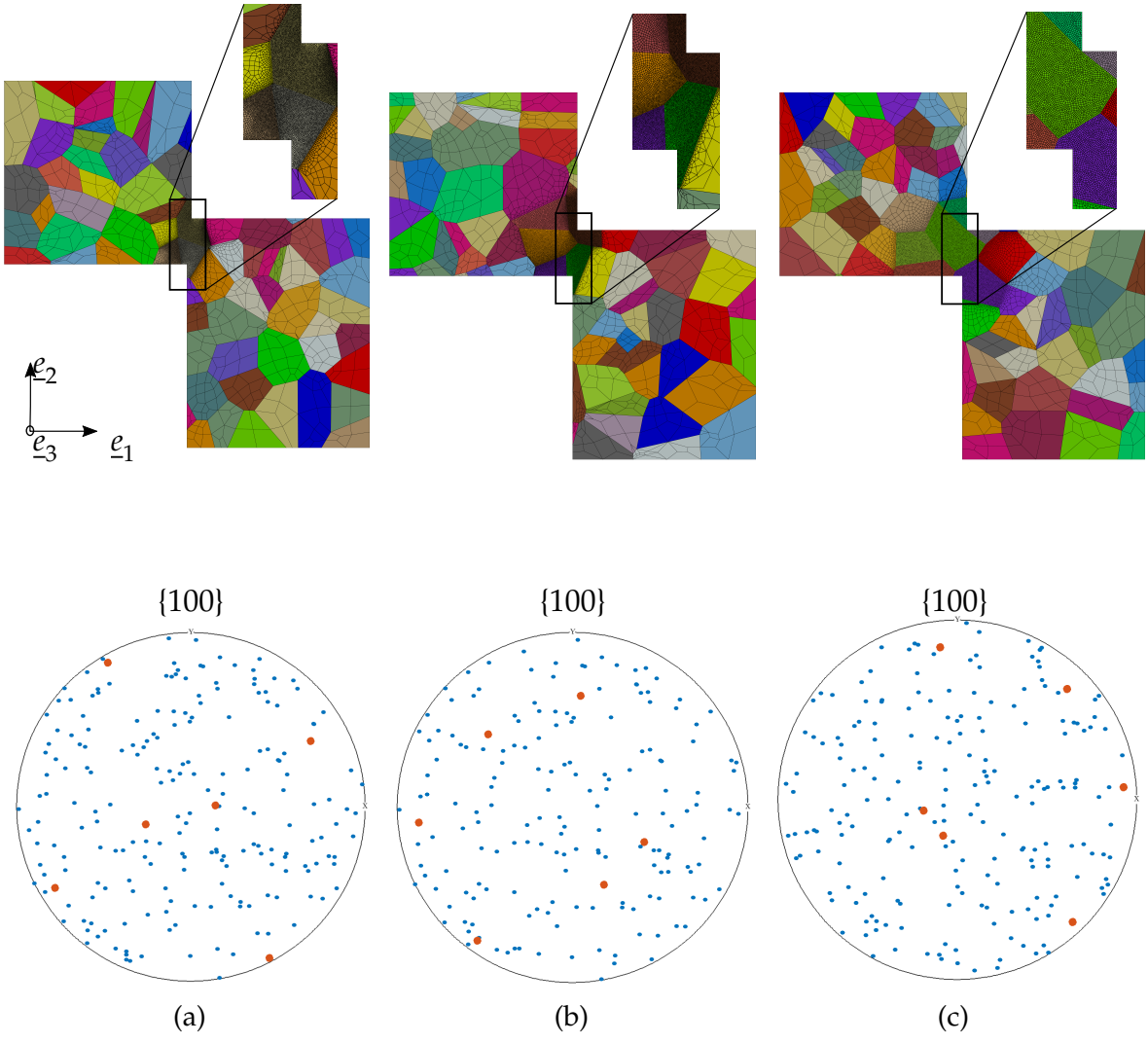

Fig. 4.18 Different realizations of the *coarse-grained* polycrystalline aggregates and corresponding pole figures: (a) Realization 1, (b) realization 2, and (3) realization 3. Colors represent individual grains and the red points in pole figures denote the orientation assigned to the grains in the shear region.

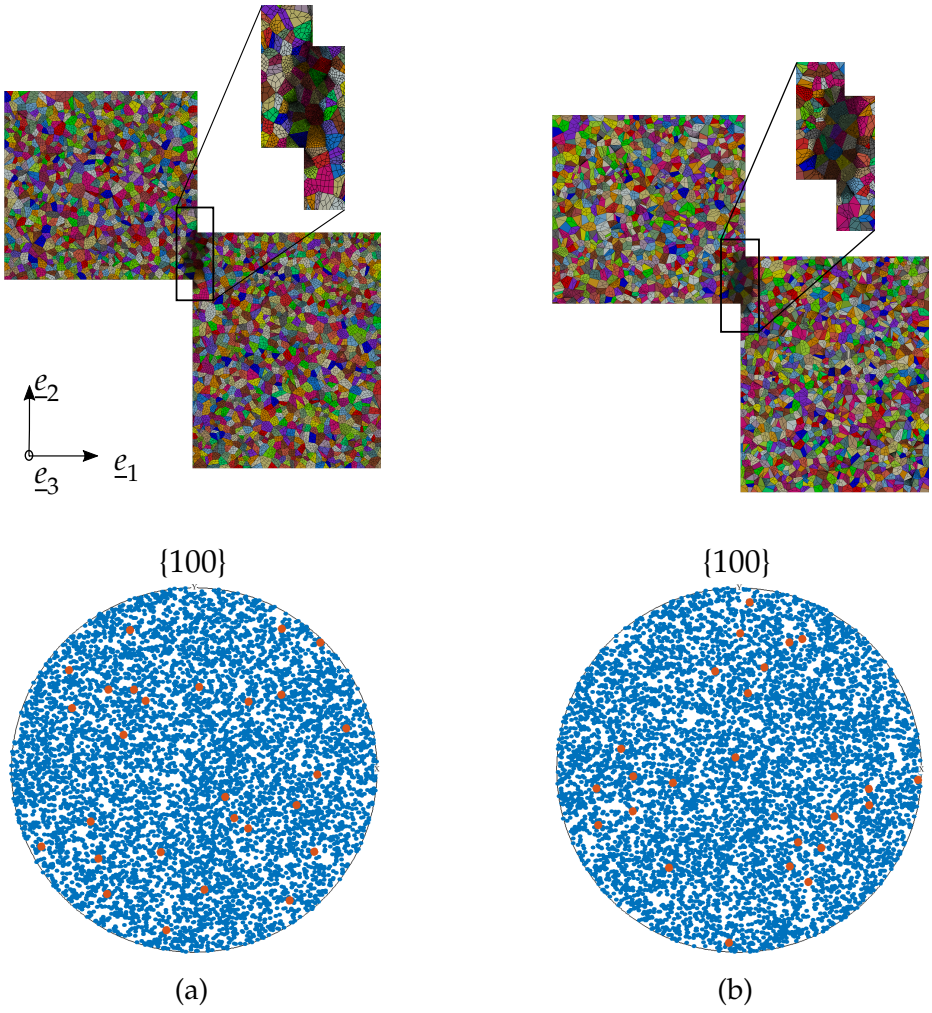

Fig. 4.19 Different realizations of the *fine-grained* polycrystalline aggregates and corresponding pole figures: (a) Realization 1, and (b) realization 2. Colors represent individual grains and the red points in the pole figures denote the orientation assigned to the grains in the shear region.

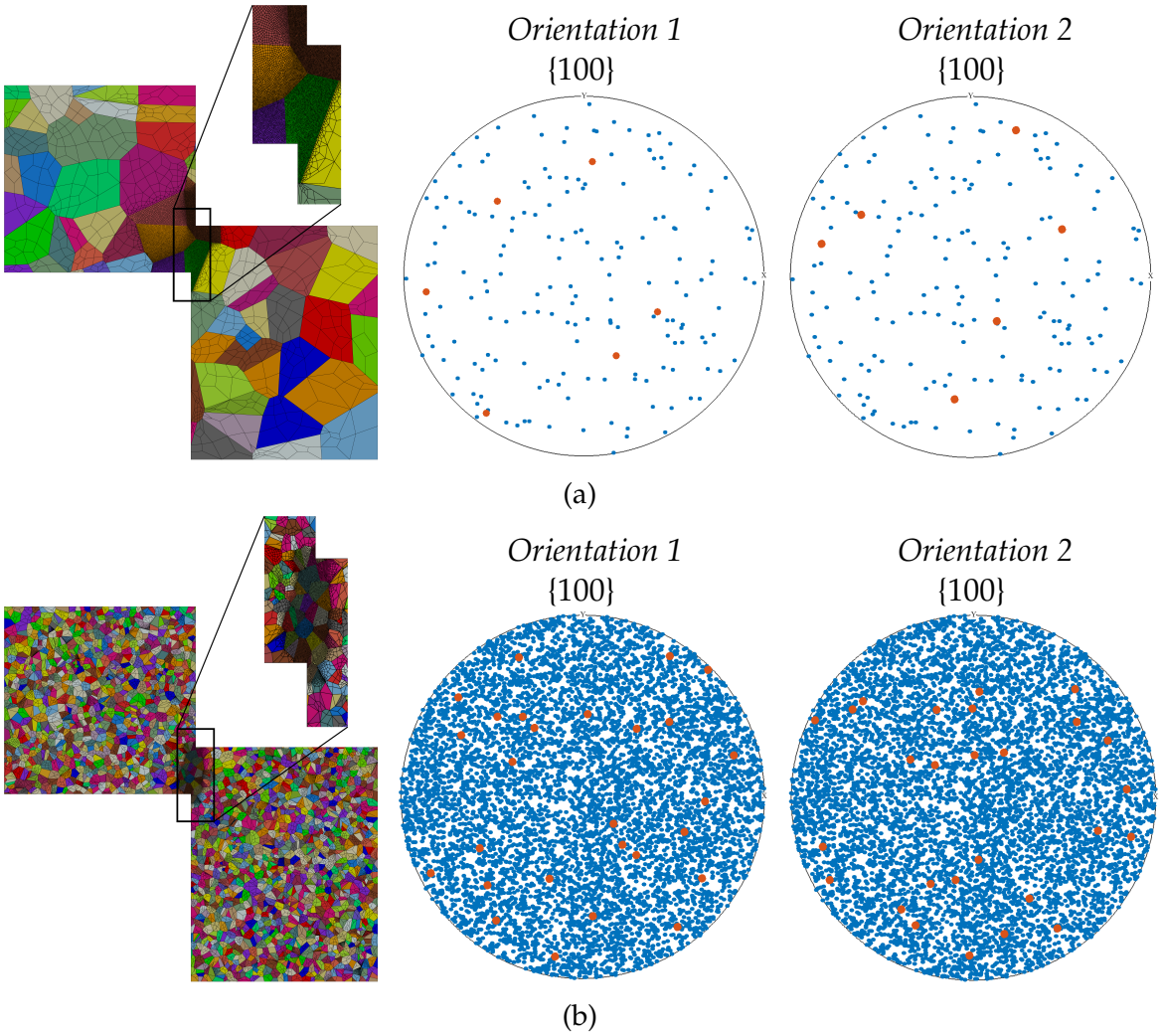

Fig. 4.20 Polycrystalline aggregates with two distinct orientation distributions assigned to the grains in the shear region (*orientation 1* and *orientation 2*) for the (a) *coarse-grained*, and (b) *fine-grained* with corresponding pole figures. The red points in the pole figure denote the orientations assigned to the grains in the shear region

are given in Fig. 4.21a and 4.21b, respectively. As shown in these figures, the resulting load required to deform the *orientation 2* in both polycrystalline aggregates is greater than the *orientation 1*, which indicates that the development and propagation of the shear band highly depends on the orientation of the grains crossed by the bands, grain boundaries acting as obstacles to shear band propagation. In *orientation 1* case, the orientations of the grains in the shear region are such that they favor plastic flow and subsequent shear band formation compared to *orientation 2*. Furthermore, less orientation dependency is observed in the *fine-grained* polycrystalline aggregates compared to the *coarse-grained* polycrystalline aggregates (see Fig. 4.21b). The formed shear bands are shown in Fig. 4.22. More significant strain localization is observed in *orientation 1* than in *orientation 2*. This indicates that some grains in *orientation 1* represent stronger obstacles to shear band transmission from grain to grain. This effect is reduced when a larger number of grains are available along the shear band path.

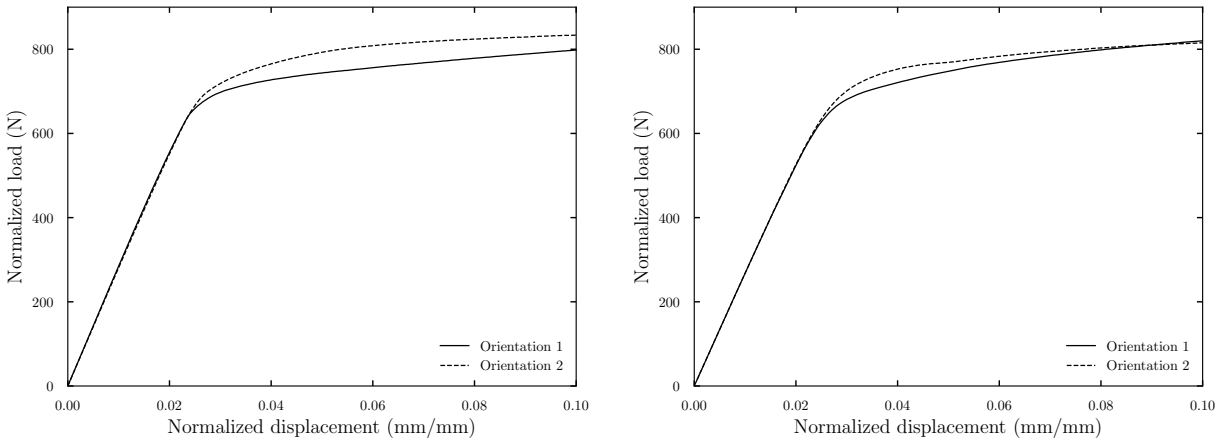

Fig. 4.21 Effect of the change in orientation of the grains in the shear region on the load-displacement curve using the micromorphic crystal plasticity model ($A = 0.04$ N) for the (a) *coarse-grained* polycrystal aggregate, and (b) *fine-grained* polycrystal aggregates subjected to *isothermal* conditions.

4.5.2.2 Grain size effect in the polycrystalline hat-shaped specimens

There are mainly two types of size effects to be considered, which are responsible for the increased strength of polycrystalline aggregates compared to single crystals, namely the *specimen size* effect and *grain size* effect (Armstrong, 1961). The specimen size effect occurs when there are few grains in the specimen cross-section. It is mainly related to the orientation dependency of the crystal plastic flow, as demonstrated in the previous subsection about the influence of number of grains along the shear band path. On the other hand, the *grain size* effect occurs when there are sufficiently many grains in the specimen cross-section. In addition to the orientation dependence of the plastic flow within the grains, internal stress concentration takes place at the grain boundaries and causes yielding and subsequent plastic flow (Armstrong, 1961). The well-known grain size effect in a polycrystalline material is the Hall-Petch size effect, which indicates that the yield strength of material is inversely proportional to the square root of grain size (Hall, 1951; Petch, 1953). Numerically, strain gradient plasticity models can be used to predict the grain size effects in polycrystalline materials, as done for instance in (Acharya and Bassani, 2000; Evers et al., 2004; Aifantis and Willis, 2005; Borg, 2007).

In the present work, firstly, the grain size effect is studied in the *isothermal* case for polycrystalline hat-shaped specimens. The realizations of polycrystalline aggregates investigated are shown in Fig. 4.18b and 4.19a for the *coarse-grained* and *fine-grained* polycrystalline aggregates, respectively. The shape and geometry of the hat-shaped specimen are such that it allows for the spontaneous formation of a shear band even in the absence of thermal softening in the numerical simulations due to the perfectly plastic crystal behavior. The cumulative plastic strain fields with the classical and micromorphic crystal plasticity models are shown in Fig. 4.23. The classical crystal plasticity model, which

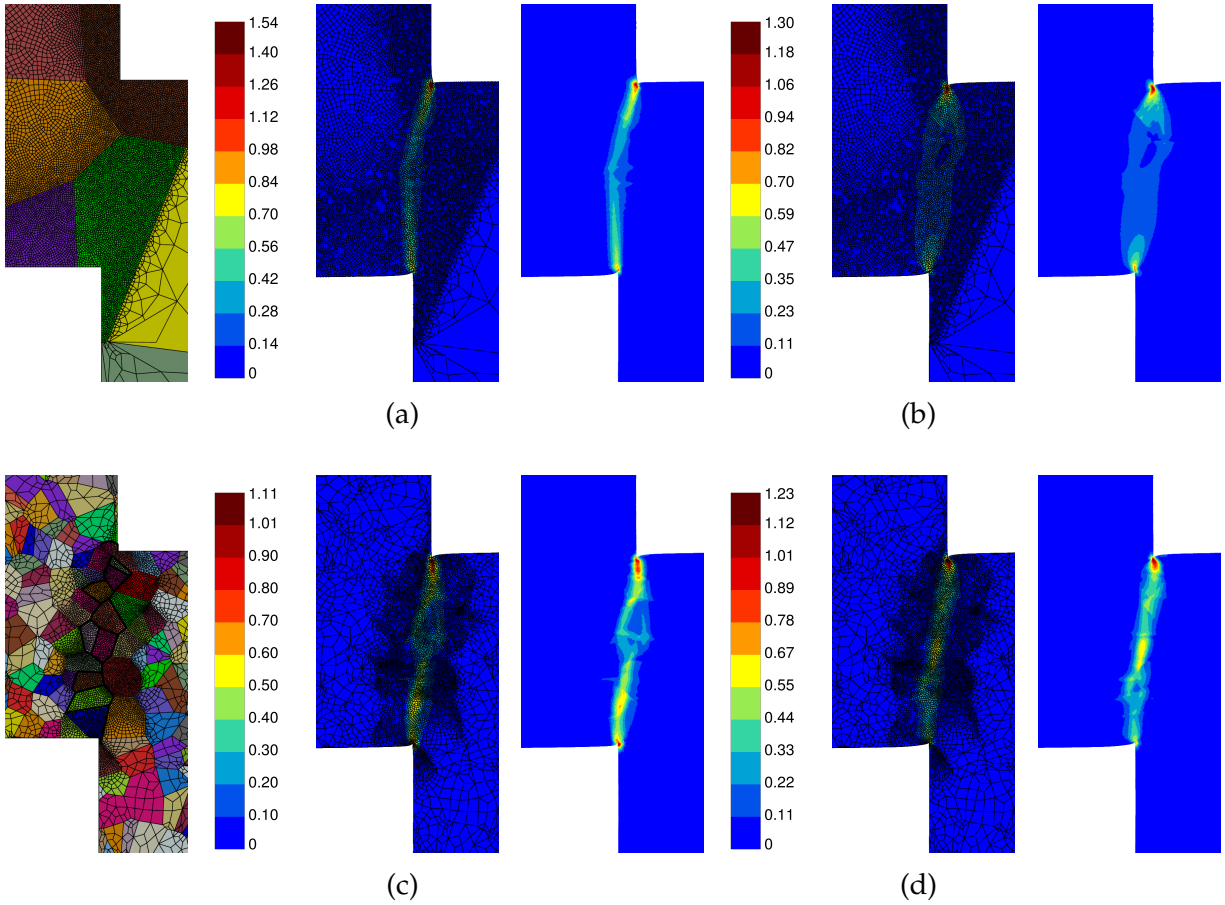

Fig. 4.22 Contour plots of cumulative plastic strain γ_{cum} using the micromorphic crystal plasticity model (A = 0.04 N) for the (a) *coarse-grained* polycrystalline aggregates assigned with *orientation 1*, and (b) *orientation 2*. (c) The *fine-grained* polycrystalline aggregates assigned with *orientation 1*, and (d) *orientation 2*. Fields are shown at the normalized imposed displacement of 0.06 mm/mm under *isothermal* conditions (T_i=923 K). For clarity the fields are shown with and without the finite element mesh.

does not feature any characteristic length scale, exhibits a pathological mesh dependency and the width of the formed shear band collapses to one element size (more precisely one Gauss point size, see Fig. 4.23a and 4.23b). Therefore, the classical crystal plasticity models cannot be used to study strain localization problems in polycrystals. In contrast, the width of the formed shear band predicted by the micromorphic crystal plasticity model is finite, see Fig. 4.23c and 4.23d. The normalized load-normalized displacement curves using the classical and micromorphic crystal plasticity models in the isothermal case are shown in Fig. 4.24. The predicted size effect is linked to the characteristic length scale ℓ through the gradient parameters A and H_χ as in Eq. (4.62). The micromorphic crystal plasticity model merely influences the hardening rate and does not affect the initial yield strength. This is because any gradient plasticity formulation based on a quadratic potential with respect to the gradient of plastic distortion cannot result in an increase in yield strength but only increases the hardening rate. The initial yield can be influenced by rank one potentials according to (Wulfinghoff et al., 2015) or using the recent approach by (Steinmann et al., 2019). The grain size effect is associated with spatial strain gradients inside the grains because of the heterogeneous plastic deformation resulting from grain-to-grain plastic strain incompatibilities. The grain boundaries act as obstacles to dislocation motion, and the strain gradient-induced GNDs pile up at grain boundaries. In addition, with the decrease in grain size, the area at the grain boundaries with GNDs density increases and leads to increased local stresses and of the resulting load. The larger number of grain boundaries in the shear region of the *fine-grained* polycrystalline aggregates obstructs the initiation and subsequent plastic flow and results in a higher resulting load.

Moreover, the effect of grain size on the load-carrying capacity subjected to *adiabatic* heating condition is now studied. Simulations are performed with two different values of the gradient parameter A, namely 0.004N, and 0.04N. The corresponding load-displacement curves for the realizations of the *coarse-grained* and *fine-grained* polycrystalline aggregates are given in Fig. 4.25a, 4.25b and Fig. 4.25c and 4.25d, respectively. The load-displacement curves exhibited by the different realizations of each polycrystalline aggregate with the same gradient parameter A are distinct from each other because of the assigned different random orientations and distinct shape of the grains in the shear region. A broader dispersion of the resulting loads is observed in realizations of the *coarse-grained* polycrystal aggregates (see Fig. 4.25a and 4.25b) compared to *fine-grained* polycrystal aggregates (see Fig. 4.25c and 4.25d). It is found that the average resulting load in *fine-grained* polycrystal aggregate remain below the *coarse-grained* polycrystal aggregate as seen from the average curves in Fig. 4.25e and 4.25f. This is probably due to the insufficient number of realizations which does not allow for statistical representativity. The results also show that higher values of A parameters lead to a reduced softening of the overall curves.

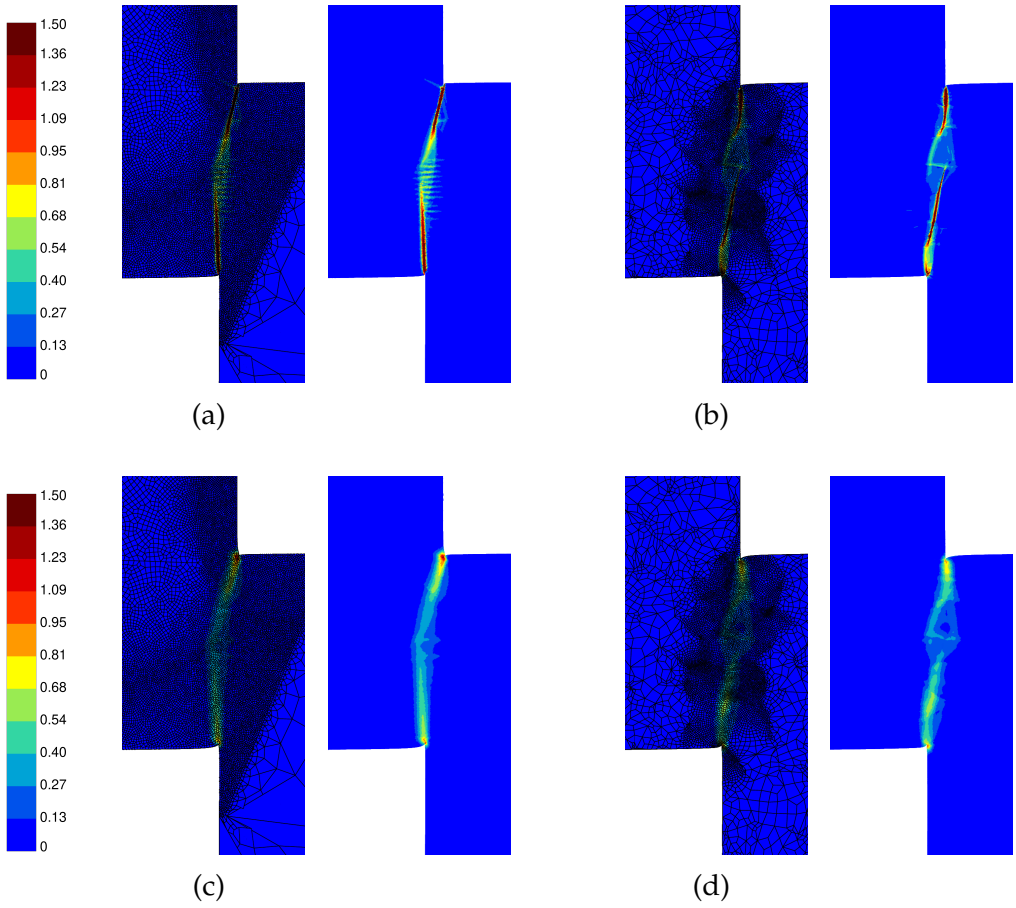

Fig. 4.23 Contour plots of cumulative plastic strain γ_{cum} using (a) the classical crystal plasticity model in *coarse-grained (orientation 1)*, and (b) *fine-grained (orientation 1)* polycrystalline aggregates, (c) using the micromorphic crystal plasticity model (A=0.04 N) in *coarse-grained (orientation 1)*, and (d) *fine-grained (orientation 1)* polycrystalline aggregates. Fields are shown at a normalized displacement of 0.06 mm/mm and under *isothermal* conditions.

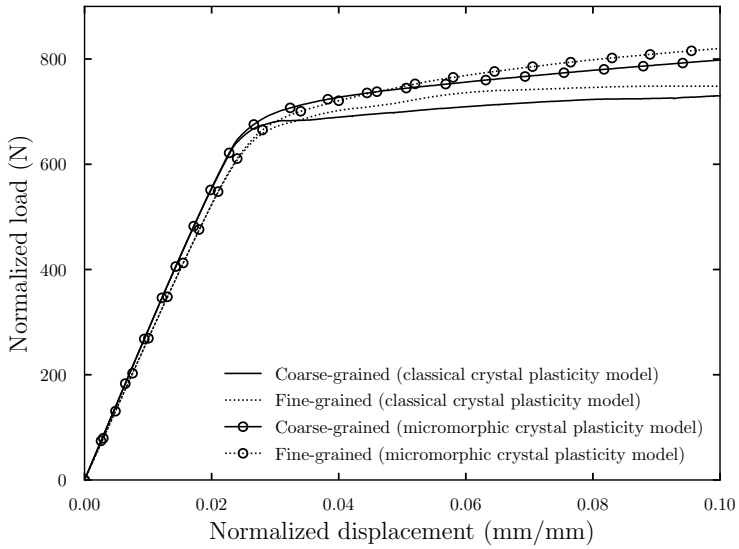

Fig. 4.24 Load-displacement curves obtained using the classical and micromorphic crystal plasticity models for the *coarse-grained* (realization 2), and *fine-grained* (realization 1) polycrystalline aggregates (hat–shaped specimens under isothermal conditions).

4.5.2.3 Effect of grain size on the shear band width

In this section the grain size effect on the width of shear bands is studied under *adiabatic* heating conditions. In the present polycrystalline simulations, deformation is highly localized within the grains of the shear region. Moreover, the grain size in the shear region plays a crucial role in the shear band formation. The shear band is triggered at the corners of the specimen, and strongly heterogeneous plastic deformation takes place between the corners. Furthermore, it is observed that some grains exhibit a larger amount of shear, while other grains remain almost undeformed. The formation of the shear band in *coarse-grained* polycrystalline aggregates for the realizations 1 and 3 (Fig. 4.26a and 4.26c) is restricted probably due to the unfavorable orientations of the grains in the shear region. In contrast, the shear band is easily formed in the realization 2 as seen from Fig. 4.26b. The orientation dependency in the shear band formation is the main reason for the wide dispersion of the resulting loads observed in *coarse-grained* polycrystalline aggregates. In contrast, in *fine-grained* polycrystalline aggregates, plastic flow in some grains is limited because of their grain boundaries and the orientation of the neighboring grains, causing subsequent plastic flow in more favorable grains as seen from Fig. 4.27a. However, less orientation dependency of the grains in the shear region is observed in the *fine-grained* polycrystalline aggregates compared to *coarse-grained* (see Fig. 4.27a and 4.27b). Fig. 4.28a and 4.28b show the cumulative plastic strain γ_{cum} variation along a node line crossing the shear region for the *coarse-grained* polycrystalline aggregates using gradient parameters $A = 0.004$ N and $A = 0.04$ N, respectively. Significant strain localization is observed for lower values of A, i.e. 0.004N compared to 0.04N. Fig. 4.28c and 4.28d show the cumulative plastic strain variation along the node line crossing the shear region for *fine-grained* polycrystalline

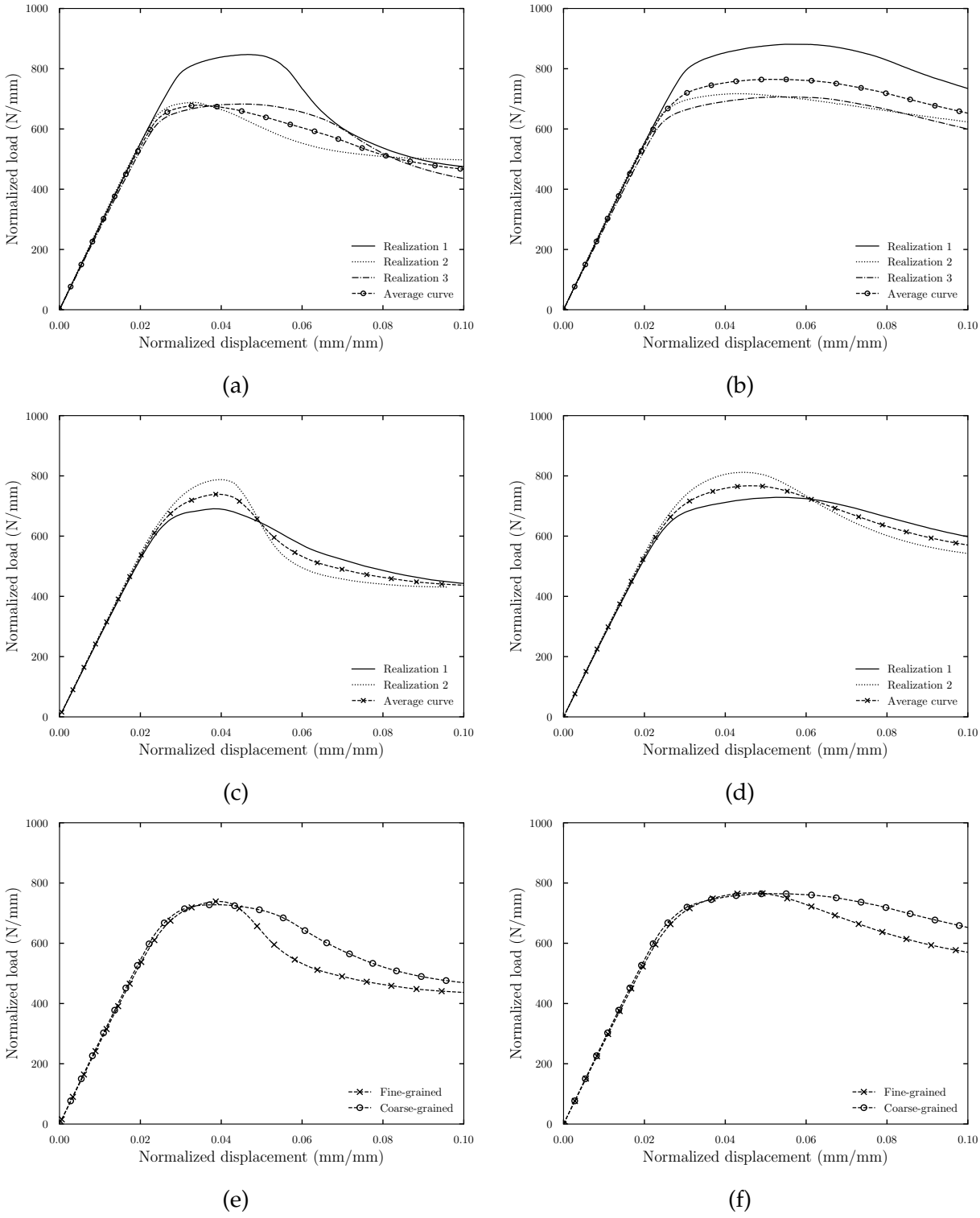

Fig. 4.25 Load-displacement curves using the micromorphic crystal plasticity model for various realizations of the polycrystalline aggregates subjected to *adiabatic* heating conditions: (a) the *coarse-grained* polycrystalline aggregates with $A = 0.004$ N, and (b) $A = 0.04$ N, (c) the *fine-grained* polycrystalline aggregates with $A = 0.004$ N, and (d) $A = 0.04$ N, (e) Average load-displacement curves with $A = 0.004$ N, and (f) $A = 0.04$ N.

aggregates with $A = 0.004$ N and $A = 0.04$ N, respectively. The shear band width is defined by the following criterion: The region in which the cumulative plastic strain is larger than 10% of the peak value. The measured widths of the shear band for the *coarse-grained* and *fine-grained* polycrystalline aggregates with the gradient parameter A of 0.004N, and 0.04N are given in Table 4.7. A larger dispersion of the shear band width is observed in the *coarse-grained* polycrystal realizations compared to the *fine-grained*, in a way similar to the predicted resulting loads.

The measurement of the shear band width along one single node line may not be sufficient in polycrystalline simulations. Therefore, the surface of the elements satisfying a specific criterion is calculated using the post-processing technique. The surface of the elements having cumulative plastic strain more than 10% of the peak value is measured. Finally, the width of the shear band w is calculated by dividing the surface of the band by the shear zone height h (see section 4.4.3 for specimen dimensions). The obtained values of the shear band widths are given in Table 4.7. The two definitions of shear band with provide similar results. Typical values of 50 micron (resp. 100 micron) are found for $A = 0.004$ N (resp. $A = 0.04$ N) irrespective of the grain size.

The present simulations are limited to adiabatic conditions although it is well-known that heat conduction can also contribute to the band structure (Yan et al., 2021). It is worth checking the typical lengths associated with heat conduction under the strain rate conditions of the simulations. The characteristic length scale of heat diffusion during a time interval t can be estimated as $\sqrt{k_t t/\rho C_\varepsilon}$, where k_t is the thermal conductivity. The parameter values considered in the work and time interval of one second result in diffusion distances of the order of 1 mm. This shows that heat conduction induced length scale is in competition with the microstructure related one. Adiabatic conditions are therefore a strong assumption in the present simulations. This pleads for coupling the present model to heat conditions in future work. This also strongly depends on the strain rate and grain size ranges in the simulations. The diffusion term in heat equation has a regularizing effect even though the involved length scales are sometimes too small for efficient FE modeling, as discussed in (Pamin et al., 2017). However, the strain gradient plasticity model should not be solely seen as a regularization method. It also introduces in the modeling microstructure aspects related to dislocation activity like pile-up formation and ensuing grain size effects, as studied in the present work. As mentioned in the introduction, Zhu et al. (1995); Tsagrakis and Aifantis (2015) analytically derived two characteristic lengths emerging from the coupling of strain gradient plasticity. The first one is related to the ratio of the strain gradient plasticity parameter and the hardening modulus. The second one involves the heat conductivity and strain gradient plasticity parameters. We have evaluated these length scales for the parameter values used in the present work. The second length scale is found to be close to 100 micron which confirms the importance of heat conduction and the competition with the microstructural length.

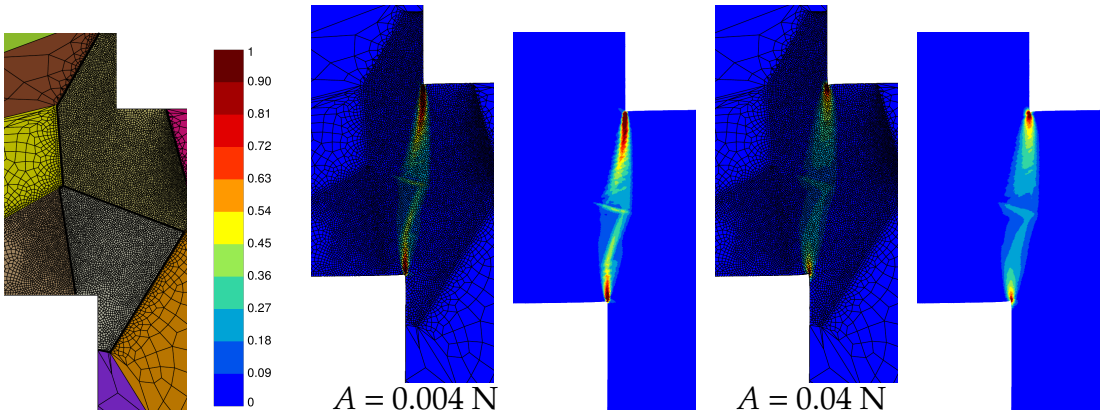

(a)

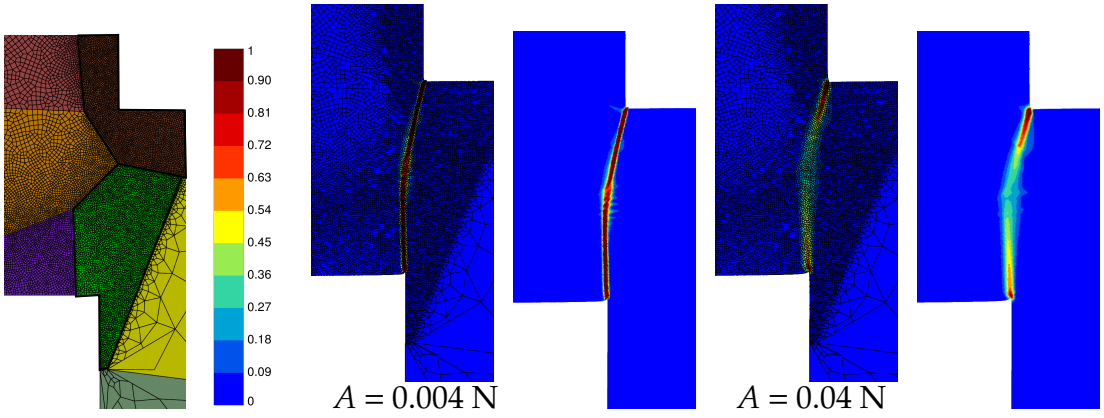

(b)

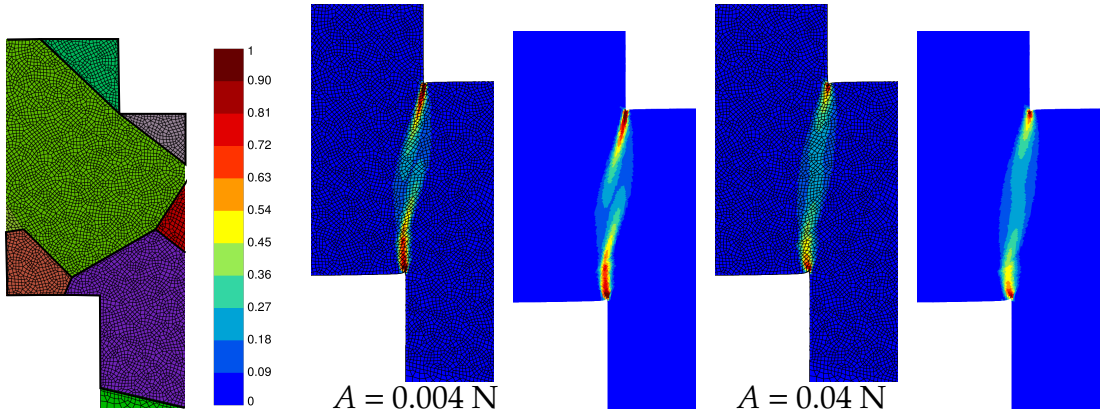

(c)

Fig. 4.26 Contour plots of cumulative plastic strain γ_{cum} in the *coarse-grained* polycrystalline aggregates subjected to *adiabatic* heating using the micromorphic crystal plasticity model ($A = 0.004$ N and $A = 0.04$ N) for three different realizations (a) realization 1, (b) realization 2, and (c) realization 3. Fields are shown at a normalized displacement of 0.052 mm/mm.

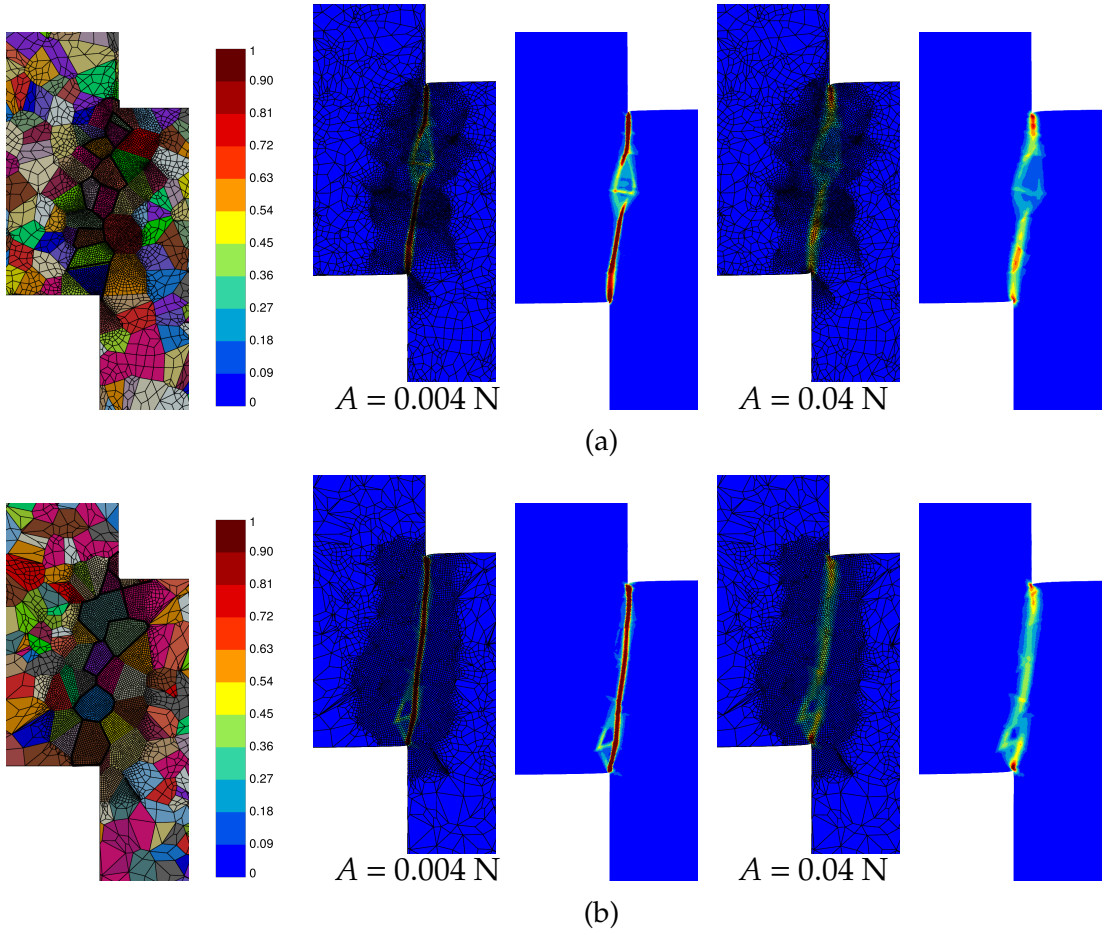

Fig. 4.27 Contour plots of cumulative plastic strain γ_{cum} in the *fine-grained* polycrystalline aggregates subjected to *adiabatic* heating using the micromorphic crystal plasticity model ($A = 0.004$ N and $A = 0.04$ N) for two different realizations (a) realization 1, and (b) realization 2. Fields are shown at a normalized displacement of 0.052 mm/mm.

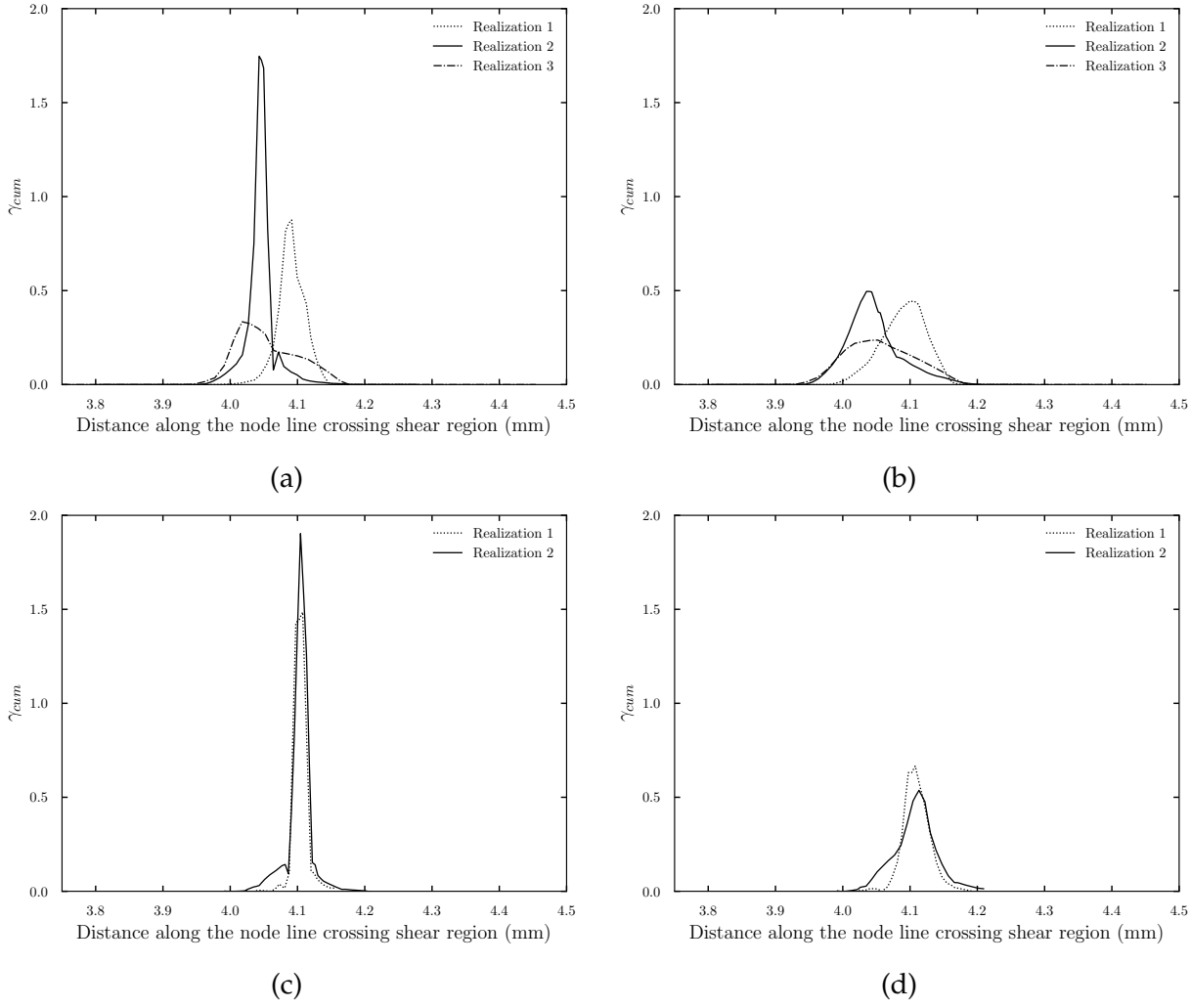

Fig. 4.28 Cumulative plastic strain variation along the node line crossing shear region using the micromorphic crystal plasticity model subjected to *adiabatic* heating in (a) *coarse-grained* polycrystalline aggregates with A = 0.004 N, and (b) A = 0.04 N. (c) The *fine-grained* polycrystalline aggregates with A = 0.004 N, and (d) A = 0.04 N. All the variations are plotted for the normalized displacement of 0.052 mm/mm.

Table 4.7 Shear band width w measured along the node line crossing the shear region and using a post-processing method.

coarse-grained	w (mm) ($A = 0.004$ N)	w (mm) Post-processing ($A = 0.004$ N)	w (mm) ($A = 0.04$ N)	w (mm) Post-processing ($A = 0.04$ N)
Realization 1	0.05	0.042	0.12	0.12
Realization 2	0.03	0.049	0.13	0.072
Realization 3	0.12	0.065	0.15	0.11
fine-grained				
Realization 1	0.03	0.036	0.05	0.12
Realization 2	0.03	0.033	0.05	0.098

4.6 Conclusions

The numerical simulation work presented here was intended to provide an insight into the mechanism of ASB formation in single and polycrystalline FCC metallic materials. The main findings obtained in this contribution can be summarized as follows:

1. A thermodynamically consistent constitutive framework for the micromorphic crystal plasticity model was used to derive temperature evolution under adiabatic conditions.

2. The micromorphic crystal plasticity model pursues the objective of regularization of the adiabatic shear band formation.

3. The orientation of the formed ASB with respect to the loading axis is affected by the crystal initial orientation. $[100]-[010]$ crystal orientation shows the stiffest response to ASB formation. On the other hand, crystals initially oriented at $[111]-[\bar{1}\bar{1}2]$ show the lowest tendency to shear band formation, and no evident shear banding is observed. Moreover, it is observed that the formed shear band width depends on the initial crystal orientation.

4. The grain size effect, *namely the finer the grain size the higher the stress*, was illustrated in the response of polycrystalline FCC metallic materials using the micromorphic crystal plasticity model subjected to *isothermal* deformation. It is shown that the micromorphic crystal plasticity model merely influences the hardening rate but does not affect the initial yield strength.

5. The resulting load and the formation of shear band is highly orientation dependent in polycrystalline simulations in the case of *coarse grained* polycrystal. The favorable orientation of the grains in the shear region results in decreased resulting load and ease of shear band formation. Furthermore, wide dispersion of the resultant load

and width of the shear band is observed in different realizations of the *coarse grained* polycrystalline aggregates.

6. The relation between observed shear band widths, characteristic length scale of the micromorphic model and grain size was analyzed. It shows that the characteristic length scale mainly controls the shear band width and that grain boundaries serve as obstacles to ASB propagation thus controlling the intensity of strain localization.

It is possible to predict stronger grain size effects in the polycrystalline simulations by considering larger number of grains in the shear region of the hat-shaped specimen. However, due to high computational costs, only two grain sizes were considered in the present work. Moreover, work-hardening was not included in the simulations to clearly isolate the micromorphic and grain size effects from classical hardening. The consideration of dislocation–based hardening in the future will require the evaluation of stored energy in order to evaluate temperature evolution under adiabatic conditions. It is common practice to consider a constant value 0.9 of the TQC. However, the experimental evidence, for instance, (Kapoor and Nemat-Nasser, 1998; Rittel et al., 2012), showed that, in reality, its value can be much less than 0.9. The thermodynamically consistent framework of the constitutive equations for the gradient crystal plasticity (reduced-order micromorphic) model presented in this work must be extended to allow for evolving TQC predicted by suitable free energy density functions. It is hoped that the predictions made in the present work will serve as incentives to perform experimental tests on single and oligo-crystalline hat–shaped specimens to precisely determine the relation between ASB width and grain size. The analysis of such tests may require the extension of the present computational approach to more realistic 3D computations.

Chapter 5

Prediction of stored energy and Taylor-Quinney coefficient in single and poly-crystals

Abstract

During the plastic deformation of metallic materials, part of expended mechanical energy diffuse as heat. The remaining portion of the plastic work is called stored energy which later converts into microstructural rearrangements. Stored energy is the main driving force for dynamic or static recovery and recrystallization. The critical aspect related to the measurement of stored energy is the fraction of plastic work converted into heat, called the Taylor-Quinney coefficient (TQC), often assumed to be a constant parameter of the order of 0.9. The prediction of the stored energy and TQC is important to understand the plastic deformation and subsequent recovery and recrystallization mechanism. An adequate prediction of stored energy and TQC in line with the experimental measurements using numerical simulations is challenging. In this work, first of all, the stored energy and TQC are predicted using a thermodynamically consistent classical crystal plasticity model for the single crystals copper and aluminum. Next, the application is made to polycrystalline aggregates. The stored energy predicted for the polycrystalline austenitic steel is compared with the experimentally measured stored energy from the literature. Besides, the predicted stored energy considering contribution of both statistically stored dislocations (SSDs) and geometrically necessary dislocations (GNDs) is compared to that obtained by considering the contribution of SSDs only. To this end, the contribution of GNDs along with SSDs is considered in the prediction of stored energy using two different grain boundary conditions, i.e. intermediate and microhard.

5.1 Introduction

During the plastic deformation of metallic materials, part of expended mechanical energy diffuses as heat. The remaining portion of the plastic work is called stored energy which

later converts into microstructural rearrangements. Stored energy is the main driving force for dynamic or static recovery and recrystallization. Different techniques used in experimental measurements of stored energy are summarized in (Bever et al., 1973). Extensive experimental work has been performed in the past to measure the stored energy in metallic materials, for instance, in (Bailey, 1963; Williams, 1965; Bever et al., 1973; Oliferuk et al., 1993, 1995).

A well-known analytical expression for the stored energy, which is a function of dislocation density, can be found in (Bailey, 1963; Bever et al., 1973). Bailey (1963) measured the stored energy of polycrystalline silver and copper under tensile loading. The analytical expression used by Bailey (1963) for the prediction of stored energy is given by $E_s = \frac{(\tau_c)^2}{\mu}$, where τ_c is given by $\tau_c = 0.5\mu b\sqrt{\rho_{avg}}$, with ρ_{avg} being the average dislocation density. Furthermore, he plotted the experimentally measured stored energy, E_s, as a function of $\frac{(\tau_c)^2}{\mu}$. The results for both metals lie close to the straight line of equation $E_s \simeq 7.7\,\frac{(\tau_c)^2}{\mu} \simeq 2\mu b^2\rho_{avg}$.

Several attempts have been made to investigate the effect of grain size on stored energy, for instance, in (Williams, 1965; Baker et al., 1995; Oliferuk et al., 1995). All these researchers concluded that with an increase in grain size the stored energy decreases. Williams (1965) found that an increase in grain size by a factor of ten decreases the stored energy by 8% at a strain of 0.3. Recently, Rittel et al. (2012) measured the stored energy of single crystal and polycrystalline copper in the strain rate range of $1000 - 8000\ s^{-1}$undergoing compressive loading. Higher stored energy was found in polycrystals than single crystals because of the presence of grain boundaries in polycrystals.

The critical aspect related to the measurement of stored energy is the fraction of plastic work converted into heat, called the Taylor-Quinney coefficient (TQC), often assumed to be a constant parameter of the order of 0.9 (Taylor and Quinney, 1934). Ravichandran et al. (2002) investigated the TQC evolution in aluminum 2024-T3 alloy and α-titanium. They found that the TQC is a function of strain but not of strain rate in the case of aluminum 2024-T3 alloy. On the other hand, TQC was strongly dependent on strain rate in α-titanium. Rittel et al. (2012) investigated the thermo-mechanical response of single and polycrystalline copper at low and high strain rates. They observed that the TQC linearly increases with strain rate and remains considerably lower than the classical value of 0.9. Rittel et al. (2017) recently measured the TQCs for 7 different metals and alloys, namely, Ti6Al4V, commercially pure titanium, Al5086, Al2024, 304L, 1020 steel, and maraging C300 under tension, compression, and dominant shear loading. A significant variation of TQC with values other than 0.9 was observed. Except for commercially pure titanium, identical TQCs were measured under tension, compression, and shear loading. In commercially pure titanium due to the presence of twinning activity in compression and shear loading results in different TQC in different deformation modes as twinning is related to heat generation.

Numerically, dislocation density-based models are often used to describe material hardening. The obtained total dislocation density is further used to calculate stored energy.

The stored energy prediction in single crystals copper under tensile loading using discrete dislocation plasticity was performed by Benzerga et al. (2005). They showed that the dislocation distribution influences the stored energy along with the total dislocation density. Moreover, they found TQCs in the range of 0.75-0.95 up to the strain of 10% and strain rate of 100 s^{-1}. In addition, crystal plasticity modeling is an essential tool to determine the stored energy and evolution of the material microstructure in thermo-mechanical processes. Håkansson et al. (2008) investigated the effect of initial texture on the stored energy in polycrystalline austenitic steel using a rate-dependent crystal plasticity model for large deformations formulated within a thermodynamic framework. A finite strain framework of crystal plasticity in a thermodynamically consistent manner is used by Jafari et al. (2017) to predict the stored energy in single and poly-crystalline aluminum under tensile loading and bi-crystal aluminum under compressive loading. The phase-field approach to predict the stored energy in polycrystalline aggregates can be found in (Abrivard et al., 2012).

A reliable dislocation density-based model is necessary to adequately represent the total dislocation density and consequently the stored energy according to (Nieto-Fuentes et al., 2018). Kositski and Mordehai (2021) showed using the molecular dynamics simulations that the dislocation mechanism is not the only mechanism responsible for the stored energy. They resort to grain boundary evolution as an additional mechanism responsible for energy storage.

Models of plastic deformation fall into two categories. On the one hand, phenomenological models are frequently used in crystal plasticity modeling. However, these models do not give a physical connection with the microscopic mechanisms of plastic deformation. The physics-based crystal plasticity models can overcome this limitation. On the other hand, the physics-based plasticity models strongly connect with the microscopic mechanisms of plastic deformation by introducing microscopic internal variables such as dislocation density in the constitutive framework. The constitutive equations must be derived in a thermodynamically consistency manner. In particular, it is necessary to check the positivity of the residual dissipation in the local balance equation. Failure to do so can violate the first and second laws of thermodynamics (Ottosen and Ristinmaa, 2005). The thermodynamic consistency of the physics-based models has received less attention compared to phenomenological models (Wu and Zaiser, 2021). Therefore, in this work, the necessity to ensure the positivity of the residual dissipation is emphasized. In addition, it is shown that the positivity of the residual dissipation in physics-based models can be ensured by imposing constraints on the model parameters.

The prediction of the stored energy and TQC is important to understand the plastic deformation and subsequent recovery and recrystallization mechanism. An adequate prediction of stored energy and TQC in line with the experimental measurements using numerical simulations is challenging. Analytical expressions used to predict the stored energy may not consider all the mechanisms responsible for stored energy. Nieto-Fuentes et al. (2018) introduced an *ad-hoc* factor in the analytical expression of stored energy to

represent the experimentally measured stored energy adequately. However, calibration of this factor for several dynamically loaded materials is necessary to get a common pattern. The present work uses a thermodynamically consistent formulation of the classical and micromorphic crystal plasticity models to predict the stored energy and TQC for single and poly-crystalline FCC metallic materials. A constant *ad-hoc* factor, ξ, in the expression of stored energy is treated as a fitting parameter so that the predicted stored energy adequately represents the experimental measurements. The stored energy is predicted for two different polycrystalline metallic materials under different loading conditions to check the predictability of this factor. To the best of our knowledge, most of the numerical work on the prediction of stored energy considers the contribution of SSDs only. The study on the prediction of stored energy considering the contribution of GNDs along with SSDs is relatively rare.

In this work, first of all, the stored energy and TQC are predicted using the classical crystal plasticity model for the single crystals copper and aluminum. Next, the application is made to polycrystalline aggregates. As the first application to polycrystalline simulations, the effect of mesh size and grain morphology on the stress-strain response is studied in detail. The stored energy predicted for the polycrystalline austenitic steel is compared with the experimentally measured stored energy from the literature. Besides, the application is made to predict the stored energy in annealed Inconel 718 deformed at high strain rates (1900 s^{-1}-2000 s^{-1}) and high temperatures (293 K-1273 K). Besides, the predicted stored energy considering contribution of both SSDs and GNDs is compared to that obtained by considering the contribution of SSDs only. Finally, the contribution of GNDs along with SSDs is considered in the prediction of stored energy using two different grain boundary conditions, i.e. *intermediate* and *microhard*.

This chapter is organized as follows: section 5.2 is devoted to analyzing the positivity of the dissipation rate to ensure thermodynamic consistency. The summary of the constitutive equations used for the numerical prediction of stored energy and TQC is given in section 5.3. In section 5.4, single crystals aluminum and copper simulations are performed to predict the stored energy and evolution of TQCs. Section 5.5 is dedicated to the prediction of stored energy and evolution of TQC in polycrystalline FCC metallic materials. Conclusions follow in section 5.6.

5.2 Positivity of the dissipation rate to ensure thermodynamic consistency

In this part we establish the constitutive framework for deriving models that are considered with thermodynamics. Let us recall the first and second laws of thermodynamics. The first law of thermodynamics with respect to the current configuration is written in the local

form as follows:

$$\rho\dot{e} = \underset{\sim}{\sigma} : \underset{\sim}{D} + Q, \tag{5.1}$$

with $\underset{\sim}{D}$ being the strain rate tensor, e the internal energy per unit mass and $Q(= r - \operatorname{div} \underline{q})$ the heat supply per unit volume and unit time, which results from an external heat source r and heat conduction $\underline{q}$. The second law of thermodynamics in the form of the local dissipation rate inequality with respect to the current configuration can be written as

$$\rho\dot{\eta} + \operatorname{div}\frac{\underline{q}}{T} - \frac{r}{T} \geq 0, \tag{5.2}$$

where η is the entropy per unit mass and T is the absolute temperature.

The Helmholtz free energy density function is introduced as

$$\Psi := e - T\eta. \tag{5.3}$$

The material under consideration is assumed to be characterized by the coupled thermo-mechanical Helmholtz free energy density function defined as

$$\Psi = \tilde{\Psi}(\underset{\sim}{E}^{the}, T, \zeta). \tag{5.4}$$

where $\underset{\sim}{E}^{the}$ is the thermo-elastic strain tensor, T is the temperature, and ζ is the internal hardening variable. Moreover, it is assumed that the free energy function can additively be decomposed as

$$\rho_0\Psi = \rho_0\tilde{\Psi}(\underset{\sim}{E}^{the}) + \rho_0\tilde{\Psi}(T) + \rho_0\sum_{r=1}^{N}\tilde{\Psi}^r(\zeta^r), \tag{5.5}$$

where ρ_0 is the volume mass density with respect to the reference configuration and $\rho_0\tilde{\Psi}^r(\zeta^r)$ is the free energy function related to the internal hardening variable ζ^r on slip system r $(= 1, 2....., N)$ with N being the total number of slip systems.

The Clausius-Duhem inequality is now expressed with respect to the reference configuration as

$$D = J\underset{\sim}{\sigma} : \underset{\sim}{D} - \rho_0(\dot{\Psi} + \eta\dot{T}) - \underline{Q} \cdot \frac{\nabla_X T}{T} \geq 0, \tag{5.6}$$

with $\underline{Q}$ being the heat conduction with respect to the reference configuration and given by $\underline{Q} = J^{\widetilde{the}}\underset{\sim}{F}^{-1} \cdot \underline{q}$ and $\nabla_X T$ the Lagrangian gradient of temperature.

The non-negative dissipation D can be split into two: non-negative mechanical dissipation $D_m \geq 0$ and non-negative thermal dissipation $D_{th} \geq 0$ such that

$$D = D_m + D_{th} \geq 0, \tag{5.7}$$

where $D_m = J\underset{\sim}{\sigma} : \underset{\sim}{D} - \rho_0(\dot{\Psi} + \eta\dot{T})$ and $D_{th} = -\underline{Q} \cdot \frac{\nabla_X T}{T}$.

The thermal inequality can also be called Fourier's inequality which states that heat must flow from hot regions to cold regions. We assume that the constitutive equation for

the heat flux vector $\underline{Q}$ is such that the thermal inequality holds:

$$D_{th} = -\underline{Q} \cdot \frac{\nabla_X T}{T} \geq 0. \tag{5.8}$$

The Clausius-Duhem inequality from Eq. (4.15) reads

$$\left(\underset{\sim}{\Pi}^e - \rho_0 \frac{\partial \tilde{\Psi}(\underset{\sim}{E}^{the}, T)}{\partial \underset{\sim}{E}^{the}}\right) : \dot{\underset{\sim}{E}}^{the} - \rho_0 \left(\eta + \frac{\partial \tilde{\Psi}}{\partial T}\right)\dot{T} - \underline{Q} \cdot \frac{\nabla_X T}{T} + D_{res} \geq 0, \tag{5.9}$$

where D_{res} is the residual dissipation given by

$$D_{res} = \underset{\sim}{\Pi}^M : \dot{\underset{\sim}{l}}^p - X\dot{\zeta}, \tag{5.10}$$

where $\underset{\sim}{\Pi}^M$ is the Mandel stress tensor defined with respect to the intermediate configuration. The definition of the Mandel stress tensor can be found in section 4.2.1. The residual dissipation in Eq. (5.10) can be further expressed as

$$D_{res} = \sum_{r=1}^{N} \tau^r \dot{\gamma}^r - \sum_{r=1}^{N} X^r \dot{\zeta}^r, \quad \text{with} \quad \underset{\sim}{\Pi}^M : \dot{\underset{\sim}{l}}^p = \sum_{r=1}^{N} \tau^r \dot{\gamma}^r, \tag{5.11}$$

where X^r is a thermodynamic force associated with the internal hardening variable ζ^r given by

$$X^r = \rho_0 \frac{\partial \tilde{\Psi}^r(\zeta^r)}{\partial \zeta^r}. \tag{5.12}$$

Any acceptable constitutive relation must fulfill the dissipation inequality. Therefore, it is crucial to select proper free energy function related to the internal hardening variable $\rho_0 \tilde{\Psi}^r(\zeta^r)$ (cf. Eq. (4.14)) and the evolution equations for ζ^r. Various approaches for the establishment of the evolution of ζ^r to ensure that the dissipation inequality is fulfilled can be found in (Ottosen and Ristinmaa, 2005). In the first approach called *direct approach*, some evolution laws are assumed for ζ^r. The positivity of the dissipation inequality is checked at each time step of the computation. The drawback of this approach is that a check needs to be performed for each material model, and general information cannot be derived for a group of models. The second approach is called *Onsager approach* in which linear relationship between internal hardening variable ζ^r and thermodynamic force X^r is assumed. This approach is proposed by Onsager (1931a,b). The linear relationship cannot be used for general plasticity and visco-plasticity as realistic materials show nonlinearity. However, it can be used for some other phenomena in which relevant material description can be derived. The third approach is called *potential approach* which generalizes the Onsager's linear approach to nonlinear theory. In this approach, dissipation potential is chosen from which internal variable evolution equations are derived. Another approach is called *convex potential function* in which the dissipation potential is a convex function of its argument such that the positivity of the dissipation rate is ensured at any instance. A

thermodynamic consistency of the constitutive equations is also discussed in the pioneering work of (Germain et al., 1983).

According to the first law of thermodynamics, a free energy potential for materials must exist, and it is important to give approximate expressions. In contrast, the existence of a dissipation potential is not necessary, but it can ease the development of thermodynamically consistent models, i.e. models that fulfill the second law of thermodynamics related to the positivity of dissipation rate. These potentials are not always provided in the literature, but they are useful to finally evaluate the TQC.

Moreover, it is crucial to select proper free energy function $\rho_0\tilde{\Psi}^r(\zeta^r)$ and expression for the evolution of ζ^r to ensure that the difference between the plastic power and stored energy rate is positive in temperature evolution equation (Eq. (4.37)). Many different expressions for $\rho_0\tilde{\Psi}^r(\zeta^r)$ based on phenomenological and physics-based models can be found in the literature. In the next section, we establish the framework for phenomenological and physics-based models that are provided by thermodynamics.

5.2.1 Examples of phenomenological models

At first, a simple thermodynamically consistent phenomenological model is considered in which contribution of the internal hardening variable ζ^r to the free energy is assumed to have the quadratic form:

$$\rho_0\tilde{\Psi}^r(\zeta^r) = \frac{1}{2}Q\zeta^r\sum_{s=1}^{N}h^{rs}\zeta^s, \tag{5.13}$$

where Q is a material parameter. The thermodynamic force X^r associated with the internal hardening variable ζ^r can be given by

$$X^r = \rho_0\frac{\partial\tilde{\Psi}^r(\zeta^r)}{\partial\zeta^r} = Q\sum_{s=1}^{N}h^{rs}\zeta^s. \tag{5.14}$$

In this model, the existence of a convex dissipation potential $\Omega(\underset{\sim}{\Pi}^M, X)$ is assumed from which flow rule and internal variable evolution equations are derived:

$$\dot{\underset{\sim}{F}}^p\cdot\underset{\sim}{F}^{p-1} = \frac{\partial\Omega}{\partial\underset{\sim}{\Pi}^M}, \quad \dot{\zeta} = -\frac{\partial\Omega}{\partial X}. \tag{5.15}$$

In addition, the dissipation potential is assumed to be of the power law form:

$$\Omega(\underset{\sim}{\Pi}^M, \tau_c^r) = \frac{K}{1+m}\sum_{r=1}^{N}\left\langle\frac{f^r}{K}\right\rangle^{m+1}, \tag{5.16}$$

where τ_c^r is the critical resolved shear stress and f^r is the Schmid-type yield function of the flow rule in the visco-plastic framework given by

$$f^r = |\tau^r| - \tau_c^r. \tag{5.17}$$

Based on the dissipation potential in Eq. (5.16), the flow and hardening rules are derived

$$\dot{\underset{\sim}{F}}^p \cdot \underset{\sim}{F}^{p-1} = \frac{\partial \Omega}{\partial \underset{\sim}{\Pi}^M} = \sum_{r=1}^{N} \frac{\partial \Omega}{\partial f^r} \frac{\partial f^r}{\partial \underset{\sim}{\Pi}^M} = \sum_{r=1}^{N} \dot{\gamma}^r (\underline{m}^r \otimes \underline{n}^r), \quad \dot{\zeta}^r = -\frac{\partial \Omega}{\partial \tau_c^r} = \dot{v}^r, \tag{5.18}$$

with v^r being the cumulative slip variable and $\dot{\gamma}^r$ is the slip rate on slip system r computed as follows:

$$\dot{\gamma}^r = \frac{\partial \Omega}{\partial f^r} \operatorname{sign}(\tau^r) = \dot{v}^r \operatorname{sign}(\tau^r), \quad \dot{v}^r = |\dot{\gamma}|^r. \tag{5.19}$$

The residual dissipation in Eq. (5.11) can be written as:

$$D_{res} = \sum_{r=1}^{N} \tau^r \dot{\gamma}^r - Q \sum_{r=1}^{N} \sum_{s=1}^{N} h^{rs} v^s |\dot{\gamma}^r|, \quad \text{with} \quad \dot{\zeta}^r = |\dot{\gamma}^r|. \tag{5.20}$$

which further can be expressed as

$$D_{res} = \sum_{r=1}^{N} \left(|\tau^r| - \left[\tau_0 + Q \sum_{s=1}^{N} h^{rs} v^s \right] + \tau_0 \right) |\dot{\gamma}^r|. \tag{5.21}$$

The residual dissipation inequality ($D_{res} \geq 0$) of the previous equation can be fulfilled in two ways: either the $|\dot{\gamma}|^r$ is zero or the term in the brackets must be positive. The second term in the brackets of the previous equation is τ_c^r with $\zeta^r = v^r$. Therefore, first two terms of the previous equation denote a yield function (Eq. (5.17)) of the visco-plastic flow rule, which is positive. Moreover, $\tau_0 \geq 0$ and hence in this simple case positivity of the residual dissipation is ensured.

The constitutive formulation presented above is simple as $\zeta^r = v^r$. It is preferred to use a saturating variable ζ^r instead of the cumulative slip v^r, which is not a satisfactory internal variable. In phenomenological models, ζ^r is reminiscent of a dislocation density-like variable. The realistic materials show nonlinear hardening behavior therefore a nonlinear isotropic hardening rule for ζ^r is assumed of the form:

$$\zeta^r = 1 - \exp(-B v^r), \quad \text{with} \quad \dot{v}^r = |\dot{\gamma}|^r, \tag{5.22}$$

where B is a material parameter. The contribution of ζ^r to the free energy is assumed to be of the form given in Eq. (5.13). Then the thermodynamic force associated with the internal

hardening variable becomes

$$X^r = \rho_0 \frac{\partial \tilde{\Psi}^r(\zeta^r)}{\partial \zeta^r} = Q \sum_{s=1}^{N} h^{rs}(1 - \exp(-Bv^s)). \tag{5.23}$$

In addition, the nonlinear evolution of the isotropic hardening variable τ_c^r is assumed to be of the form

$$\tau_c^r = \tau_0 + Q \sum_{s=1}^{N} h^{rs}(1 - \exp(-Bv^s). \tag{5.24}$$

The residual dissipation in (5.11) reads

$$D_{res} = \sum_{r=1}^{N} \left(|\tau^r| - Q \sum_{s=1}^{N} h^{rs}(1 - \exp(-Bv^s)(B \exp(-Bv^s)) \right) |\dot{\gamma}^r|, \tag{5.25}$$

which can be further expressed as follows:

$$D_{res} = \sum_{r=1}^{N} \left(|\tau^r| - \left[\tau_0 + Q \sum_{s=1}^{N} h^{rs}(1 - \exp(-Bv^s)) \right] + \tau_0 + X^r(1 - B \exp(-Bv^r)) \right) |\dot{\gamma}^r|. \tag{5.26}$$

Similar to the previously considered simple case, the inequality $D_{res} \geq 0$ can be fulfilled in two ways: either the $|\dot{\gamma}|^r$ is zero or the corresponding terms in the brackets are positive. The second term in the brackets of the previous equation is τ_c^r. Therefore, first two terms of the previous equation denote a yield function (Eq. (5.17)) of the visco-plastic flow rule, which is positive. Besides, $\tau_0 \geq 0$ and the last term is also positive. The thermodynamic consistency of this phenomenological model can also be found in (Busso and Cailletaud, 2005).

Phenomenological models have the advantage that free energy functions are explicitly postulated; sometimes, a dissipation potential is also proposed. But the models may be too simple compared to experimental results. In contrast, physics-based internal variables have been proposed in the literature. But explicit expressions of free energy function are not provided in most cases. In the next section, we establish the framework that is provided by thermodynamics for physics-based models taken from the literature and the model used in the present work.

5.2.2 Examples of physics-based models

This section constructs the dislocation density-based model that ensures thermodynamic consistency. In many conventional dislocation density-based crystal plasticity theories, dislocation density ρ^r on the slip system r is considered as an internal variable, for instance, in (Kubin et al., 2008; Knezevic and Beyerlein, 2018; Bronkhorst et al., 2019). Unlike the conventional theories, Lieou and Bronkhorst (2020) derived the evolution of dislocation density from energetic and entropic considerations alone with constraints of the first and

second laws of thermodynamics. The formulation is based on the Langer-Bouchbinder-Lookman thermodynamic dislocation theory proposed in (Langer et al., 2010; Langer, 2015). Based on the energetic considerations alone, the evolution of dislocation density is proportional to plastic work rate and not only to the plastic slip rate as in conventional theories.

5.2.2.1 Physics-based model from the literature

Model by Abrivard et al. (2012)

Following the work of (Abrivard et al., 2012), the free energy function associated with the internal hardening variable ζ^r is given by

$$\rho_0 \tilde{\Psi}^r(\zeta^r) = \frac{1}{2}\xi\mu(\zeta^r)^2, \tag{5.27}$$

where ξ is the statistical constant of the order of 0.3. The thermodynamic force associated with the internal hardening variable becomes

$$X^r = \rho_0 \frac{\partial \tilde{\Psi}^r(\zeta^r)}{\partial \zeta^r} = \xi\mu\zeta^r. \tag{5.28}$$

In (Abrivard et al., 2012) it is assumed that the internal hardening variable ζ^r depends on the SSDs as follows:

$$\zeta^r = b\sqrt{\sum_{s=1}^{N} h^{rs}\rho^s}, \tag{5.29}$$

and $\dot{\zeta}^r$ can be written as

$$\dot{\zeta}^r = \frac{b}{2\sqrt{\sum_{s=1}^{N} h^{rs}\rho^s}} \sum_{s=1}^{N} h^{rs}\dot{\rho}^s. \tag{5.30}$$

From (5.28) and (5.30) the dissipation related to the internal hardening variable reads

$$\sum_{r=1}^{N} X^r \dot{\zeta}^r = \frac{1}{2}\xi\mu b^2 \sum_{r=1}^{N}\sum_{s=1}^{N} h^{rs}\dot{\rho}^s. \tag{5.31}$$

One possible evolution equation for the dislocation density is given by

$$\dot{\rho}^r = \frac{1}{b}\left(k_c\sqrt{\sum_{s=1}^{N}\rho^s} - 2y_c\rho^r\right), \tag{5.32}$$

where k_c is the mobility constant and y_c is the critical annihilation distance between opposite sign dislocations. The first term in the previous equation corresponding to dislocation generation, and the second term to dislocation annihilation. Inserting (5.32) in (5.31) leads

to

$$\sum_{r=1}^{N} X^r \dot{\zeta}^r = \frac{1}{2}\xi\mu b^2 \sum_{r=1}^{N}\sum_{s=1}^{N} h^{rs} \frac{1}{b}\left[k_c \sqrt{\sum_{u=1}^{N} \rho^u} - 2y_c\rho^r\right]|\dot{\gamma}^r|. \tag{5.33}$$

Inserting previous equation in (5.11) gives

$$D_{res} = \sum_{r=1}^{N}\left(|\tau^r| - \frac{\xi\mu b}{2}\sum_{s=1}^{N} h^{rs}\left[k_c \sqrt{\sum_{u=1}^{N} \rho^u} - 2y_c\rho^r\right]\right)|\dot{\gamma}^r|. \tag{5.34}$$

In addition, the nonlinear evolution of the isotropic hardening variable τ_c^r is assumed to be dependent on the SSD density as follows:

$$\tau_c^r = \tau_0 + \mu b \sqrt{\sum_{s=1}^{N} h^{rs}\rho^s}. \tag{5.35}$$

To ensure the positivity of the residual dissipation in (5.34) by imposing constraints on the model parameters, a simplified case can be considered where all components of the interaction matrix h^{rs} are unity. Then (5.34) reads

$$D_{res} = \sum_{r=1}^{N}\left(|\tau^r| - \frac{\xi\mu b}{2}\left[k_c \sqrt{\sum_{s=1}^{N} \rho^s} - 2y_c\rho^r\right]\right)|\dot{\gamma}^r|, \tag{5.36}$$

which further can be written by introducing τ_c^r from Eq. (5.35) as follows:

$$D_{res} = \sum_{r=1}^{N}\left((|\tau^r| - \tau_c^r) + \tau_0 + \mu b \sqrt{\sum_{s=1}^{N} \rho^s}\left[1 - \frac{\xi k_c}{2}\right] + \mu b d_c \rho^r\right)|\dot{\gamma}^r|. \tag{5.37}$$

The residual dissipation inequality ($D_{res} \geq 0$) in the previous equation holds when $|\dot{\gamma}^r|$ is 0 or the corresponding terms in the brackets are positive. The first term in the previous equation is a Schmid-type yield function (Eq. 5.17) which is positive. Moreover, $\tau_0 \geq 0$ and the third term can be made positive by imposing constraints on the model parameter k_c such that $k_c \geq \frac{2}{\xi}$. Besides, the last term of the previous equation is also positive.

5.2.2.2 Physics-based model used in present work

In the present work, the contribution of the internal hardening variable ζ^r to the free energy function is assumed to have the quadratic form:

$$\rho_0 \tilde{\Psi}^r(\zeta^r) = \frac{1}{2}\mu\xi(\zeta^r)^2, \quad \text{with} \quad \zeta^r = \sqrt{\sum_{s=1}^{N} h^{rs}\varrho^s}, \tag{5.38}$$

where ξ is an *ad-hoc* factor of the order unity. The adimentional dislocation density $\varrho^r (= \rho^r b^2)$ is expressed by Eq. (2.15). Then, the thermodynamic force X^r associated with ζ^r can be expressed as follows:

$$X^r = \rho_0 \frac{\partial \tilde{\Psi}^r(\zeta^r)}{\partial \zeta^r} = \mu \xi \zeta^r. \tag{5.39}$$

The expression for dissipation related to the internal hardening variable by inserting for $\dot{\varrho}^r$ from Eq. (2.15) becomes

$$\sum_{r=1}^{N} X^r \dot{\zeta}^r = \frac{1}{2}\mu\xi \sum_{r=1}^{N}\sum_{s=1}^{N} h^{rs}\dot{\varrho}^r = \frac{1}{2}\mu\xi \sum_{r=1}^{N}\sum_{s=1}^{N} h^{rs}\left[\left(\frac{\sqrt{\sum_{u=1}^{N} b^{ru}\varrho^u}}{\kappa_c} - d_c\varrho^r\right)|\dot{\gamma}^r|\right]. \tag{5.40}$$

Inserting previous equation in (5.11) gives the residual dissipation of the form:

$$D_{res} = \sum_{r=1}^{N}\left(|\tau^r| - \frac{1}{2}\mu\xi\left[\sum_{s=1}^{N} h^{rs}\left(\frac{\sqrt{\sum_{u=1}^{N} b^{ru}\varrho^u}}{\kappa_c} - d_c\varrho^r\right)\right]\right)|\dot{\gamma}^r|. \tag{5.41}$$

Moreover, in the present work, the evolution of the isotropic hardening variable τ_c^r is assumed to be of the form:

$$\tau_c^r = \tau_0 + \mu\sqrt{\sum_{s=1}^{N} h^{rs}\varrho^s}. \tag{5.42}$$

The following two simplified cases can be considered to ensure the positivity of the residual dissipation in Eq. (5.41) by imposing constraints on the model parameters.

Case 1: It is assumed that all components of the dislocation interaction matrix h^{rs} and b^{rs}, which determine the Taylor stress τ_c^r and dislocation mean free path, respectively, are unity such that

$$D_{res} = \sum_{r=1}^{N}\left(|\tau^r| - \frac{1}{2}\mu\xi\left[\left(\frac{\sqrt{\sum_{u=1}^{N}\varrho^u}}{\kappa_c} - d_c\varrho^r\right)\right]\right)|\dot{\gamma}^r|, \tag{5.43}$$

which further can be written as

$$D_{res} = \sum_{r=1}^{N}\left(|\tau^r| - \frac{\mu\xi}{2\kappa_c}\sqrt{\sum_{u=1}^{N}\varrho^u} + \frac{1}{2}\mu\xi d_c\varrho^r\right)|\dot{\gamma}^r|. \tag{5.44}$$

The residual dissipation in the previous equation can also be expressed by using τ_c^r as follows:

$$D_{res} = \sum_{r=1}^{N}\left(|\tau^r| - \tau_c^r + \tau_0 + \mu\sqrt{\sum_{u=1}^{N}\varrho^u} - \frac{\mu\xi}{2\kappa_c}\sqrt{\sum_{u=1}^{N}\varrho^u} + \frac{1}{2}\mu\xi d_c\varrho^r\right)|\dot{\gamma}^r|, \tag{5.45}$$

which further gives

$$D_{res} = \sum_{r=1}^{N} \left((|\tau^r| - \tau_c^r) + \tau_0 + \mu \sqrt{\sum_{u=1}^{N} \varrho^u} \left[1 - \frac{\xi}{2\kappa_c} \right] + \frac{1}{2} \mu \xi d_c \varrho^r \right) |\dot{\gamma}^r|. \tag{5.46}$$

The residual dissipation inequality ($D_{res} \geq 0$) of the previous equation holds when $|\dot{\gamma}^r|$ is 0 or the corresponding terms in the brackets are positive. The first term in the brackets is a Schmid-type yield function (Eq. (5.17)) which is positive. The third term can be made positive by imposing constraints on the model parameter κ_c such that $\kappa_c \geq \frac{\xi}{2}$. Besides, $\tau_0 \geq 0$ and the last term of the previous equation is also positive.

Case 2: It is assumed that the dislocation interaction matrices h^{rs} and b^{rs} are diagonal matrices with all diagonal components equal to 1 such that the evolution of the isotropic hardening variable τ_c^r becomes

$$\tau_c^r = \tau_0 + \mu \sqrt{\varrho^r}, \tag{5.47}$$

and (5.41) can be expressed as follows:

$$D_{res} = \sum_{r=1}^{N} \left((|\tau^r| - \tau_c^r) + \tau_0 + \mu \sqrt{\varrho^r} \left[1 - \frac{\xi}{2\kappa_c} \right] + \frac{1}{2} \mu \xi d_c \varrho^r \right) |\dot{\gamma}^r|. \tag{5.48}$$

The residual dissipation inequality ($D_{res} \geq 0$) in the previous equation holds when $|\dot{\gamma}^r|$ is 0 or the corresponding terms in the brackets are positive. The first term in the brackets of the previous equation is a yield function of the flow rule (Eq. (5.17)) which is positive. The third term can be made positive by imposing constraints on the model parameter κ_c such that $\kappa_c \geq \frac{\xi}{2}$. Besides, $\tau_0 \geq 0$ and the last term of the previous equation is also positive.

Explicit expressions for the free energy density function are typically not provided in dislocation density-based models in contrast to phenomenological models. These expression assists in establishing the constitutive framework in a thermodynamic manner. In this study, we analytically demonstrated that the positivity of the residual dissipation in dislocation density-based models could be ensured by imposing constraints on the model parameters.

In the present work, general case of residual dissipation presented in Eq. (5.41) is considered. Furthermore, in the simulations, the positivity of the residual dissipation is ensured by checking the monotonic increase of temperature with the deformation. In the next sections, expressions used for predicting the stored energy, Taylor-Quinney coefficient, and temperature evolution in the context of classical and micromorphic crystal plasticity models are summarized.

5.3 Expression for stored energy, temperature rise and Taylor-Quinney coefficient

In this section, the expressions used for numerical prediction of the stored energy, temperature evolution, and TQC are summarized.

Expressions in the context of classical crystal plasticity

- **Stored energy**

The expression for the stored energy based on the proposed thermodynamically consistent framework, cf. Eq. (5.38), for the classical crystal plasticity model is given by

$$E_c = \rho_0 \sum_{r=1}^{N} \tilde{\Psi}^r(\zeta^r) = \frac{1}{2}\mu\xi \sum_{r=1}^{N} (\zeta^r)^2, \quad \text{with} \quad \zeta^r = \sqrt{\sum_{s=1}^{N} h^{rs}\varrho^s}. \tag{5.49}$$

The volume averaged stored energy over whole FE model is given by

$$E^c_{avg} = \frac{1}{V}\int_V E_c \, dV. \tag{5.50}$$

- **Total adimensional dislocation density**

$$\varrho_s = \sum_{r=1}^{N} \varrho^r_0 + \int_0^t \sum_{r=1}^{N} \dot{\varrho}^r dt \tag{5.51}$$

The volume averaged adimensional dislocation density over whole FE model is given by

$$\varrho_{avg} = \frac{1}{V}\int_V \varrho_s \, dV. \tag{5.52}$$

- **Temperature evolution under adiabatic conditions**

The temperature evolution for the classical crystal plasticity model can be given by

$$\dot{T} = \frac{\underset{\sim}{\Pi}^M : \dot{\underset{\sim}{F}}^p \underset{\sim}{F}^{p-1} - X\dot{\zeta}}{\rho C_\varepsilon}. \tag{5.53}$$

Inserting (5.11) and (5.40) into the previous equation gives

$$\dot{T} = \frac{\sum_{r=1}^{N} \tau^r \dot{\gamma}^r - \frac{1}{2}\mu\xi \sum_{r=1}^{N}\sum_{s=1}^{N} h^{rs}\dot{\varrho}^r}{\rho C_\varepsilon}. \tag{5.54}$$

• **Taylor-Quinney coefficient (TQC)**

The *integral* form of TQC is given by

$$\beta_{int} = \frac{\int_0^t \sum_{r=1}^{N} \tau^r \dot{\gamma}^r \, dt - \frac{1}{2}\mu\xi \int_0^t \sum_{r=1}^{N}\sum_{s=1}^{N} h^{rs} \dot{\varrho}^r \, dt}{\int_0^t \sum_{r=1}^{N} \tau^r \dot{\gamma}^r \, dt}. \tag{5.55}$$

The volume averaged Taylor-Quinney coefficient over whole FE model is given by

$$\beta_{avg} = \frac{1}{V}\int_V \beta_{int} \, dV. \tag{5.56}$$

Expressions in the context of micromorphic crystal plasticity

• **Stored energy**

We assume that an inelastic part of the free energy function which includes the contribution of GNDs along with SSDs to be of the form given by

$$\Psi = \tilde{\Psi}(\zeta^r, e_p, \underline{K}). \tag{5.57}$$

Moreover, it is assumed that the free energy density function can additively be decomposed as

$$\rho_0 \Psi = \rho_0 \sum_{r=1}^{N} \tilde{\Psi}^r(\zeta^r) + \rho_0 \tilde{\Psi}(e_p) + \rho_0 \tilde{\Psi}(\underline{K}). \tag{5.58}$$

The quadratic form of the free energy function, $\rho_0 \tilde{\Psi}^r(\zeta^r)$, associated with the internal hardening variable ζ^r is given in Eq. (5.49). This free energy function takes into account the contribution of SSDs. The quadratic form of the free energy E_p related to the e_p is given by

$$E_p = \rho_0 \tilde{\Psi}(e_p) = \frac{1}{2} H_\chi e_p^2, \quad \text{with} \quad e_p = \gamma_{cum} - \gamma_\chi. \tag{5.59}$$

Furthermore, the quadratic form of the free energy E_g, which includes the characteristic length scale and takes into account the contribution of GNDs, is given by

$$E_g = \rho_0 \tilde{\Psi}(\underline{K}) = \frac{1}{2} A \underline{K} \cdot \underline{K}, \quad \text{with} \quad \underline{K} = \frac{\partial \gamma_\chi}{\partial \underline{X}} = \text{Grad}\, \gamma_\chi. \tag{5.60}$$

Therefore, from Eq. (5.40), (5.60) and (5.59) the free energy function in (5.57) becomes

$$E_s = \rho_0 \sum_{r=1}^{N} \tilde{\Psi}^r(\zeta^r) + \rho_0 \tilde{\Psi}(e_p) + \rho_0 \tilde{\Psi}(\underline{K}) = \frac{1}{2}\mu\xi \sum_{r=1}^{N} (\zeta^r)^2 + \frac{1}{2} H_\chi e_p^2 + \frac{1}{2} A \underline{K} \cdot \underline{K}. \tag{5.61}$$

The volume averaged stored energy over whole FE model is given by

$$E^{p}_{avg} = \frac{1}{V}\int_{V} E_p \, dV, \quad E^{g}_{avg} = \frac{1}{V}\int_{V} E_g \, dV, \quad E^{s}_{avg} = \frac{1}{V}\int_{V} E_s \, dV. \tag{5.62}$$

• Temperature evolution under adiabatic conditions

The temperature evolution for the micromorphic crystal plasticity model is given by Eq. (4.37). Inserting (5.11) and (5.40) into (4.37) gives

$$\dot{T} = \frac{\sum_{r=1}^{N} \tau^r \dot{\gamma}^r + S\dot{\gamma}_{cum} - \frac{1}{2}\mu\xi \sum_{r=1}^{N}\sum_{s=1}^{N} h^{rs}\dot{\varrho}^r}{\rho C_\varepsilon}. \tag{5.63}$$

• Taylor-Quinney coefficient (TQC)

The *integral* form of TQC is given by

$$\beta_{int} = \frac{\int_0^t \sum_{r=1}^{N} (\tau^r \dot{\gamma}^r + S\dot{\gamma}_{cum})\, dt - \frac{1}{2}\mu\xi \int_0^t \sum_{r=1}^{N}\sum_{s=1}^{N} h^{rs}\dot{\varrho}^r \, dt}{\int_0^t \sum_{r=1}^{N} (\tau^r \dot{\gamma}^r + S\dot{\gamma}_{cum})\, dt}. \tag{5.64}$$

The volume averaged Taylor-Quinney coefficient over whole FE model is given by Eq. (5.56).

5.4 Single crystals simulations

5.4.1 Simulation setup

In a preliminary study, simulations are performed for aluminum and copper single crystals subjected to tensile loading to predict the evolution of stored energy and TQC. FE simulations are performed based on the constitutive framework of classical crystal plasticity model presented in section 4.2.1 and 4.2.2. Besides, simulations are performed with a simplified geometry of 0.06 mm × 0.06 mm × 0.06 mm cube having 8 C3D8 type elements which are 8 node linear brick elements. The applied boundary conditions are presented in Fig. 5.1.

Two orientations of the single crystal considered are <001> and <111> such that the [001] and [111] crystal direction align with the loading direction, respectively. In FCC crystals, the crystallographic slip occurs on the 12 {111}<110> slip systems (see Table A.1). The experimental stress-strain responses from the work of (Hosford et al., 1960) for single crystals aluminum and (Takeuchi, 1975) for single crystals copper are used to calibrate

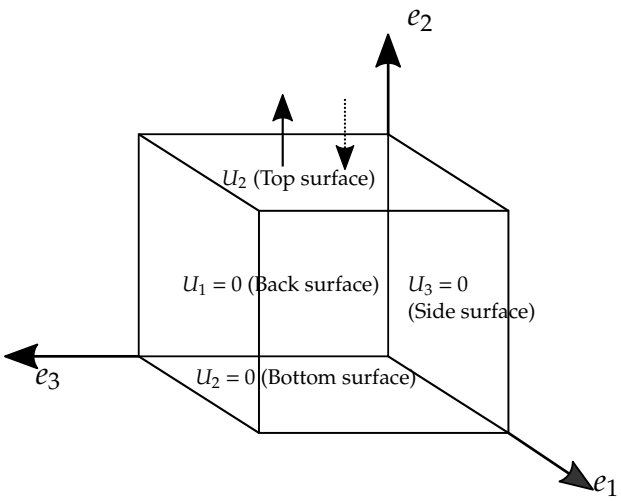

Fig. 5.1 Schematic showing the applied boundary conditions, namely BC1, in single and poly-crystalline simulations.

Table 5.1 Euler angles for the crystal orientations with misorientation of $< 1°$(Abrivard, 2009).

Crystal orientations	Euler angles (°)
<001>	$\phi_1 = 0.4,\ \phi = 1.0\ ,\ \phi_2 = 0.0$
<111>	$\phi_1 = 54.8,\ \phi = 135.0\ ,\ \phi_2 = 180.0$

material parameters. A misorientation of $< 1°$ is applied from the tensile axis as in the experimental tests of (Hosford et al., 1960) and (Takeuchi, 1975). The corresponding Euler angles are given in Table 5.1. All their experiments were performed at room temperature and applied strain rates of 7.5×10^{-5} s^{-1} and 10^{-3} s^{-1} for single crystals aluminum and copper, respectively. Simulations are performed with these strain rates.

5.4.2 Results and discussion

• <001> and <111> crystal orientations

The dislocation density-based hardening model captures the stress-strain responses in good agreement with the experimentally measured responses for <001> and <111> crystal orientations as shown in Fig. 5.2. The material hardening parameter κ_c mainly governs the initial slope of the stress-strain curve, while parameter d_c controls the saturation. Numerical values of the material constants and fitted material parameters for the single crystals aluminum and copper are summarized in Table 5.2 and 5.3, respectively. The material parameters are fitted using <001> crystal orientation (Fig. 5.2). The tensile axis <001> and <111> are oriented for multi-slip with 8 and 6 equally favored slip systems, respectively. The initial hardening rate of the <111> crystal orientation is higher than <001> crystal orientation. The initial dislocation density $\rho^r (= \varrho_0^r / b^2)$ is assumed to be $1 \times 10^{10}\,\mathrm{m}^{-2}$

Table 5.2 Material constants and fitted material parameters for the simulations of single crystals aluminum under tensile loading. The interaction matrix coefficients ($h_0 - h_5$) are taken from (Kubin et al., 2008).

C_{11}	C_{12}	C_{44}	ρ Eq. (5.54)	C_ε Eq. (5.54)	τ_0 (fitted) Eq. (5.42)	b
108 GPa	61.3 GPa	28.5 GPa	2700 kg m^{-3}	900 Jkg^{-1}K^{-1}	0.6 MPa	0.286 nm
μ	ϱ_0^r (fitted) Eq. (5.51)	K (fitted) Eq. (2.12)	m (fitted) Eq. (2.12)	κ_c (fitted) Eq. (2.15)	d_c (fitted) Eq. (2.15)	h_0 Eq. (5.42)
27 GPa	8×10^{-10}	0.5 MPa.s$^{1/m}$	5	27	100	0.122
h_1 Eq. (5.42)	h_2 Eq. (5.42)	h_3 Eq. (5.42)	h_4 Eq. (5.42)	h_5 Eq. (5.42)	ξ Eq. (5.49)	
0.122	0.07	0.625	0.137	0.122	1	

Table 5.3 Material constants and fitted material parameters for simulations of the single crystals copper under tensile loading. The interaction matrix coefficients ($h_0 - h_5$) are taken from (Kubin et al., 2008).

C_{11}	C_{12}	C_{44}	ρ Eq. (5.54)	C_ε Eq. (5.54)	τ_0 (fitted) Eq. (5.42)	b
170 GPa	124 GPa	75 GPa	8960 kgm^{-3}	385 Jkg^{-1}K^{-1}	0.5 MPa	0.257 nm
μ	ϱ_0^r (fitted) Eq. (5.51)	K (fitted) Eq. (2.12)	m (fitted) Eq. (2.12)	κ_c (fitted) Eq. (2.15)	d_c (fitted) Eq. (2.15)	h_0 Eq. (5.42)
41 GPa	8×10^{-10}	0.5 MPa.s$^{1/m}$	4	20	25	0.122
h_1 Eq. (5.42)	h_2 Eq. (5.42)	h_3 Eq. (5.42)	h_4 Eq. (5.42)	h_5 Eq. (5.42)	ξ Eq. (5.49)	
0.122	0.07	0.625	0.137	0.122	1	

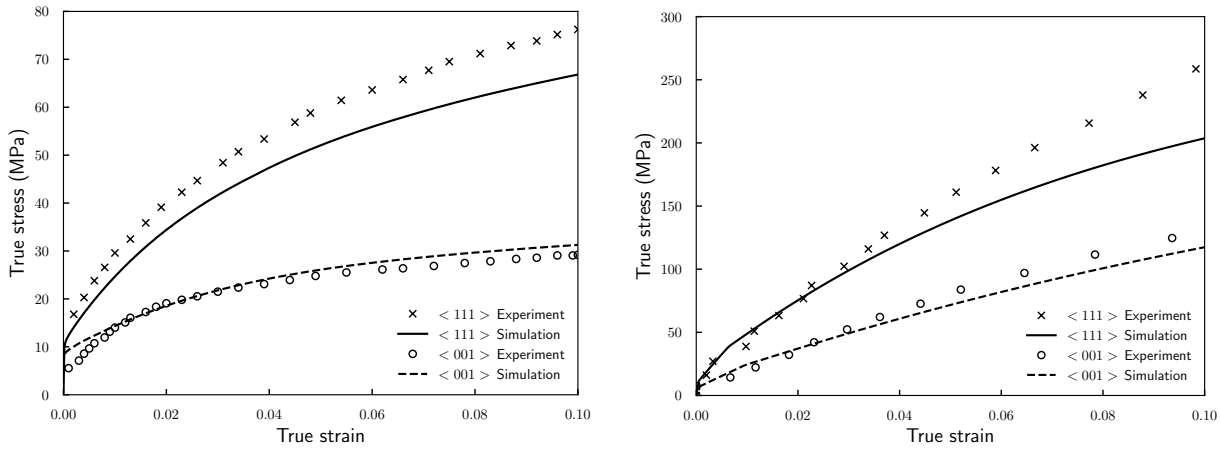

(a) (b)

Fig. 5.2 Comparison of stress-strain responses for <001> and <111> crystal orientations at 298K temperature: (a) aluminum single crystals validated against the experimental results of (Hosford et al., 1960), and (b) copper single crystals validated against the experimental results of (Takeuchi, 1975).

for both single crystals and chosen the same for all slip systems. The total dislocation density evolution for single crystals aluminum and copper is presented in Fig. 5.3a and 5.3b, respectively. As shown in these figures, the dislocation density increases rapidly and saturates with further increase in plastic strain.

The stored energy is predicted using a thermodynamically consistent formulation of the classical crystal plasticity model, (cf. Eq. (5.38)). Fig. 5.4 shows that the stored energy is strongly orientation dependent. Similar to the dislocation density evolution, the stored energy increases rapidly and saturates with further increase in plastic strain. The variation of TQCs for single crystals aluminum and the copper is shown in Fig. 5.5a and 5.5b, respectively. These figures show that the TQCs predicted for the single crystals aluminum and copper remain above the commonly used value of 0.9 because of the negligible difference between plastic power and stored energy rate.

The experimental measurements of TQC are available in the literature for single crystal copper of <123> orientation. In the next section, numerically predicted TQC is compared with experimental measurements for this particular crystal orientation.

• <123> crystal orientation

Rittel et al. (2012) measured the TQC for single crystal copper of <123> orientation under compressive loading subjected to quasi-static and high strain rates deformation. The average TQC values were in the range of $0.2-0.3$ in quasi-static deformation while $0.65-0.85$ in high-strain rates deformation. To compare the experimentally measured TQC values, simulations are performed with <123> crystal orientation subjected to compressive loading with direction [123] parallel to the loading direction.

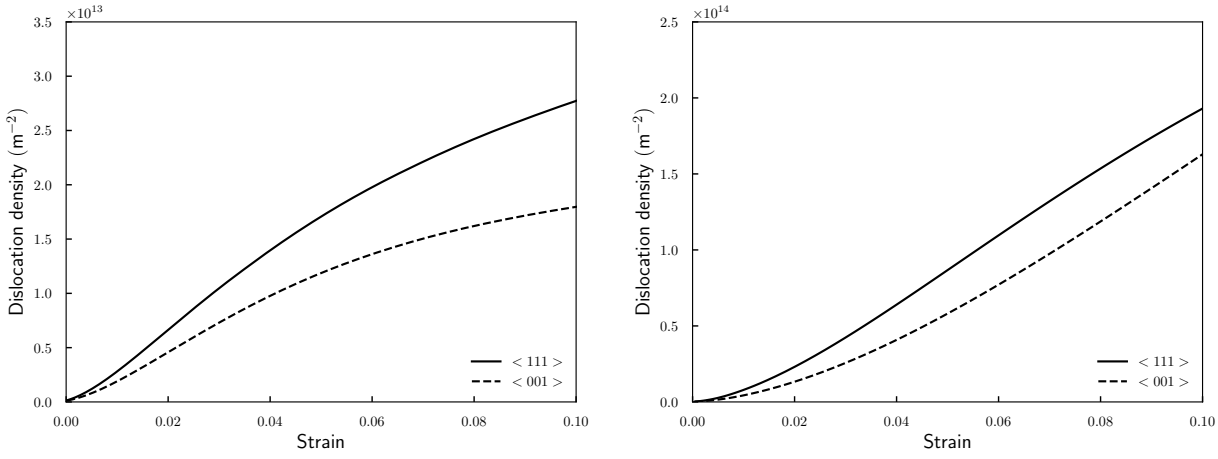

(a) (b)

Fig. 5.3 Predicted dislocation densities $\rho^r (= \varrho_0^r / b^2)$ within the single crystals (<001> and <111>) at an initial temperature of 298 K for (a) aluminum and (b) copper.

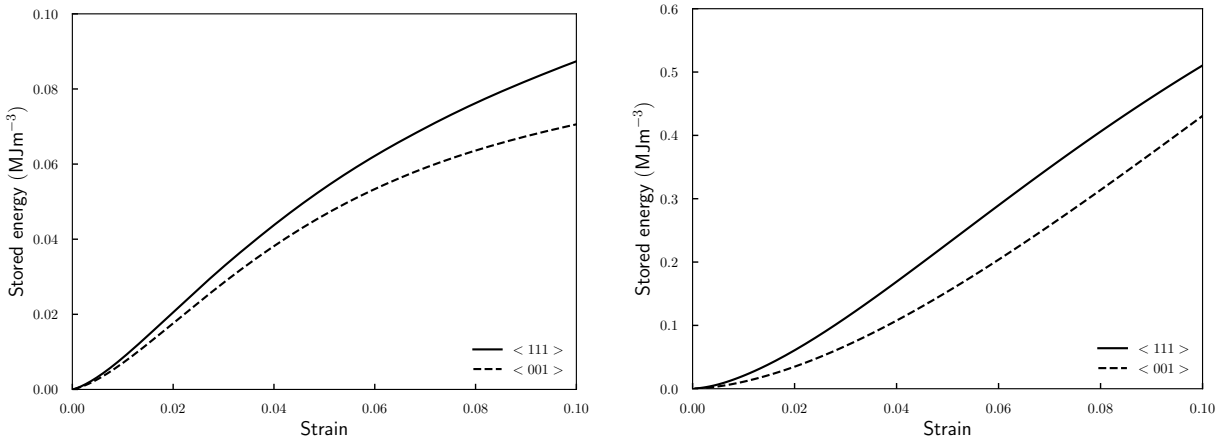

(a) (b)

Fig. 5.4 Predicted stored energy using the thermodynamically consistent formulation (Eq. (5.49)) for the single crystals (<001> and <111>) at an initial temperature of 298 K for (a) aluminum and (b) copper.

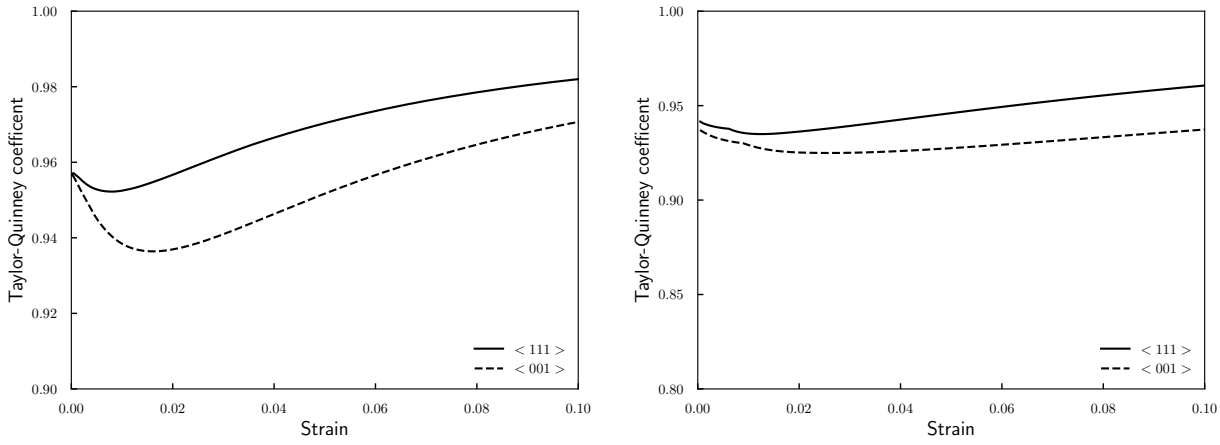

(a) (b)

Fig. 5.5 Predicted Taylor-Quinney coefficient (β_{int}) using the thermodynamic formulation (Eq. (5.55)) for the single crystals (<001> and <111>) at an initial temperature of 298 K for (a) aluminum and (b) copper.

The material parameters used in simulations are given in Table 5.3. The experimentally measured stress-strain responses and corresponding predicted responses are shown in Fig. 5.6a. The <123> compression axis is oriented for single slip. The used viscosity parameters capture the strain rate sensitivity observed in the experimental work. However, a discrepancy can be observed in overall stress-strain responses. A reason for this discrepancy may be that numerically <123> crystal orientation triggers a single slip at the initial deformation stage, but multiple slip systems are activated in a later stage. The effect of boundary conditions on the responses is also investigated in the next section.

The predicted dislocation density evolution using boundary conditions shown in Fig. 5.1 is presented in Fig. 5.6b. The predicted stored energy and TQCs at two strain rates (0.1 $s^{-1}$and 3000 s^{-1}) are shown in Fig. 5.7a and 5.7b, respectively. The high strain rate deformation stores more energy compared to low strain rate where heat dissipation is dominant (Fig. 5.7a). Moreover, the predicted TQCs are higher than the experimentally measured values by Rittel et al. (2012) (Fig. 5.7b). One of the possible reasons for this discrepancy can be that total dislocation density predicted by the model is significantly lower than the actual experimental values which were not measured. The total dislocation density necessary to predict the stored energy and consequently the TQC need to be at least of the order of $10^{15}\,m^{-2}$. However, the dislocation density obtained by numerical simulations is of the order of $10^{14}\,m^{-2}$ (Fig. 5.6b). To use an analytical expression of stored energy (Eq. (5.38)) in numerical predictions, a reliable dislocation density-based model may be necessary accounting for the total dislocation density. Another possible reason can be the analytical expression of the stored energy itself, which does not take into account all the mechanisms responsible for the stored energy.

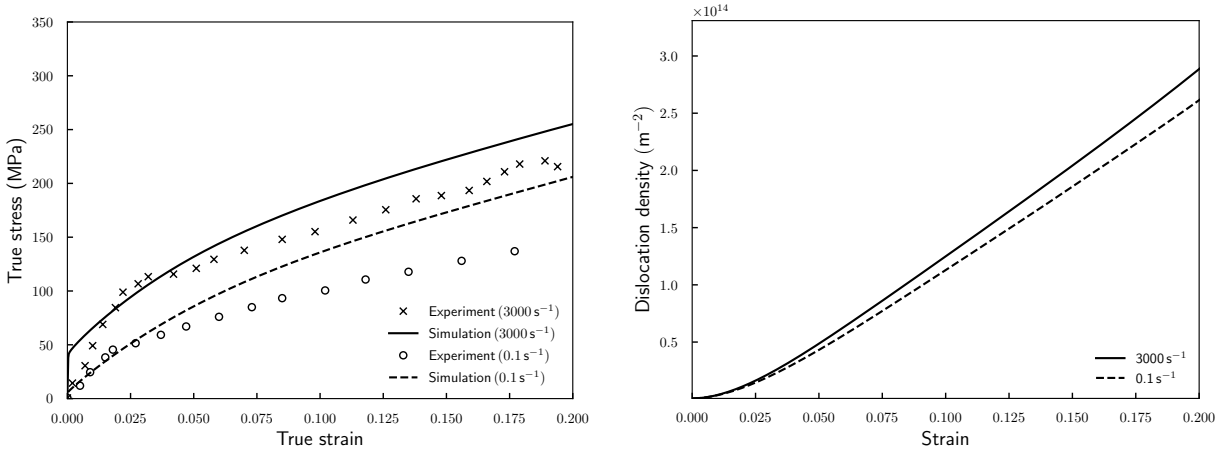

(a) (b)

Fig. 5.6 (a) Comparison of stress-strain responses against the experimental data obtained from the work of (Rittel et al., 2012) for single crystal copper (<123>) under compressive loading using boundary condition BC1 (Fig. 5.1). (b) Predicted dislocation density $\rho^r (= \varrho^r / b^2)$ evolution at two different strain rates for single crystal copper (<123>).

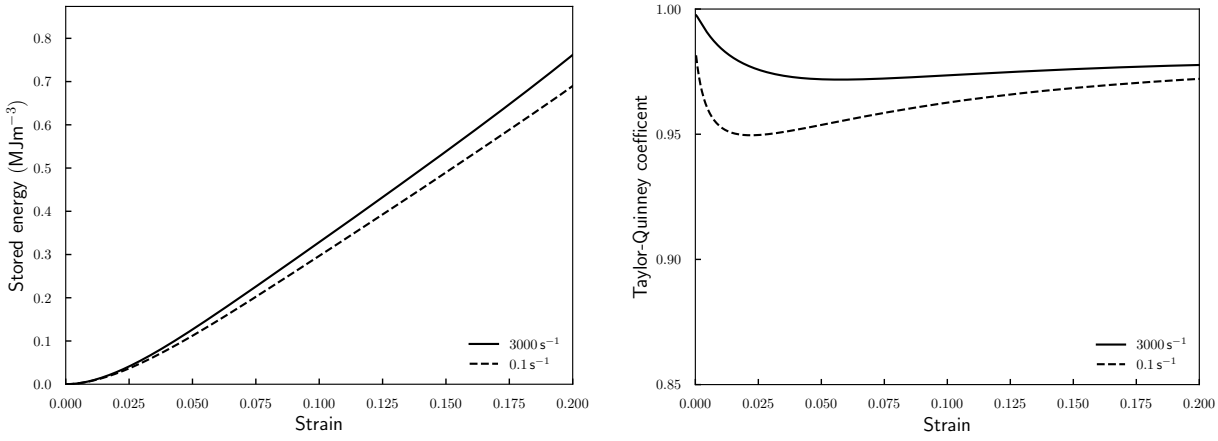

(a) (b)

Fig. 5.7 Evolution of the predicted (a) stored energy according to Eq. (5.49) and (b) Taylor-Quinney coefficient (Eq. (5.55)) for single crystal copper (<123>) with $\xi = 1$ under compressive loading using boundary condition BC1 (Fig. 5.1).

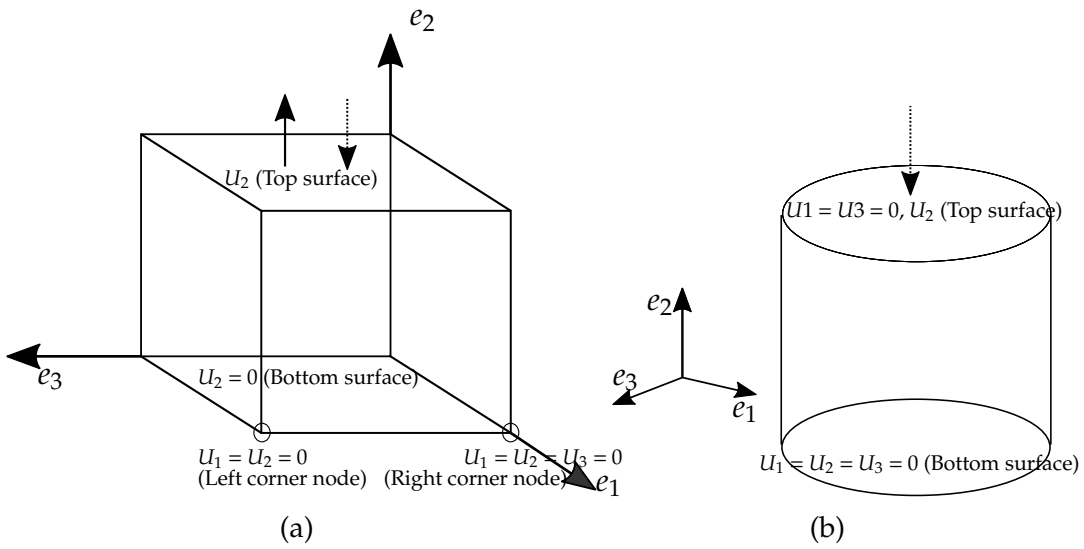

Fig. 5.8 Schematic showing the alternative boundary conditions applied in single crystal copper simulations (a) BC2 and (b) BC3.

- **Effect of boundary conditions on the stress-strain response**

To investigate the effect of boundary conditions on the responses, the simulations are performed with two alternative boundary conditions, namely BC2 and BC3, presented in Fig. 5.8a and 5.8b, respectively. The material parameters used in simulations are summarized in Table 5.3. The specimen geometry considered for the BC2 is as described in section 5.4.1. On the other hand, for the BC3, a cylindrical specimen having a diameter of 6 mm and height 6 mm as in the experimental work of (Rittel et al., 2012) is considered. The geometry is discretized with 1000 C3D8 elements. The predicted stress-strain responses for <001> and <111> crystal orientations using BC2 and corresponding experimental responses are presented in Fig. 5.9. As presented in these figures, the predicted stress-strain responses with BC2 are in good agreement with the experimental responses. Besides, the predicted responses for <123> crystal orientation with BC2 and BC3 are shown in Fig. 5.10a and 5.10b, respectively. These figures show that the discrepancy still exist with the alternative boundary conditions. The BC2 boundary conditions give a too soft responses, while BC3 gives a too stiff responses compared to experimental results.

5.5 Polycrystals simulations

In this section, polycrystalline simulations are performed to predict the stored energy and TQC. First of all, study of the effect of mesh size and grain morphology on the volume averaged stress-strain responses over whole FE model and local fields is performed. Next, the prediction of stored energy and TQC is carried out using the classical crystal plasticity model, i.e. considering contribution of SSDs only. Finally, a comparison of the predicted

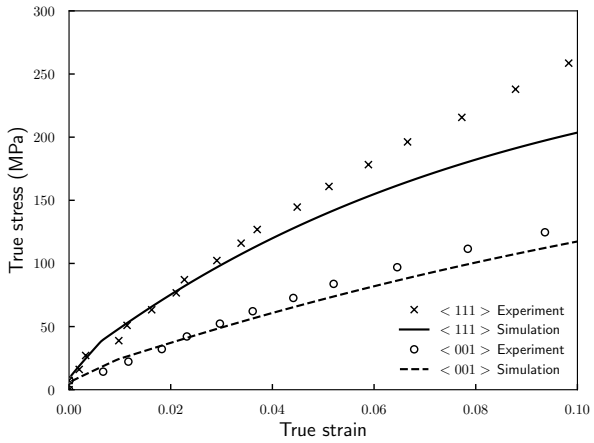

Fig. 5.9 Comparison of stress-strain responses using boundary condition BC2 for <001> and <111> copper single crystal against the experimental data obtained from the work of (Takeuchi, 1975) under tensile loading.

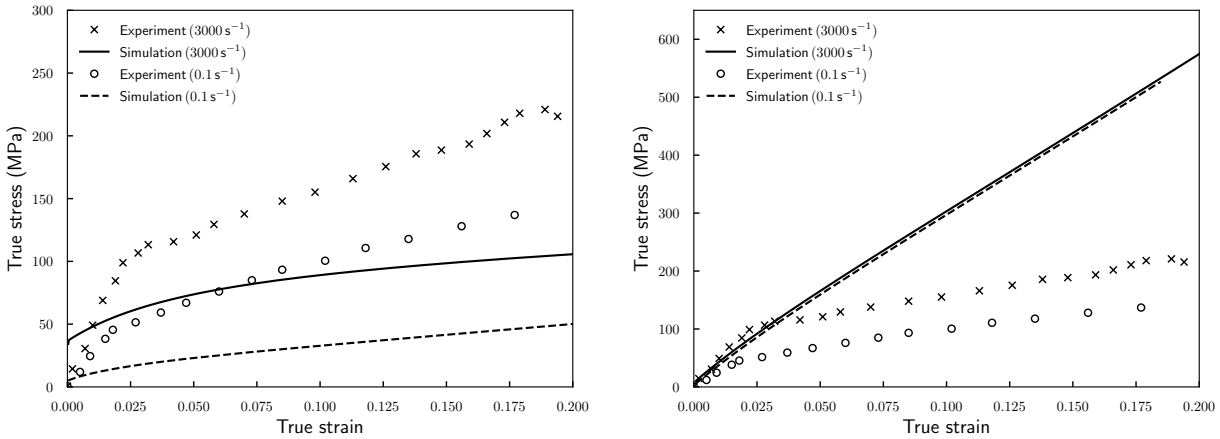

(a) (b)

Fig. 5.10 Comparison of stress-strain responses for <123> crystal orientation against the experimental data obtained from the work of (Rittel et al., 2012) under compressive loading using boundary condition (a) BC2 (Fig. 5.8a) and (b) BC3 (Fig. 5.8b).

stored energy by considering both the contribution of SSDs and GNDs to that of the simulations with contribution of SSDs only is performed.

5.5.1 Effect of mesh size and grain morphology

In general, RVEs with cubic meshes are used to predict the texture evolution and the global stress-strain responses, for instance, in (Kalidindi et al., 1992; Alankar et al., 2009). They found that the global stress-strain curves using RVEs having cubic meshes are well represented. However, the local fields inside grains were not considered. The more realistic microstructure can be presented using dodecahedra, for instance, in (Mika and Dawson, 1998, 1999). In addition, a more realistic shape of the grains can be represented by the meshes generated using Voronoï tessellation as in (Barbe et al., 2001a; Diard et al., 2005). Some studies are devoted to include experimentally determined 3D microstructure in crystal plasticity modeling so that the local fields and global stress-strain responses can be compared to experimental results, for instance in (Musienko et al., 2007).

• RVEs with cubic meshes

In this work, a detailed study of the effect of mesh size and grain morphology on the stress-strain behavior is performed using the classical crystal plasticity model according to section 4.2.1 and 4.2.2. At first, three RVEs of $0.3\,\text{mm} \times 0.3\,\text{mm} \times 0.3\,\text{mm}$, discretized with structured mesh using C3D20R elements, which are 20 node quadratic reduced integration brick elements, are considered for the study (Fig. 5.11). Furthermore, each RVE consists of 64 grains assigned with random orientations. To study the mesh size effect, each grain of the RVE is discretized with 1 element (Fig. 5.11a), 8 elements (Fig. 5.11b), and 27 elements (Fig. 5.11c). The material parameters used in this polycrystalline study are given in Table 5.3. Besides, the applied boundary conditions to the RVE are presented in Fig. 5.1.

The predicted volume averaged stress-strain responses over whole FE model using three RVEs consisting of the structured mesh are displayed in Fig. 5.12a. The stress-strain curves obtained using RVE having 27 elements per grain show softer response compared to RVEs with 1 and 8 elements per grain (keeping 64 grains per RVE). In addition, tests are performed to study the effect of the number of grains on the stress-strain behavior using RVEs having 64, 512, and 1000 grains (keeping 1 elements per grain). Fig. 5.12b show that there is no considerable effect of number of grains on the stress-strain behavior.

• RVEs generated by Voronoï tessellations

In addition to cuboidal grains, RVEs of $0.3\,\text{mm} \times 0.3\,\text{mm} \times 0.3\,\text{mm}$ are generated by Voronoï tessellations (see Fig. 5.13). To study the effect of mesh size, RVE of 64 grains is meshed with two different mesh sizes, namely the *coarse* (1774 nodes, 8274 elements) and *fine* (16402 nodes, 85251 elements) using C3D4R elements, which are 4 node linear reduced integration tetrahedral elements. The cumulative plastic strain fields are shown in Fig. 5.15. As shown

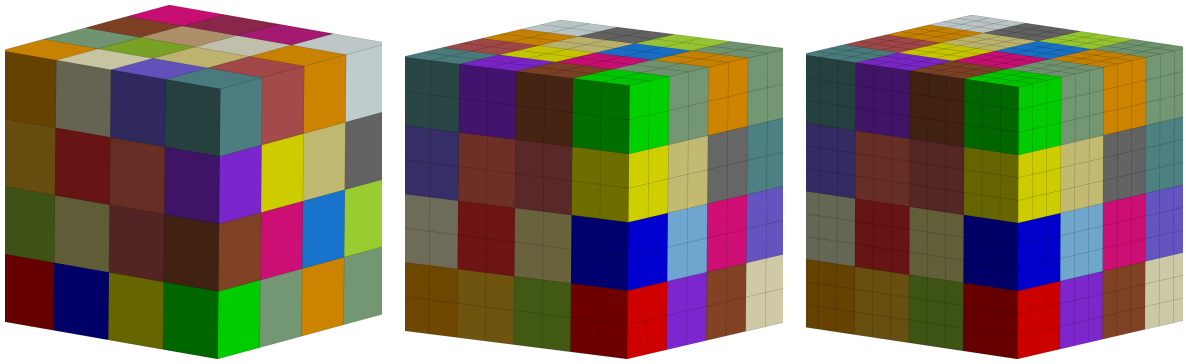

(a) (b) (c)

Fig. 5.11 Structured FE mesh; 64 grains with random orientation: (a) 1 element per grain, (b) 8 elements per grain, and (c) 27 elements per grain. Color represents the individual grains.

in these figures, *fine* meshed RVE captures the heterogeneity of the local fields in contrast to almost homogeneous field predicted by *coarse* meshed RVE. This suggests that more elements per grain or fine enough mesh size within the grain is required to predict the heterogeneity of the local fields. Moreover, the predicted stress-curves are shown in Fig. 5.16a. From this figure, the *fine* meshed RVE show stiffer response compared to *coarse* meshed RVE (keeping the same total number of grains in both RVEs).

In addition to the effect of mesh size, the effect of grain morphology on the averaged stress-strain response is studied. Three RVEs considered for the study are with 64, 125, and 200 grains (Fig. 5.14). The predicted averaged stress-strain curves are shown in Fig. 5.16b. This figure shows that no significant difference between the predicted averaged stress-strain curves is observed with changing the total number of grains in the RVE. However, it may give a softer response by further increasing the total number of grains as observed in the simulations of RVEs with cuboidal grains.

This study shows that the 64-grain RVE having cuboidal grains with 27 elements per grain and 64 grain *fine* meshed RVE generated by Voronoï tessellations give a satisfactory global stress-strain response. Concerning the prediction of local fields, a fine enough mesh size is necessary for each grain. For further study on the prediction of stored energy and TQC, both RVEs mentioned above are used.

5.5.2 Prediction of stored energy considering contribution of SSDs

In this section, firstly, stored energy and TQC are predicted for the polycrystalline austenitic steel under tensile loading considering contribution of only SSDs (using the classical crystal plasticity model). The predicted stored energy is compared with the experimental data obtained from the work of (Oliferuk et al., 1993). Then the application is made to predict the stored energy in Inconel 718 under compressive loading at high strain rates and high temperatures.

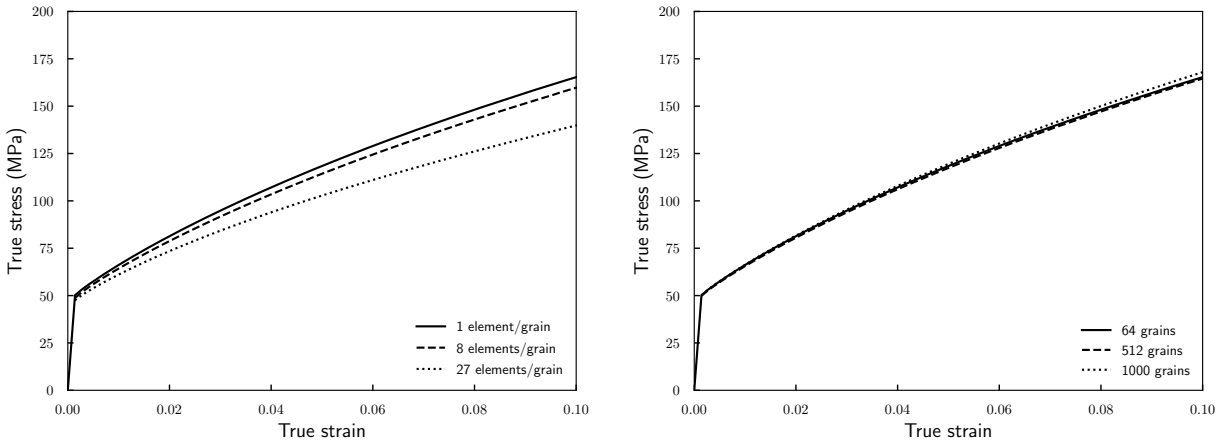

(a) (b)

Fig. 5.12 Volume averaged stress-strain responses over whole FE model obtained under tensile loading using cuboidal grains to study the effect of (a) number of elements per grain (RVE of 64 grains) and (b) total number of grains in the RVE (1 element per grain).

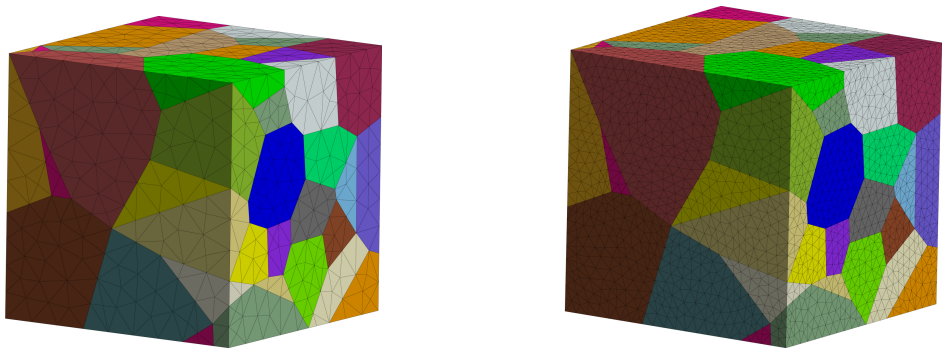

(a) (b)

Fig. 5.13 FE mesh of grains generated by Voronoï tessellation; 64 grains with random orientation: (a) *coarse* (1774 nodes, 8274 elements) and (b) *fine* (16402 nodes, 85251 elements) meshed. Color represents the individual grains.

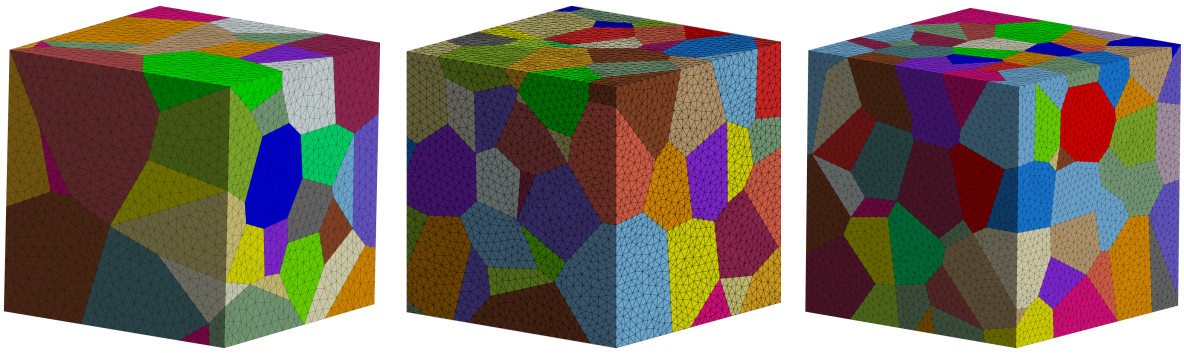

(a) (b) (c)

Fig. 5.14 RVE generated by Voronoï tessellation: (a) 64 grains, (b) 125 grains, and (c) 200 grains. Color represents the individual grains.

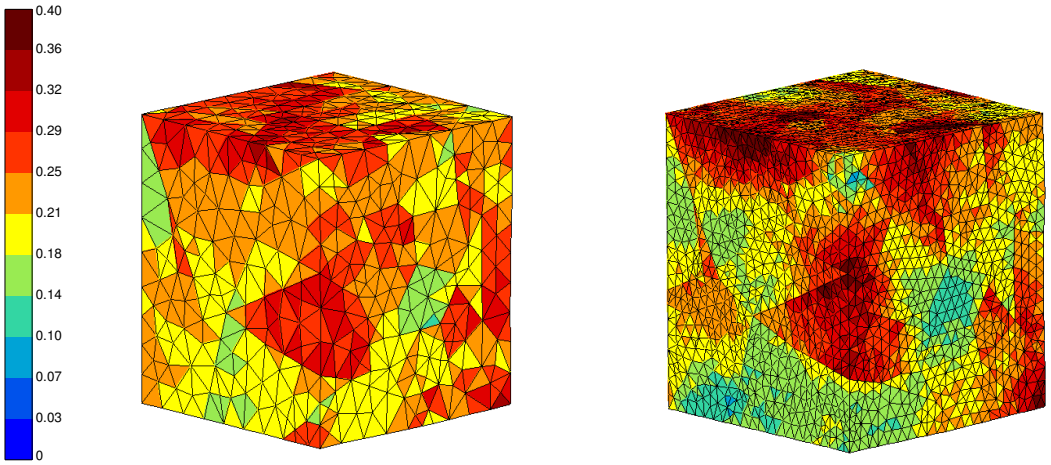

(a) (b)

Fig. 5.15 Cumulative plastic strain fields in unstructured FE mesh for the tensile loading of polycrystalline copper using 64 grains Voronoï tessellation assigned with random orientation: (a) *coarse* and (b) *fine* meshed. The fields are shown on the deformed configuration.

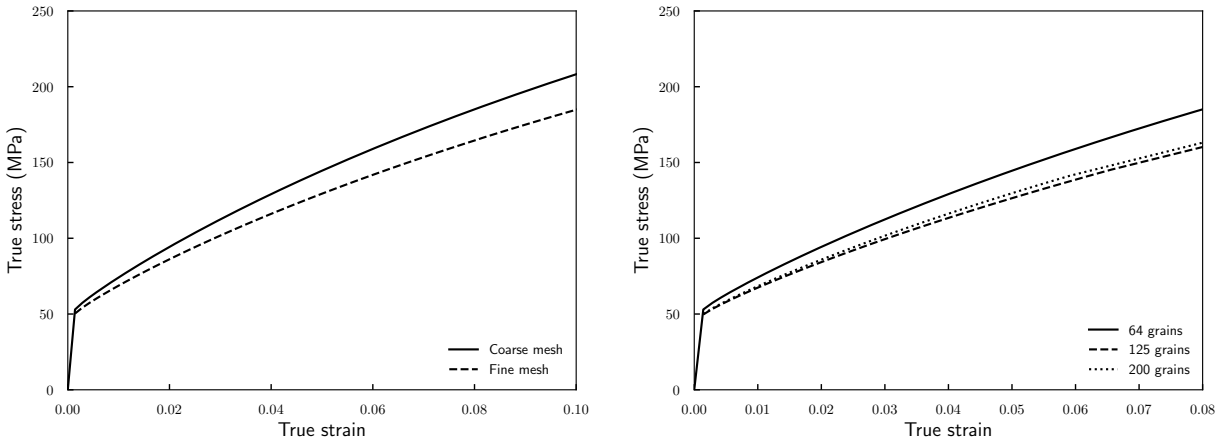

(a) (b)

Fig. 5.16 Volume averaged stress-strain responses over whole FE model obtained using grains created by Voronoï tessellation to study the effect of (a) mesh size (RVE of 64 grains) and (b) total number of grains in the RVE.

• Stored energy and TQC in polycrystalline austenitic steel

The material parameters τ_0, ϱ_0^r, κ_c, d_c, K, and m are calibrated against the experimental stress-strain data of (Oliferuk et al., 1993) for an average grain size of 80 µm. The coefficients of interaction matrix ($h_0 - h_5$) are adopted from the work of (Hure et al., 2016). The initial dislocation density $\rho^r (= \varrho_0^r / b^2)$ is assumed to be $1 \times 10^{10}\,\mathrm{m}^{-2}$ and chosen the same for all slip systems. The RVE of $0.27\,\mathrm{mm} \times 0.27\,\mathrm{mm} \times 0.27\,\mathrm{mm}$ is used to describe the polycrystalline austenitic steel. It is generated using Voronoï tessellation having 64 grain assigned with a random orientation. Besides, each grain of the RVE is approximately of 80 µm size. The applied boundary conditions to the RVE are presented in Fig. 5.1. The fitted averaged stress-strain response against the experimental response is shown in Fig. 5.17a. The material constants and fitted material parameters are summarized in Table 5.4.

The prediction of stored energy and TQC is performed using the expressions (5.49) and (5.55), respectively. A comparison of the predicted volume average stored energy over whole FE model (Eq. (5.50)) with the classical crystal plasticity model using ξ of 1 against the experimental data of (Oliferuk et al., 1993) is shown in Fig. 5.17b. As shown in this figure, with $\xi = 1$ predicted stored energy is underestimated. Similar observations are also made in single crystal copper (<123> crystal orientation) simulations where numerically predicted stored energy and, consequently, the TQC is underestimated compared to experimental results (cf. section 5.4.2). Therefore, next, ξ is increased in such a way that it gives good agreement with the experimental measurements.

The predicted volume average stored energy over whole FE model with $\xi = 10$ is shown in Fig. 5.17b. This figure shows that with $\xi = 10$, the predicted stored energy is in line with the experimental measurements. Moreover, the evolution of TQC with strain is predicted using ξ of 1 and 10 (Fig. 5.18). The predicted evolution of TQC with $\xi = 1$ is varies between 0.95 to 0.98. The lowest value of TQC measured by (Oliferuk et al., 1993) was about 0.58. With $\xi = 10$, the predicted TQC is in the range of 0.55 to 0.70. The expression of stored energy given by Bailey (1963) for both polycrystalline silver and copper gives an *ad-hoc* factor of the order of 2 as explained in section 5.1. However, in this work, for polycrystalline austenitic steel based on the numerical simulations, we found an *ad-hoc* factor of the order of 10.

In the next section, simulations are performed on annealed Inconel 718 subjected to high strain rates and temperature compressive loading with $\xi = 10$ to check the predictability of the stored energy and TQC.

• Stored energy and TQC in Inconel 718

After emphasizing the importance of an *ad-hoc* factor in the prediction of stored energy and TQC, the application is made to polycrystalline Inconel 718 undergoing high strain rates and high temperatures compressive loading. The predicted stress-strain responses and corresponding experimental responses from the work of (Moretti et al., 2021) for the

Table 5.4 Numerical values of material parameters used for the numerical simulation of polycrystalline austenitic steel under tensile loading. The elastic constants and dislocation interaction coefficient are taken from (Hure et al., 2016).

C_{11}	C_{12}	C_{44}	ρ Eq. (5.54)	C_ε Eq. (5.54)	τ_0 (fitted) Eq. (5.42)	b
199 GPa	136 GPa	105 GPa	7965 kgm^{-3}	532 $\text{Jkg}^{-1}\text{K}^{-1}$	80 MPa	0.254 nm
μ	ϱ_0^r (fitted) Eq. (5.51)	K (fitted) Eq. (2.12)	m (fitted) Eq. (2.12)	κ_c (fitted) Eq. (2.15)	d_c (fitted) Eq. (2.15)	h_0 Eq. (5.42)
65.6 GPa	6.4×10^{-10}	10 $\text{MPa.s}^{1/m}$	15	19.4	22.8	0.124
h_1 Eq. (5.42)	h_2 Eq. (5.42)	h_3 Eq. (5.42)	h_4 Eq. (5.42)	h_5 Eq. (5.42)	A Eq. (5.61)	H_χ Eq. (5.61)
0.124	0.07	0.625	0.137	0.122	0.02 N	5×10^4 MPa
ξ Eq. (5.49)						
1 and 10						

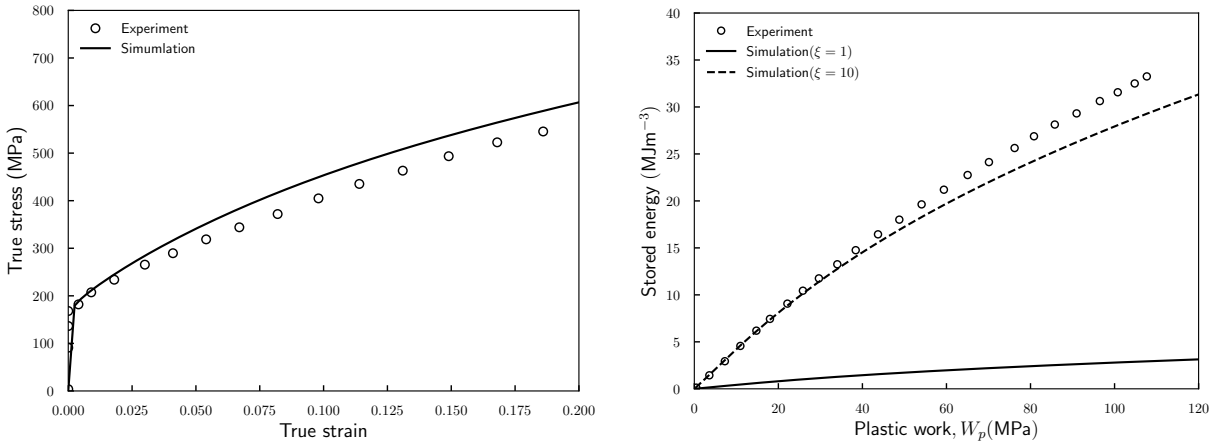

(a) (b)

Fig. 5.17 Polycrystalline austenitic steel under tensile loading: (a) averaged stress-strain curve validated against the experimental work of (Oliferuk et al., 1993), and (b) predicted volume averaged stored energy over whole FE model ($\xi = 1$ and 10) (Eq. (5.49), (5.50)) and comparison against the experimental measurements from the work of (Oliferuk et al., 1993).

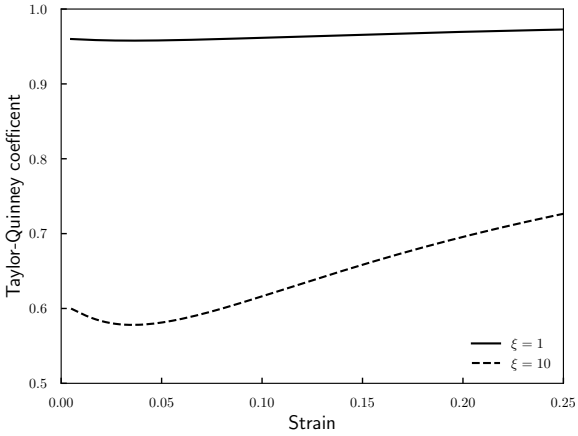

Fig. 5.18 Predicted evolution of volume averaged Taylor-Quinney coefficient over whole FE model (Eq. (5.55), (5.56)) using numerical simulations with two different values of an *ad-hoc* factor (1 and 10).

Table 5.5 Numerical values of material parameters used for the numerical simulation of polycrystalline Inconel 718 under compressive loading. The elastic constants and dislocation interaction coefficient are taken from (Kubin et al., 2008).

C_{11}	C_{12}	C_{44}	ρ Eq. (5.54)	C_ε Eq. (5.54)	b	μ
194 GPa	142 GPa	90 GPa	7800 kgm^{-3}	435 Jkg^{-1}K^{-1}	0.249 nm	77.2 GPa
ϱ_0^r (fitted) Eq. (5.51)	κ_c (fitted) Eq. (2.15)	d_c (fitted) (293K) Eq. (2.15)	d_c (fitted) (673K) Eq. (2.15)	d_c (fitted) (1073K) Eq. (2.15)	h_0 Eq. (5.42)	h_1 Eq. (5.42)
6.2×10^{-9}	18.8	18.4	31.4	42.4	0.124	0.124
h_2 Eq. (5.42)	h_3 Eq. (5.42)	h_4 Eq. (5.42)	h_5 Eq. (5.42)	ξ Eq. (5.49)		
0.07	0.625	0.137	0.122	10		

annealed specimens using the classical crystal plasticity model are shown in Fig. 5.19a. The material constants and fitted material parameters are summarized in Table 5.5. In addition, the material parameters τ_0, K, m are considered as temperature-dependent. These calibrated temperature-dependent material parameters are given in Table 5.6. Moreover, the constant parameter d_c in the dislocation density-based model, which controls the saturation of the stress-strain behavior, is taken as temperature-dependent (Table 5.5). The initial dislocation density $\rho^r (= \varrho_0^r/b^2)$ is assumed to be $1\times10^{11}\,\mathrm{m}^{-2}$ and chosen the same for all slip systems.

The material parameters are calibrated against the experimental stress-strain response at a temperature of 673 K and strain rate of $1900\,\mathrm{s}^{-1}$. There is no considerable difference in the strain rates used (1900 s^{-1} and 2000 s^{-1}); therefore, no significant effect of strain rates on the flow strength is observed. As a general trend, with increasing temperature, the flow strength of Inconel 718 decreases and consequently the plastic work and dislocation

Table 5.6 Temperature dependent material parameters used in the numerical simulations for the annealed Inconel 718. The temperature dependent τ_0 is used in the evolution of critical resolved shear stress given in Eq. (5.42). The temperature dependent viscosity parameter K and m are involved in rate–dependent flow rule according to Eq. (2.12).

Temperature (K)	τ_0 (MPa) Eq. (5.42)	K(MPa.s$^{1/m}$) Eq. (2.12)	m Eq. (2.12)
298	210	5	10
923	150	5	10
1073	80	8	6
1173	60	17	4.5
1323	10	40	4
1523	1	50	2

density. The dislocation density evolution is shown in Fig. 5.19b. As shown in this figure, the dislocation density rapidly increases in an initial deformation stage and saturates in the later deformation stage. Moreover, samples deformed at lower temperatures show higher dislocation density evolution than those deformed at a high temperature. Note that the calibrated material parameters of Inconel 718 presented in chapter 4 are for the aged samples against the experimental work of (Iturbe et al., 2017). The stored energy evolution is shown in Fig. 5.20a. The stored energy evolution shows a similar trend as dislocation density evolution. It increases rapidly at the initial stage of deformation and saturates with a further increase in deformation. Moreover, the evolution of TQCs is displayed in Fig. 5.20b. From this figure, the predicted lowest value of TQC using $\xi = 10$ is 0.825. As discussed in the previous section, polycrystalline austenitic steel shows a lowest TQC value of 0.58 with $\xi = 10$ (Fig. 5.18).

This study suggests that the precise determination of ξ needs experimental calibration. Moreover, ξ parameter vary from material to material and may depend on the strain rate, temperature, and type of loading.

5.5.3 Prediction of stored energy considering contribution of SSDs and GNDs

In this section, the stored energy and TQC are predicted considering contribution of both SSDs and GNDs, i.e. using the micromorphic crystal plasticity model. The predicted stored energy is compared with the predictions made by considering the contribution of SSDs only, i.e. using the classical crystal plasticity model. The constitutive framework of the micromorphic crystal plasticity model used in this study can be found in section 4.2.3. The analytical expressions used for the prediction of the stored energy and TQC are given in Eq. (5.61) and (5.64), respectively.

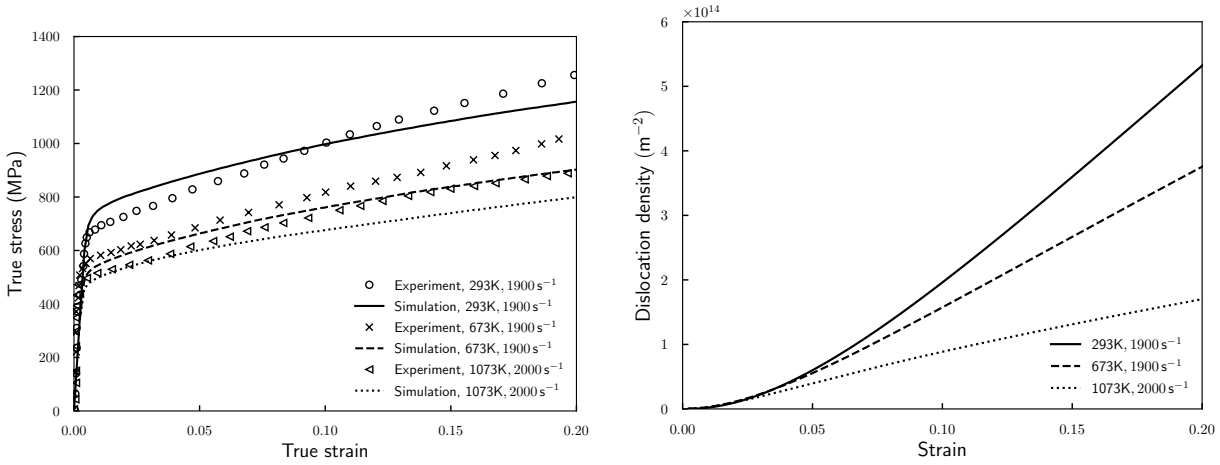

(a) (b)

Fig. 5.19 Annealed Inconel 718 under compressive loading: (a) predicted averaged stress-strain curves at high strain rates (1900 s^{-1}-2000 s^{-1}) and high initial temperatures (293 K-1273 K) and comparison against the experimental data obtained from the work of (Moretti et al., 2021) and (b) predicted evolution averaged dislocation density (Eq. (5.52)) as a function of strain.

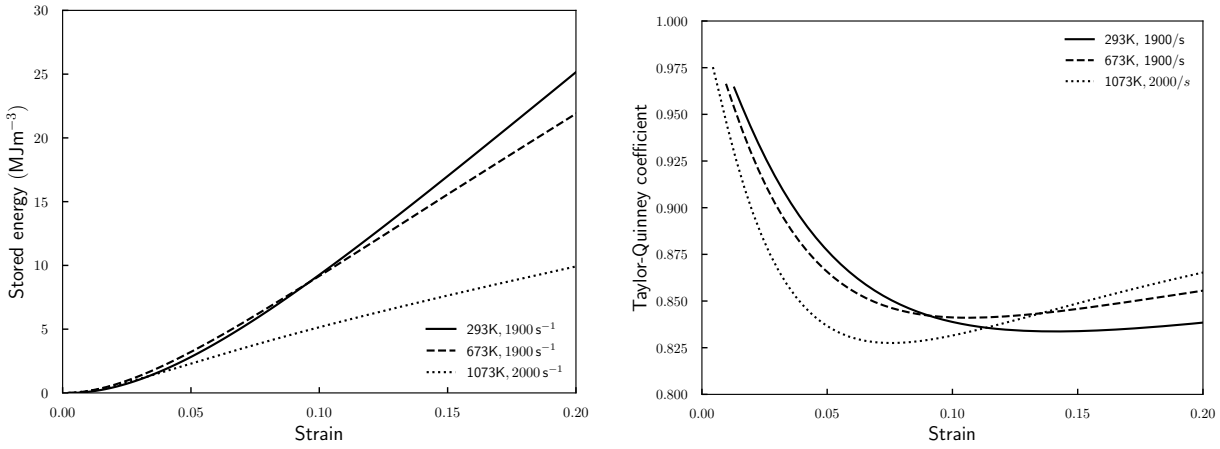

(a) (b)

Fig. 5.20 Predicted evolution of volume averaged (a) stored energy (Eq. (5.49), (5.50)) and (b) Taylor-Quinney coefficient (Eq. (5.55), (5.56)) as a function of strain for Inconel 718 under compressive loading using $\xi = 10$.

The material constants and calibrated material parameters are summarized in Table 5.4. The grain boundary conditions are considered as an *intermediate* between *microfree* and *microhard* conditions. The microslip variable γ_χ is assumed to be continuous at the interface. The surface traction $\underline{T}$ and generalized surface traction M in Eq. (2.21) are also continuous. The gradient parameter A is chosen as 0.02 N such that predicted stress-strain response remains close to experimental response obtained from the work of (Oliferuk et al., 1993). The fitted average stress-strain response against the experimental data is shown in Fig. 5.21a. The expression used for the characteristic length scale is given by $\ell = \sqrt{\frac{A(H+H_\chi)}{|H|H_\chi}}$. The hardening modulus H is found by the procedure described in section 3.3.2.3. The calculated characteristic length scale is about 2 µm ($A = 2\times10^{-2}$ N, $H_\chi = 5\times10^4$ MPa, and $H = 3000$ MPa). The calibration of gradient parameter and consequently the characteristic length scale is possible based on the tensile stress-strain responses obtained at different grain sizes. However, in this study only one grain size is considered.

Stored energy is predicted using an *ad-hoc* factor ξ of 1. The comparison of the predicted stored energy using the classical and micromorphic crystal plasticity models is shown in Fig. 5.21b. This figure shows that the predicted volume averaged stored energy over whole FE model using the micromorphic crystal plasticity model is higher than that of the classical crystal plasticity model. The classical crystal plasticity model lacks a characteristic length scale that is associated with the GNDs. On the other hand, the presence of characteristic length scale in the micromorphic crystal plasticity model can take into account the contribution of GNDs along with SSDs and therefore gives an increased total dislocation density and, consequently, the stored energy.

The contribution of each term in the micromorphic crystal plasticity model to the total stored energy, refer to Eq. (5.61), is presented in Fig. 5.22a. As shown in this figure, the contribution of term E^c_{avg}, which takes into account the contribution of SSDs is higher than E^g_{avg} and E^p_{avg} ($E^c_{avg} > E^g_{avg} > E^p_{avg}$). The contribution of GNDs in total stored energy is taken account by the term E_g (Eq. (5.60)).

Furthermore, additional simulations are performed with microhard grain boundary conditions. The microhard grain boundary conditions corresponds to vanishing microslip γ_χ at the grain boundaries, i.e. $\gamma_\chi = 0$. This grain boundary condition is accomplished by setting the nodal values of γ_χ on the grain surface to zero. The comparison of the obtained responses using microhard with $A = 2\times10^{-2}$ N and 2×10^{-5} N to that of the results from the experimental test is presented in Fig. 5.22b. The response obtained using $A = 2\times10^{-2}$ N is too strong compared to experimental results. On the other hand, $A = 2\times10^{-5}$ N gives a significantly lower response than $A = 2\times10^{-2}$ N. However, the gradient parameter A should be reduced further for more realistic predictions. A comparison of the predicted total stored energy with *intermediate* and *microhard* grain boundary conditions is shown in Fig. 5.23. The predicted total stored energy with the microhard grain boundary conditions is significantly higher than that of the intermediate grain boundary conditions due to the high hardening rate obtained due to the former grain boundary conditions.

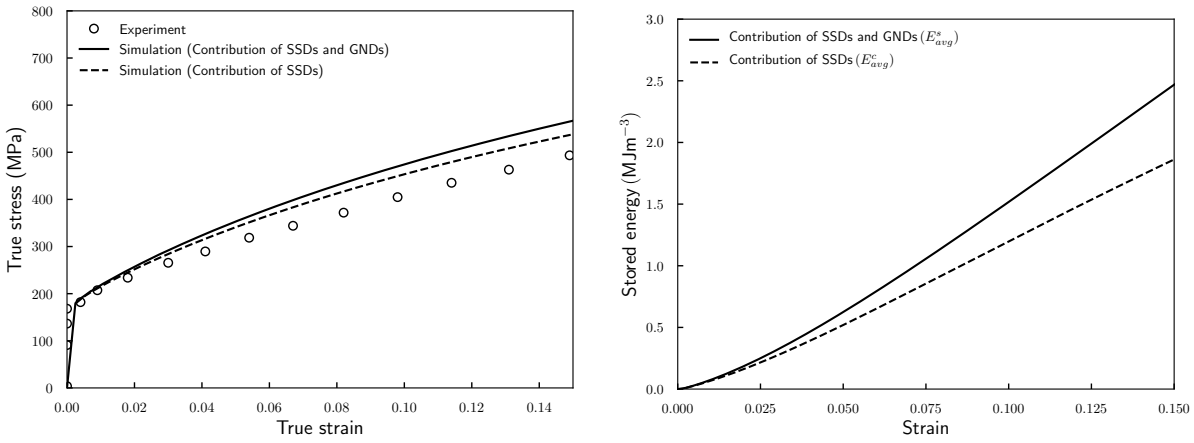

(a) (b)

Fig. 5.21 Polycrystalline austenitic steel under tensile loading: (a) average stress-strain responses predicted considering the contribution of SSDs and GNDs, and SSDs only. (b) Predicted evolution of volume averaged stored energy (using $\xi = 1$) considering the contribution of SSDs and GNDs (Eq. (5.61), (5.62)), and SSDs only (Eq. (5.49), (5.50)). The stress-strain responses are validated against the experimental work of (Oliferuk et al., 1993).

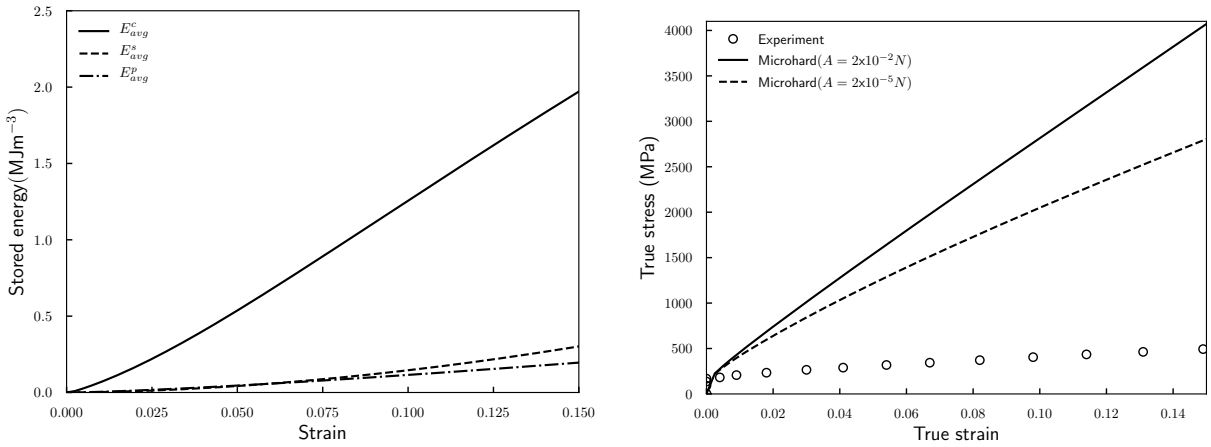

(a) (b)

Fig. 5.22 (a) Contribution of each term to the total stored energy in micromorphic crystal plasticity model (Eq. (5.61)). (b) Predicted stress-strain responses using microhard grain boundary condition using $A = 2\times10^{-2}$ N and 2×10^{-5} N. The experimental stress-strain responses are from the work of (Oliferuk et al., 1993).

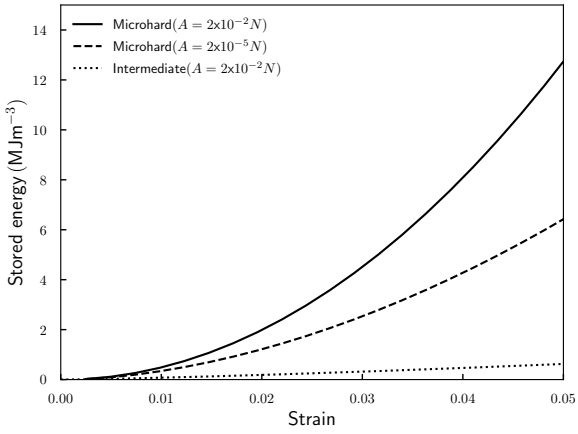

Fig. 5.23 Comparison of the predicted volume averaged stored energy (Eq. (5.61), (5.62)) over whole FE model using *microhard* and *intermediate* grain boundary conditions with $\xi = 1$.

The grain boundary conditions play an essential role in polycrystals as they affect the dislocation motion and hence, the strain hardening behavior. The microfree and microhard grain boundary conditions respectively lead to lower and upper bounds for the polycrystal response. These two grain boundary conditions do not apply to all sorts of grain boundary behavior as they cannot capture the underlying physics. One approach to obtain interface behavior between these two extreme conditions is by introducing interface energy as in (Aifantis and Willis, 2005). The intermediate grain boundary conditions, for instance, in (Fredriksson and Gudmundson, 2006; Ekh et al., 2011; Husser et al., 2017) with finite resistance against the dislocation gliding gives more realistic dislocation-grain boundary interactions. More general grain boundary conditions have been proposed allowing for the transition from microhard conditions to microfree (or constant generalized tractions) once a threshold is reached at the grain boundary by Wulfinghoff and Böhlke (2013).

5.6 Conclusions

The numerical simulation work presented in this chapter was intended to provide an insight into the prediction of the stored energy and evolution of TQC in single and poly-crystalline FCC metallic materials. The following conclusions can be drawn from the study:

- It is necessary to check the positivity of the residual dissipation in the local balance equation. Failure to do so can violate the first and second laws of thermodynamics. We analytically demonstrated using simplified cases that the positivity of the residual dissipation rate in dislocation density-based models could be ensured by imposing constraints on the model parameters.
- The numerical prediction of stored energy and TQC for aluminum and copper single crystals (<001> and <111> crystal orientations) is performed using the classical

crystal plasticity model. The predicted TQC values for aluminum and copper single crystals are higher than the common value of 0.9. The experimentally measured average TQC values from the work of (Rittel et al., 2012) for single crystals copper having <123> orientation was in the range of $0.2 - 0.3$ in quasi-static deformation while $0.65 - 0.85$ in high-strain rates deformation. However, in the present study numerically predicted values are in the range of $0.95 - 0.98$ for both quasi-static and high strain rate deformation. This suggests that a reliable dislocation density-based model is necessary to predict the dislocation density and consequently the stored energy and TQC in line with the experimental measurements.

- In the polycrystalline simulations, the role of an *ad-hoc* factor ξ is discussed. The value of $\xi = 1$ underestimates the predicted stored energy compared to the experimentally measured values for the austenitic steel. On the other hand, predicted stored energy with $\xi = 10$ shows good agreement with the experimentally measured values.

- A comparison of the predicted stored energy considering the contribution of SSDs only to that of the prediction made by considering the contribution of both SSDs and GNDs is carried out using the *intermediate* grain boundary conditions. It is found that the predicted stored energy is moderately higher in a latter consideration.

- The *microhard* grain boundary conditions show too strong response compared to experimental results. The material hardening parameters which takes into account the contribution of SSDs should be calibrated using the classical crystal plasticity model for single crystals. The calibration of gradient parameter A and consequently the characteristic length scale which takes into account the contribution of GNDs should be performed using the micromorphic crystal plasticity model based on the experimental stress-strain responses obtained using different grain sizes.

Chapter 6

Implementation of micromorphic plasticity theory in commercial FE software

The work presented in this chapter is performed by collaborating with ESI Group and **Raffaele Russo** (ESR5), a Ph.D. student at the University of the Basque Country - UPV/EHU and Mines ParisTech.

Abstract

Good quality manufacturing operation simulations are essential to obtain reliable numerical predictions of the processes. In many cases, it is possible to observe that the deformation localizes in narrow areas, and since the primary deformation mode is under shear, these areas are called shear bands. In classical continuum mechanics models, the deformation localization may lead to spurious mesh dependency if the material locally experiences thermal or plastic strain softening. One option to regularize such a non-physical behavior is to resort to non-local continuum mechanics theories. This paper adopts a scalar micromorphic approach, which includes a characteristic length scale in the constitutive framework to enforce the plastic strain gradient theory to regularize the solution. Since many manufacturing process simulations are often assessed through finite element methods with an explicit solver to facilitate convergence, we present an original model formulation and procedure for the implementation of the micromorphic continuum in an explicit finite element code. The approach is illustrated in the case of the VPS explicit solver from ESI Group. According to the original formulation, we propose an easy way to implement a scalar micromorphic approach by taking advantage of an analogy with the thermal balance equation. The numerical implementation is verified against the analytical solution of a semi-infinite glide problem. Finally, the correctness of the method is addressed by successfully predicting size effects both in a cutting and a bending tests.

This chapter has been submitted to a journal.

6.1 Introduction

The micromorphic scheme has been proven to be a straightforward and relatively simple procedure to govern an additional degrees of freedom or additional state variables of the continuum to achieve non-local regularization effects (Forest, 2009, 2016b). It has been used already in several other contributions (Poh et al., 2011; Anand et al., 2012; Mazière and Forest, 2013; Saanouni and Hamed, 2013; Diamantopoulou et al., 2017; Davaze et al., 2021). Among the cited works, the only ones to adapt and implement the micromorphic approach for an explicit time-dependent problems can be found in (Saanouni and Hamed, 2013; Diamantopoulou et al., 2017; Davaze et al., 2021). These authors presented a time-dependent framework, in which the governing equations for the micromorphic variables include a second-order time derivative of the micromorphic variables. Additional coefficients associated with this term were included to characterize the inertia of the micromorphic variables, a role that is usually assigned to the density of the governing equations of displacement fields. Furthermore, (Davaze et al., 2021) included some dissipation terms associated with the first-order time derivative of the micromorphic variable in governing equation so to avoid any oscillation of the solution caused by the form of the partial differential equation (PDE) (specifically induced by the presence of a second-order time derivative term). They used the theory to achieve mesh-regularization for fracture growth simulations in metals. Exploring the extent of such an approach for manufacturing operation simulations was not their target.

In this work, we make use of a scalar micromorphic approach to govern the strain gradient effect and to restore mesh independency. The classical continuum mechanics model is enhanced with one additional degree of freedom. The governing equation for such an additional variable will be directly derived by the definition of an internal power. The micromorphic approach will be used to control the distribution of the cumulative plastic strain. Therefore, the additional degree of freedom will be enforced to follow this quantity through a penalty term.

In this context, our contribution aims at investigating the size effect predictions and regularization properties of a time-dependent strain gradient plasticity theory. This theory is implemented through a scalar micromorphic framework using an explicit formulation, in which a viscous micromorphic-related variable is included, but no micromorphic inertia is present. The main novelty of the proposed method lies in the easiness of the implementation of the theory in an already-well-structured finite element solver. The framework that we will present can, in fact, simply be solved through a common thermal-field solver, and such crucial aspect will be properly addressed in the present chapter.

The formulation of the analytical model is provided in section 6.2 in which both the kinematics and the energetic aspects of the theory are presented, alongside its thermodynamic description, so that the recoverable and dissipative contributions are explicitly stated as such. The section concludes with the pivotal analogy between the thermal and the

micromorphic balance equations, which further simplifies any possible implementation of the theory in a FE software.

The layout of the chapter is as follows. Section 6.3 will be used to present a simple analytical solution that will be useful to verify the implementation of the model in a finite element framework. Finally, in Section 6.4 the numerical method will be used to simulate two manufacturing operations in which significant strain gradients effect are expected to take place, namely the shear/trimming operation and the bending test. The mesh-dependency will be analyzed, along with the size-effect in terms of cumulative plastic strain distribution. Conclusion follow in section 6.5.

6.2 Theoretical formulation: Micromorphic plasticity in explicit scheme

In this section, the theoretical formulation of the micromorphic plasticity model implemented in the explicit FE software VPS/Pam-Crash® from ESI is presented. At first, the kinematics of the theory will be provided, from which the balance equations can be derived, the definition of the Helmholtz free energy, and of the Clausius-Duhem inequality will follow. Finally, the section will conclude with the numerical implementation of micromorphic theory in VPS explicit.

6.2.1 Kinematics and balance equations

The kinematics of the model follows the one commonly used in the classical continuum mechanics. The second-order strain tensor is defined as

$$\underset{\sim}{\varepsilon} = sym[\underline{u} \otimes \underline{\nabla}], \tag{6.1}$$

with $\underline{u}$ being the displacement vector and $\underline{\nabla}$ denotes the gradient of a vector. Furthermore, the total strain tensor is additively decomposed into an elastic part $\underset{\sim}{\varepsilon}^e$ and a plastic part $\underset{\sim}{\varepsilon}^p$ as follows:

$$\underset{\sim}{\varepsilon} = \underset{\sim}{\varepsilon}^e + \underset{\sim}{\varepsilon}^p, \tag{6.2}$$

$$\dot{\underset{\sim}{\varepsilon}} = sym[\underline{v} \otimes \underline{\nabla}]. \tag{6.3}$$

where $\underline{v}$ is the velocity vector. Two types of DOF are applied to the material point: the classical displacement vector $\underline{u}$ and the additional scalar micromorphic variable p_χ associated with the cumulative plastic strain p through the penalty term H_χ. Then every node is endowed with 3 displacement and 1 micromorphic variable:

$$\text{DOF} = \{\underline{u}, p_\chi\}. \tag{6.4}$$

Based on the definition of the strain and micromorphic variable, we can write the internal and kinetic power densities of the body as dependent on the strain, the micromorphic variable and its gradient:

$$p^{(i)} = \underset{\sim}{\sigma} : \dot{\underset{\sim}{\varepsilon}} + a^* \dot{p}_\chi + \underline{b}^* \cdot \underline{\nabla} \dot{p}_\chi, \tag{6.5}$$

$$p^{(k)} = \rho \underline{\ddot{u}} \cdot \underline{\dot{u}}, \tag{6.6}$$

where ρ is the mass density and $\underline{\ddot{u}}$ is the acceleration vector. The parameters a^* and $\underline{b}^*$ are generalized stresses associated with the micromorphic variable and its gradient, respectively. In this formulation, the densities of power generated by external forces and contact forces can be written as follows:

$$p^{(e)} = \underline{f}^{(e)} \cdot \underline{\dot{u}} + a^e \dot{p}_\chi + \underline{b}^e \cdot \underline{\nabla} \dot{p}_\chi, \tag{6.7}$$

$$p^{(c)} = \underline{f}^c \cdot \underline{\dot{u}} + a^c \dot{p}_\chi, \tag{6.8}$$

with $\underline{f}^e$ being the density of body force, a^e and $\underline{b}^e$ are the generalized body stresses associated to p_χ and its gradient, respectively. In addition, $\underline{f}^c$ and a^c are the classical traction and the micromorphic traction, respectively. The contact power density defined in Eq. (6.8) clearly states that the gradient of the micromorphic variable is not linked to any boundary effect. The global power balance law can be written as:

$$\int_\Omega \left(p^{(i)} + p^{(k)} \right) d\Omega = \int_\Omega p^{(e)} d\Omega + \int_{\partial\Omega} p^{(c)} d\mathrm{S}, \tag{6.9}$$

which, through Eq. (6.5), (6.6), (6.7) and (6.8), transforms into:

$$\begin{aligned} \int_\Omega \underline{\dot{u}} \cdot [-\sigma \cdot \underline{\nabla} - \underline{f}^e + \rho \underline{\ddot{u}}] d\Omega + \int_\Omega \dot{p}_\chi [(\underline{b}^e - \underline{b}^*) \cdot \underline{\nabla} + a^* - a^e] d\Omega \\ + \int_{\partial\Omega} \underline{\dot{u}} \cdot [-\underline{f}^c + \underset{\sim}{\sigma} \cdot \underline{n}] dS + \int_{\partial\Omega} \dot{p}_\chi [-a^c + (\underline{b}^e - \underline{b}^*) \cdot \underline{n}] dS = 0. \end{aligned} \tag{6.10}$$

Based on the principle of virtual power (Forest, 2009), the equilibrium equations are obtained as:

$$\begin{cases} \rho \underline{\ddot{u}} = \underset{\sim}{\sigma} \cdot \underline{\nabla} + \underline{f}^e, & (6.11) \\ \left(\underline{b}^* - \underline{b}^e \right) \cdot \underline{\nabla} = a^* - a^e, & (6.12) \end{cases}$$

There is a possibility here to explicitly define the kinetic and damping energy of the continuum as function of the micromorphic variable as well. Such type of descriptions have already been proposed by other researchers, for instance, in (Nedjar, 2001; Saanouni and Hamed, 2013; Davaze et al., 2021). In the present work, however, we will include instead a viscous contribution of the micromorphic variable in the constitutive model of the continuum.

which are bounded by the following Neumann boundary conditions:

$$\begin{cases} \underset{\sim}{\sigma} \cdot \underline{n} = \underline{f}^c, & (6.13) \\ \left(\underline{b}^* - \underline{b}^e\right) \cdot \underline{n} = a^c, & (6.14) \end{cases}$$

where $\underline{n}$ is the outer normal to the surface closing the domain Ω.

6.2.2 Helmholtz free energy potential

The constitutive model of the medium characterizing the shape of both the classical and the generalized stresses are provided via the definition of their associated potential. The free energy density function is assumed to depend on the following state variables:

$$\Psi\{\underset{\sim}{\varepsilon}^e, p, p_\chi, \nabla p_\chi\}, \tag{6.15}$$

namely, the elastic strain $\underset{\sim}{\varepsilon}^e$, the cumulative plastic strain p, the micromorphic variable p_χ, and its gradient ∇p_χ. The chosen potential has the form:

$$\Psi(\underset{\sim}{\varepsilon}^e, p, p_\chi, \nabla p_\chi) = \frac{1}{2} \underset{\sim}{\varepsilon}^e : \underset{\approx}{\Lambda} : \underset{\sim}{\varepsilon}^e + \tilde{\Psi}(p) + \tilde{\Psi}(p, p_\chi, \nabla p_\chi) \tag{6.16}$$

where $\tilde{\Psi}(p)$ is the plastic contribution to the Helmholtz free energy (in case of hardening/softening it accounts for the expansion/shrinking of the yield surface in the stress space). The following linear isotropic plastic behavior is assigned to the material:

$$\tilde{\Psi}(p) = \frac{1}{2} H p^2, \tag{6.17}$$

with H being the hardening modulus. A simple quadratic potential gives

$$\tilde{\Psi}(p, p_\chi, \nabla p_\chi) = \frac{1}{2} H_\chi (p - p_\chi)^2 + \frac{1}{2} \nabla p_\chi \cdot \underset{\sim}{A} \cdot \nabla p_\chi \tag{6.18}$$

where $\underset{\sim}{A}$ is the gradient parameter assumed to be constant in space such that $\underset{\sim}{A} = A \underset{\sim}{I}$. Moreover, nonlinear hardening laws are possible but not considered here for simplicity.

6.2.3 Clausius-Duhem inequality

Expanding the time derivative of Helmholtz free potential with respect to the variables on which it depends, and by retrieving the additive elasto-plastic decomposition of the strain, the Clausius-Duhem inequality reads:

$$\left(\underset{\sim}{\sigma} - \frac{\partial \tilde{\Psi}}{\partial \underset{\sim}{\varepsilon}^e}\right) : \dot{\underset{\sim}{\varepsilon}}^e + \underset{\sim}{\sigma} : \dot{\underset{\sim}{\varepsilon}}^p + \left(a^* - \frac{\partial \tilde{\Psi}}{\partial p_\chi}\right) + \left(\underline{b}^* - \frac{\partial \tilde{\Psi}}{\nabla p_\chi}\right) \cdot \nabla \dot{p}_\chi - \frac{\partial \tilde{\Psi}}{\partial p} \dot{p} \geq 0. \tag{6.19}$$

Based on the Clausius-Duhem inequality following state laws can be derived:

$$\underset{\sim}{\sigma} = \frac{\partial \tilde{\Psi}}{\partial \underset{\sim}{\varepsilon}^e} = \underset{\approx}{\Lambda} : \underset{\sim}{\varepsilon}^e, \quad \underline{b}^* = \frac{\partial \tilde{\Psi}}{\nabla p_\chi}, \quad X_R = \frac{\partial \tilde{\Psi}}{\partial p}, \tag{6.20}$$

with X_R as the thermodynamic force associated to variation of the cumulative plastic strain. Regarding the dissipation produced by variation of the micromorphic variable, its positiveness can be ensured, as originally suggested by Gurtin (1996) and Forest (2009), by imposing that the generalized stress possesses a recoverable part and a dissipative part that depends on $\dot{p}_\chi$ itself:

$$a^* = \frac{\partial \tilde{\Psi}}{\partial p_\chi} + C_\chi \dot{p}_\chi, \tag{6.21}$$

where C_χ is a parameter related to viscous micromorphic effects. The residual dissipation rate can now be written as:

$$\sigma : \dot{\varepsilon}^p - X_R \dot{p} + C_\chi \dot{p}_\chi^2 \geq 0. \tag{6.22}$$

The positiveness of the new parameters A and C_χ then ensures the positive definiteness of the micromorphic contributions in the free energy density and in the dissipation rate.

6.2.4 Partial differential equation governing the micromorphic variable and enhanced hardening law

By considering the explicit definition of the Helmholtz free energy potential given in Eq. (6.18), the generalized stresses reads:

$$a^* = -H_\chi \left(p - p_\chi\right) + C_\chi \dot{p}_\chi, \quad \underline{b}^* = A \underline{\nabla} p_\chi. \tag{6.23}$$

The previous equation indicates that the micromorphic variable p_χ and the cumulative plastic strain p are related to each other through the penalty term H_χ. In order for the micromorphic variable to closely match the value of the cumulative plastic strain, it is necessary to ensure that the value of H_χ is relatively large. At this stage, it is possible to re-write the additional PDE governing the micromorphic distribution by plugging the selected constitutive behavior into it. In absence of higher-order body forces (a^e and $\underline{b}^e$), Eq. (6.12) can be written as:

$$C_\chi \dot{p}_\chi = A \nabla^2 p_\chi + H_\chi \left(p - p_\chi\right), \tag{6.24}$$

where ∇^2 indicates the Laplacian. The previous equation represent the only additional equation that must be solved combined with the ones governing the displacement fields.

Previous researchers already explored the potential of the micromorphic theory in rate-dependent analysis under explicit integration schemes using a modified version of Eq. (6.24). For instance, (Saanouni and Hamed, 2013) proposed a theory in which the the second-order time derivative of p_χ takes the place of the first-order time derivative in

Eq. (6.24). Therefore, in analogy with the PDE governing the displacement fields, a form of inertia was associated to the micromorphic variable, whereas, in case of the present investigation, a viscous term associated to the micromorphic variable is considered. The PDE governing the micromorphic field can be rewritten as:

$$\frac{C_\chi}{H_\chi}\dot{p}_\chi = \ell^2\nabla^2 p_\chi + (p - p_\chi) \quad \text{with,} \quad \ell = \sqrt{\frac{A}{H_\chi}}, \tag{6.25}$$

with ℓ being the characteristic length scale endowing the theory with the regularization and capturing size–dependent strengthening property. To fully solve (6.25), it must be coupled with a constitutive model for the plastic behavior of the medium. Starting from the yield function:

$$f(\underset{\sim}{\sigma}, X_R) = \sigma_{eq} - \sigma_0 - X_R, \tag{6.26}$$

where σ_{eq} is the von Mises equivalent stress measure and σ_0 is the initial yield stress. Assuming associated plasticity and the normality rule to hold, the rate of the plastic strain can be written as:

$$\dot{\underset{\sim}{\varepsilon}}^p = \dot{p}\frac{\partial f}{\partial \underset{\sim}{\sigma}} = \dot{p}\,\underset{\sim}{n}, \tag{6.27}$$

and the dissipation in Eq. (6.22) takes the form:

$$(\underset{\sim}{\sigma} : \underset{\sim}{n} - X_R)\,\dot{p} + C_\chi \dot{p}_\chi^2 \geq 0, \tag{6.28}$$

and in case of plastic loading:

$$(\sigma_{eq} - X_R)\,\dot{p} + C_\chi \dot{p}_\chi^2 = \sigma_0\,\dot{p} + C_\chi \dot{p}_\chi^2 \geq 0. \tag{6.29}$$

The thermodynamic force associated with the cumulative plastic strain can be given as follows:

$$X_R = H p + H_\chi (p - p_\chi). \tag{6.30}$$

6.2.5 Micromorphic-thermal analogy

The comparison between the scalar micromorphic model described in the previous section and the classical thermo-mechanical theory will be outlined here. The development of the latter theory will not be fully reported, but we will make use of the main governing equations of the thermal field to draw the comparison with the micromorphic theory previously developed. On the one hand, the additional variable in the present theory, p_χ, ought to be solved through the PDE (6.24), whereas, on the other hand, the additional degree of freedom of the classical thermo-mechanical theory, that is temperature T, must be solved through a different PDE, and here the two equations are reported (where the

Table 6.1 Analogy between the micromorphic gradient plasticity model and thermal analysis.

	Micromorphic	Heat
DOF	p_χ	T
Constitutive law	$\underline{b}^* = A\nabla p_\chi$	$\underline{q} = -k_t \nabla T$
Balance law	$C_\chi \dot{p}_\chi = A\,\nabla^2 p_\chi + H_\chi\left(p - p_\chi\right)$	$\rho C_\varepsilon \dot{T} = k_t\,\nabla^2 T + r$

Fourier conduction law is assumed to be valid for the heat flux)

$$C_\chi \dot{p}_\chi = A\nabla^2 p_\chi + H_\chi(p - p_\chi), \tag{6.31}$$

$$\rho C_\varepsilon \dot{T} = k_t \nabla^2 T + r, \tag{6.32}$$

where C_ε is the specific heat capacity of the material, r is a source term and k_t is the thermal conductivity of the material, that we assumed to be independent from temperature. Although the two equations are used to govern completely different fields, a straightforward parallelism among them can be identified. In Table 6.1, a comparison between different aspects of the two theories are reported. The analogy between these two theories inspired the idea of adapting an already implemented numerical resolution scheme (meant to be used for the thermal field) for the micromorphic variable. The main objective of the present investigation is, in fact, the analysis of the feasibility of such idea. The main advantage of the proposed method is that the micromorphic theory can be easily implemented in an explicit resolution scheme, while requiring very limited access and marginal effort in modify the original code. This aspect obviously makes the implementation of this theory more attractive than others methodology which would require high level of accessibility to the main solver, since both new element and material definitions would need to be developed. Such an analogy has been used in the past for coupling chemical diffusion and mechanics in the implicit version of ABAQUS (Diaz et al., 2016). The analogy has also been recognized and used to implement gradient plasticity and gradient damage models in the implicit version of the code ABAQUS (Seupel et al., 2018). Note that in these implementations, the viscous term, i.e. the transient term proposed in the present work, is absent.

The two PDEs are in fact so similar that in order to solve for the micromorphic variable, instead of the temperature, only two minor modifications need to be done. Given the comparison between the two PDEs (Eq. (6.31) and Eq. (6.32)), and given the form of the yield function in Eq. (6.26), the elements that require non-trivial modifications are the source term r and the yield radius: the former has to coincide with the difference between the cumulative plastic strain and the micromorphic variable (amplified by the H_χ parameter),

and the latter has to take into account the extra hardening due to the micromorphic variable:

$$r = H_\chi(p - p_\chi), \tag{6.33}$$

$$f = \sigma_{eq} - \sigma_0 - Hp - H_\chi(p - p_\chi), \tag{6.34}$$

whereas the coefficients present in the thermal balance equation can be easily substituted with the parameters characterizing the micromorphic PDE. Implementing the conditions (6.33) and (6.34) represents the only real, yet minor, effort that is required to make use of the present theory, assuming the existence of a thermal solver and the possibility of applying small modifications.

6.2.6 Influence on the C_χ parameter

The additional parameter C_χ naturally arises from the development of the chosen constitutive material model for the generalized stress a. In order to obtain the final form of the governing Eq. (6.24), so that the thermal-micromorphic analogy is valid, the presence of the C_χ parameter is required, and it should not vanish in the case of the implementation of the transient problem. However, from the analysis of Eq. (6.23), it is clear that the parameter C_χ regulates the development of the viscous part of the micromorphic variable, and therefore that a viscous part of the micromorphic variable exists. Being this an additional material parameter, the question on the calibration of such value must be addressed.

The purpose of using the micromorphic analysis, in the present investigation, is to gain indirect control on the distribution of the cumulative plastic strain and its gradient, thus the constraint on the micromorphic variable to closely follow the value of the cumulative plastic strain through the penalty parameter. The present theory also accounts for the development of viscous stresses generated by non-negligible strain rates, and the micromorphic variable follows the value of the cumulative plastic strain, regardless of whether the plastic strain increment is caused by quasi-static or viscous stresses. The adoption of large values of the C_χ parameters (compared to H_χ) would allow the viscous part of the micromorphic variable to produce additional meaningful generalized stress (see Eq. (6.23)), therefore altering the value that it should have, based only on the difference between micromorphic variable and cumulative plastic strain (effectively producing the same stress as if this difference was larger). Therefore, too large values of C_χ would somehow corrupt and interfere with the equivalence between cumulative plastic strain and micromorphic variable. On the contrary, by neglecting any meaningful contribution of the viscous micromorphic term to exist, we lose the analogy with transient thermal analysis proposed here for the implementation.

Therefore, for the present investigation, the C_χ parameter must exist, so that the thermal-micromorphic analogy holds, but its value should not be too large. The allowed magnitude for this parameter will be tested by checking an analytical solution in the static case, considered in Section 6.3.1.

6.2.7 Numerical implementation

The micromorphic plasticity model has been implemented in VPS Explicit (Group et al., 2000), a FE software developed by ESI Group solving both dynamics and heat problems. In order to account for the large deformation expected during manufacturing operations, the theory has been developed according to the VPS standard method, that is, using rate-type constitutive equations. This does not alter the theory so far presented, since the micromorphic part remains unchanged. The additive decomposition is applied to the strain rate tensor $\underset{\sim}{D}$, which can be split into an elastic $\underset{\sim}{D}^e$ and a plastic contributions $\underset{\sim}{D}^p$:

$$\underset{\sim}{D} = \underset{\sim}{D}^e + \underset{\sim}{D}^p. \tag{6.35}$$

The elastic constitutive model is rewritten by means of a hypoelasticity relation:

$$\overset{\circ}{\underset{\sim}{\sigma}} = \underset{\approx}{\Lambda} : \underset{\sim}{D}^e, \tag{6.36}$$

where $\overset{\circ}{\underset{\sim}{\sigma}}$ is the Jaumann stress rate, and it can be re-written as:

$$\overset{\circ}{\underset{\sim}{\sigma}} = \dot{\underset{\sim}{\sigma}} - \underset{\sim}{W} \cdot \underset{\sim}{\sigma} + \underset{\sim}{\sigma} \cdot \underset{\sim}{W}, \tag{6.37}$$

where $\underset{\sim}{W}$ is the spin tensor. The FE solution is obtained by establishing the weak form of Eq. (6.11) and (6.12) using the Galerkin method. The dynamic balance equation (6.11) is weighted with the test velocities $\underline{\dot{u}}$ whereas the micromorphic balance equation (6.12) is weighted with the test micromorphic variable rates $\dot{p}_\chi$. Integration over the domain is achieved by the use of the divergence theorem to lower the order of the derivatives. The natural boundary conditions are incorporated as forcing terms, leading to the equations to be discretized by finite-element interpolations. The discretization of the displacement and micromorphic fields over the domain is achieved by using proper-order interpolation functions. The following algebraic equations are derived:

$$\underset{\sim}{M}_m \cdot \underline{\ddot{u}} = \underline{F}_{ext} - \underline{F}_{int}, \tag{6.38}$$

$$\underset{\sim}{C}_\chi \cdot \underline{\dot{p}}_\chi = \underline{a}_r - \underline{a}_{int}, \tag{6.39}$$

where $\underset{\sim}{M}_m$ is the mass matrix, $\underline{F}_{ext}$ is the vector of external nodal forces, $\underline{F}_{int}$ is the vector of internal nodal forces, $\underset{\sim}{C}_\chi$ is the viscosity parameter matrix, $\underline{a}_r$ is the vector containing the nodal generalized forces generated by the source terms and $\underline{a}_{int}$ is the vector of nodal generalized forces induced by Laplacian of the micromorphic variable. In Eq. (6.39) the similarity with the discretized algebraic equation to solve the heat equation in thermal analysis can be appreciated once again. In fact, VPS Explicit uses the same form of equation to solve the heat equation:

$$\underset{\sim}{C} \cdot \dot{\underline{T}}_N = \underline{Q}_{\partial\Omega} + \underline{Q}_\Omega - \underline{Q}_K, \tag{6.40}$$

where $\underline{T}_N$ is the nodal temperature vector, $\underset{\sim}{C}$ is the heat capacity matrix, $\underline{Q}_{\partial\Omega}$ is the nodal heat flow depending on the heat flux on the outer surface $\partial\Omega$, $\underline{Q}_{\Omega}$ is the nodal heat flow depending on the internal heat source and $\underline{Q}_K$ is the internal nodal heat flow depending on the heat flux inside the domain Ω.

A central difference explicit scheme associated to the lumped mass matrix is used to solve Eq. (6.38), whereas a forward Euler scheme associated with the viscosity lumped matrix is implemented to solve Eq. (6.39). A weak micromorphic-mechanical coupling is implemented in VPS Explicit, that is, the two equations are solved separately. The micromorphic field influences the plastic behavior of the continuum (through condition (6.33)), and, in return, the cumulative plastic strain (the difference between the cumulative plastic strain and the micromorphic variable) acts as a source term in the micromorphic balance equation (in condition (6.34)).

Regarding the mechanical behavior, a user material routine implements the mechanical model as previously defined. The values of the micromorphic variables at the Gauss quadrature points are interpolated by mean of the interpolation functions from the nodal values. So the user material routine not only integrates the mechanical behavior but also computes the source term $H_\chi(p - p_\chi)$ at the Gauss points. Regarding the micromorphic treatment, a specific function is developed inside the thermal solver in order to recover the source term from the material computations previously evaluated. The main algorithmic steps of the explicit resolution over a time step Δt may be summarized by the following scheme:

Algorithm 1 Algorithmic steps of the explicit resolution scheme implemented in VPS Explicit.

Mechanics: at time t_n, compute $\underset{\sim}{M}_m$, $\underline{F}_{ext}$ and $\underline{F}_{int}$;
Micromorphic: at time t_n, compute $\underset{\sim}{C}_\chi$, $\underline{a}_r$ and $\underline{a}_{int}$;
Stability condition: compute the time step Δt;
Micromorphic: explicit time integration, compute $p_{\chi t_1}$;
Mechanics: explicit time integration, compute $\underline{\dot{u}}_{n+1/2}$ and $\underline{\dot{u}}_{n+1}$;
Next Step: compute $t_{n+1} = t_n + \Delta t$.

6.3 Validation of the implemented numerical model

6.3.1 Analytical solution

The analytical solution is developed for the rate-independent static case as a reference for validation of the FE scheme at the static limit. It is inspired from similar solution proposed by Mazière and Forest (2015); Scherer et al. (2019, 2020). Further to that, similar solution in the context of crystal plasticity model can be found in section 4.3.1. Consider a periodic strip made of a thick rectangular plate of the width W along X_1 direction, the length L along X_2 direction, and the thickness T along X_3 direction (cf. Fig. 4.1) undergoing simple shear.

A macroscopic deformation $\bar{\varepsilon}$ is applied such that

$$\underline{u} = \underset{\sim}{\bar{\varepsilon}} \cdot \underline{X} + \underline{v}(\underline{X}), \quad \text{with} \quad \underset{\sim}{\bar{\varepsilon}} = \bar{\varepsilon}_{12}(\underline{e}_1 \otimes \underline{e}_2 + \underline{e}_2 \otimes \underline{e}_1), \tag{6.41}$$

where $\underline{v}$ is the periodic displacement fluctuation. Due to equilibrium conditions, the shear stress component is homogeneous so that the equivalent stress σ_{eq} is invariant along $\underline{X}_1$, $\underline{X}_2$ and $\underline{X}_3$, hence

$$\sigma_{eq}(\underline{X}_1, \underline{X}_2, \underline{X}_3) = \sigma_{eq}. \tag{6.42}$$

The yield condition including the linear softening term and the micromorphic contribution (with $C_\chi = 0$ here) can be written as

$$f = \sigma_{eq} - (\sigma_0 + Hp + H_\chi(p - p_\chi)) = 0 \quad \text{with} \quad H < 0. \tag{6.43}$$

The PDE governing the micromorphic variable is given by

$$A\frac{\partial^2 p_\chi}{\partial X_2^2} = H_\chi(p_\chi - p). \tag{6.44}$$

Elimination of the variable p in the previous equation by means of the yield condition (6.43) leads to the following form of the PDE to be solved for p_χ:

$$A\frac{\partial^2 p_\chi}{\partial X_2^2} - \frac{HH_\chi}{H + H_\chi}p_\chi + \frac{H_\chi}{H + H_\chi}(\sigma_{eq} - \sigma_0) = 0. \tag{6.45}$$

In case of linear softening (6.45) takes the form

$$\frac{\partial^2 p_\chi}{\partial X_2^2} - \left(\frac{2\pi}{\lambda}\right)^2 p_\chi = -\left(\frac{2\pi}{\lambda}\right)^2 \kappa, \tag{6.46}$$

where λ is the characteristic width of the deformation zone. The PDE (6.46) governing p_χ is only valid in the region $X_2 \in [\frac{-\lambda}{2}, \frac{\lambda}{2}]$ and the solution is of the form given in Eq. (4.50).

For symmetry reasons, $p_\chi(X_2) = p_\chi(-X_2)$ leads to $\alpha_2 = 0$. At the elastic/plastic interfaces, i.e at $X_2 = \pm\frac{\lambda}{2}$, continuity of micromorphic variable p_χ and of the generalized stress normal to the interface $\underline{M} \cdot \underline{X}_2$ must hold, hence

$$p_\chi\left(\pm\frac{\lambda}{2}\right) \simeq p\left(\pm\frac{\lambda}{2}\right) = 0, \tag{6.47}$$

$$\underline{M}\left(\pm\frac{\lambda}{2}\right) \cdot \underline{X}_2 = A\frac{dp_\chi}{dX_2}\bigg|_{X_2 = \pm\frac{\lambda}{2}} = 0. \tag{6.48}$$

where we make the approximation that p_χ is sufficiently close to p, i.e. that the penalty coefficient is large enough. Combining (6.47) and (6.48) with (4.50) leads to

$$\alpha_1 = \frac{(\sigma_{eq} - \sigma_0)}{H}. \tag{6.49}$$

The constants λ is as given in Eq. (4.49) and κ are defined by

$$\kappa = \left(\frac{\lambda}{2\pi}\right)^2 \frac{H_\chi}{A(H + H_\chi)}(\sigma_{eq} - \sigma_0). \tag{6.50}$$

Moreover, the equivalent stress is expressed as

$$\sigma_{eq} = \frac{\mu}{L} \int_{\frac{-L}{2}}^{\frac{L}{2}} \left(\frac{\varepsilon_{12} - p}{2}\right) dX_2, \tag{6.51}$$

where μ is the elastic shear modulus. From the yield condition, p can be replaced by $\frac{\sigma_{eq} - \sigma_0 + H_\chi p_\chi}{H + H_\chi}$ in Eq. (6.51) and integration gives an expression for σ_{eq} as a function of applied macroscopic shear $\bar{\varepsilon}_{12}$ and then the uniform shear stress writes

$$\sigma_{eq} = \frac{\bar{\varepsilon}_{12} + \frac{\sigma_0}{Z_e}}{\frac{1}{\mu} + \frac{1}{Z_e}}, \quad \text{with} \quad \frac{1}{Z_e} = \frac{\lambda}{HL}. \tag{6.52}$$

6.3.2 FE solution

The FE simulations are performed with a periodic strip subjected to shear loading. The associated 2D coordinate system and geometry are shown in Fig. 4.1. The strip has been meshed with 3D 8-nodes elements onto which plane strain conditions were applied by imposing zero out-of-plane displacement to all the nodes. The nodes at the bottom of the strip ($X_2 = -L/2$) were clamped along X_1 and X_2. The nodes on the top surface ($X_2 = L/2$) were clamped along X_2 and a Dirichlet type of boundary condition was applied along X_1 whereas the displacements along X_2 were fixed. Linear shape functions have been used to interpolate the nodal fields, and full integration schemes have been used for the material behavior. Numerically, in order to trigger the strain localization in a periodic strip, a small defect is introduced at the centre (Fig. 4.1). The defect is one element having an initial yield stress 3% less than the matrix. Isotropic elasticity is considered. The material parameters used for the analytical solution and FE simulations are presented in Table 6.2.

Fig. 6.1a and 6.1b show the cumulative plastic strain fields with the classical and micromorphic plasticity models using two different mesh discretizations, namely the *coarse* and the *fine* mesh (using 101 and 303 elements respectively). The classical plasticity model exhibits pathological mesh dependency and width of the formed shear band always collapse to one element irrespective of the mesh size. In contrast, the width of the formed shear band with the micromorphic model is finite and independent of the mesh size. This

Table 6.2 Numerical values of material parameters used for the simulation of a periodic strip undergoing simple shear.

E	ν	ρ	σ_0 Eq. (6.43)	H Eq. (6.43)	H_χ Eq. (6.43)
75 GPa	0.3	2.8×10^3 Kgm^{-3}	100 MPa	-500 MPa	10^6 MPa
A Eq. (6.24)	C_χ Eq. (6.24)	L Eq. (6.52)			
0.08N	90 MPa.s	1.0 mm			

indicates the capabilities of the implemented micromorphic theory in an explicit scheme to solve the shear strain localization problem. Furthermore, the cumulative plastic strain variation along X_2 obtained from the FE solution is validated against the analytical solution developed for the rate-independent case (cf. Eq. (4.50)), see Fig. 6.2a. The FE simulation is validated for $\bar{\varepsilon}_{12} = 0.01$. Moreover, simulations are performed by changing the simulation time while keeping the same applied total shear strains. Fig. 6.2b shows that the perfect agreement with an analytical solution is obtained for $t = 10$ sec. which corresponds to low enough strain rate to make the viscous contribution in 6.25 negligible. Larger strain rates are seen to limit the localization since the maximum strain in the band decreases for increasing strain rates. Since the total strain is imposed, this means that a higher elastic strain compensates the lower plastic strain which means that stress values are higher.

In order to retrieve the quasi-static solution, also the viscous parameter C_χ have to be chosen small enough. The reason is to minimize as much as possible any viscous-like component of the generalized stress a^* in Eq. (6.23) to retrieve the rate–independent solution. Metals at high temperatures are known to be strain rate sensitive. This effect is generally taken into account by means of an appropriate visco-plastic flow rule, for instance based on a Norton-type power law. In the present work, rate-independent plasticity only has been considered but the generalization to visco-plasticity is straightforward in the proposed framework. Note that the proposed model presents an additional strain rate sensitivity, via the viscosity parameter C_χ. This will require appropriate calibration for instance using strain field measurements during localization.

6.4 Numerical examples

In this section, the applicability of the implemented scalar micromorphic strain gradient theory is tested for two additional cases: a shearing operation process and a bending test. The aim of this section is to exploit the analogy explained in section 6.2.5, whose numerical implementation has been previously presented, to prove that simulations of manufacturing operations using the micromorphic continuum under an explicit integration scheme can be successfully performed.

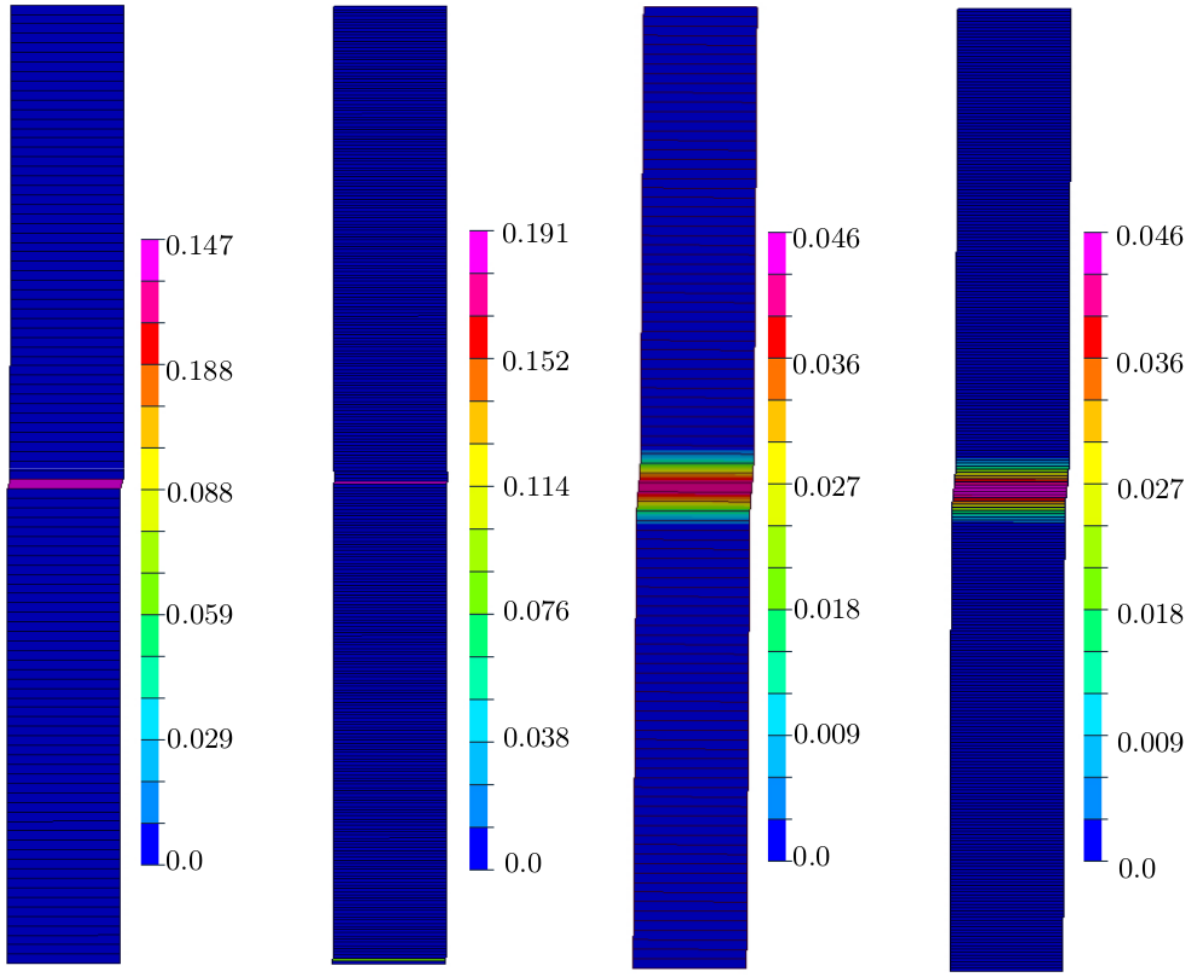

(a) (b)

Fig. 6.1 Localization of plastic strain in a periodic strip undergoing simple shear for two different mesh sizes (*fine* and *coarse*) using the (a) classical plasticity model, and (b) micromorphic plasticity model.

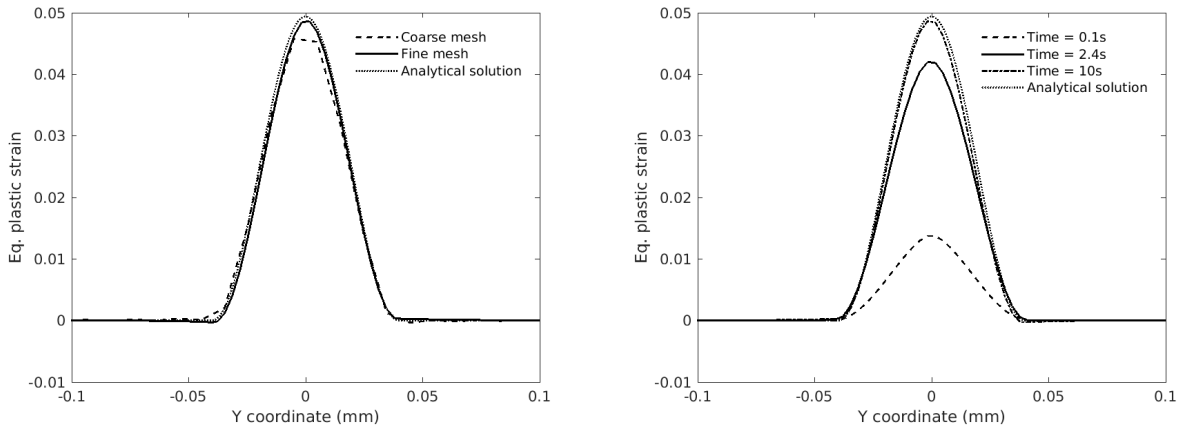

(a) (b)

Fig. 6.2 Bending tests using micromorphic plasticity model: (a) cumulative plastic strain field during bending process, and (b) normalized bending moment vs. rotation angle for different values of high-order modulus A.

Industry best practice discourages the employment of complex numerical methods to produce simulations, mainly to guarantee a high degree of reliability of the results and computational efficiency in terms of CPU time. Regarding this reasonable concerns, the results that will be presented here are to be considered as proof of the simplicity of the method, which requires only one additional parameter to be calibrated, that is A (see the discussion on the C_χ parameter in section 6.2.6).

As previously explained in the introduction, the relevance of the application of regularization procedures in manufacturing operations is vital, especially in cases in which the thermal power has a major presence. Thermal softening can take place when high rates of plastic strain are produced, and similar softening can be reproduced by assigning a negative slope to the hardening function in Eq. (6.30). The regularization potential of the proposed method is investigated in the shearing operation section. Moreover, one of the missing features of the classical continuum mechanics is the capability of predicting any size effect. This becomes of major relevance whenever the deformation localizes is small regions or in the case of forming of micro-components (Zhu et al., 2020; Li et al., 2009). The ability of the proposed method to capture the size effect is proven in the bending section.

6.4.1 Shearing operation

The shear band formation is a commonly observed phenomenon in manufacturing operations in case of heavy deformation, for instance, high-speed shaping, forging, machining, and several other processes (Molinari et al., 2002; Burns and Davies, 2002). Numerically, the shear band simulation shows spurious mesh dependency when we consider a classical plasticity approach with strain softening. Dynamics combined with viscosity or/and heat conduction are known to provide regularization but the involved length scales are often too small for efficient FE modeling so that strain gradient or micromorphic plasticity is still useful to introduce physically more realistic length scales (Stathas and Stefanou, 2021; Wcisło and Pamin, 2017). Shearing operation is most commonly used in the metal forming industries for sheet metal cutting. In this section, the implemented micromorphic approach is used for the regularization of shear band formation in shearing operation.

The shearing operation is performed on a sheet of 5 mm thickness under plane strain conditions with one element across the width. The geometry and applied boundary conditions are shown in Fig. 6.3. The sheet has been meshed with 3D 8-nodes elements with linear shape functions and full integration schemes. The lower tool is fixed, while velocity is applied to the upper tool in the downward direction. At the initial deformation stage, a linearly increasing velocity up to $4\,\mathrm{mm\,s^{-1}}$ is applied. Once the velocity of $4\,\mathrm{mm\,s^{-1}}$ is achieved, it is kept constant in the later stage of the deformation. The contact between the deformable sheet and tools is taken into account using a constant coefficient of friction 0.3. The tools are considered as rigid bodies, while the sheet is assigned with an elasto-plastic material behavior using linear strain softening. Isotropic elasticity is considered. The used material parameters in the numerical simulations are presented in Table 6.3.

Table 6.3 Numerical values of material parameters used for the simulation of the shearing operation.

E	ν	ρ	σ_0 Eq. (6.43)	H Eq. (6.43)
75 GPa	0.3	$2.8 \times 10^3\,\mathrm{kgm}^{-3}$	100 MPa	-500 MPa
H_χ Eq. (6.43)	A Eq. (6.24)	C_χ Eq. (6.24)		
10^6MPa	[128, 320, 800] N	90 MPa.s		

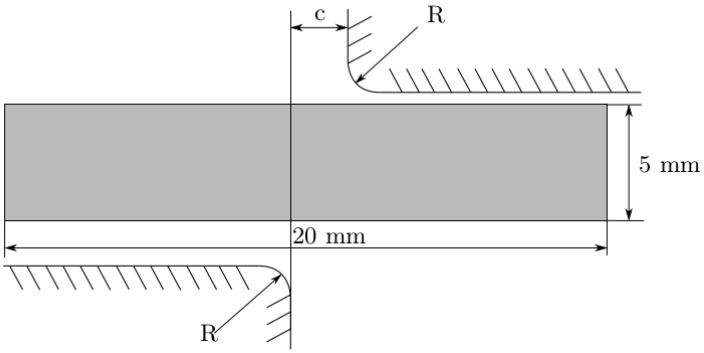

Fig. 6.3 Geometry used for the shear operation simulation..

At first, simulations are performed with classical plasticity using two different mesh discretizations: the *coarse* mesh and the *fine* mesh, with 3200 and 105600 nodes in the shear region, respectively. The limitation of the classical plasticity model, known as pathological mesh dependency in the strain localization problem can be observed from Fig. 6.4a and 6.4e by the contours of the cumulative plastic strain. The magnitude of the cumulative plastic strain is different for two different mesh discretizations, and it increases with finer mesh. Furthermore, the observed width of the shear band is different for two different mesh discretizations and it always collapses to one element size irrespective of the mesh size. In contrast, the formed width of the shear band using the micromorphic approach is finite and does not depend on the mesh density as seen from Fig. 6.4b and 6.4f. In addition, the magnitude of the cumulative plastic strain reaches asymptotic values while reducing the mesh size. Furthermore, the effect of the diffusivity coefficient A on the shear band widths is investigated. Fig. 6.5 shows the variation of cumulative plastic strain for three different values of the gradient parameters A, 128 N, 320 N, and 800 N. As the value of A increases the intensity of plastic strain gradient within the shear region reduces. As expected from the analytical expression for the length scale in Eq. (4.49), the width of the shear band increases with an increase in the A value. For the three different values of the A parameter, 128 N, 320 N and 800 N, the observed widths of the shear bands are 2.4 mm, 2.8 mm, and 3.5 mm, respectively.

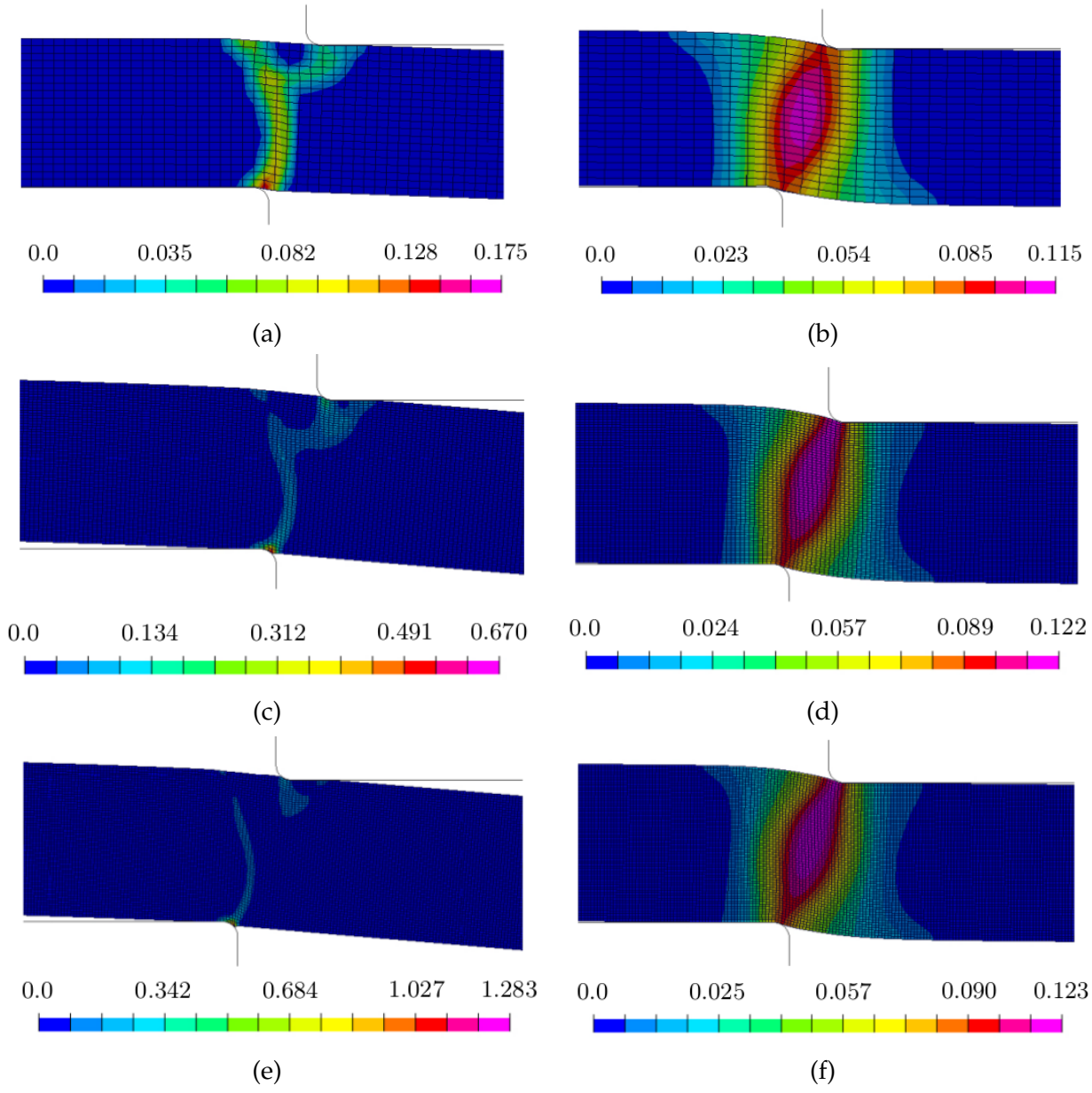

Fig. 6.4 Mesh size effect on the plastic strain localization during shearing simulation using (a), (c) and the (e) classical plasticity model (b), (d) and the (f) micromorphic plasticity model. From the top to the bottom, increasing mesh size.

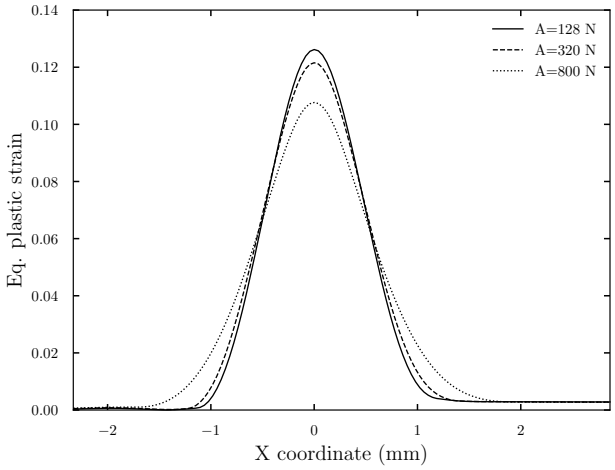

Fig. 6.5 Effect of the variation of the characteristic length scale on the plastic strain distribution during shearing simulation.

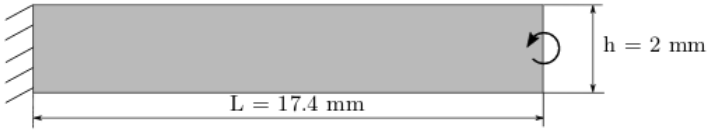

Fig. 6.6 Geometry and the applied boundary conditions on the beam used for the bending simulations.

6.4.2 Bending tests

The bending tests are used to verify that the implemented micromorphic model is able to capture the size effect for hardening plasticity. Many studies have been experimentally highlighted the presence of extra hardening in the bending moment, whenever the specimen geometry was reaching sub-micron dimension, approaching grain size. (Fleck et al., 1994) reported hardening behavior in a copper wire under torsion for wire diameters in the order of $10-100\,\mu m$, whereas tensile tests performed on the same wires found no evidence of size effect. (Stölken and Evans, 1998) designed a micro-bend test to measure the plastic characteristic length scale associated with the strain gradient, subsequently reporting the results pertaining to thin ($12.5\,\mu m \mapsto 50\,\mu m$) Nickel foils.

In Fig. 6.6, the geometry and boundary conditions applied to the specimen are reported. The specimen has been discretized using 3D type of elements under plane strain conditions. Linear shape functions are used to interpolate nodal values, and full integration scheme is used for the elements. One element spans the 1 mm width. The left face of the beam is fixed, whereas a material rotation is enforced on the nodes of the right face through a coupling involving the nodes of the right face and an auxiliary node. The resultant bending moment is probed at the auxiliary node. A total rotation of 45° is applied. The size effect can be experimentally encountered whenever the geometry of the specimen reduces down to approximately the grain size of the metal. Virtually, the same phenomenon could be

Table 6.4 Numerical values of material parameters used for the simulation of the bending test

E	ν	ρ	σ_0	H	H_χ
75 GPa	0.3	$2.8\times10^3\,\mathrm{kgm}^{-3}$	100 MPa	200 MPa	10^6MPa
A	C_χ				
128-800 N	10^3 MPa.s				

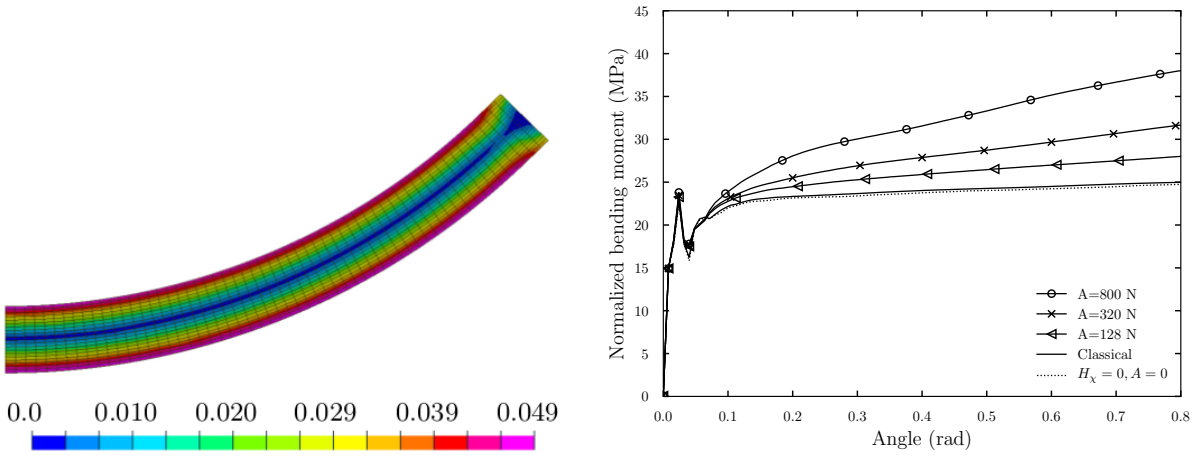

(a) (b)

Fig. 6.7 Bending tests using micromorphic plasticity model: (a) cumulative plastic strain field during bending process, and (b) normalized bending moment vs. rotation angle for different values of high-order modulus A.

achieved by keeping constant the geometry of the specimen and simultaneously increasing the characteristic length scale. The effectiveness of the formulation in predicting the size effect through the bending test has been verified by employing the latter method. The numerical framework previously presented does not explicitly make use of the grain size, but a characteristic length scale in Eq. (6.25) was identified, and this will serve the same purpose. The use of larger or smaller characteristic length scale will respectively induce a stiffer or softer global response of the specimen. Three different values of the gradient parameter A have been used. The other material parameters used in the simulation of the bending tests are reported in Table 6.4. In the attempt of replicating a quasi-static bending test, the chosen value of the C_χ parameters is relatively small, so that any viscous contribution of the micromorphic variable would be negligible.

In Fig. 6.7a the distribution of the cumulative plastic strain for the bending test using the micromorphic plasticity model is reported. Besides the edge effect induced by the boundary condition at the right surface, the solution appears to be invariant along the longitudinal direction of the strip. The FE solutions obtained using the classical and micromorphic plasticity models in terms of normalized bending moment vs. applied

rotation are shown in Fig. 6.7b. The probed bending moment has been normalized with respect to the first moment of area of the beam cross-section, that is $w_h h^2$, where w_h is the width of the rectangular cross-section, and h is the height of the rectangular cross-section. From Figure 6.7b, it can be appreciated that the classical solution is retrieved by using the micromorphic approach with a null penalty term H_χ and null gradient parameter A. Three values of the gradient parameter (respectively three different characteristic lengths scales) are used for the test: 128 N, 320 N, and 800 N. The curves belonging to the micromorphic plasticity theory clearly demonstrate the ability of the method to capture the size effect. The extra hardening reported in Fig. 6.7b follows the same trend as the one relative to the experimental tests reported by (Stölken and Evans, 1998).

In the case of bending, the micromorphic medium does not need to regularize any localization phenomenon; rather, it has to predict an additional hardening, as presented in the manuscript. The characteristic length scale can be identified in this case by $\ell = \sqrt{\frac{A(H+H_\chi)}{|H|H_\chi}}$. The obtained characteristic length scales using A = 128 N, 320 N, and 800 N are 0.8 mm, 1.26 mm, and 2.0 mm, respectively. These characteristic length scales can be normalized by the thickness h of the beam. The obtained ℓ/h ratio for A = 128 N, 320 N and 800 N are 0.40 mm, 0.63 mm and 1.0 mm, respectively. Fig. 6.7b shows that for high ℓ/h ratio, i.e. high A value, stronger response can be predicted.

The plasticity material model used for the bending test is characterized by a linear hardening behavior (Tab. 6.4). From the analysis of the curves, it can be inferred that the regularization, and subsequently the size effect, is affecting the solution only in the plastic regime, whereas the initial elastic stiffness of the curves is the same regardless of the characteristic length scale used in the model. This is the expected behavior, given the fact that the present micromorphic plasticity theory regulates the localization of the plastic field. Thus, there should be no difference between the curves in the elastic regime. In hardening plasticity, the plastic strain gradient contribution leads to an increased apparent hardening of the beam in the plastic regime.

6.5 Conclusions

In this chapter, a micromorphic strain gradient plasticity model has been formulated and implemented in a commercial explicit finite element code in order to perform simulations of manufacturing operations in time-dependent environments. The reasons to account for the strain gradient while simulating manufacturing operations deal with regularization of strain localization phenomena in softening plasticity, on the one hand, and prediction of size effects in hardening plasticity. The originality of the approach lies in the use of the micromorphic model instead of strict strain gradient plasticity and in the introduction of a viscosity contribution to the micromorphic plastic evolution. The advantage of these two ingredients is that they ease the numerical implementation in a commercial finite element code by mimicking the transient heat equations. Earlier formulations are based on strict

strain gradient plasticity without transient term, on the one hand, or on the introduction of micromorphic inertia instead of the proposed viscous term.

The main outcome of the present research lies in the proof that it is possible to implement an explicit micromorphic model in a relatively easy and straightforward manner. This was achieved by slightly modifying the pre-existing routines of material integration and thermal field resolution in the VPC/PAMCRASH software developed by ESI. This proof of concept is meant to demonstrate that limited effort is required to implement the micromorphic theory in any other software that allows for minor modification in their procedures.

The implemented theory has been demonstrated to recover the analytical solution for a semi-infinite glide layer under quasi-static loading conditions. The supplementary shearing tests highlighted the need to use of the strain gradient theory in case deformation localizes, and the typical extra hardening in bending has also been modeled.

Most importantly, it has been proven that the size effect can be predicted with this method and that manufacturing operations can be simulated with such theory with a limited increase in computational cost and only one additional material parameter (the characteristic length). The same model can therefore be used to address regularization issues in softening plasticity and *smaller is harder* size effects in microforming. Further work should be dedicated to develop case studies involving real material data and more complex 3D specimen geometries. In particular the consideration of adiabatic shear banding can be included in the approach in a way similar to the work done in (Russo et al., 2020a) whereas full coupling with heat conduction phenomenon would require more intrusive programming in the considered commercial code.

Chapter 7

Conclusions and outlook

7.1 Conclusions

Inhomogeneous deformation of micron-scale components shows non-conventional plastic behavior such as size–dependent strengthening called size effect. It is well known that the classical crystal plasticity models fail to capture size effects due to the lack of characteristic length scales in the constitutive framework. This limitation of the classical crystal plasticity models can be overcome using strain gradient crystal plasticity models. Therefore, the first objective of this thesis was to predict the size effects in single crystal microwire torsion tests under severe deformation.

Strain softening, mainly due to the temperature rise, is a common phenomenon in severe deformation processes, which ultimately results in the formation of an intense shear band called the adiabatic shear band (ASB). Applications of classical crystal plasticity models to strain localization problems show spurious mesh dependency. Strain gradient crystal plasticity models can be used to overcome this limitation of classical crystal plasticity models. Therefore, the second objective was to investigate the ASB formation process in single and poly-crystalline FCC metallic materials.

Strain gradient crystal plasticity models, specifically the reduced-order micromorphic crystal plasticity and Lagrange multiplier-based models, are used to predict the size effect and investigate the ASB formation process.

Recent experimental studies, for instance (Landau et al., 2016; Mourad et al., 2017; Longère, 2018), showed that the ASB formation process is influenced by dynamic recrystallization along with thermal softening. Stored energy is the main driving force for dynamic recrystallization. The prediction of the stored energy and Taylor-Quinney coefficient (TQC) is essential to understand the plastic deformation and subsequent recovery and recrystallization processes. Therefore, the third objective of this thesis was to predict the stored energy and TQC in single and poly-crystalline FCC metallic materials.

The computational cost of strain gradient plasticity models is high due to the additional degrees of freedom. Therefore, these models have limited applications in practical engineering problems. Moreover, the numerical implementation of strain gradient plasticity models

is challenging due to the complicated constitutive framework. Therefore, the final objective of this work was to propose an easy way to implement this model in commercial FE software.

In the first part of the thesis, the size effects in monotonic loading of the single crystal microwire torsion tests were predicted using the micromorphic crystal plasticity and Lagrange multiplier-based models. These are reduced-order models with one additional degree of freedom called *Lagrange multiplier* present in the former model compared to the latter model. The predicted size effect using the Lagrange multiplier-based model under monotonic and cyclic loading of the microwires was compared with the *CurlF*^{p} model proposed by Kaiser and Menzel (2019b). Note that the *CurlF*^{p} model is a strain gradient plasticity model and thus should be compared more directly to the Lagrange multiplier-based model. Moreover, a post-processing technique was used to predict the SSD and GND density distribution in monotonic and cyclic loading of microwires. To this end, the reduced-order models were used to develop a scaling law based on the monotonic loading of the microwires. The main findings of the study were as follows:

- It was shown that both reduced-order models deliver the same response for small characteristic length scales. However, for large characteristic length scales, the micromorphic crystal plasticity model shows saturation in torque vs. surface strain response in contrast to the Lagrange multiplier-based model, which did not show saturation.

- The predicted size effect using the Lagrange multiplier-based and *CurlF*^{p} models were in good agreement for the monotonic loading of the microwire torsion tests. However, for cyclic loading, the Lagrange multiplier-based model shows isotropic hardening in contrast to the kinematic hardening shown by the *CurlF*^{p} model.

- The evolution of SSD and GND density was investigated for monotonic and cyclic loading of the microwire torsion tests using the Lagrange multiplier-based model. In cyclic loading, a significant increase in SSD and GND density was observed at the end of each cycle compared to previous cycles.

- The size effects are characterized by power law relationships between the normalized torque and R/ℓ, with R being the radius of the microwire and ℓ being a characteristic length of the model. The scaling laws were developed using the reduced-order models for monotonic loading of the microwires. The micromorphic crystal plasticity model showed a power-law with exponent $n = -0.6$ and -0.85 for $H_\chi = 10^4$ MPa and 3×10^4 MPa, respectively. In contrast, the Lagrangian multiplier-based model predicted no saturation at small R/ℓ ratios and showed a power law with $n = -1$.

In the second part of the thesis, a thermodynamically consistent framework for the classical and micromorphic crystal plasticity models was developed. This framework was used to investigate adiabatic shear banding in single and poly-crystals FCC metallic

materials. The formation of ASB was studied using single and poly-crystalline hat-shaped specimens. The main conclusions drawn from the study were as follows:

- The orientation of the formed ASB with respect to the loading axis in single crystals was affected by the initial crystal orientation. In particular, one special crystal orientation is found resistant to shear banding.
- The grain size effect, *the finer the grain size the higher the resulting load*, was illustrated in polycrystalline FCC metallic materials using the micromorphic crystal plasticity model subjected to isothermal deformation.
- The resulting load and the formation of the shear band were highly orientation dependent in polycrystalline simulations.

In the third part of the thesis, an advanced thermodynamically consistent crystal plasticity framework was used to predict the stored energy and TQC in FCC metallic materials. The importance of ensuring the positivity of the dissipation rate was emphasized. Furthermore, the predictions of stored energy and TQC were performed for single crystals using the classical crystal plasticity model. As the first application to polycrystalline simulations, the effect of the mesh size and grain morphology on the average stress-strain response was studied in detail. Then, the stored energy was predicted for the polycrystalline austenitic steel, and a comparison was made with the experimental measurements from the literature. An *ad-hoc* factor was defined to represent the experimentally measured stored energy adequately. Finally, the predicted stored energy considering contribution of both SSDs and GNDs was compared to that obtained by considering the contribution of SSDs only. The following conclusions were drawn from the study:

- The predicted values of the TQC for single crystals copper and aluminum showed that a reliable dislocation density-based model is necessary to adequately represent the experimental measurements.
- In the polycrystalline simulations, the role of an *ad-hoc* factor was discussed. This factor was considered as a fitting parameter in order for the predicted stored energy to agree with the experimental measurements.
- The predicted stored energy by considering contributions of both SSDs and GNDs was found to be higher than those of SSDs only, but still insufficient to account for experimental results.

In the last part of the thesis, we proposed an easy way to implement micromorphic plasticity model in a commercial FE software. We used an analogy between the micromorphic plasticity theory and classical thermo-mechanics for the implementation. This model was implemented in the explicit finite element software VPS/Pam-Crash® from ESI. The main conclusions of the study were as follows:

- It was shown that the micromorphic plasticity theory could be implemented in an explicit framework in a relatively easy and straightforward manner, with only minor modifications in their procedures.
- The implemented theory in commercial FE software was able to predict the size effect and regularize shear band formation.

7.2 Outlook

In the present work, the shortcoming of the reduced-order model to predict the size effect in cyclic loading of the microwire torsion tests was shown. The simulation of kinematic-type hardening is, in fact, possible with a reduced-order model using an alternative formulation in which the free energy potential depends on the gradient of the microslip variable. In future works, efforts will be devoted to developing this alternative formulation to take into account kinematic hardening.

In polycrystalline hat-shaped simulations due to high computational costs, only two grain sizes were considered to predict the grain size effect. Future work will be dedicated to predict grain size effect considering more number of grains in the shear region of the hat-shaped specimen. Moreover, heat conduction was neglected in hat-shaped simulations, although it plays a significant role at the grain scale for the strain rates and grain sizes considered in this work. Extension of the work considering the coupling of strain gradient crystal plasticity and heat conduction is therefore necessary in the future to highlight the competition between characteristic length scales emerging from microstructure and thermal effects. In addition, grain boundary sliding and decohesion are additional important deformation and damage mechanisms at high temperatures. They are not included in the present work, but this is possible as demonstrated in (Musienko et al., 2004). Coupling strain gradient crystal plasticity and grain boundary sliding/opening remain challenging tasks.

The work performed on the ASB formation can be extended to more severe loading conditions (including remeshing techniques) and relate to the experimental results on machining process at high strain rates obtained by Haythem Zouabi (ESR7). Moreover, future work will be devoted to implementing a thermodynamically consistent framework of the classical and micromorphic crystal plasticity models in an open-source automated massively parallel FEniCS framework in collaboration with Tamara Dancheva (ESR6).

In the present work, the predicted stored energy, which is a function of total dislocation density, does not adequately represent the experimental measurements from the literature. The used dislocation density-based model may not be reliable to predict the total dislocation density evolution and consequently the stored energy. Future work will be devoted to giving more physical meaning to the dislocation density-based model.

Moreover, implemented micromorphic plasticity model in explicit FE software VPS/Pam-Crash® from ESI Group will be applied to the industrial manufacturing processes which involve strain localization due to the severe deformation, for instance: deep drawing, stamping, rolling, and so forth.

References

Abdul-Aziz, A., Kalluri, S., 1991. Estimation of the engineering elastic constants of a directionally solidified superalloy for finite element structural analysis. Technical Report 187036. NASA.

Abrivard, G., 2009. A coupled crystal plasticity - phase field formulation to describe microstructural evolution in polycrystalline aggregates during recrystallisation. Theses. École Nationale Supérieure des Mines de Paris. URL: https://pastel.archives-ouvertes.fr/pastel-00533060.

Abrivard, G., Busso, E., Forest, S., Appolaire, B., 2012. Phase field modelling of grain boundary motion driven by curvature and stored energy gradients. part I: theory and numerical implementation. Philosophical Magazine 92, 3618–3642. doi:10.1080/14786435.2012.713135.

Abu Al-Rub, R., Voyiadjis, G., 2004. Determination of the material intrinsic length scale of gradient plasticity theory. International Journal for Multiscale Computational Engineering 2, 377–400. doi:10.1615/IntJMultCompEng.v2.i3.30.

Abu Al-Rub, R.K., Voyiadjis, G.Z., 2004. Analytical and experimental determination of the material intrinsic length scale of strain gradient plasticity theory from micro- and nano-indentation experiments. International Journal of Plasticity 20, 1139–1182. doi:10.1016/j.ijplas.2003.10.007.

Abu Al-Rub, R.K., Voyiadjis, G.Z., 2006. A physically based gradient plasticity theory. International Journal of Plasticity 22, 654–684. doi:10.1016/j.ijplas.2005.04.010.

Acharya, A., Bassani, J., 1995. Incompatible lattice deformations and crystal plasticity. American Society of Mechanical Engineers, Applied Mechanics Division, AMD 200, 75–80.

Acharya, A., Bassani, J., 2000. Lattice incompatibility and a gradient theory of crystal plasticity. Acta Mater 47, 11597–1611. doi:10.1016/S0022-5096(99)00075-7.

Ahad, F., Enakoutsa, K., Solanki, K., Bammann, D., 2014. Nonlocal modeling in high-velocity impact failure of 6061-t6 aluminum. International Journal of Plasticity 55, 108–132. doi:10.1016/j.ijplas.2013.10.001.

Aifantis, E.C., 1984. On the microstructural origin of certain inelastic models. Journal of Engineering Materials and technology 106, 326–330. doi:10.1115/1.3225725.

Aifantis, E.C., 1987. The physics of plastic deformation. International Journal of Plasticity 3, 211–247. doi:10.1016/0749-6419(87)90021-0.

Aifantis, K., Willis, J., 2005. The role of interfaces in enhancing the yield strength of composites and polycrystals. Journal of the Mechanics and Physics of Solids 53, 1047–1070. doi:10.1016/j.jmps.2004.12.003.

Alankar, A., Mastorakos, I.N., Field, D.P., 2009. A dislocation-density-based 3d crystal plasticity model for pure aluminum. Acta Materialia 57, 5936–5946. doi:10.1016/j.actamat.2009.08.028.

Anand, L., Aslan, O., Chester, S.A., 2012. A large-deformation gradient theory for elastic–plastic materials: Strain softening and regularization of shear bands. International Journal of Plasticity 30-31, 116–143. doi:10.1016/j.ijplas.2011.10.002.

Anand, L., Kim, K., Shawki, T., 1987. Onset of shear localization in viscoplastic solids. Journal of the Mechanics and Physics of Solids 35, 407–429. doi:10.1016/0022-5096(87)90045-7.

Anand, L., Kothari, M., 1996. A computational procedure for rate-independent crystal plasticity. Journal of the Mechanics and Physics of Solids 44, 525–558. doi:10.1016/0022-5096(96)00001-4.

Anand, L., Spitzig, W., 1980. Initiation of localized shear bands in plane strain. Journal of the Mechanics and Physics of Solids 28, 113–128. doi:10.1016/0022-5096(80)90017-4.

Aravas, N., Kim, K., Leckie, F., 1990. On the calculations of the stored energy of cold work. Journal of Engineering Materials and Technology 112, 465–470. doi:10.1115/1.2903358.

Armstrong, R., 1961. On size effects in polycrystal plasticity. Journal of the Mechanics and Physics of Solids 9, 196–199. doi:10.1016/0022-5096(61)90018-7.

Arsenlis, A., Parks, D., 1999. Crystallographic aspects of geometrically-necessary and statistically-stored dislocation density. Acta Materialia 47, 1597–1611. doi:10.1016/S1359-6454(99)00020-8.

Arsenlis, A., Parks, D.M., 2002. Modeling the evolution of crystallographic dislocation density in crystal plasticity. Journal of the Mechanics and Physics of Solids 50, 1979–2009. doi:10.1016/S0022-5096(01)00134-X.

Arzt, E., 1998. Size effects in materials due to microstructural and dimensional constraints: a comparative review. Acta Materialia 46, 5611–5626. doi:10.1016/S1359-6454(98)00231-6.

Asaro, R.J., 1985. Material modelling and failure modes in metal plasticity. Mechanics of Materials 4, 343–373. doi:10.1016/0167-6636(85)90032-8.

Asaro, R.J., Rice, J., 1977. Strain localization in ductile single crystals. Journal of the Mechanics and Physics of Solids 25, 309–338. doi:10.1016/0022-5096(77)90001-1.

Ashby, M.F., 1970. The deformation of plastically non-homogeneous materials. The Philosophical Magazine: A Journal of Theoretical Experimental and Applied Physics 21, 399–424. doi:10.1080/14786437008238426.

Aslan, O., Cordero, N., Gaubert, A., Forest, S., 2011. Micromorphic approach to single crystal plasticity and damage. International Journal of Engineering Science 49, 1311–1325. doi:10.1016/j.ijengsci.2011.03.008.

Bachmann, F., Hielscher, R., Schaeben, H., 2010. Texture analysis with MTEX-free and open source software toolbox. Solid State Phenomena 160, 63–68. doi:10.4028/www.scientific.net/SSP.160.63.

Bailey, J.E., 1963. The dislocation density, flow stress and stored energy in deformed polycrystalline copper. The Philosophical Magazine: A Journal of Theoretical Experimental and Applied Physics 8, 223–236. doi:10.1080/14786436308211120.

Baker, I., Liu, L., Mandal, D., 1995. The effect of grain size on the stored energy of cold work as a function of strain for polycrystalline nickel. Scripta Metallurgica et Materialia; (United States) 32:2. doi:10.1016/S0956-716X(99)80031-4.

Bandstra, J., Koss, D., 2001. Modeling the ductile fracture process of void coalescence by void-sheet formation. Materials Science and Engineering: A 319-321, 490–495. doi:10.1016/S0921-5093(00)02007-4.

Barbe, F., Decker, L., Jeulin, D., Cailletaud, G., 2001a. Intergranular and intragranular behavior of polycrystalline aggregates. part 1: F.e. model. International Journal of Plasticity 17, 513–536. doi:10.1016/S0749-6419(00)00061-9.

Barbe, F., Parisot, R., Forest, S., Cailletaud, G., 2001b. Calibrating a homogenized polycrystal model from large scale fe computations of polycrystalline aggregates. Journal de Physique IV 11, 5–277. doi:10.1051/jp4:2001534.

Bardella, L., Panteghini, A., 2015. Modelling the torsion of thin metal wires by distortion gradient plasticity. Journal of the Mechanics and Physics of Solids 78, 467–492. doi:10.1016/j.jmps.2015.03.003.

Bardella, L., Segurado, J., Panteghini, A., Llorca, J., 2013. Latent hardening size effect in small-scale plasticity. Modelling and Simulation in Materials Science and Engineering 21, 055009. doi:10.1088/0965-0393/21/5/055009.

Basinski, Z.S., Hume-Rothery, W., 1957. The instability of plastic flow of metals at very low temperatures. Proceedings of the Royal Society of London. Series A. Mathematical and Physical Sciences 240, 229–242. doi:10.1098/rspa.1957.0079.

Batra, R., Chen, L., 2001. Effect of viscoplastic relations on the instability strain, shear band initiation strain, the strain corresponding to the minimum shear band spacing, and the band width in a thermoviscoplastic material. International Journal of Plasticity 17, 1465–1489. doi:http://10.0.3.248/S0749-6419(01)00004-3.

Batra, R., Kim, C., 1991. Effect of thermal conductivity on the initiation, growth and bandwidth of adiabatic shear bands. International Journal of Engineering Science 29, 949–960. doi:10.1016/0020-7225(91)90168-3.

Batra, R., Kim, C., 1992. Analysis of shear banding in twelve materials. International Journal of Plasticity 8, 425–452. doi:10.1016/0749-6419(92)90058-K.

Baucom, J., Zikry, M., 1999. Perturbation analysis of high strain-rate shear localization in b.c.c. crystalline materials. Acta Mechanica 137, 109–129. doi:10.1007/BF01313148.

Bayerschen, E., 2017. Single-crystal gradient plasticity with an accumulated plastic slip: Theory and applications. KIT Scientific Publishing.

Bayerschen, E., Prahs, A., Wulfinghoff, S., Ziemann, M., Gruber, P.A., Walter, M., Böhlke, T., 2016. Modeling contrary size effects of tensile- and torsion-loaded oligocrystalline gold microwires. Journal of Materials Science 51, 7451–7470. doi:10.1007/s10853-016-0020-7.

Benzerga, A., Bréchet, Y., Needleman, A., Van der Giessen, E., 2005. The stored energy of cold work: Predictions from discrete dislocation plasticity. Acta Materialia 53, 4765–4779. doi:10.1016/j.actamat.2005.07.011.

Bertram, A., 2003. Finite thermoplasticity based on isomorphisms. International Journal of Plasticity 19, 2027–2050. doi:10.1016/S0749-6419(03)00057-3.

Bertram, A., 2015. Finite gradient elasticity and plasticity: a constitutive thermodynamical framework. Continuum Mechanics and Thermodynamics 27. doi:10.1007/s00161-015-0417-6.

Bertram, A., Krawietz, A., 2012. On the introduction of thermoplasticity. Acta Mechanica 223, 2257–2268. doi:10.1007/s00707-012-0700-6.

Berveiller, M., Zaoui, A., 1978. An extension of the self-consistent scheme to plastically-flowing polycrystals. Journal of the Mechanics and Physics of Solids 26, 325–344. doi:10.1016/0022-5096(78)90003-0.

Besson, J., 2009. Damage of ductile materials deforming under multiple plastic or viscoplastic mechanisms. International Journal of Plasticity 25, 2204–2221. doi:https://doi.org/10.1016/j.ijplas.2009.03.001.

Besson, J., Cailletaud, G., Chaboche, J.L., Forest, S., Blétry, M., Gladwell, G., 2010. Inelastic constitutive laws at finite deformation doi:10.1007/978-90-481-3356-7_6.

Bever, M., Holt, D., Titchener, A., 1973. The stored energy of cold work. Progress in Materials Science 17, 5–177. doi:10.1016/0079-6425(73)90001-7.

Biermann, H., Ungár, T., Pfannenmüller, T., Hoffmann, G., Borbély, A., Mughrabi, H., 1993. Local variations of lattice parameter and long-range internal stresses during cyclic deformation of polycrystalline copper. Acta Metallurgica et Materialia 41, 2743–2753. doi:10.1016/0956-7151(93)90143-G.

Bittencourt, E., Needleman, A., Gurtin, M., Van der Giessen, E., 2003. A comparison of nonlocal continuum and discrete dislocation plasticity predictions. Journal of the Mechanics and Physics of Solids 51, 281–310. doi:10.1016/S0022-5096(02)00081-9.

Böhm, H.J., 2004. A short introduction to continuum micromechanics, in: Mechanics of Microstructured Materials. Springer Vienna, Vienna, pp. 1–40. doi:10.1007/978-3-7091-2776-6_1.

Borg, U., 2007. A strain gradient crystal plasticity analysis of grain size effects in polycrystals. European Journal of Mechanics - A/Solids 26, 313–324. doi:10.1016/j.euromechsol.2006.09.006.

Borg, U., Niordson, C.F., Kysar, J.W., 2008. Size effects on void growth in single crystals with distributed voids. International Journal of Plasticity 24, 688–701. doi:10.1016/j.ijplas.2007.07.015.

de Borst, R., Sluys, L., Mühlhaus, H., Pamin, J., 1993. Fundamental issues in finite element analyses of localization of deformation. Engineering Computations 10, 99–121. doi:10.1108/eb023897.

Boukadia, J., Sidoroff, F., 1988. Simple shear and torsion of a perfectly plastic single crystal in finite transformations. Archives of Mechanics 40, 497–513.

Brepols, T., Wulfinghoff, S., Reese, S., 2017. Gradient-extended two-surface damage-plasticity: Micromorphic formulation and numerical aspects. International Journal of Plasticity 97, 64–106. doi:10.1016/j.ijplas.2017.05.010.

Bronkhorst, C., Mayeur, J., Livescu, V., Pokharel, R., Brown, D., Gray, G., 2019. Structural representation of additively manufactured 316l austenitic stainless steel. International Journal of Plasticity 118, 70–86. doi:10.1016/j.ijplas.2019.01.012.

Bronkhorst, C.A., Kalidindi, S.R., Anand, L., 1992. Polycrystalline plasticity and the evolution of crystallographic texture in fcc metals. Philosophical Transactions of the Royal Society of London. Series A: Physical and Engineering Sciences 341, 443–477. doi:10.1098/rsta.1992.0111.

Burns, T., Davies, M., 2002. On repeated adiabatic shear band formation during high-speed machining. International Journal of Plasticity 18, 487–506. doi:10.1016/S0749-6419(01)00006-7.

Busso, E., Meissonnier, F., O'Dowd, N., 2000. Gradient-dependent deformation of two-phase single crystals. Journal of the Mechanics and Physics of Solids 48, 2333–2361. doi:10.1016/S0022-5096(00)00006-5.

Busso, E.P., Cailletaud, G., 2005. On the selection of active slip systems in crystal plasticity. International Journal of Plasticity 21, 2212–2231. doi:10.1016/j.ijplas.2005.03.019.

Cailletaud, G., Diard, O., Feyel, F., Forest, S., 2003a. Computational crystal plasticity: From single crystal to homogenized polycrystals. Technische Mechanik 23, 130–145.

Cailletaud, G., Forest, S., Jeulin, D., Feyel, F., Galliet, I., Mounoury, V., Quilici, S., 2003b. Some elements of microstructural mechanics. Computational Materials Science 27, 351–374. doi:10.1016/S0927-0256(03)00041-7.

Cailletaud, G., Pilvin, P., 1994. Utilisation de modèles polycristallins pour le calcul par éléments finis. Revue Européenne des Éléments Finis 3, 515–541.

Čebron, M., Kosel, F., 2014. Stored energy predictions from dislocation-based hardening models and hardness measurements for tensile-deformed commercial purity copper. Strojniški vestnik - Journal of Mechanical Engineering 60, 462–474. doi:10.5545/SV-JME.2013.1569.

Cermelli, P., Gurtin, M.E., 2001. On the characterization of geometrically necessary dislocations in finite plasticity. Journal of the Mechanics and Physics of Solids 49, 1539–1568. doi:10.1016/S0022-5096(00)00084-3.

Chambon, R., Caillerie, D., Hassan, N.E., 1998. One-dimensional localisation studied with a second grade model. European Journal of Mechanics - A/Solids 17, 637–656. doi:10.1016/S0997-7538(99)80026-6.

Chang, Y.W., Asaro, R.J., 1980. Lattice rotations and localized shearing in single crystals. Arch. Mech. 32, 369–388. doi:10.1016/S0191-8141(97)00016-3.

Chokshi, A., Rosen, A., Karch, J., Gleiter, H., 1989. On the validity of the hall-petch relationship in nanocrystalline materials. Scripta Metallurgica 23, 1679–1683. doi:10.1016/0036-9748(89)90342-6.

Cordero, N., Forest, S., Busso, E., Berbenni, S., Cherkaoui, M., 2012a. Grain size effects on plastic strain and dislocation density tensor fields in metal polycrystals. Computational Materials Science 52, 7–13. doi:10.1016/j.commatsci.2011.02.043.

Cordero, N.M., Forest, S., Busso, E.P., 2012b. Generalised continuum modelling of grain size effects in polycrystals. Comptes Rendus Mécanique 340, 261–274. doi:10.1016/j.crme.2012.02.009.

Cordero, N.M., Forest, S., Busso, E.P., 2013. Micromorphic modelling of grain size effects in metal polycrystals. GAMM-Mitteilungen 36, 186–202. doi:10.1002/gamm.201310011.

Cordero, N.M., Gaubert, A., Forest, S., Busso, E.P., Gallerneau, F., Kruch, S., 2010. Size effects in generalised continuum crystal plasticity for two-phase laminates. Journal of the Mechanics and Physics of Solids 58, 1963–1994. doi:10.1016/j.jmps.2010.06.012.

Coudon, F., Cailletaud, G., Cormier, J., Marcin, L., 2019. A multiscale model for nickel-based directionally solidified materials. International Journal of Plasticity 115, 1–17. doi:10.1016/j.ijplas.2018.10.003.

Das, S., Hofmann, F., Tarleton, E., 2018. Consistent determination of geometrically necessary dislocation density from simulations and experiments. International Journal of Plasticity 109, 18–42. doi:10.1016/j.ijplas.2018.05.001.

Davaze, V., Vallino, N., Langrand, B., Besson, J., Feld-Payet, S., 2021. A non-local damage approach compatible with dynamic explicit simulations and parallel computing. International Journal of Solids and Structures 228, 110999. doi:10.1016/j.ijsolstr.2021.02.010.

DeMange, J.J., Prakash, V., Pereira, J.M., 2009. Effects of material microstructure on blunt projectile penetration of a nickel-based super alloy. International Journal of Impact Engineering 36, 1027–1043. doi:10.1016/j.ijimpeng.2009.01.007.

Demiral, M., Roy, A., Sayed, T.E., Silberschmidt, V.V., 2014. Numerical modelling of micro-machining of f.c.c. single crystal: Influence of strain gradients. Computational Materials Science 94, 273–278. doi:10.1016/j.commatsci.2014.05.058.

Dève, H.E., Asaro, R.J., 1989. The development of plastic failure modes in crystalline materials: Shear bands in FCC polycrystals. Metallurgical Transactions A 20, 579–593. doi:10.1007/BF02667576.

Diamantopoulou, E., Liu, W., Labergere, C., Badreddine, H., Saanouni, K., Hu, P., 2017. Micromorphic constitutive equations with damage applied to metal forming. International Journal of Damage Mechanics 26, 314–339. doi:10.1177/1056789516684650.

Diard, O., Leclercq, S., Rousselier, G., Cailletaud, G., 2005. Evaluation of finite element based analysis of 3d multicrystalline aggregates plasticity: Application to crystal plasticity model identification and the study of stress and strain fields near grain boundaries. International Journal of Plasticity 21, 691–722. doi:10.1016/j.ijplas.2004.05.017.

Diaz, A., Alegre, J., Cuesta, I., 2016. Coupled hydrogen diffusion simulation using a heat transfer analogy. International Journal of Mechanical Sciences 115-116, 360–369. doi:10.1016/j.ijmecsci.2016.07.020.

Dillamore, I.L., Roberts, J.G., Bush, A.C., 1979. Occurrence of shear bands in heavily rolled cubic metals. Metal Science 13, 73–77. doi:10.1179/msc.1979.13.2.73.

Dillard, T., Forest, S., Ienny, P., 2006. Micromorphic continuum modelling of the deformation and fracture behaviour of nickel foams. European Journal of Mechanics - A/Solids 25, 526–549. doi:10.1016/j.euromechsol.2005.11.006.

Dodd, B., Bai, Y., 2012. Preface, in: Dodd, B., Bai, Y. (Eds.), Adiabatic Shear Localization (Second Edition). second edition ed.. Elsevier, Oxford, p. ix. doi:10.1016/B978-0-08-097781-2.00015-0.

Dorothy, H.L., 2018. Numerical modelling of coupled adiabatic shear banding and micro-voiding assisted dynamic ductile failure. Ph.D. thesis. Université Paul Sabatier - Toulouse III. URL: https://tel.archives-ouvertes.fr/tel-02307383.

Dunne, F.P.E., Kiwanuka, R., Wilkinson, A.J., 2012. Crystal plasticity analysis of micro-deformation, lattice rotation and geometrically necessary dislocation density. Proceedings of the Royal Society A: Mathematical, Physical and Engineering Sciences 468, 2509–2531. doi:10.1098/rspa.2012.0050.

Duszek-Perzyna, M., Perzyna, P., 1996. Adiabatic shear band localization of inelastic single crystals in symmetric double-slip process. Archive of Applied Mechanics 66, 369–384. doi:10.1007/BF00803672.

Duszek-Perzyna, M.K., Perzyna, P., 1993. Adiabatic shear band localization in elastic-plastic single crystals. International Journal of Solids and Structures 30, 61–89. doi:10.1016/0020-7683(93)90132-Q.

Déprés, C., Robertson, C., Fivel, M., 2006. Low-strain fatigue in aisi 316l steel surface grains: a 3d discrete dislocation dynamics modelling of the early cycles ii- persistent slip markings and micro-crack nucleation. Phil Mag 86, 79–97. doi:10.1080/14786430500341250.

Ekh, M., Bargmann, S., Grymer, M., 2011. Influence of grain boundary conditions on modeling of size-dependence in polycrystals. Acta Mechanica 218, 103–113. doi:10.1007/s00707-010-0403-9.

Engel, U., Eckstein, R., 2002. Microforming—from basic research to its realization. Journal of Materials Processing Technology 125-126, 35–44. doi:10.1016/S0924-0136(02)00415-6.

Eringen, A., Suhubi, E., 1964. Nonlinear theory of simple microelastic solids. Int. J. Engng Sci. 2, 189–203, 389–404. doi:10.1016/0020-7225(64)90004-7.

Eringen, A.C., 1999. Microcontinuum field theories. Springer, New York.

Eshelby, J.D., Peierls, R.E., 1957. The determination of the elastic field of an ellipsoidal inclusion, and related problems. Proceedings of the Royal Society of London. Series A. Mathematical and Physical Sciences 241, 376–396. doi:10.1098/rspa.1957.0133.

Evers, L., Brekelmans, W., Geers, M., 2004. Scale dependent crystal plasticity framework with dislocation density and grain boundary effects. International Journal of Solids and Structures 41, 5209–5230. doi:10.1016/j.ijsolstr.2004.04.021.

Fekete, B., Szekeres, A., 2015. Investigation on partition of plastic work converted to heat during plastic deformation for reactor steels based on inverse experimental-computational method. European Journal of Mechanics - A/Solids 53, 175–186. doi:10.1016/j.euromechsol.2015.05.002.

Fisher, J., Hart, E., Pry, R., 1953. The hardening of metal crystals by precipitate particles. Acta Metallurgica 1, 336–339. doi:10.1016/0001-6160(53)90109-6.

Fleck, N., Hutchinson, J., 1993. A phenomenological theory for strain gradient effects in plasticity. Journal of the Mechanics and Physics of Solids 41, 1825–1857. doi:10.1016/0022-5096(93)90072-N.

Fleck, N., Hutchinson, J., 1997. Strain gradient plasticity. Advances in Applied Mechanics 33, 295–361.

Fleck, N., Muller, G., Ashby, M., Hutchinson, J., 1994. Strain gradient plasticity: Theory and experiment. Acta Metallurgica et Materialia 42, 475–487. doi:10.1016/0956-7151(94)90502-9.

Flipon, B., Keller, C., Quey, R., Barbe, F., 2020. A full-field crystal-plasticity analysis of bimodal polycrystals. International Journal of Solids and Structures 184, 178–192. doi:10.1016/j.ijsolstr.2019.02.005.

Forest, S., 1998. Modeling slip, kink and shear banding in classical and generalized single crystal plasticity. Acta Materialia 46, 3265–3281. doi:10.1016/S1359-6454(98)00012-3.

Forest, S., 2009. Micromorphic approach for gradient elasticity, viscoplasticity, and damage. Journal of Engineering Mechanics 135, 117–131. doi:10.1061/(asce)0733-9399(2009)135:3(117).

Forest, S., 2016a. Nonlinear regularisation operators as derived from the micromorphic approach to gradient elasticity, viscoplasticity and damage. Proc. R. Soc. A 472, 20150755. doi:10.1098/rspa.2015.0755.

Forest, S., 2016b. Nonlinear regularization operators as derived from the micromorphic approach to gradient elasticity, viscoplasticity and damage. Proc. R. Soc. A 472, 20150755. doi:10.1098/rspa.2015.0755.

Forest, S., Lorentz, E., 2004. Localization phenomena and regularization methods, in: Besson, J. (Ed.), Local approach to fracture. Les presses de l'ecole des mines de paris. Ecole d'été "Mécanique de l'endommagement et approche locale de la rupture" (MEALOR), juillet 2004, pp. 311–371.

Forest, S., Olschewski, J., Ziebs, J., Kühn, H.J., Meersmann, J., Frenz, H., 1996. The elastic/plastic deformation behaviour of various oriented SC16 single crystals under combined tension/torsion fatigue loading, in: Lütjering, G., Nowack, H. (Eds.), Sixth International Fatigue Congress, Pergamon. pp. 1087–1092.

Forest, S., Sievert, R., 2003. Elastoviscoplastic constitutive frameworks for generalized continua. Acta Mechanica 160, 71–111. doi:10.1007/s00707-002-0975-0.

Fortin, M., Glowinski, R., 1983. Chapter iii on decomposition-coordination methods using an augmented lagrangian, in: Studies in Mathematics and Its Applications. Elsevier. volume 15, pp. 97–146. doi:10.1016/S0168-2024(08)70028-6.

Frank, F.C., Stroh, A.N., 1952. On the theory of kinking. Proceedings of the Physical Society. Section B 65, 811–821. doi:10.1088/0370-1301/65/10/311.

Fredriksson, P., Gudmundson, P., 2006. Competition between interface and bulk dominated plastic deformation in strain gradient plasticity. Modelling and Simulation in Materials Science and Engineering 15, S61–S69. doi:10.1088/0965-0393/15/1/s06.

Gama, B.A., Lopatnikov, S.L., Gillespie, John W, J., 2004. Hopkinson bar experimental technique: A critical review . Applied Mechanics Reviews 57, 223–250. doi:10.1115/1.1704626.

Gao, H., Huang, Y., 2001. Taylor-based nonlocal theory of plasticity. International Journal of Solids and Structures 38, 2615–2637. doi:10.1016/S0020-7683(00)00173-6.

Geers, M., Peerlings, R., Brekelmans, W., 2000. Phenomenological nonlocal approaches based on implicit gradient-enhanced damage. Acta Mechanica 144, 1–15. doi:10.1007/BF01181824.

Germain, P., Son Nguyen, Q., Suquet, P., 1983. Continuum Thermodynamics. Journal of Applied Mechanics 50, 1010–1020.

Geuzaine, C., Remacle, J.F., 2009. Gmsh: A 3-D finite element mesh generator with built-in pre- and post-processing facilities. International Journal for Numerical Methods in Engineering 79, 1309–1331. doi:10.1002/nme.2579.

Gilman, J.J., 1994. Micromechanics of shear banding. Mechanics of Materials 17, 83–96. doi:10.1016/0167-6636(94)90051-5.

Group, E., et al., 2000. Pam-crash theory notes manual. Pam System International .

Groves, G.W., Kelly, A., 1963. Independent slip systems in crystals. The Philosophical Magazine: A Journal of Theoretical Experimental and Applied Physics 8, 877–887. doi:10.1080/14786436308213843.

Guan, Y., Chen, B., Zou, J., Britton, T.B., Jiang, J., Dunne, F.P., 2017. Crystal plasticity modelling and hr-dic measurement of slip activation and strain localization in single and oligo-crystal ni alloys under fatigue. International Journal of Plasticity 88, 70–88. doi:10.1016/j.ijplas.2016.10.001.

Guo, S., He, Y., Lei, J., Li, Z., Liu, D., 2017. Individual strain gradient effect on torsional strength of electropolished microscale copper wires. Scripta Materialia 130, 124–127. doi:10.1016/j.scriptamat.2016.11.029.

Guo, S., He, Y., Tian, M., Liu, D., Li, Z., Lei, J., Han, S., 2020. Size effect in cyclic torsion of micron-scale polycrystalline copper wires. Materials Science and Engineering: A 792, 139671. doi:10.1016/j.msea.2020.139671.

Gupta, S., Ma, A., Hartmaier, A., 2015. Investigating the influence of crystal orientation on bending size effect of single crystal beams. Computational Materials Science 101, 201–210. doi:10.1016/j.commatsci.2014.12.038.

Gurtin, M.E., 1996. Generalized ginzburg-landau and cahn-hilliard equations based on a microforce balance. Physica D: Nonlinear Phenomena 92, 178–192. doi:10.1016/0167-2789(95)00173-5.

Gurtin, M.E., 2002. A gradient theory of single-crystal viscoplasticity that accounts for geometrically necessary dislocations. Journal of the Mechanics and Physics of Solids 50, 5–32. doi:10.1016/S0022-5096(01)00104-1.

Gurtin, M.E., Anand, L., 2005. A theory of strain-gradient plasticity for isotropic, plastically irrotational materials. part i: Small deformations. Journal of the Mechanics and Physics of Solids 53, 1624–1649. doi:10.1016/j.jmps.2004.12.008.

Gurtin, M.E., Needleman, A., 2005. Boundary conditions in small-deformation, single-crystal plasticity that account for the burgers vector. Journal of the Mechanics and Physics of Solids 53, 1–31. doi:10.1016/j.jmps.2004.06.006.

H. Neuhäuser, i.F.N.E., 1983. Dislocation in Solids. volume 6. Holland Publishing Company.

Hall, E.O., 1951. The deformation and ageing of mild steel: III discussion of results. Proceedings of the Physical Society. Section B 64, 747–753. doi:10.1088/0370-1301/64/9/303.

Haque, M., Saif, M., 2003. Strain gradient effect in nanoscale thin films. Acta Materialia 51, 3053–3061. doi:10.1016/S1359-6454(03)00116-2.

Harren, S., Dève, H., Asaro, R., 1988. Shear band formation in plane strain compression. Acta Metallurgica 36, 2435–2480. doi:10.1016/0001-6160(88)90193-9.

Hill, R., 1962. Acceleration waves in solids. Journal of the Mechanics and Physics of Solids 10, 1–16. doi:10.1016/0022-5096(62)90024-8.

Hill, R., 1965. A self-consistent mechanics of composite materials. Journal of the Mechanics and Physics of Solids 13, 213–222. doi:10.1016/0022-5096(65)90010-4.

Hill, R., 1966. Generalized constitutive relations for incremental deformation of metal crystals by multislip. Journal of the Mechanics and Physics of Solids 14, 95–102. doi:10.1016/0022-5096(66)90040-8.

Hill, R., Rice, J., 1972. Constitutive analysis of elastic-plastic crystals at arbitrary strain. Journal of the Mechanics and Physics of Solids 20, 401–413. doi:10.1016/0022-5096(72)90017-8.

Horstemeyer, M., Lim, J., Lu, W.Y., Mosher, D., Baskes, M., Prantil, V., Plimpton, S., 2002. Torsion/simple shear of single crystal copper. Journal of Engineering Materials and Technology-transactions of The Asme 124. doi:10.1115/1.1480407.

Hosford, W., Fleischer, R., Backofen, W.A., 1960. Tensile deformation of aluminum single crystals at low temperatures. Acta Metallurgica 8, 187–199. doi:10.1016/0001-6160(60)90127-9.

Hull, D., Bacon, D., 2011. Preface, in: Hull, D., Bacon, D. (Eds.), Introduction to Dislocations (Fifth Edition). fifth edition ed.. Butterworth-Heinemann, Oxford, pp. ix–x. doi:10.1016/B978-0-08-096672-4.00012-8.

Hure, J., El Shawish, S., Cizelj, L., Tanguy, B., 2016. Intergranular stress distributions in polycrystalline aggregates of irradiated stainless steel. Journal of Nuclear Materials 476, 231–242. doi:10.1016/j.jnucmat.2016.04.017.

Husser, E., Soyarslan, C., Bargmann, S., 2017. Size affected dislocation activity in crystals: Advanced surface and grain boundary conditions. Extreme Mechanics Letters 13, 36–41. doi:10.1016/j.eml.2017.01.007.

Håkansson, P., Wallin, M., Ristinmaa, M., 2008. Prediction of stored energy in polycrystalline materials during cyclic loading. International Journal of Solids and Structures 45, 1570–1586. doi:10.1016/j.ijsolstr.2007.10.009.

Iturbe, A., Giraud, E., Hormaetxe, E., Garay, A., Germain, G., Ostolaza, K., Arrazola, P., 2017. Mechanical characterization and modelling of inconel 718 material behavior for machining process assessment. Materials Science and Engineering: A 682, 441–453. doi:10.1016/j.msea.2016.11.054.

J. Boukadia, A. Chenaoui, F.S., 1993. Simple shear in fcc single crystals at large deformations, in: Hussein, M.I. (Ed.), Large Plastic Deformations: Fundamental Aspects and Applications to Metal Forming (1st ed.). Advances in Applied Mechanics. doi:https://doi.org/10.1201/9780203749173.

Jafari, M., Jamshidian, M., Ziaei-Rad, S., 2017. A finite-deformation dislocation density-based crystal viscoplasticity constitutive model for calculating the stored deformation energy. International Journal of Mechanical Sciences 128-129, 486–498. doi:10.1016/j.ijmecsci.2017.05.016.

Jebahi, M., Forest, S., 2021. Scalar-based strain gradient plasticity theory to model size-dependent kinematic hardening effects. Continuum Mechanics and Thermodynamics doi:10.1007/s00161-020-00967-0.

Jin, T., Mourad, H.M., Bronkhorst, C.A., Livescu, V., 2018. Finite element formulation with embedded weak discontinuities for strain localization under dynamic conditions. Comput. Mech. 61, 3–18. doi:10.1007/s00466-017-1470-8.

Johansson, J., Persson, C., Lai, H., Colliander, M.H., 2016. Microstructural examination of shear localisation during high strain rate deformation of alloy 718. Materials Science and Engineering: A 662, 363–372. doi:10.1016/j.msea.2016.03.080.

Johansson, J., Persson, C., Testa, G., Ruggiero, A., Bonora, N., Hörnqvist Colliander, M., 2017. Effect of microstructure on dynamic shear localisation in alloy 718. Mechanics of Materials 109, 88–100. doi:10.1016/J.MECHMAT.2017.03.020.

Kaiser, T., Menzel, A., 2019a. A dislocation density tensor-based crystal plasticity framework. Journal of the Mechanics and Physics of Solids 131, 276–302. doi:10.1016/j.jmps.2019.05.019.

Kaiser, T., Menzel, A., 2019b. An incompatibility tensor-based gradient plasticity formulation-Theory and numerics. Computer Methods in Applied Mechanics and Engineering 345, 671–700. doi:10.1016/j.cma.2018.11.013.

Kalidindi, S., Bronkhorst, C., Anand, L., 1992. Crystallographic texture evolution in bulk deformation processing of fcc metals. Journal of the Mechanics and Physics of Solids 40, 537–569. doi:10.1016/0022-5096(92)80003-9.

Kanit, T., Forest, S., Galliet, I., Mounoury, V., Jeulin, D., 2003. Determination of the size of the representative volume element for random composites: statistical and numerical approach. International Journal of Solids and Structures 40, 3647–3679. doi:10.1016/S0020-7683(03)00143-4.

Kapoor, R., Nemat-Nasser, S., 1998. Determination of temperature rise during high strain rate deformation. Mechanics of Materials 27, 1–12. doi:10.1016/S0167-6636(97)00036-7.

Keller, C., Hug, E., Habraken, A., Duchene, L., 2012. Finite element analysis of the free surface effects on the mechanical behavior of thin nickel polycrystals. International Journal of Plasticity 29, 155–172. doi:10.1016/j.ijplas.2011.08.007.

Knezevic, M., Beyerlein, I.J., 2018. Multiscale modeling of microstructure-property relationships of polycrystalline metals during thermo-mechanical deformation. Advanced Engineering Materials 20, 1700956. doi:10.1002/adem.201700956.

Knysh, P., Korkolis, Y., 2015. Determination of the fraction of plastic work converted into heat in metals. Mechanics of Materials 86. doi:10.1016/j.mechmat.2015.03.006.

Kocks, U., Mecking, H., 2003. Physics and phenomenology of strain hardening: the fcc case. Progress in Materials Science 48, 171–273. doi:10.1016/S0079-6425(02)00003-8.

Koehler, J.S., 1941. On the dislocation theory of plastic deformation. Phys. Rev. 60, 397–410. doi:10.1103/PhysRev.60.397.

Kositski, R., Mordehai, D., 2021. Employing molecular dynamics to shed light on the microstructural origins of the taylor-quinney coefficient. Acta Materialia 205, 116511. doi:10.1016/j.actamat.2020.116511.

Kröner, E., 1958. Berechnung der elastischen konstanten des vielkristalls aus den konstanten des einkristalls. Zeitung Physik 151, 504–518.

Kubin, L., Devincre, B., Hoc, T., 2008. Modeling dislocation storage rates and mean free paths in face-centered cubic crystals. Acta materialia 56, 6040–6049. doi:10.1016/j.actamat.2008.08.012.

Kubin, L.P., Canova, G., Condat, M., Devincre, B., Pontikis, V., Bréchet, Y., 1992. Dislocation microstructures and plastic flow: A 3d simulation, in: Non Linear Phenomena in Materials Science II, Trans Tech Publications Ltd. pp. 455–472. doi:10.4028/www.scientific.net/SSP.23-24.455.

Kuroda, M., Tvergaard, V., 2006. Studies of scale dependent crystal viscoplasticity models. Journal of the Mechanics and Physics of Solids 54, 1789–1810. doi:10.1016/j.jmps.2006.04.002.

Landau, P., Osovski, S., Venkert, A., Gartnerova, V., Rittel, D., 2016. The genesis of adiabatic shear bands. Scientific Reports 6.

Langer, J., Bouchbinder, E., Lookman, T., 2010. Thermodynamic theory of dislocation-mediated plasticity. Acta Materialia 58, 3718–3732.

Langer, J.S., 2015. Statistical thermodynamics of strain hardening in polycrystalline solids. Physical Review E 92. doi:10.1103/physreve.92.032125.

Lee, E.H., Liu, D.T., 1967. Finite strain elastic plastic theory with application to plane wave analysis. Journal of Applied Physics 38, 19–27. doi:10.1063/1.1708953.

Lewandowski, M., Stupkiewicz, S., 2018. Size effects in wedge indentation predicted by a gradient-enhanced crystal-plasticity model. International Journal of Plasticity 109, 54–78. doi:10.1016/j.ijplas.2018.05.008.

Li, L., Zhou, Q., Zhou, Y., Cao, J., 2009. Numerical study on the size effect in the ultra-thin sheet's micro-bending forming process. Materials Science and Engineering: A 499, 32–35. doi:10.1016/j.msea.2007.11.101.

Lieou, C.K., Bronkhorst, C.A., 2020. Thermodynamic theory of crystal plasticity: Formulation and application to polycrystal fcc copper. Journal of the Mechanics and Physics of Solids 138, 103905. doi:10.1016/j.actamat.2010.03.009.

Lieou, C.K., Mourad, H.M., Bronkhorst, C.A., 2019. Strain localization and dynamic recrystallization in polycrystalline metals: Thermodynamic theory and simulation framework. International Journal of Plasticity 119, 171–187. doi:10.1016/j.ijplas.2019.03.005.

Lin, T., 1957. Analysis of elastic and plastic strains of a face-centred cubic crystal. Journal of the Mechanics and Physics of Solids 5, 143–149.

Ling, C., 2017. Modeling the intragranular ductile fracture of irradiated steels. Effects of crystal anisotropy and strain gradient. Theses. PSL Research University. URL: https://pastel.archives-ouvertes.fr/tel-01699226.

Ling, C., Besson, J., Forest, S., Tanguy, B., Latourte, F., Bosso, E., 2016. An elastoviscoplastic model for porous single crystals at finite strains and its assessment based on unit cell simulations. International Journal of Plasticity 84, 58–87. doi:10.1016/j.ijplas.2016.05.001.

Ling, C., Forest, S., Besson, J., Tanguy, B., Latourte, F., 2018. A reduced micromorphic single crystal plasticity model at finite deformations. application to strain localization and void growth in ductile metals. International Journal of Solids and Structures 134, 43–69. doi:0.1016/j.ijsolstr.2017.10.013.

Lisiecki, L., Nelson, D., Asaro, R., 1982. Lattice rotations, necking and localized deformation in fcc single crystals. Scripta Metallurgica 16, 441–448.

Liu, D., He, Y., Dunstan, D.J., Zhang, B., Gan, Z., Hu, P., Ding, H., 2013. Anomalous plasticity in the cyclic torsion of micron scale metallic wires. Phys. Rev. Lett. 110, 244301. doi:10.1103/PhysRevLett.110.244301.

Liu, D., He, Y., Tang, X., Ding, H., Hu, P., Cao, P., 2012. Size effects in the torsion of microscale copper wires: Experiment and analysis. Scripta Materialia 66, 406–409.

Liu, Y., Ngan, A., 2001. Depth dependence of hardness in copper single crystals measured by nanoindentation. Scripta Materialia 44, 237–241. doi:10.1016/S1359-6462(00)00598-4.

Longère, P., Dragon, A., Trumel, H., De Resseguier, T., Deprince, X., Petitpas, E., 2003. Modelling adiabatic shear banding via damage mechanics approach. Archives of Mechanics 55, 3–38. URL: https://hal.archives-ouvertes.fr/hal-00357446.

Longère, P., 2018. Respective/combined roles of thermal softening and dynamic recrystallization in adiabatic shear banding initiation. Mechanics of Materials 117, 81–90. doi:10.1016/j.mechmat.2017.10.003.

Longère, P., Dragon, A., Deprince, X., 2008. Numerical Study of Impact Penetration Shearing Employing Finite Strain Viscoplasticity Model Incorporating Adiabatic Shear Banding. Journal of Engineering Materials and Technology 131. doi:10.1115/1.3030880.

Longère, P., Dragon, A., Trumel, H., Deprince, X., 2005. Adiabatic shear banding-induced degradation in a thermo-elastic/viscoplastic material under dynamic loading. International Journal of Impact Engineering 32, 285–320. doi:https://doi.org/10.1016/j.ijimpeng.2005.03.002.

Ma, Q., Clarke, D., 1995. Size dependent hardness of silver single crystals. Journal of Materials Research 10, 853–863. doi:10.1557/JMR.1995.0853.

Macdougall, D., 2000. Determination of the plastic work converted to heat using radiometry. Experimental Mechanics 40, 298–306. doi:10.1007/BF02327503.

Malvern, L.E., 1969. Introduction to the mechanics of continuum medium. Englewood Cliffs.

Mandel, J., 1965. Generalisation de la theorie de plasticite de W. T. Koiter. International Journal of Solids and Structures 1, 273–295.

Mandel, J., 1973a. Equations constitutives et directeurs dans les milieux plastiques et viscoplastiques. International Journal of Solids and Structures 9, 725–740. doi:10.1016/0020-7683(73)90120-0.

Mandel, J., 1973b. Equations constitutives et directeurs dans les milieux plastiques et viscoplastiques. Int. J. Solids Structures 9, 725–740. doi:10.1016/0020-7683(73)90120-0.

Marano, A., Gélébart, L., Forest, S., 2021. FFT-based simulations of slip and kink bands formation in 3D polycrystals: influence of strain gradient crystal plasticity. Journal of the Mechanics and Physics of Solids 149, 104295. doi:10.1016/j.jmps.2021.104295.

Marchenko, A., Mazière, M., Forest, S., Strudel, J.L., 2016. Crystal plasticity simulation of strain aging phenomena in α-titanium at room temperature. International Journal of Plasticity 85, 1–33. doi:10.1016/j.ijplas.2016.05.007.

Marin, E., Dawson, P., 1998. On modelling the elasto-viscoplastic response of metals using polycrystal plasticity. Computer Methods in Applied Mechanics and Engineering 165, 1–21. doi:10.1016/S0045-7825(98)00034-6.

Mason, J., Rosakis, A., Ravichandran, G., 1994. On the strain and strain rate dependence of the fraction of plastic work converted to heat: an experimental study using high speed infrared detectors and the Kolsky bar. Mechanics of Materials 17, 135–145. doi:10.1016/0167-6636(94)90054-X.

Mayeur, J., McDowell, D., 2014. A comparison of gurtin type and micropolar theories of generalized single crystal plasticity. International Journal of Plasticity 57, 29–51. doi:10.1016/j.ijplas.2014.01.010.

Mayeur, J.R., McDowell, D.L., Bammann, D.J., 2011. Dislocation-based micropolar single crystal plasticity: Comparison of multi- and single criterion theories. Journal of the Mechanics and Physics of Solids 59, 398–422. doi:10.1016/j.jmps.2010.09.013.

Mazière, M., Forest, S., 2013. Strain gradient plasticity modeling and finite element simulation of Lüders band formation and propagation. Continuum Mechanics and Thermodynamics 27, 83–104. doi:10.1007/s00161-013-0331-8.

Mazière, M., Forest, S., 2015. Strain gradient plasticity modeling and finite element simulation of Lüders band formation and propagation. Continuum Mechanics and Thermodynamics 27, 83–104. doi:10.1007/s00161-013-0331-8.

Mazière, M., Forest, S., 2015. Strain gradient plasticity modeling and finite element simulation of Lüders band formation and propagation. Continuum Mechanics and Thermodynamics 27, 83–104. doi:10.1007/s00161-013-0331-8.

McElhaney, K.W., Vlassak, J.J., Nix, W.D., 1998. Determination of indenter tip geometry and indentation contact area for depth-sensing indentation experiments. Journal of Materials Research 13, 1300–1306. doi:10.1557/JMR.1998.0185.

Meyers, M., Xu, Y., Xue, Q., Pérez-Prado, M., McNelley, T., 2003. Microstructural evolution in adiabatic shear localization in stainless steel. Acta Materialia 51, 1307–1325. doi:10.1063/1.1483603.

Miehe, C., Schröder, J., Schotte, J., 1999. Computational homogenization analysis in finite plasticity simulation of texture development in polycrystalline materials. Computer Methods in Applied Mechanics and Engineering 171, 387–418. doi:10.1016/S0045-7825(98)00218-7.

Mika, D., Dawson, P., 1999. Polycrystal plasticity modeling of intracrystalline boundary textures. Acta Materialia 47, 1355–1369. doi:10.1016/S1359-6454(98)00386-3.

Mika, D.P., Dawson, P.R., 1998. Effects of grain interaction on deformation in polycrystals. Materials Science and Engineering: A 257, 62–76. doi:10.1016/S0921-5093(98)00824-7.

Molinari, A., Musquar, C., Sutter, G., 2002. Adiabatic shear banding in high speed machining of ti–6al–4v: experiments and modeling. International Journal of Plasticity 18, 443–459. doi:10.1016/S0749-6419(01)00003-1.

Moretti, M.A., Dalai, B., Åkerström, P., Arvieu, C., Jacquin, D., Lacoste, E., Lindgren, L.E., 2021. High Strain Rate Deformation Behavior and Recrystallization of Alloy 718. Metallurgical and Materials Transactions A doi:10.1007/s11661-021-06463-7.

Mourad, H., Bronkhorst, C., Livescu, V., Plohr, J., Cerreta, E., 2017. Modeling and simulation framework for dynamic strain localization in elasto-viscoplastic metallic materials subject to large deformations. International Journal of Plasticity 88, 1–26. doi:10.1016/j.ijplas.2016.09.009.

Mourad, H.M., Bronkhorst, C.A., Livescu, V., Plohr, J.N., Cerreta, E.K., 2016. Modeling and simulation framework for dynamic strain localization in elasto-viscoplastic metallic materials subject to large deformations. International Journal of Plasticity 88, 1–26. doi:10.1016/j.ijplas.2016.09.009.

Mura, T., 1994. A theory of fatigue crack initiation. Materials Science and Engineering: A 176, 61–70. doi:10.1016/0921-5093(94)90959-8.

Musienko, A., Cailletaud, G., Diard, O., 2004. Damage, opening and sliding of grain boundaries, in: Ahzi, S., Cherkaoui, M., Khaleel, M.A., Zbib, H.M., Zikry, M.A., Lamatina, B. (Eds.), IUTAM Symposium on Multiscale Modeling and Characterization of Elastic-Inelastic Behavior of Engineering Materials, Springer Netherlands, Dordrecht. pp. 149–156.

Musienko, A., Tatschl, A., Schmidegg, K., Schmidegg, K., Kolednik, O., Pippan, R., Cailletaud, G., 2007. Three-dimensional finite element simulation of a polycrystalline copper specimen. Acta Materialia 55, 4121–4136. doi:10.1016/j.actamat.2007.01.053.

Nedjar, B., 2001. Elastoplastic-damage modelling including the gradient of damage: Formulation and computational aspects. International Journal of Solids and Structures 38, 5421–5451. doi:10.1016/S0020-7683(00)00358-9.

Needleman, A., 1988. Material rate dependence and mesh sensitivity in localization problems. Computer Methods in Applied Mechanics and Engineering 67, 69–85. doi:10.1016/0045-7825(88)90069-2.

Nellemann, C., Niordson, C., Nielsen, K., 2017. An incremental flow theory for crystal plasticity incorporating strain gradient effects. International Journal of Solids and Structures 110-111, 239–250. doi:10.1016/j.ijsolstr.2017.01.025.

Nellemann, C., Niordson, C., Nielsen, K., 2018. Hardening and strengthening behavior in rate-independent strain gradient crystal plasticity. European Journal of Mechanics - A/Solids 67, 157–168. doi:10.1016/j.euromechsol.2017.09.006.

Nemat-Nasser, S., Isaacs, J.B., Liu, M., 1998. Microstructure of high-strain, high-strain-rate deformed tantalum. Acta Materialia 46, 1307–1325. doi:10.1016/S1359-6454(97)00746-5.

Nieto-Fuentes, J., Rittel, D., Osovski, S., 2018. On a dislocation-based constitutive model and dynamic thermomechanical considerations. International Journal of Plasticity 108, 55–69. doi:10.1016/j.ijplas.2018.04.012.

Niordson, C.F., Kysar, J.W., 2014. Computational strain gradient crystal plasticity. Journal of the Mechanics and Physics of Solids 62, 31–47. doi:10.1016/j.jmps.2013.08.014.

Nix, W.D., Gao, H., 1998. Indentation size effects in crystalline materials: A law for strain gradient plasticity. Journal of the Mechanics and Physics of Solids 46, 411–425. doi:10.1016/S0022-5096(97)00086-0.

Nouailhas, D., Cailletaud, G., 1995. Tension-torsion behavior of single-crystal superalloys - Experiment and finite-element analysis. Int. J. Plasticity 8, 451–470.

Nye, J., 1953. Some geometrical relations in dislocated crystals. Acta Metallurgica 1, 153–162. doi:10.1016/0001-6160(53)90054-6.

Oliferuk, W., Swiatnicki, W.A., Grabski, M.W., 1995. Effect of the grain size on the rate of energy storage during the tensile deformation of an austenitic steel. Materials Science and Engineering: A 197, 49–58. doi:10.1016/0921-5093(94)09766-6.

Oliferuk, W., Świåtnicki, W.A., Grabski, M.W., 1993. Rate of energy storage and microstructure evolution during the tensile deformation of austenitic steel. Materials Science and Engineering: A 161, 55–63. doi:10.1016/0921-5093(93)90475-T.

Onsager, L., 1931a. Reciprocal relations in irreversible processes. I. Phys. Rev. 37, 405–426. doi:10.1103/PhysRev.37.405.

Onsager, L., 1931b. Reciprocal relations in irreversible processes. II. Phys. Rev. 38, 2265–2279. doi:10.1103/PhysRev.38.2265.

Orowan, E., 1942. A type of plastic deformation new a type of plastic deformation new in metals. Nature 149, 643–644. doi:10.1038/149643a0.

Orowan, E., 1947. Discussion, symposium on internal stresses. Inst. Metals, Londan , 451.

Osovski, S., Rittel, D., Venkert, A., 2013. The respective influence of microstructural and thermal softening on adiabatic shear localization. Mechanics of Materials 56, 11–22. doi:10.1016/j.mechmat.2012.09.008.

Ottosen, N.S., Ristinmaa, M., 2005. 21 - thermodynamic framework for constitutive modeling, in: Ottosen, N.S., Ristinmaa, M. (Eds.), The Mechanics of Constitutive Modeling. Elsevier Science Ltd, Oxford, pp. 551–589. doi:10.1016/B978-008044606-6/50021-7.

Pamin, J., Wcisło, B., Kowalczyk-Gajewska, K., 2017. Gradient-enhanced large strain thermoplasticity with automatic linearization and localization simulations. Journal of Mechanics of Materials and Structures 12, 123–146. doi:10.2140/jomms.2017.12.123.

Panteghini, A., Bardella, L., 2016. On the finite element implementation of higher-order gradient plasticity, with focus on theories based on plastic distortion incompatibility. Computer Methods in Applied Mechanics and Engineering 310, 840–865. doi:10.1016/j.cma.2016.07.045.

Panteghini, A., Bardella, L., 2018. On the role of higher-order conditions in distortion gradient plasticity. Journal of the Mechanics and Physics of Solids 118, 293–321. doi:10.1016/j.jmps.2018.05.019.

Panteghini, A., Bardella, L., 2020. Modelling the cyclic torsion of polycrystalline micron-sized copper wires by distortion gradient plasticity. Philosophical Magazine 100, 2352–2364. doi:10.1080/14786435.2020.1766144.

Peerlings, R., Geers, M., de Borst, R., Brekelmans, W., 2001. A critical comparison of nonlocal and gradient-enhanced softening continua. International Journal of Solids and Structures 38, 7723–7746. doi:10.1016/S0020-7683(01)00087-7.

Peirs, J., Verleysen, P., Degrieck, J., 2008. The use of hat-shaped specimens for dynamic shear testing. Foundations of Civil and Environmental Engineering 11, 97–111.

Perzyna, P., 2002. Thermodynamical theory of inelastic single crystals. Engineering Transactions 50, 107–164. doi:10.24423/engtrans.517.2002.

Perzyna, P., Korbel, K., 1996. Analysis of the influence of the substructure of a crystal on shear band localization phenomena of plastic deformation. Mechanics of Materials 24, 141–158. doi:10.1016/S0167-6636(96)00032-4.

Perzyna, P., Korbel, K., 1998. Analysis of the influence of various effects on criteria for adiabatic shear band localization in single crystals. Acta Mechanica 129, 31–62. doi:10.1007/BF01379649.

Petch, N.J., 1953. The cleavage strength of polycrystals. J. Iron Steel Inst. 174, 25–28.

Poh, L.H., Peerlings, R.H.J., Geers, M.G.D., Swaddiwudhipong, S., 2011. An implicit tensorial gradient plasticity model - Formulation and comparison with a scalar gradient model. International Journal of Solids and Structures 48, 2595–2604. doi:10.1016/j.ijsolstr.2011.05.019.

Polizzotto, C., Borino, G., 1998. A thermodynamics-based formulation of gradient-dependent plasticity. European Journal of Mechanics - A/Solids 17, 741–761. doi:10.1016/S0997-7538(98)80003-X.

Poole, W., Ashby, M., Fleck, N., 1996. Micro-hardness of annealed and work-hardened copper polycrystals. Scripta Materialia 34, 559–564. doi:10.1016/1359-6462(95)00524-2.

Pradeep Raja, C., Ramesh, T., 2021. Influence of size effects and its key issues during micro-forming and its associated processes – A review. Engineering Science and Technology, an International Journal 24, 556–570. doi:10.1016/j.jestch.2020.08.007.

Qian, X., Zhang, S., Swaddiwudhipong, S., Shen, L., 2013. Temperature dependence of material length scale for strain gradient plasticity and its effect on near-tip opening displacement. Fatigue I& Fracture of Engineering Materials I& Structures 37. doi:10.1111/ffe.12096.

Quey, R., Dawson, P., Barbe, F., 2011. Large-scale 3D random polycrystals for the finite element method: Generation, meshing and remeshing. Computer Methods in Applied Mechanics and Engineering 200, 1729–1745. doi:10.1016/j.cma.2011.01.002.

Quey, R., Renversade, L., 2018. Optimal polyhedral description of 3D polycrystals: Method and application to statistical and synchrotron X-ray diffraction data. Computer Methods in Applied Mechanics and Engineering 330, 308–333. doi:10.1016/j.cma.2017.10.029.

Quilici, S., Forest, S., Cailletaud, G., 1998. On size effects in torsion of multi- and polycrystalline specimens. Journal de Physique IV 8, Pr8–325–332.

Ralston, K., Birbilis, N., Weyland, M., Hutchinson, C., 2010. The effect of precipitate size on the yield strength-pitting corrosion correlation in Al–Cu–Mg alloys. Acta Materialia 58, 5941–5948. doi:10.1016/j.actamat.2010.07.010.

Ravichandran, G., Rosakis, A.J., Hodowany, J., Rosakis, P., 2002. On the conversion of plastic work into heat during high strain rate deformation. AIP Conference Proceedings 620, 557–562. doi:10.1063/1.1483600.

Rice, J., 1971. Inelastic constitutive relations for solids: An internal-variable theory and its application to metal plasticity. Journal of the Mechanics and Physics of Solids 19, 433–455. doi:10.1016/0022-5096(71)90010-X.

Ristinmaa, M., Wallin, M., Ottosen, N., 2007. Thermodynamic format and heat generation of isotropic hardening plasticity. Acta Mechanica 194, 103–121. doi:10.1007/s00707-007-0448-6.

Rittel, D., 1999. On the conversion of plastic work to heat during high strain rate deformation of glassy polymers. Mechanics of Materials 31, 131–139. doi:10.1016/S0167-6636(98)00063-5.

Rittel, D., Kidane, A., Alkhader, M., Venkert, A., Landau, P., Ravichandran, G., 2012. On the dynamically stored energy of cold work in pure single crystal and polycrystalline copper. Acta Materialia 60, 3719–3728. doi:10.1016/j.actamat.2012.03.029.

Rittel, D., Zhang, L., Osovski, S., 2017. The dependence of the taylor–quinney coefficient on the dynamic loading mode. Journal of the Mechanics and Physics of Solids 107, 96–114. doi:10.1016/j.jmps.2017.06.016.

Rogers, H.C., 1979. Adiabatic plastic deformation. Annual Review of Materials Science 9, 283–311. doi:10.1146/annurev.ms.09.080179.001435.

Roters, F., Eisenlohr, P., Hantcherli, L., Tjahjanto, D., Bieler, T., Raabe, D., 2010. Overview of constitutive laws, kinematics, homogenization and multiscale methods in crystal plasticity finite-element modeling: Theory, experiments, applications. Acta Materialia 58, 1152–1211. doi:10.1016/j.actamat.2009.10.058.

Royer, R., Cahuc, O., Gérard, A., 2012. Strain Gradient Plasticity Applied To Material Cutting. Journal of Advanced Materials Research 423, 103–132. doi:10.4028/www.scientific.net/AMR.423.103.

Royer, R., Laheurte, R., Darnis, P., Gérard, A., Cahuc, O., 2011. Strain gradient plasticity theory applied to machining. AIP Conference Proceedings 1353, 591–596. doi:10.1063/1.3589579.

Rudnicki, J., Rice, J., 1975. Conditions for the localization of deformation in pressure-sensitive dilatant materials. Journal of the Mechanics and Physics of Solids 23, 371–394. doi:10.1016/0022-5096(75)90001-0.

Russo, R., Forest, S., Girot Mata, F.A., 2020a. Thermomechanics of Cosserat medium: modeling adiabatic shear bands in metals. Continuum Mechanics and Thermodynamics doi:10.1007/s00161-020-00930-z.

Russo, R., Girot Mata, F.A., Forest, S., Jacquin, D., 2020b. A review on strain gradient plasticity approaches in simulation of manufacturing processes. Journal of Manufacturing and Materials Processing 4. doi:10.3390/jmmp4030087.

Ryś, M., Forest, S., Petryk, H., 2020. A micromorphic crystal plasticity model with the gradient-enhanced incremental hardening law. International Journal of Plasticity , 102655doi:10.1016/j.ijplas.2019.102655.

Ryś, M., Forest, S., Petryk, H., 2020. A micromorphic crystal plasticity model with the gradient-enhanced incremental hardening law. International Journal of Plasticity 128, 102655. doi:10.1016/j.ijplas.2019.102655.

Saanouni, K., Hamed, M., 2013. Micromorphic approach for finite gradient-elastoplasticity fully coupled with ductile damage: Formulation and computational aspects. International Journal of Solids and Structures 50, 2289–2309. doi:10.1016/j.ijsolstr.2013.03.027.

Scherer, J., Besson, J., Forest, S., Hure, J., Tanguy, B., 2019. Strain gradient crystal plasticity with evolving length scale: Application to voided irradiated materials. European Journal of Mechanics-A/Solids 77, 103768.

Scherer, J.M., Phalke, V., Besson, J., Forest, S., Hure, J., Tanguy, B., 2020. Lagrange multiplier based vs micromorphic gradient-enhanced rate-(in)dependent crystal plasticity modelling and simulation. Computer Methods in Applied Mechanics and Engineering 372, 113426. doi:ttps://doi.org/10.1016/j.cma.2020.113426.

Segel, L.A., 1977. Mathematics applied to continuum mechanics. Society for industrial and applied mathematics.

Segurado, J., Lebensohn, R.A., LLorca, J., 2018. Chapter one - computational homogenization of polycrystals, in: Hussein, M.I. (Ed.), Advances in Crystals and Elastic Metamaterials, Part 1. Elsevier. volume 51 of *Advances in Applied Mechanics*, pp. 1–114. doi:10.1016/bs.aams.2018.07.001.

Seupel, A., Hütter, G., Kuna, M., 2018. An efficient FE-implementation of implicit gradient-enhanced damage models to simulate ductile failure. Engineering Fracture Mechanics 199, 41–60. doi:10.1016/j.engfracmech.2018.01.022.

Shu, J., 1998. Scale–dependent deformation of porous single crystals. International Journal of Plasticity 14, 1085–1107. doi:10.1016/S0749-6419(98)00048-5.

Simo, J., Miehe, C., 1992. Associative coupled thermoplasticity at finite strains: Formulation, numerical analysis and implementation. Computer Methods in Applied Mechanics and Engineering 98, 41–104. doi:10.1016/0045-7825(92)90170-O.

dong Song, W., lei Hu, M., sheng Zhang, H., xi Jin, Y., 2018. Effects of different heat treatments on the dynamic shear response and shear localization in inconel 718 alloy. Materials Science and Engineering: A 725, 76–87. doi:10.1016/j.msea.2018.04.010.

Stathas, A., Stefanou, I., 2021. The role of viscous regularization in dynamical problems, strain localization and mesh dependency. arXiv .

Steinmann, P., Kergaßner, A., Landkammer, P., Zbib, H.M., 2019. A novel continuum approach to gradient plasticity based on the complementing concepts of dislocation and disequilibrium densities. Journal of the Mechanics and Physics of Solids 132, 103680. doi:10.1016/j.jmps.2019.103680.

Stelmashenko, N., Walls, M., Brown, L., Milman, Y., 1993. Microindentations on w and mo oriented single crystals: An stm study. Acta Metallurgica et Materialia 41, 2855–2865. doi:10.1016/0956-7151(93)90100-7.

Stölken, J., Evans, A., 1998. A microbend test method for measuring the plasticity length scale. Acta Materialia 46, 5109–5115. doi:10.1016/S1359-6454(98)00153-0.

Takeuchi, T., 1975. Work hardening of copper single crystals with multiple glide orientations. Transactions of the Japan Institute of Metals 16, 629–640. doi:10.2320/matertrans1960.16.629.

Tandon, G.P., Weng, G.J., 1988. A Theory of Particle-Reinforced Plasticity. Journal of Applied Mechanics 55, 126–135. doi:10.1115/1.3173618.

Taylor, G.I., 1938. Plastic strain in metals. Journal of the Institute of Metals 62, 307–324.

Taylor, G.I., Elam, C.F., 1923. Bakerian lecture: The distortion of an aluminium crystal during a tensile test. Proceedings of the Royal Society of London. Series A, Containing Papers of a Mathematical and Physical Character 102, 643–667.

Taylor, G.I., Elam, C.F., 1925. The plastic extension and fracture of aluminium crystals. Proceedings of the Royal Society of London. Series A, Containing Papers of a Mathematical and Physical Character 108, 28–51.

Taylor, G.I., Quinney, H., 1934. The Latent Energy Remaining in a Metal after Cold Working. Proceedings of the Royal Society of London Series A 143, 307–326.

Teodosiu, C., Sidoroff, F., 1976. A theory of finite elastoviscoplasticity of single crystals. International Journal of Engineering Science 14, 165–176. doi:10.1016/0020-7225(76)90085-9.

Timothy, S., 1987. The structure of adiabatic shear bands in metals: A critical review. Acta Metallurgica 35, 301–306. doi:10.1016/0001-6160(87)90238-0.

Tresca, H., 1878. On further applications of the flow of solids. Journal of the Franklin Institute 106, 263–270. doi:10.1016/0016-0032(78)90311-3.

Tsagrakis, I., Aifantis, E.C., 2015. On the effect of strain gradient on adiabatic shear banding. Metallurgical and Materials Transactions A 46, 4459–4467. doi:10.1007/s11661-014-2586-5.

Uchic, M.D., Dimiduk, D.M., Florando, J.N., Nix, W.D., 2004. Sample dimensions influence strength and crystal plasticity. Science 305, 986–989. doi:10.1126/science.1098993.

Vignjevic, R., Djordjevic, N., Vuyst, T.D., Gemkow, S., 2018. Modelling of strain softening materials based on equivalent damage force. Computer Methods in Applied Mechanics and Engineering 335, 52–68. doi:10.1016/j.cma.2018.01.049.

Voyiadjis, G., Asce, F., Faghihi, D., Zhang, C., 2011. Analytical and experimental determination of rate- and temperature-dependent length scales using nanoindentation experiments. Journal of Nanomechanics and Micromechanics 1. doi:10.1061/(ASCE)NM.2153-5477.0000027.

Voyiadjis, G.Z., Al-Rub, R.K.A., 2005. Gradient plasticity theory with a variable length scale parameter. International Journal of Solids and Structures 42, 3998–4029. doi:10.1016/j.ijsolstr.2004.12.010.

Voyiadjis, G.Z., Song, Y., 2019. Strain gradient continuum plasticity theories: Theoretical, numerical and experimental investigations. International Journal of Plasticity 121, 21–75. doi:10.1016/j.ijplas.2019.03.002.

Voyiadjis, G.Z., Yaghoobi, M., 2019. Chapter 1 - introduction: Size effects in materials, in: Voyiadjis, G.Z., Yaghoobi, M. (Eds.), Size Effects in Plasticity. Academic Press, pp. 1–79. doi:10.1016/B978-0-12-812236-5.00001-3.

Voyiadjis, G.Z., Zhang, C., 2015. The mechanical behavior during nanoindentation near the grain boundary in a bicrystal fcc metal. Materials Science and Engineering: A 621, 218–228. doi:10.1016/j.msea.2014.10.070.

Wang, W., Huang, Y., Hsia, K., Hu, K., Chandra, A., 2003. A study of microbend test by strain gradient plasticity. International Journal of Plasticity 19, 365–382. doi:10.1016/S0749-6419(01)00066-3.

Wcisło, B., Pamin, J., 2017. Local and non-local thermomechanical modeling of elastic-plastic materials undergoing large strains. International Journal for Numerical Methods in Engineering 109, 102–124. doi:10.1002/nme.5280.

Wcisło, B., Pamin, J., Kowalczyk-Gajewska, K., Menzel, A., 2018. Numerical analysis of ellipticity condition for large strain plasticity. AIP Conference Proceedings 1922, 140008. doi:10.1063/1.5019150.

Weinberger, C.R., Cai, W., 2010. Plasticity of metal wires in torsion: Molecular dynamics and dislocation dynamics simulations. Journal of the Mechanics and Physics of Solids 58, 1011–1025. doi:10.1016/j.jmps.2010.04.010.

Williams, R., 1965. The stored energy of copper deformed at 24°C. Acta Metallurgica 13, 163–168. doi:10.1016/0001-6160(65)90192-6.

Willis, J., 1969. Some constitutive equations applicable to problems of large dynamic plastic deformation. Journal of the Mechanics and Physics of Solids 17, 359–369. doi:10.1016/0022-5096(69)90023-4.

Wolf, J., Longère, P., Crété, J.P., Cadou, J.M., 2019. Strain localization in ductile materials: Assessment of three x-fem-based enrichment methods. Mechanics Research Communications 99, 1–7. doi:10.1016/j.mechrescom.2019.05.010.

Wu, R., Zaiser, M., 2021. Thermodynamic considerations on a class of dislocation-based constitutive models. arXiv:2106.14358.

Wulfinghoff, S., Böhlke, T., 2012. Equivalent plastic strain gradient enhancement of single crystal plasticity: theory and numerics. Proceedings of the Royal Society A: Mathematical, Physical and Engineering Sciences 468, 2682–2703. doi:10.1098/rspa.2012.0073.

Wulfinghoff, S., Böhlke, T., 2013. Equivalent plastic strain gradient crystal plasticity-enhanced power law subroutine. GAMM-Mitteilungen 36, 134–148.

Wulfinghoff, S., Forest, S., Böhlke, T., 2015. Strain gradient plasticity modeling of the cyclic behavior of laminate microstructures. Journal of the Mechanics and Physics of Solids 79, 1–20. doi:10.1016/j.jmps.2015.02.008.

Xiong, Q., Li, Z., Shimada, T., Kitamura, T., 2021. Energy storage and dissipation of elastic-plastic deformation under shock compression: Simulation and analysis. Mechanics of Materials 158, 103876. doi:10.1016/j.mechmat.2021.103876.

Xiong, Y., Li, N., Jiang, H., Li, Z., Xu, Z., Liu, L., 2014. Microstructural evolutions of AA7055 aluminum alloy under dynamic and quasi-static compressions. Acta Metallurgica Sinica (English Letters) 27, 272–278. doi:10.1007/s40195-014-0041-7.

Xu, Y., Zhang, J., Bai, Y., 2008. Shear localization in dynamic deformation: Microstructural evolution. Metallurgical and Materials Transactions A 39, 811–843. doi:10.1007/s11661-007-9431-z.

Xue, Q., Gray, G., Henrie, B., Maloy, S., Chen, S., 2005. Influence of shock prestraining on the formation of shear localization in 304 stainless steel. Metallurgical and Materials Transactions A 36, 1471–1486. doi:10.1007/s11661-005-0239-4.

Yalcinkaya, T., Brekelmans, W., Geers, M., 2012. Non-convex rate dependent strain gradient crystal plasticity and deformation patterning. International Journal of Solids and Structures 49, 2625–2636. doi:10.1016/j.ijsolstr.2012.05.029.

Yan, N., Li, Z., Xu, Y., Meyers, M.A., 2021. Shear localization in metallic materials at high strain rates. Progress in Materials Science 119, 100755. doi:https://doi.org/10.1016/j.pmatsci.2020.100755.

Yang, Q., Stainier, L., Ortiz, M., 2006. A variational formulation of the coupled thermo-mechanical boundary-value problem for general dissipative solids. Journal of the Mechanics and Physics of Solids 54, 401–424. doi:10.1016/j.jmps.2005.08.010.

Zaera, R., Rodríguez-Martínez, J., Rittel, D., 2013. On the taylor–quinney coefficient in dynamically phase transforming materials. application to 304 stainless steel. International Journal of Plasticity 40, 185–201. doi:10.1016/j.ijplas.2012.08.003.

Zbib, H.M., Aifantis, E.C., 1988. On the structure and width of shear bands. Scripta Metallurgica 22, 703–708.

Zehnder, A.T., 1991. A model for the heating due to plastic work. Mechanics Research Communications 18, 23–28. doi:10.1016/0093-6413(91)90023-P.

Zhang, H.M., Dong, X.H., Wang, Q., Li, H., 2013. Micro-bending of metallic crystalline foils by non-local dislocation density based crystal plasticity finite element model. Transactions of Nonferrous Metals Society of China 23, 3362–3371. doi:10.1016/S1003-6326(13)62876-9.

Zhang, X., Aifantis, K.E., Senger, J., Weygand, D., Zaiser, M., 2014. Internal length scale and grain boundary yield strength in gradient models of polycrystal plasticity: How do they relate to the dislocation microstructure? Journal of Materials Research 29, 2116–2128. doi:10.1557/jmr.2014.234.

Zhang, Y., Lorentz, E., Besson, J., 2018. Ductile damage modelling with locking-free regularised GTN model. International Journal for Numerical Methods in Engineering 113, 1871–1903. doi:10.1002/nme.5722.

Zhang, Z., Eakins, D.E., Dunne, F.P., 2016. On the formation of adiabatic shear bands in textured HCP polycrystals. International Journal of Plasticity 79, 196–216. doi:10.1016/j.ijplas.2015.12.004.

Zhao, J., Sheng, D., Zhou, W., 2005. Shear banding analysis of geomaterials by strain gradient enhanced damage model. International Journal of Solids and Structures 42, 5335–5355. doi:10.1016/j.ijsolstr.2005.02.029.

Zhu, H., Zbib, H., Aifantis, E.C., 1995. On the role of strain gradients in adiabatic shear banding. Acta Mechanica 111, 111–124. doi:10.1007/BF01187731.

Zhu, J., Lin, Y., Liu, S., Ma, X., Wang, G., 2020. Plasticity and size effects of micro-forming sheet processed by electropulsing. Materials and Manufacturing Processes 35, 1146–1155. doi:10.1080/10426914.2020.1772482.

Appendix A

Slip systems in FCC unit cell and form of the dislocation interaction matrices

- **Slip systems in FCC unit cell**

In FCC crystals, the crystallographic slip occurs on the twelve {111}<110> slip systems; four {111} planes and three <110> directions (Fig. A.1). The definition of the octahedral slip systems is given in Table A.1.

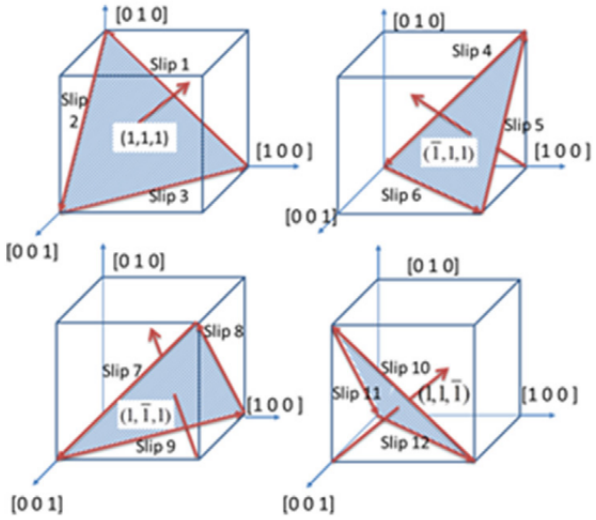

Fig. A.1 Octahedral slip systems in FCC metallic materials (Guan et al., 2017).

Table A.1 Definition of the octahedral slip systems.

Normal vector $\underline{n}$	(111)			(1$\bar{1}$1)			($\bar{1}$11)			(11$\bar{1}$)		
Slip direction $\underline{m}$	[$\bar{1}$01]	[0$\bar{1}$1]	[$\bar{1}$10]	[$\bar{1}$01]	[011]	[110]	[0$\bar{1}$1]	[110]	[101]	[$\bar{1}$10]	[101]	[011]
Slip system index	B_4	B_2	B_5	D_4	D_1	D_6	A_2	A_6	A_3	C_5	C_3	C_1

Form of the dislocation interaction matrices

In FCC single crystals, the matrix h^{ru} (r, u=1,2,...,12) has 12×12 coefficients. The matrix h^{ru} is constructed as follows (Ling et al., 2018):

$$
[h^{ru}] = \begin{array}{c} \begin{array}{cccccccccccc} A_2 & A_3 & A_6 & B_2 & B_4 & B_5 & C_1 & C_3 & C_5 & D_1 & D_4 & D_6 \end{array} \\ \begin{bmatrix} h_0 & h_1 & h_1 & h_3 & h_4 & h_4 & h_2 & h_4 & h_5 & h_2 & h_5 & h_4 \\ & h_0 & h_1 & h_4 & h_2 & h_5 & h_4 & h_3 & h_4 & h_5 & h_2 & h_4 \\ & & h_0 & h_4 & h_5 & h_2 & h_5 & h_4 & h_2 & h_4 & h_4 & h_3 \\ & & & h_0 & h_1 & h_1 & h_2 & h_5 & h_4 & h_2 & h_4 & h_5 \\ & & & & h_0 & h_1 & h_5 & h_2 & h_4 & h_4 & h_3 & h_4 \\ & & & & & h_0 & h_4 & h_4 & h_3 & h_5 & h_4 & h_2 \\ & & & & & & h_0 & h_1 & h_1 & h_3 & h_4 & h_4 \\ & & \text{symmetric} & & & & & h_0 & h_1 & h_4 & h_2 & h_5 \\ & & & & & & & & h_0 & h_4 & h_5 & h_2 \\ & & & & & & & & & h_0 & h_1 & h_1 \\ & & & & & & & & & & h_0 & h_1 \\ & & & & & & & & & & & h_0 \end{bmatrix} \end{array} \begin{array}{c} A_2 \\ A_3 \\ A_6 \\ B_2 \\ B_4 \\ B_5 \\ C_1 \\ C_3 \\ C_5 \\ D_1 \\ D_4 \\ D_6 \end{array}
\tag{A.1}
$$

For symmetry reason number of coefficients are reduced to 6, i.e. $h_0 - h_5$. In the matrix coefficient h_0 corresponds to self hardening, h_1 to coplanar interaction, h_2 to Hirth locks, h_3 to collinear interaction, h_4 to glissile junctions and h_5 to Lomer locks. The matrix b^{ru} has the same structure as h^{ru}.

Appendix B

Single crystal simple shear test

Simple shear test at a finite strain on a single volume element is performed using the classical crystal plasticity model to study the validity of the used finite deformation constitutive framework in the present work (cf. chapter 2, section 2.2). The validity of the model is performed via a brief comparison of the predicted shear stress-shear strain response with the results presented in (Boukadia and Sidoroff, 1988; J. Boukadia, 1993).

An elasto-viscoplastic single crystal formulation is used for the simulation of simple shear case according to section 2.2.3. The material behavior is considered as an elastic-perfectly plastic. A rate–dependent flow rule is adopted to facilitate the determination of active slip systems. The schematic of the simple glide test is shown in Fig. B.1. The initial orientation of the crystal with respect to loading axes of simple shear is as follows:

$$\underline{e}_1 = [100] \quad \underline{e}_2 = [010] \quad \underline{e}_3 = [001].$$

The numerical values of the material parameters used are given in Table B.1. The shear stress-strain response plotted at one Gauss point of the volume element is shown in Fig. B.2a. As shown in this figure, cyclic behavior is obtained for the stress distribution. Such a cyclic behavior is also observed by Boukadia and Sidoroff (1988); J. Boukadia (1993) under large deformations and rotations for simple shear tests. The crystal follows the corotational frame, and during the endless rotation of the crystal, some slip systems are successively activated and deactivated during the endless rotation of the crystal. However, 8 slip systems are always simultaneously activated as shown in Fig. B.2b. The effect of different crystal orientations on the stress-strain response in simple shear tests is studied in (Besson et al., 2010).

Table B.1 Numerical values of material parameters used for the numerical simulation of simple shear test.

C_{11}	C_{12}	C_{44}	τ_0	m	K
198.6 GPa	136.2 GPa	104.7 GPa	150 MPa	10	10 MPa.s$^{1/m}$

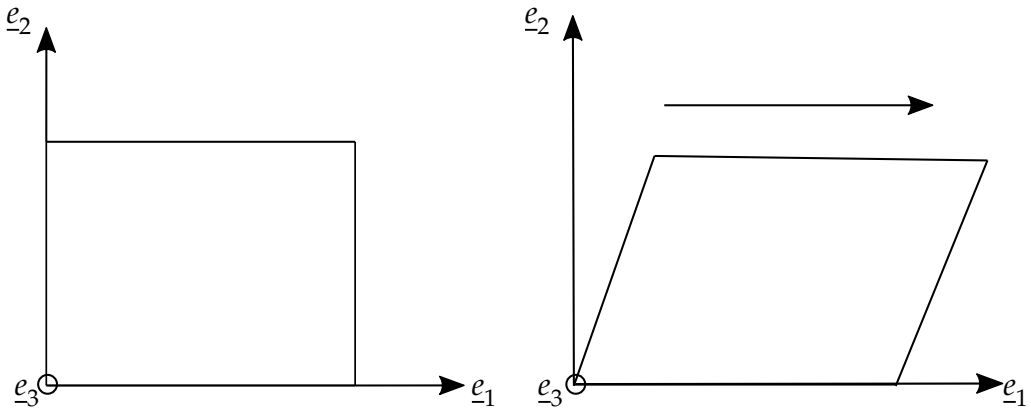

Fig. B.1 Schematic of the simple shear test.

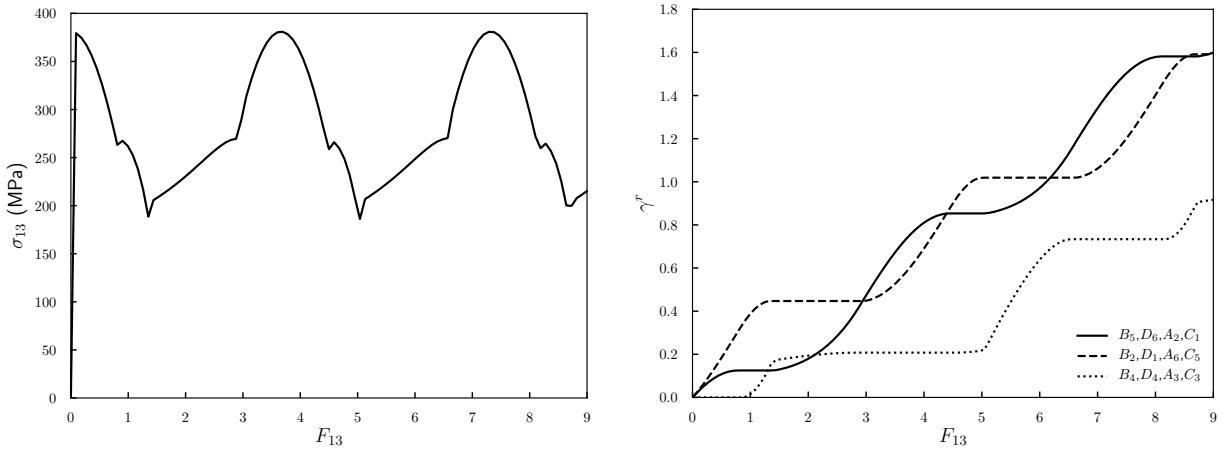

(a) (b)

Fig. B.2 Simple shear test of a single crystal of initial orientation <001>: (a) shear stress-strain response, and (b) slip system activity.

Appendix C

Dislocation density tensor calculation

In this appendix, several topics about curl operation and related dislocation density calculations are presented.

• Curl of a second-order tensor

There are several definitions available in the literature to compute the curl of a second-order tensor. However, consistent application of these curl definition leads to same results as demonstrated in (Das et al., 2018). The derivation of the three most commonly used definitions to compute the curl of a second-order tensor in a Cartesian orthonormal coordinate frame are as follows:

- $\text{curl}^1(\underset{\sim}{T})$ (Malvern, 1969; Segel, 1977):

$$\text{curl}^1(\underset{\sim}{T}) = (\nabla \times \underset{\sim}{T})_{ij} = \left(\underline{e}_r \frac{\partial}{\partial x_r}\right) \times T_{sj}\, \underline{e}_s \otimes \underline{e}_j = (\underline{e}_r \times \underline{e}_s) \otimes \underline{e}_j \frac{\partial T_{sj}}{\partial x_r}, \tag{C.1}$$

which can be further written as

$$\text{curl}^1(\underset{\sim}{T}) = (\nabla \times \underset{\sim}{T})_{ij} = \epsilon_{rsi} T_{sj,r}. \tag{C.2}$$

- $\text{curl}^2(\underset{\sim}{T})$ (Acharya and Bassani, 2000; Cordero et al., 2010; Aslan et al., 2011):

$$\text{curl}^2(\underset{\sim}{T}) = (\underset{\sim}{T} \times \nabla)_{ij} = (T_{is}\, \underline{e}_i \otimes \underline{e}_s) \times \left(\underline{e}_r \frac{\partial}{\partial e_i}\right) = T_{is}\, \underline{e}_i \otimes (\underline{e}_s \times \underline{e}_r) \frac{\partial}{\partial x_r} \tag{C.3}$$

Thus,

$$\text{curl}^2(\underset{\sim}{T}) = (\underset{\sim}{T} \times \nabla)_{ij} = (\underline{e}_i \otimes \underline{e}_j) \epsilon_{srj} \frac{\partial T_{is}}{\partial x_r} = \epsilon_{srj} T_{is,r} = -\epsilon_{jrs} T_{is,r}. \tag{C.4}$$

- $\text{curl}^3(\underset{\sim}{T})$ (Arsenlis and Parks, 1999; Cermelli and Gurtin, 2001):

If $\underline{f}$ is a vector then,

$$\nabla \times (\underline{f} \cdot \underset{\sim}{T}) = (\nabla \times \underset{\sim}{T}) \cdot \underline{f}, \tag{C.5}$$

$$\underline{v} = \underline{f} \cdot \underset{\sim}{T} = f_j T_{js} \underline{e}_s. \tag{C.6}$$

Therefore,

$$(\nabla \times \underline{v})_k = \left(\underline{e}_r \frac{\partial}{\partial x_r}\right) \times f_j T_{js} \underline{e}_s = (\underline{e}_r \times \underline{e}_s) f_j \left(\frac{\partial}{\partial x_r}\right) T_{js} = \epsilon_{rsi} f_j T_{js,r} \underline{e}_k,$$

$$= (\epsilon_{rsi} T_{js,r} \underline{e}_i \otimes \underline{e}_j) \cdot \underline{f} = (\nabla \times \underset{\sim}{T}) \cdot \underline{f}. \tag{C.7}$$

Finally,

$$\text{curl}^3(\underset{\sim}{T}) = (\nabla \times \underset{\sim}{T})_{ij} = \epsilon_{rsi} T_{js,r}. \tag{C.8}$$

Let c be the line integral with respect to the current configuration bounding surface s having unit normal $\underline{n}$, then the application of Stokes' theorem to smooth vector field $\underline{f}$

$$\oint_c \underline{f} \cdot dx = \int_s (\text{curl}\, \underline{f}) \cdot \underline{n}\, ds, \tag{C.9}$$

and to the tensor field gives

$$\oint_c \underset{\sim}{T} \cdot dx = \int_s (\text{curl}\, \underset{\sim}{T}) \cdot \underline{n}\, ds. \tag{C.10}$$

• Dislocation density tensor calculation

In the finite strain crystal plasticity, it is assumed that the lattice is only distorted elastically. In continuum theories of plasticity, it is commonly accepted that intermediate plastic configuration is not compatible (Acharya and Bassani, 1995). This incompatibility of the intermediate configuration is due to presence of GNDs (closure failure of the Burgers circuit). An elastic and a plastic part of the deformation gradient are incompatible tensor fields such that

$$\text{Curl}\, \underset{\sim}{F}^e \neq 0, \quad \text{Curl}\, \underset{\sim}{F}^p \neq 0, \tag{C.11}$$

even though the total deformation gradient is compatible

$$\text{Curl}\, \underset{\sim}{F} = 0. \tag{C.12}$$

The definition of the dislocation density tensor based on the small and finite deformation theory is given in the following sections. Used notations are as follows: grad, div, and curl for the differential operators defined with respect to the current configuration, and Grad, Div, and Curl for the differential operators defined with respect to the reference configuration. Besides, the curl of a second-order tensor is defined according to Eq. (C.4).

• Small deformation

Gurtin and Anand (2005) proposed a theory for small deformation strain gradient plasticity for isotropic materials in absence of rotations. The theory of classical small deformation is based on the decomposition of displacement gradient additively into an elastic and the

plastic part such that

$$\text{Grad}\,\underset{\sim}{u} = \underset{\sim}{H}^e + \underset{\sim}{H}^p, \quad \text{tr}\,\underset{\sim}{H}^p \equiv 0, \tag{C.13}$$

with $\underset{\sim}{H}^e$ being the rotation and stretch tensor, $\underset{\sim}{H}^p$ is the lattice distortion tensor, and tr stands for the trace of a second-order tensor. Moreover, in this plasticity theory, an elastic and a plastic strain tensors are given by

$$\underset{\sim}{E}^e = \frac{1}{2}(\underset{\sim}{H}^e + \underset{\sim}{H}^{eT}), \quad \underset{\sim}{E}^p = \frac{1}{2}(\underset{\sim}{H}^p + \underset{\sim}{H}^{pT}). \tag{C.14}$$

Furthermore, the plastic rotation tensor is expressed as

$$\underset{\sim}{W}^p = \frac{1}{2}(\underset{\sim}{H}^p - \underset{\sim}{H}^{pT}). \tag{C.15}$$

In addition, the resultant Burgers vector in the reference configuration is given by

$$\underline{B} = \oint_C \underset{\sim}{H}^p \cdot \underline{dX}, \tag{C.16}$$

where C denote the line integral with respect to the reference configuration bounding surface S having unit normal $\underline{N}$. The application of Stokes' theorem to previous equation gives

$$\underline{B} = \int_S (\text{Curl}\,\underset{\sim}{H}^p) \cdot \underline{N}\, dS. \tag{C.17}$$

The dislocation density tensor for small deformation plasticity is defined by

$$(\underset{\sim}{D}_d)_{ij} = (\text{Curl}\,\underset{\sim}{H}^p)_{ij} = -\epsilon_{jrs} H_{is,r}\, \underline{e}_i \otimes \underline{e}_j. \tag{C.18}$$

• Finite deformation

The closure failure with respect to the current configuration is defined as follows (Acharya and Bassani, 2000):

$$\underline{b} = \oint_c \underset{\sim}{F}^{e-1} \cdot \underline{dx}. \tag{C.19}$$

Applying Stokes' theorem to the previous equation gives

$$\underline{b} = \int_s (\text{curl}\,\underset{\sim}{F}^{e-1}) \cdot \underline{n}\, ds. \tag{C.20}$$

Therefore, the dislocation density tensor $\underset{\sim}{D}_d$ with respect to the current configuration is given by

$$(\underset{\sim}{D}_d)_{ij} = (\text{curl}\,\underset{\sim}{F}^{e-1})_{ij} = -\epsilon_{jrs} F^{e-1}_{is,r}\, \underline{e}_i \otimes \underline{e}_j, . \tag{C.21}$$

The resultant Burgers vector in the reference configuration is given by

$$\underline{B} = \oint_C \underset{\sim}{F}^{e-1} \cdot \underset{\sim}{F} \cdot \underline{dX} = \oint_C \underset{\sim}{F}^{p} \cdot \underline{dX} = \int_S (\mathrm{Curl}\,(\underset{\sim}{F}^{p})) \cdot \underline{N}\, dS. \tag{C.22}$$

Applying Nanson's formula, $\underline{N}dS = \underset{\sim}{F}^{T} \frac{\underline{n}}{J} ds$, gives

$$\underline{B} = \int_s (\mathrm{Curl}\,(\underset{\sim}{F}^{p})) \cdot \underset{\sim}{F}^{T} \cdot \frac{\underline{n}\, ds}{J}. \tag{C.23}$$

Therefore, the alternative definition of the dislocation density tensor

$$\underset{\sim}{D}_d = \frac{1}{J} (\mathrm{Curl}\,(\underset{\sim}{F}^{p})) \cdot \underset{\sim}{F}^{T} = \mathrm{curl}\,(\underset{\sim}{F}^{e-1}). \tag{C.24}$$

• Dislocation density tensor in pure bending of a single crystal

As the crystal is subjected to a plastic strain gradient, GNDs must be stored to accommodate this plastic strain gradient. The approximation of GND density in a single-slip problem is given by Fleck et al. (1994) as follows:

$$\rho_G = \frac{1}{b} \frac{\partial \gamma}{\partial e_1}, \tag{C.25}$$

where $\frac{\partial \gamma}{\partial e_1}$ denote the variation of shear strain γ in e_1 direction. Let $d\phi_i$ be the lattice rotation angle associated with the displacement vector de_i then

$$d\phi_i = k_{ij} de_j, \tag{C.26}$$

with k_{ij} being the curvature tensor. The relation between curvature tensor $\underset{\sim}{k}$ and dislocation density tensor $\underset{\sim}{D}_d$ is given by Ashby (1970) as follows:

$$k_{ij} = (D_d)_{ji} - \frac{1}{2} \delta_{ij} (D_d)_{kk}. \tag{C.27}$$

In the case of pure bending, the only non-vanishing component of the curvature tensor is

$$k_{31} = \frac{d\phi_3}{de_1}, \tag{C.28}$$

which corresponds to the bending about e_3-axis. Therefore, the dislocation density tensor for pure bending is given by

$$\underset{\sim}{D}_d = \begin{bmatrix} 0 & 0 & (D_d)_{13} \\ 0 & 0 & 0 \\ 0 & 0 & 0 \end{bmatrix}. \tag{C.29}$$

Table C.1 Numerical values of material parameters used for the numerical simulation of pure bending test.

E	ν	τ_0	m	K
200 GPa	0.33	150 MPa	10	10 MPa.s$^{1/m}$

Moreover, in the present work, the dislocation density tensor components are computed with FE simulation for the single crystal pure bending tests using the classical crystal plasticity model. A post-processing technique is used to evaluate Curl$(\underset{\sim}{F}^p)$ (see also, Busso et al. (2000); Abrivard (2009)). The four-point bending test provides the validity of the implemented post-processing code to compute the dislocation density tensor because of the known active component in the pure bending test. The linear variation of plastic strain across the section of the beam results in a constant strain gradient at a region of plastic strain and consequently the GND density as demonstrated in (Dunne et al., 2012). Moreover, the definition of the curl presented in Eq. (C.4) is used. The details of the used post-processing technique can be found in section 3.3.2.

This study considers a single crystal symmetric rectangular beam of 0.5 mm × 0.1 mm × 0.08 mm dimension having one element across the thickness. The applied boundary conditions are reported in Fig. C.1a. The beam is discretized with C3D20R elements under plane strain conditions. The left face of the beam is fixed in $\underline{e}_1$ direction. The support and load are applied at a distance of 0.14 mm and 0.38 mm from the left face. The initial orientation of the crystal is

$$\underline{e}_1 = [100] \quad \underline{e}_2 = [010] \quad \underline{e}_3 = [001].$$

Isotropic elasticity is considered. The material behavior is considered as an elastic-perfectly plastic. The material parameters used in the simulation are summarized in Table C.1. The distribution of cumulative plastic strain field is shown in Fig. C.1b. As shown in this figure, the plastic strain is concentrated at the center portion of the beam. The components of the dislocation density tensor are computed on the element set shown with red color in Fig. C.1a. The evolution of the components of the dislocation density tensor over this element set is shown in Fig. C.2. As shown in this figure, the only active component of the dislocation density tensor is the $(D_d)_{13}$, which corresponds to the definition of the dislocation density tensor in pure being presented above (Eq. (C.29)). This shows that the implemented post-processing code to compute the dislocation density tensor is valid.

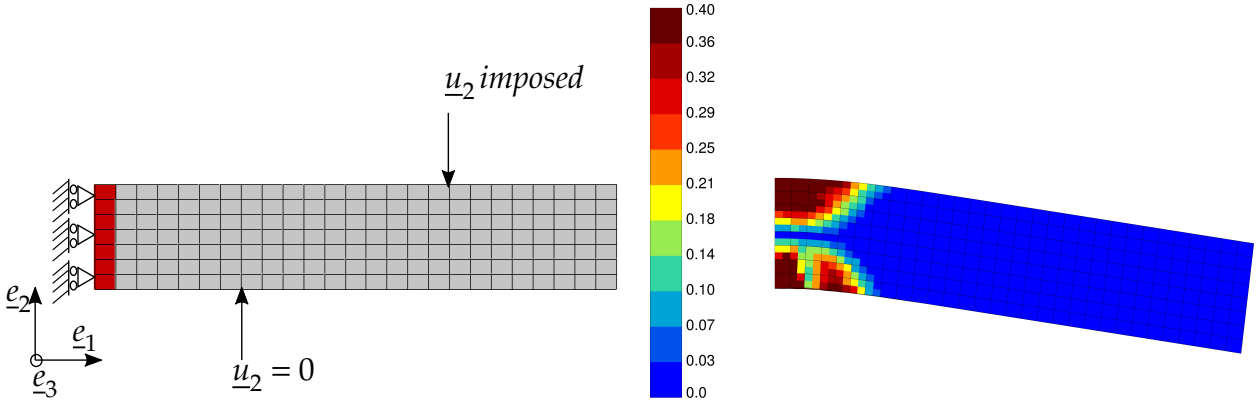

(a) (b)

Fig. C.1 (a) Geometry and applied boundary conditions in four-point bending test. The dislocation density tensor components are computed on the elements marked with red color. (b) Cumulative plastic strain field in single crystal pure bending test.

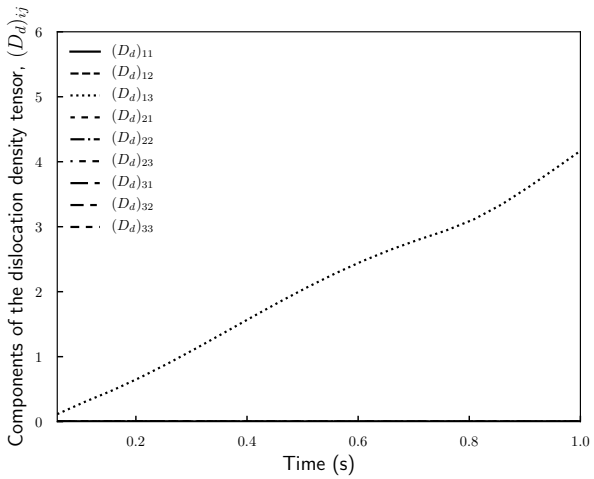

Fig. C.2 Evolution of the dislocation density tensor components obtained using post-processing on the elements marked with red color in Fig. C.1a.

RÉSUMÉ

Les modèles classiques de plasticité cristalline ne parviennent pas à capturer les effets de taille observés expérimentalement, à savoir, plus la taille est petite, plus la force est grande. Ces modèles montrent également une dépendance du maillage dans les problèmes de localisation de déformation due à l'absence d'une échelle de longueur caractéristique dans le cadre constitutif. Les modèles de plasticité cristalline à gradient de déformation peuvent surmonter les limites susmentionnées des modèles de plasticité de cristalline classiques. Cependant, la mise en œuvre du modèle de plasticité à gradient de déformation dans le logiciel commercial des techniciens de maintenance est difficile en raison du cadre constitutif complexe. Dans le présent travail, les modèles de plasticité des cristalline à gradient de déformation, spécifiquement la plasticité des cristalline micromorphique réduit et les modèles fondés sur le multiplicateur de Lagrange, sont utilisés pour prédire l'effet de taille dans des tests de torsion de microfils monocristallins. Une comparaison est effectuée entre l'effet de taille prévu en utilisant le modèle fondés sur le multiplicateur de Lagrange et celui fait par le modèle $CurlF^p$ de la littérature, qui est fondés sur le tenseur de densité de dislocation complet. De plus, la localisation des déformations due à l'élévation de la température est étudiée. Une formulation thermodynamique cohérente des équations constitutives est proposée pour les modèles de plasticité cristalline classique et micromorphique. Ce cadre thermodynamique cohérent est appliqué pour étudier le processus de formation de bandes de cisaillement adiabatique dans des matériaux métalliques cubiques à face centrées (CFC) monocristallins et poly-cristallins. Cinq orientations cristallines différentes d'un seul spécimen en forme de chapeau sont considérées pour étudier la formation, l'intensité et l'orientation des bandes de cisaillement. La formation de bandes de cisaillement adiabatiques et l'effet granulométrique sont étudiés dans des agrégats polycristallins en forme de chapeau. Il est également essentiel de prévoir l'énergie stockée pour comprendre la déformation plastique et les mécanismes de récupération et de recristallisation qui en découlent. Des modèles thermodynamiques de plasticité des cristalline classiques et micromorphique sont utilisés pour prédire l'énergie stockée dans des matériaux métalliques CFC monocristallins et polycristallins. À cette fin, nous proposons un moyen facile de mettre en œuvre le modèle de plasticité micromorphique dans le logiciel commercial modèle d'éléments finis en utilisant l'analogie entre la thermomécanique classique et la théorie de la plasticité micromorphique.

MOTS CLÉS

Effet de taille, Bande de cisaillement adiabatique, Monocristalline, Polycristalline, Plasticité cristalline à gradient de déformation, Modèle réduit, énergie stockée, thermomécanique.

ABSTRACT

Classical crystal plasticity models fail to capture experimentally observed size effects, namely, the smaller the size the greater the strength. These models also show spurious mesh dependency in strain localization problems due to the lack of a characteristic length scale in the constitutive framework. Strain gradient crystal plasticity models can overcome above mentioned limitations of the classical crystal plasticity models. However, implementing the strain gradient plasticity model in commercial finite element (FE) software is challenging due to the complex constitutive framework. In the present work, strain gradient crystal plasticity models, specifically reduced-order micromorphic crystal plasticity and Lagrange multiplier-based models, are used to predict the size effect in single crystals microwire torsion tests. A comparison is performed between the predicted size effect using the Lagrange multiplier-based model and that made by the $CurlF^p$ model from the literature, which is based on the complete dislocation density tensor. Moreover, strain localization due to temperature rise is investigated. A thermodynamically consistent formulation of the constitutive equations is proposed for the classical and micromorphic crystal plasticity models. This thermodynamically consistent framework is applied to investigate the adiabatic shear band (ASB) formation process in single and poly-crystalline Face-Centered Cubic (FCC) metallic materials. Five different crystal orientations of a single crystal hat-shaped specimen are considered to study the formation, intensity, and orientation of shear bands. The formation of ASB and the grain size effect are investigated in hat-shaped polycrystalline aggregates. Moreover, predicting the stored energy is essential to understand the plastic deformation and subsequent recovery and recrystallization mechanisms. Thermodynamically consistent classical and micromorphic crystal plasticity models are used to predict the stored energy in single and poly-crystalline FCC metallic materials. To this end, we propose an easy way to implement the micromorphic plasticity model in commercial FE software using the analogy between classical thermo-mechanics and micromorphic plasticity theory.

KEYWORDS

Size effect, Adiabatic shear band; Single crystals; Polycrystalline; FCC metallic materials; Strain gradient crystal plasticity; reduced-order models; Stored energy; Thermo-mechanics.